



UNIVERSITAT DE
BARCELONA

Exotic phases of matter in low dimensional lattices: from quantum liquids to kinetic magnetism

Ivan Morera Navarro

ADVERTIMENT. La consulta d'aquesta tesi queda condicionada a l'acceptació de les següents condicions d'ús: La difusió d'aquesta tesi per mitjà del servei TDX (www.tdx.cat) i a través del Dipòsit Digital de la UB (diposit.ub.edu) ha estat autoritzada pels titulars dels drets de propietat intel·lectual únicament per a usos privats emmarcats en activitats d'investigació i docència. No s'autoritza la seva reproducció amb finalitats de lucre ni la seva difusió i posada a disposició des d'un lloc aliè al servei TDX ni al Dipòsit Digital de la UB. No s'autoritza la presentació del seu contingut en una finestra o marc aliè a TDX o al Dipòsit Digital de la UB (framing). Aquesta reserva de drets afecta tant al resum de presentació de la tesi com als seus continguts. En la utilització o cita de parts de la tesi és obligat indicar el nom de la persona autora.

ADVERTENCIA. La consulta de esta tesis queda condicionada a la aceptación de las siguientes condiciones de uso: La difusión de esta tesis por medio del servicio TDR (www.tdx.cat) y a través del Repositorio Digital de la UB (diposit.ub.edu) ha sido autorizada por los titulares de los derechos de propiedad intelectual únicamente para usos privados enmarcados en actividades de investigación y docencia. No se autoriza su reproducción con finalidades de lucro ni su difusión y puesta a disposición desde un sitio ajeno al servicio TDR o al Repositorio Digital de la UB. No se autoriza la presentación de su contenido en una ventana o marco ajeno a TDR o al Repositorio Digital de la UB (framing). Esta reserva de derechos afecta tanto al resumen de presentación de la tesis como a sus contenidos. En la utilización o cita de partes de la tesis es obligado indicar el nombre de la persona autora.

WARNING. On having consulted this thesis you're accepting the following use conditions: Spreading this thesis by the TDX (www.tdx.cat) service and by the UB Digital Repository (diposit.ub.edu) has been authorized by the titular of the intellectual property rights only for private uses placed in investigation and teaching activities. Reproduction with lucrative aims is not authorized nor its spreading and availability from a site foreign to the TDX service or to the UB Digital Repository. Introducing its content in a window or frame foreign to the TDX service or to the UB Digital Repository is not authorized (framing). Those rights affect to the presentation summary of the thesis as well as to its contents. In the using or citation of parts of the thesis it's obliged to indicate the name of the author.

EXOTIC PHASES OF MATTER IN LOW
DIMENSIONAL LATTICES: FROM QUANTUM
LIQUIDS TO KINETIC MAGNETISM

Doctoral Thesis
IVAN MORERA NAVARRO

UNIVERSITAT DE BARCELONA
DEPARTAMENT DE FÍSICA QUÀNTICA I ASTROFÍSICA



UNIVERSITAT DE
BARCELONA

EXOTIC PHASES OF MATTER IN LOW DIMENSIONAL LATTICES:
FROM QUANTUM LIQUIDS TO KINETIC MAGNETISM

Memòria presentada per optar al grau de doctor per la
Universitat de Barcelona
Programa de doctorat en Física

Autor
IVAN MORERA NAVARRO

Director
PROF. BRUNO JULIÁ-DÍAZ

Tutor
PROF. JOAN SOTO RIERA



UNIVERSITAT_{DE}
BARCELONA

ABSTRACT

By harnessing the synergies between atomic, optical, and condensed matter physics, we can enhance our understanding of quantum many-body systems. In the last few decades, atomic systems have provided controllable and tunable platforms where we can test and study different quantum many-body theories. More recently, the fabrication of two-dimensional materials has opened a new field of study in condensed matter physics, which also holds the promise of providing controllable setups to explore exotic phases of matter. These phases may arise when different mechanisms compete and favor different ground state configurations. In this Thesis, we focus on two classes of lattice systems with competing mechanisms. The first class concerns fluids with both repulsive and attractive interactions, which can result in the appearance of quantum liquid phases. The second class corresponds to systems with geometric frustration, where the minimization of kinetic energy is incompatible with the underlying lattice geometry.

In the first part of this Thesis, we show how quantum liquid phases emerge in ultracold atomic systems loaded into high one-dimensional optical lattices. We study different microscopic systems, including two-component bosonic mixtures, single-component dipolar systems, and single-component systems with two- and three-body interactions. For the bosonic mixture, we investigate Bogoliubov's theory in the weakly interacting regime and derive an effective dimerized theory in the strongly interacting regime. Both theories capture the liquefaction of the mixture and predict a phase transition to a dimerized gas. We perform large-scale, unbiased tensor network simulations, which we contrast with our theoretical predictions, and we find an excellent agreement between them in different regimes of parameters. Moreover, we characterize the different phase transitions with our numerical simulations. Then, we demonstrate that a single-component dipolar system liquefies in the strongly interacting regime due to the presence of superexchange processes. We provide an effective theory that captures the liquefaction and the formation of self-bound Mott insulators. In addition, we provide the two-particle excitation spectrum and observe that its structure provides insights into the many-body phases. Finally, we study the universality of quantum gases and liquids in one dimension and provide a self-consistent theory to solve a quantum fluid with two- and three-body interactions. We demonstrate that quantum gases exhibit universal properties, while quantum liquids do not, since the equation of state depends on microscopic details of the theory. Moreover, we show that the long-distance tails of quantum droplets exhibit a universal decay.

In the second part of this Thesis, we investigate the effects of kinetic frustration on the many-body properties of spin-1/2 fermionic and bosonic systems. Firstly, we study frustrated ladder geometries, such as the zigzag ladder and the square ladder with a perpendicular magnetic flux. For the zigzag ladder, we find that fermionic (bosonic) systems exhibit an effective attractive (repulsive) interaction between holes and spin flips induced solely by kinetic energy and geometric frustration. In the square ladder with a perpendicular magnetic flux, both fermionic and bosonic systems show effective attractive interactions between holes and spin flips. We analyze the formation of multi-body composites and determine their phase diagram. Moreover, we explore the many-body problem where multi-body composites self-organize to form different many-body phases, including a magnetic polaron gas and a pair density wave. We also discuss various protocols for cold atom experiments that could detect these multi-body composites. Secondly, we examine the impact of kinetic frustration on the magnetic properties of a spin-1/2 fermionic system in a triangular lattice at finite and zero temperature. We demonstrate that the system exhibits a magnetic transition as it is doped away from half-filling.

Specifically, the system becomes antiferromagnetic (ferromagnetic) when doped below (above) half-filling. At finite temperature, we observe the system's tendency to form magnetic orders by inspecting the behavior of the magnetic susceptibility. Next, we explore the formation of magnetic many-body phases at low temperatures, including the magnetic polaron gas and the antiferromagnetic spin bag phase. The former is characterized by the formation of magnetization plateaus and the latter by binding of holes. Finally, we provide the temperature dependence of the charge-spin-spin correlation function.

In summary, this Thesis explores the formation of exotic phases of matter that appear when different mechanisms compete to minimize the energy of a many-body system. Such phases could potentially be realized with cold atoms in optical lattices or two-dimensional moiré materials.

RESUM

Aprofitant les sinergies entre la física atòmica, òptica i de la matèria condensada, podem millorar la nostra comprensió dels sistemes quàntics de molts cossos. En les darreres dècades, els sistemes atòmics han proporcionat plataformes controlables i sintonitzables en què podem provar i estudiar diferents teories quàntiques de molts cossos. Més recentment, la fabricació de materials bidimensionals ha obert un nou camp d'estudi a la física de la matèria condensada, que també promet proporcionar plataformes controlables on explorar fases exòtiques de la matèria. Aquestes fases poden sorgir quan diferents mecanismes competeixen i afavoreixen configuracions diferents de l'estat fonamental d'energia. En aquesta Tesi, ens centrem en dues classes de sistemes reticulars amb mecanismes que competeixen entre ells. La primera classe correspon a fluids amb interaccions tant repulsives com atractives, que poden donar lloc a l'aparició de fases líquides quàntiques. La segona classe correspon a sistemes amb frustració geomètrica, on la minimització de l'energia cinètica és incompatible amb la geometria de la xarxa.

A la primera part d'aquesta Tesi, mostrem com emergeixen fases líquides quàntiques en sistemes atòmics ultrafreds carregats en xarxes òptiques unidimensionals. Estudiem diferents sistemes microscòpics incloent barreges bosòniques de dues components, sistemes dipolars d'una component i sistemes d'una component amb interaccions a tres i dos cossos. Per a la barreja bosònica investiguem la teoria de Bogoliubov en el règim d'interacció feble i derivem una teoria efectiva dimeritzada en el règim d'interacció forta. Ambdues teories capturen la líquiefacció de la barreja i prediuen una transició de fase a un gas dimeritzat. Realitzem simulacions de xarxes tensorials insesgades a gran escala que contrastem amb les nostres prediccions teòriques i trobem una excel·lent concordança entre elles en diferents règims de paràmetres. A més, caracteritzem les diferents transicions de fases amb les nostres simulacions numèriques. A continuació, demostrem que un sistema dipolar d'una component es liqua en el règim de forta interacció a causa de la presència de processos "superexchange". Proporcionem una teoria efectiva que captura la líquiefacció i la formació d'aïllants de Mott autolligats. Addicionalment, proporcionem l'espectre d'excitació de dues partícules i observem que la seva estructura permet comprendre les fases de molts cossos. Finalment, estudiem la universalitat dels gasos i líquids quàntics en una dimensió i proporcionem una teoria autoconsistent per resoldre un fluid quàntic en una dimensió amb interaccions de dos i tres cossos. Demostrem que els gasos quàntics mostren propietats universals, mentre que els líquids no, ja que l'equació d'estat depèn dels detalls microscòpics de la teoria. A més, demostrem que les cues de llarga distància de les gotes quàntiques presenten un decaïment universal.

A la segona part d'aquesta Tesi, explorem els efectes de la frustració cinètica en les propietats de molts cossos de sistemes d'espín-1/2 fermiònics i bosònics. En primer lloc, investiguem geometries d'escala frustrada, incloent-hi l'escala en ziga-zaga i l'escala quadrada amb un flux magnètic perpendicular. Per a l'escala en ziga-zaga, trobem que els sistemes fermiònics (bosònics) presenten una interacció efectiva atractiva (repulsiva) entre els forats i els espins voltejats, induïda únicament per l'energia cinètica i la frustració geomètrica. A l'escala quadrada amb un flux magnètic perpendicular, tant els sistemes fermiònics com els bosònics presenten interaccions atractives efectives entre els forats i els espins voltejats. Estudiem la formació de compostos multicos i determinem el seu diagrama de fases. A més, investiguem el problema de molts cossos en què els compostos multicos s'autoorganitzen per formar diferents fases de molts cossos, incloent-hi un gas de polarons magnètics i una ona de densitat de parells. També discutim diferents protocols per a experiments amb àtoms ultrafreds que podrien emprar-se per detectar aquests compostos multicos. En segon lloc, estudiem l'impacte de la

frustració cinètica sobre les propietats magnètiques d'un sistema fermiònic d'espín-1/2 en una xarxa triangular a temperatura finita i zero. Demostrem que el sistema exhibeix una transició magnètica en funció del dopatge. Concretament, el sistema es torna antiferromagnètic (ferromagnètic) quan es dopa per sota (per sobre) de quan està mig ple. A temperatura finita observem la tendència del sistema a formar ordres magnètics inspeccionant el comportament de la susceptibilitat magnètica. A continuació, explorem la formació de fases magnètiques de molts cossos a baixes temperatures. Estudiem el gas polar magnètic caracteritzat per la formació d'altiplans de magnetització i explorem la fase de bossa d'espín antiferromagnètica. Finalment, proporcionem la dependència amb la temperatura de la funció de correlació càrrega-espín-espín.

En resum, aquesta Tesi explora la formació de fases exòtiques de la matèria que apareixen quan diferents mecanismes competeixen per minimitzar l'energia d'un sistema de molts cossos, el qual es podria realitzar potencialment amb àtoms ultrafreds en xarxes òptiques o materials de moiré bidimensionals.

ACKNOWLEDGMENTS

This Thesis would not have been possible without the help and support of many people and institutions. Therefore, it is my duty to acknowledge all those who have helped me during these years.

First of all, I would like to acknowledge financial support by Grant No. PID2020-114626GB-I00 from the MICIN/AEI/10.13039/501100011033 and by the Ministerio de Economía, Industria y Competitividad (MINECO, Spain) under grant No. FIS2017- 87534-P. I also thank financial support from Secretaria d'Universitats i Recerca del Departament d'Empresa i Coneixement de la Generalitat de Catalunya, co-funded by the European Union Regional Development Fund within the ERDF Operational Program of Catalunya (project QuantumCat, ref. 001-P001644).

I would like to thank my supervisor Bruno Juliá-Díaz for his support and guidance during these years. I started working with Bruno during my undergraduate studies when he already gave me the opportunity to join the group and work in very exciting projects. Since then, we have been working together for six years and I am proud of the good physics research we have accomplished together. Besides, he has not only been a reference as a physicist but he has also taught me many things about the professional world. Thank you for trusting me and for your closeness. I have had a great time during the development of this Thesis mainly thanks to you.

I am grateful to Artur Polls who unfortunately cannot see the end of this journey. He originally started to co-supervise this Thesis and was always a referent to me. He was a humble person despite being a tremendous expert in many fields of physics. It was always a pleasure to discuss with him and it was fun to find him in the corridors of the faculty. We miss you very much.

I would like to express my sincere gratitude to Eugene Demler for his warm hospitality at Harvard University and at ETH Zürich. I am grateful for all the collaborations we have initiated together and for the broad vision of the field that you have given me. With you I have had the opportunity to work with many people across the world and learned a lot of physics.

I would like to express my gratitude to all the collaborators who have given me the opportunity to work with them. For that, I wish to thank Grigori E. Astrakharchik, Manuel Valiente, Rafał Oldziejewski, Felipe Isaule, Irénée Frérot, Antonio Muñoz, Annabelle Bohrdt, Wen Wei Ho, Marton Kanász-Nagy, Atac Imamoglu, Livio Ciorciaro and Tomasz Smolenski. Especially, thank you Grigori for all the discussions we had together at the Universitat de Barcelona, where you taught me many things about one-dimensional ultracold atomic fluids.

I would like to thank all the people who have been part of this journey. Among them, I want to start with my close friends in Barcelona: Carlos, Jalil, Ari, Conao, Nil, Héctor, Dani, and Ayoub. Thank you for sharing so many adventures, laughs, beers, and meals with me. Especially, thank you Ari, Conao, and Jalil for the short but intense time we spent together in l'Eixample. I am sure we still have many more years to come. I am also grateful to the friends I made during my Thesis at the Universitat de Barcelona: Diego, Cristian, Íñigo, Miguel, Mikel, Carlos, Aniol, and Marc. Thank you for making my daily life at the university much more enjoyable. I would also like to thank Sam and Sarah for their hospitality at their home in Somerville, and thank you Julio and Nahom for those walks around Cambridge during the difficult times of the pandemic. I am also very grateful to Aaron, Alex, and Pasha with whom I spent a wonderful time in Zürich and enjoyed our discussions in the office. I hope there will be many more in the near future. I would like to thank Marta, Marina, Laia, and Helena who have always welcomed me into their group. And how can I forget Beñat? You will always be welcome in my home. Finally, I would like to express my gratitude to Ana, Jose, and Mario

who have always treated me as a member of their family.

I would like to thank my family. Moltes gràcies mama per ser-hi sempre. En aquests anys m'has ensenyat a ser una persona forta i a superar els obstacles que ens posa la vida. Moltes gràcies Òscar i Marc perquè la vida no seria la mateixa sense vosaltres. Mai oblidaré la nostra infantesa junts. Encara que en els últims anys hem passat per moments difícils, hem pogut seguir endavant i estic segur que el nostre vincle no es trencarà mai. També voldria agrair-te a tu papa. Tot i que no puguis estar aquí per veure el final d'aquest viatge, estic segur que estaries molt content i orgullós. Com que aquesta és la primera tesi de la família (almenys pel que sabem) és tant meva com vostra.

Finally, I would like to express my gratitude to a person who has become very important in the last few years. Thank you, Paula, for all the love, support, and attention you have given me. I am truly grateful to have found such an especial person as you are. You always listen to me carefully and offer your help. Together we have started this adventure which I am sure has many years ahead of it. Especially now, that we have included Auri on it. I love you both with all my heart.

LIST OF PUBLICATIONS

This Thesis is based on the following papers:

- [1] Ivan Morera, Grigori E. Astrakharchik, Artur Polls, and Bruno Juliá-Díaz. *Quantum droplets of bosonic mixtures in a one-dimensional optical lattice*. Phys. Rev. Research, 2, 022008, (2020).
- [2] Ivan Morera, Grigori E. Astrakharchik, Artur Polls, and Bruno Juliá-Díaz. *Universal dimerized quantum droplets in a one-dimensional lattice*. Phys. Rev. Lett., 126, 023001, (2021).
- [3] Ivan Morera, Annabelle Bohrdt, Wen Wei Ho, and Eugene Demler. *Attraction from frustration in ladder systems*. arXiv.2106.09600. Submitted to Phys. Rev. Res.
- [4] Ivan Morera, Bruno Juliá-Díaz, and Manuel Valiente. *Universality of quantum liquids and droplets in one dimension*. Phys. Rev. Res., 4, L042024, (2022).
- [5] Ivan Morera, Márton Kanász-Nagy, Tomasz Smolenski, Livio Ciorciaro, Atac Imamoglu, and Eugene Demler. *High-temperature kinetic magnetism in triangular lattices*. arXiv. 2209.05398. Submitted to Phys. Rev. Lett.
- [6] Ivan Morera, Rafal Oldziejewski, Grigori E. Astrakharchik, and Bruno Juliá-Díaz. *Superexchange liquefaction of strongly correlated lattice dipolar bosons*. Phys. Rev. Lett., 130, 023602, (2023).

Moreover, the author of this Thesis has worked in the following publications:

- [7] Ivan Morera, Artur Polls, and Bruno Juliá-Díaz. *Entanglement structure of the two-component Bose-Hubbard model as a quantum simulator of a Heisenberg chain*. Scientific Reports, 9, 9424, (2019).
- [8] Ivan Morera, Irénée Frérot, Artur Polls, and Bruno Juliá-Díaz. *Entanglement entropy in low-energy field theories at a finite chemical potential*. Phys. Rev. Res., 2, 033016, (2020).
- [9] Felipe Isaule, Ivan Morera, Pietro Massignan, and Bruno Juliá-Díaz. *Renormalization-group study of bose polarons*. Phys. Rev. A, 104, 023317, (2021)
- [10] Felipe Isaule, Ivan Morera, Artur Polls, and Bruno Juliá-Díaz. *Functional renormalization for repulsive bose-bose mixtures at zero temperature*. Phys. Rev. A, 103, 013318, (2021).
- [11] Felipe Isaule and Ivan Morera. *Weakly-interacting bose-bose mixtures from the functional renormalisation group*. Condensed Matter, 7(1), 9, (2022).

TABLE OF CONTENTS

Abstract	v
Resum	vii
Acknowledgments	ix
List of publications	xi
1 Introduction	1
1.1 Ultracold atomic systems	2
1.2 Two-dimensional moiré materials	4
1.3 Tensor networks	6
1.4 Outline of this Thesis	10
2 Preliminaries I: Ultracold atoms in an optical lattice	12
2.1 Cold atomic systems	13
2.2 Single-particle problem	14
2.3 Derivation of the Bose-Hubbard Hamiltonian	16
2.4 Physics of the Bose-Hubbard model	18
2.4.1 Superfluid phase	19
2.4.2 Mott insulator phase	22
2.4.3 Quantum phase transition	23
2.5 Two-particle problem	24
3 Preliminaries II: Hubbard physics in transition metal dichalcogenide moiré compounds	30
3.1 Transition metal dichalcogenides	30
3.2 Heterostructure transition metal dichalcogenide compounds	33
3.3 The Fermi-Hubbard model	34
I Ultracold atomic quantum liquids induced by direct interactions in optical lattices	41
4 Bose-Bose mixtures in a one-dimensional optical lattice	43
4.1 Two-component Bose-Hubbard model	44
4.2 Weak coupling regime	45
4.2.1 Bogoliubov's decoupling	45
4.2.2 Lee-Huang-Yang energy in the lattice	47
4.2.3 Equation of state: quantum liquids	49

4.2.4	Comparison with DMRG simulations	51
4.3	Strong coupling regime	54
4.3.1	Dimerized effective theory	54
4.3.2	Effective dimer-dimer interaction	56
4.3.3	Liquid to gas transition	58
4.3.4	Many-dimer problem	60
4.4	Quantum correlations	63
4.5	Phase diagram	65
4.6	Conclusions and outlook	66
5	Dipolar bosons in a one-dimensional optical lattice	68
5.1	Extended Bose-Hubbard model	71
5.1.1	Self-bound Mott-insulator	71
5.1.2	Superexchange liquefaction	75
5.2	Dipolar bosons loaded in a high 1D optical lattice	76
5.2.1	Experimental considerations	77
5.2.2	Numerical details	77
5.3	Equilibrium properties of two dipolar bosons	78
5.4	Many-body equilibrium properties of dipolar bosons	79
5.4.1	Gas to liquid transition	81
5.4.2	Phase diagram	82
5.5	Non-equilibrium properties of dipolar bosons	83
5.5.1	Dynamic structure factor and lattice sum rules	83
5.5.2	Speed of sound	88
5.6	Conclusions and outlook	90
6	Universality of quantum fluids in one dimension	91
6.1	Effective low-energy theories	92
6.1.1	Discretization of the continuum models	93
6.1.2	Setting the coupling strengths	95
6.2	Quantum gases and liquids with three-body interactions	96
6.2.1	Self-consistent decoupling	97
6.2.2	Improved mean-field theory	99
6.3	Universality of quantum gases	100
6.4	Universality of quantum droplets	101
6.5	Universality of quantum liquids	104
6.6	Conclusions and outlook	105
II	Binding induced by kinetic frustration: applications to cold atoms and moiré systems	107
7	Attraction from frustration in ladder systems	109
7.1	Kinetic frustration	112
7.1.1	Imaginary time picture	113
7.1.2	Attraction from frustration	115
7.2	Microscopic model	116
7.2.1	Single particle dispersion for the zigzag ladder	117
7.2.2	Single particle dispersion for the square ladder with a flux	118
7.3	Numerical techniques	118
7.4	Spin-1/2 fermions in the zigzag ladder	119
7.4.1	Hole-magnon bound states	119
7.4.2	Finite size scaling	121
7.4.3	Correlation function	122

7.4.4	Multi-body composites	122
7.4.4.1	Analysis of the 1H2M trimer	124
7.4.4.2	2H2M: Effective repulsive interactions	125
7.4.4.3	2H3M: Hole pairing	125
7.4.4.4	1HNM: Antiferromagnetic spinbag	127
7.4.5	Dynamical probes	131
7.4.6	Many-body phases	133
7.4.6.1	Luttinger liquid of composite fermions	134
7.4.6.2	Pair density wave	135
7.5	Spin-1/2 bosons in the zigzag ladder	136
7.5.1	Anti-bound states	136
7.5.2	The Bose-Fermi mapping	136
7.6	Spin-1/2 fermions and bosons in a square ladder with a perpendicular magnetic flux	137
7.7	Conclusions and outlook	137
8	Magnetism induced by kinetic frustration	141
8.1	Kinetic magnetism at finite temperature	143
8.1.1	Numerical details	144
8.1.2	Linear response: magnetic susceptibility	145
8.1.3	Non-linear response: saturation field	148
8.2	Kinetic magnetic phases at zero temperature	150
8.2.1	Effects of non-local interactions	151
8.3	Applications for cold atom experiments	152
8.3.1	High-temperature expansion	152
8.4	Conclusions and outlook	155
9	Conclusions and future perspectives	156
9.1	Ultracold atomic quantum liquids induced by direct interactions in optical lattices	156
9.2	Binding induced by kinetic frustration: applications to cold atoms and moiré systems	158
A	Tensor network algorithms	161
A.1	Density matrix renormalization group	161
A.1.1	Renormalization group perspective	161
A.1.2	Variational perspective	165
A.1.2.1	Canonical form	166
A.1.2.2	Matrix product operator	169
A.1.2.3	DMRG in the tensor network language	171
A.2	Time-evolving block decimation algorithm	175
A.3	Finite temperature through purification	178
B	Linear predictor algorithm	181
	Bibliography	231

INTRODUCTION

The previous century was characterized by a paradigm shift in our comprehension of the physical world. From Max Planck’s examination of black-body radiation ([Planck, 1901](#)) to Albert Einstein’s analysis of the photoelectric effect ([Einstein, 1905](#)), along with groundbreaking experiments such as the Stern-Gerlach ([Gerlach and Stern, 1922](#)), and the Davisson-Germer one ([Davisson and Germer, 1928](#)), it became increasingly clear that classical physics alone could not provide a comprehensive explanation of the Universe. The result of these series of breakthroughs was the emergence of a new theory, quantum mechanics, based on the uncertainty principle, quantization, particle-wave duality, and quantum superposition. These principles have enabled humankind to gain a fundamental understanding of light and matter, while also leading to a technological breakthrough that triggered the first quantum revolution. Quantum mechanics allowed for the development of revolutionary technologies like the laser, the transistor, and the semiconductor. The latter has played an especially critical role in shaping modern society as most electronic devices rely on semiconductor technology. As such, quantum mechanics serves as one of the key foundations of the “Information age”, and our smartphones and computers would not exist without it.

However, the first quantum revolution did not make full use of the principles of quantum mechanics as most of the devices were too noisy and operated in a “semiclassical regime”. In contrast, the 21st century is witnessing a second quantum revolution where researchers are creating quantum technologies that harness the principles of quantum mechanics in a controlled manner ([Dowling and Milburn, 2003](#)). Quantum technologies involve manipulating individual quantum systems like atoms, photons, superconducting circuits, etc, to perform tasks that are impossible at the classical level. These technologies have allowed for the creation of quantum communication networks that are safer than classical networks, quantum sensors that outperform classical methods in precision measurements, and quantum computers that have an exponential efficiency compared to classical computers ([Dowling and Milburn, 2003](#)). At the forefront of these technologies are quantum simulators, which are platforms for simulating complex quantum systems that are impossible to simulate on classical computers ([Feynman, 1982](#); [Lloyd, 1996](#)). These platforms enable researchers to explore the physical properties of a complex sys-

tem in a precise and controlled manner. One of the most exciting applications of quantum simulators is their use in studying quantum many-body physics, where interactions between multiple quantum particles lead to exotic and emergent phenomena such as superconductivity, superfluidity, quantum magnetism, correlated insulators, quantum phase transitions, and more. Quantum simulators offer a unique opportunity to study these phenomena because the interactions between particles can be controlled and tuned.

Ultracold atoms are a prime example of a quantum simulator as they can be trapped and manipulated using lasers, and the interactions between atoms can also be controlled (Lewenstein et al., 2012; Bloch et al., 2012). This technology has enabled researchers to simulate numerous condensed matter systems over the past few decades. Furthermore, recent developments in material manipulation have given rise to a new category of human-engineered two-dimensional materials, such as graphene, that have opened up new avenues for quantum simulation research as new exotic electronic phases have been found and they can be controlled and also tuned (Andrei et al., 2021).

With the rapid development of new quantum technologies, quantum simulators are expected to play an increasingly important role in scientific research and industrial applications. Their potential for solving complex problems and simulating large-scale quantum systems is likely to have a significant impact on fields such as materials science, chemistry, finance and cryptography. Consequently, the field of quantum simulators is rapidly expanding and holds great potential for revolutionizing modern society.

1.1 Ultracold atomic systems

Cold atomic systems are comprised of neutral atoms cooled to ultra-low temperatures, typically a few microkelvin or even nanokelvin, using different cooling and trapping techniques that exploit light-matter interactions (Hänsch and Schawlow, 1975; Ashkin, 1978; Phillips and Metcalf, 1982; Chu et al., 1985, 1986; Dalibard and Cohen-Tannoudji, 1989). At such extremely low temperatures, bosonic particles enter a quantum degenerate regime, leading to the phenomenon of Bose-Einstein condensation (BEC), where all particles occupy the same quantum state (Pitaevskii, 2003; Pethick and Smith, 2008). Since the experimental discovery of BEC in a cold atom system (Anderson et al., 1995; Bradley et al., 1995; Davis et al., 1995), the field has exploded in the last few decades. Initially, it focused on exploiting the quantum coherence properties of BECs and studying their superfluid properties, including the formation of quantized vortices (Jaksch et al., 1998; Bloch, 2005; Bloch et al., 2008). However, the community rapidly noticed that cold atomic systems can be used as quantum simulators of far more complicated condensed matter systems (Lewenstein et al., 2012; Bloch et al., 2012). By trapping cold atoms in a periodic optical potential, the so-called optical lattice, a Hubbard-type model can be simulated (Jaksch et al., 1998). The Hubbard model was originally introduced to understand the effects of correlations between electrons in a solid due to their strong repulsive Coulomb interaction (Gutzwiller, 1963; Kanamori, 1963; Hubbard, 1963). While the model is a very simplistic picture of the behavior of electrons in a real solid-state system, it accurately describes bosons (Bose-Hubbard model) or fermions (Fermi-Hubbard model) loaded in an optical lattice (Lewenstein et al., 2012; Bloch

et al., 2012). Therefore, cold atoms in an optical lattice offer a unique opportunity to tackle fundamental questions in condensed matter physics. Moreover, the Hubbard parameters (kinetic energy and interaction energy) can be tuned by changing the height of the optical lattice or by tuning the s -wave scattering of the atoms using Feshbach resonances (Inouye et al., 1998; Courteille et al., 1998; Chin et al., 2010). By controlling these parameters, experimentalists can enter different regimes, including the weakly interacting regime where a superfluid (metallic) phase is formed for bosons (fermions) and the strongly interacting regime where a Mott insulator phase is expected (Mott, 1968; Fisher et al., 1989). Between these two regimes, a quantum phase transition (QPT) occurs, which is a phase transition at zero temperature and is therefore driven solely by quantum fluctuations stemming from Heisenberg's uncertainty principle (Sachdev, 1989). The experimental observation of the QPT was one of the great successes of cold atoms as quantum simulators of a condensed matter system (Greiner et al., 2002; Stöferle et al., 2004; Spielman et al., 2007, 2008). Furthermore, utilizing cold atoms as quantum simulators of the Fermi-Hubbard model has the potential to shed light on the enigmatic phenomenon of high- T_c superconductivity by studying the effects of doping on the Mott phase (Hofstetter et al., 2002).

In the last decades, cold atoms have been widely employed as quantum simulators of other physical systems. For example, the so-called superexchange processes leading to antiferromagnetic insulators (Kramers, 1934; Anderson, 1950), have been simulated in cold atom systems (Duan et al., 2003; Trotzky et al., 2008b; Fukuhara et al., 2013a; Jepsen et al., 2020b). Therefore, cold atoms can be used to simulate quantum magnetism including the formation spin liquids in frustrated geometries (Savary and Balents, 2016). Moreover, Hall physics can be simulated by introducing synthetic static gauge field in the system (Sørensen et al., 2005; Juliá-Díaz et al., 2011; Dalibard et al., 2011; Atala et al., 2014; Struck et al., 2012; Cooper and Dalibard, 2013; Aidelsburger et al., 2013; Miyake et al., 2013; Jotzu et al., 2014; Celi et al., 2014; Goldman et al., 2016; An et al., 2017). In addition, cold atoms can also lead to interesting applications for high-energy physics as they can be employed to simulate lattice gauge theories including Abelian and non-Abelian theories (Aidelsburger et al., 2022).

Recently, the paradigm of cold atoms has been challenged by the discovery of quantum liquid phases in two-component bosonic mixtures and single-component dipolar systems (Schmitt et al., 2016; Ferrier-Barbut et al., 2016; Chomaz et al., 2016; Ferrier-Barbut et al., 2018; D'Errico et al., 2019; Cabrera et al., 2018; Semeghini et al., 2018). For decades, cold atoms have behaved as quantum gases thermodynamically, meaning that the system does not have a preferred density and can always lower its energy by expanding and decreasing its density. This is the typical situation in experiments: when the external trap is opened, the cloud starts to expand, allowing experimentalists to obtain the momentum distribution of the cloud. Cold atoms, being quantum gases, fall into the general theory of fluids by van der Waals (Hansen and McDonald, 2013). Cold atom systems are so dilute that they are not sensitive to the attractive long-range tail of van der Waals interaction, and therefore they only experience a repulsive short-range potential, which can be taken into account as an effective repulsive contact potential. Therefore, the microscopic interaction is not able to produce a liquid phase.

It was demonstrated that the liquefaction of cold atom systems comes from a competition between classical and quantum contributions to the energy of the system (Petrov, 2015). In this way, a quantum

liquid can be produced, which can be eight orders of magnitude more dilute than the other quantum liquid known in nature, liquid Helium (Petrov, 2018). This discovery has led to an important message: even in the weakly interacting regime, quantum fluctuations might dramatically change the ground state, and therefore, one should not trust mean-field theory. Therefore, cold atoms open new ways for studying quantum liquids that were inaccessible with liquid Helium. By trapping a quantum liquid in an optical lattice, we can study the microscopic mechanism leading to the liquefaction of the system while being able to tune the parameters of the system in a controlled way as we show in this Thesis. Moreover, the study of quantum liquids might challenge our understanding of quantum many-body theories. In general, quantum liquids exhibit stronger correlations than quantum gases and multi-body correlations are more important which cannot be simply captured by mean-field theories (Hansen and McDonald, 2013). A quantum liquid is a many-body phase where collective binding appears and avoids phase separation at the same time. Therefore, there might be interesting connections with superconducting phases where electron binding appears but the many-body phase is stable against phase separation.

1.2 Two-dimensional moiré materials

The recent discovery of strongly correlated phases of matter in two-dimensional van der Waals moiré materials has opened a new field of research in condensed matter physics (Andrei et al., 2021). Moiré systems are a new class of human manufactured materials which are obtained when a pair of two-dimensional (2D) crystals with a small difference in lattice constant or orientation are overlaid (He et al., 2021). When two identical 2D crystals are stacked on top of each other and twisted at a certain small angle, a new periodic structure emerges known as a moiré pattern, see Fig. 1.1. If the original crystals are hexagonal then, the moiré pattern corresponds to a triangular geometry. Interestingly, the periodicity of the structure dramatically changes at small twisting angles, and the moiré lattice spacing can become one or two orders of magnitude larger than the original crystalline lattice spacing (He et al., 2021). As a result, the lattice spacing changes from a few angstroms to a few nanometers. This change in scale is expected to drastically alter the behavior of the material. By increasing the lattice spacing, we are flattening the dispersion relation of the material, which means that we are suppressing kinetic energy (Bistritzer and MacDonald, 2011). As a result, strongly correlated many-body phenomena may be expected. For example, when two sheets of graphene are stacked on top of each other and then twisted at a certain angle $\sim 1.1^\circ$, the bilayer structure exhibits superconducting phases and correlated insulators (Cao et al., 2018a,b). This material has been named magic angle twisted bilayer graphene (MATBG) and it displays the highest ratio of superconducting electrons, making it the best superconductor ever discovered. Additionally, MATBG has non-trivial topological bands (Tarnopolsky et al., 2019; Liu et al., 2019; Song et al., 2019; Po et al., 2019; Hejazi et al., 2019; Song et al., 2021) which, combined with the strong electronic correlations, provide a unique opportunity for studying the quantum anomalous Hall effect (Bultinck et al., 2020b; Lian et al., 2021; Wu and Das Sarma, 2020; Bultinck et al., 2020a; Kwan et al., 2021; Liu and Dai, 2021) and realizing Chern insulators (Ledwith et al., 2020; Abouelkomsan et al., 2020; Repellin and Senthil, 2020; Sheffer and Stern, 2021). However,

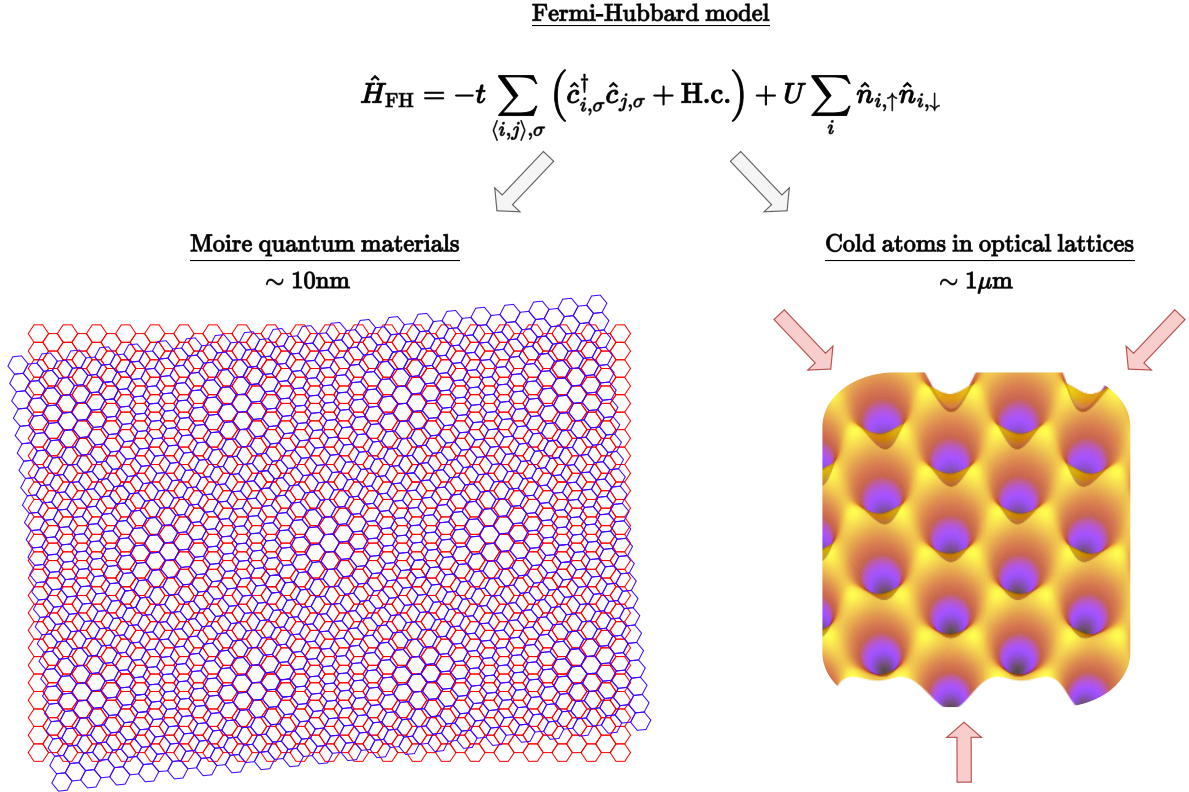


Figure 1.1: The Fermi-Hubbard model in a triangular geometry can nowadays be simulated using moiré materials and fermionic cold atoms in optical lattices. By stacking two 2D hexagonal crystals and twisting them with a small angle, a moiré pattern emerges corresponding to a triangular geometry with a typical moiré lattice spacing of 10 nm. By interfering three laser beams a periodic 2D triangular potential trapping neutral fermionic atoms can be created with typical lattice spacing ranging from hundreds of nanometers to few micrometers.

understanding the effective Hubbard model behind MATBG has been a very tedious task which still remains open due to the large number of degrees of freedom (including spin, valley and layer indexes) and the non-trivial topological character of the dispersing bands (Koshino et al., 2018; Kang and Vafeek, 2018; Po et al., 2018). Other two-dimensional moiré materials, such as heterostructure transition metal dichalcogenides (TMDs), also exhibit unique properties complementary to the ones found in MATBG (Geim and Grigorieva, 2013; Novoselov et al., 2016; Liu et al., 2016). However, heterostructure TMDs have the advantage of having a simpler theoretical description due to their heterostructure nature and the strong spin-orbit coupling, resulting in a reduced number of active bands (Wu et al., 2018b). Furthermore, TMDs exhibit a much stronger Coulomb interaction than MATBG, leading to the emergence of Wigner crystals (Regan et al., 2020; Huang et al., 2021; Smoleński et al., 2021; Zhou et al., 2021) and stripe phases (Jin et al., 2021) at rational filling factors. As a result, heterostructure TMDs hold the potential to quantum simulate the Hubbard model in the strongly correlated regime, enabling the study of the Mott transition (Tang et al., 2020). TMDs also offer a promising platform to study the effects of geometric frustration, including the formation of chiral spin liquids (Zhang et al.,

2021) and magnetism induced by kinetic frustration (Lee et al., 2022; Zhang and Fu, 2022), as we show in Chap. 7 and Chap. 8. On the other hand, homobilayer TMDs are less explored but offer the possibility of investigating multi-orbital Hubbard models with non-trivial topological bands (Devakul et al., 2021; Xu et al., 2022b).

Heterostructure TMDs offer high tunability of Hubbard parameters, as in cold atom systems, while being sensitive to accessible external electric (Li et al., 2012; Ghiotto et al., 2021). Moreover, the unique strong spin-orbit coupling of these materials leads to valley-dependent optical selection rules (Cao et al., 2012; Mak et al., 2012; Zeng et al., 2012; Xiao et al., 2012; Xu et al., 2014). The combination of these features with the large exciton binding energies (Splendiani et al., 2010; Ramasubramaniam, 2012; Qiu et al., 2013; Jones et al., 2013) allows for the use of optical probes to read out the electronic and magnetic properties of the material, creating an interface between optics and solid-state physics. Studies of bilayer TMDs are in their infancy and further research is needed to understand the impact of the moiré pattern on the electronic and magnetic properties of the material. In the near future, experiments will provide more information about the validity of the Hubbard model description, and *ab initio* calculations could shed light on the effects of the moiré potential on the electronic structure. One might expect strong synergies to emerge between cold atoms loaded in triangular optical lattices and heterostructure TMDs, as both hold the promise of quantum simulating the Fermi-Hubbard model in a triangular geometry and providing new insights into the microscopic mechanisms underlying high-Tc superconductivity, see Fig. 1.1.

1.3 Tensor networks

To understand the formation of quantum many-body phases in strongly correlated systems, we need to perform large scale, unbiased numerical simulations. Quantum Monte Carlo (QMC) methods have been successfully employed for decades to simulate quantum many-body systems which do not suffer from the so-called sign problem, i.e., when one does not deal with fermions or frustrated systems (Becca and Sorella, 2017). However, when this is not the case, we have to resort to other numerical techniques. Exact diagonalization (ED) techniques try to fully or partially diagonalize the matrix representation of the Hamiltonian, but they cannot be scaled up to deal with large systems (Lin, 1990; Zhang and Dong, 2010; Raventós et al., 2017). Consider a quantum many-body system living on a discrete lattice of N_s sites where each site n has a local Hilbert space of dimension d with basis $|i_n\rangle$ and the total Hilbert space is formed by the tensor product of all local Hilbert spaces. The dimension of the total Hilbert space increases exponentially with the number of sites d^{N_s} , and therefore, the matrix representation of the Hamiltonian corresponds to a matrix of size $d^{N_s} \times d^{N_s}$. Thus, trying to perform ED on large systems is not feasible and we encounter a problem of space and time. First, we do not have enough space in our RAM memory to store such an immense matrix. We cannot even store the array encoding an eigenvector of the system. Second, fully diagonalizing the Hamiltonian will take too much time. Even though we can employ Lanczos algorithm if we want to focus on the lowest part of the spectrum, the space problem will not allow us to use Lanczos algorithm for large systems (Lanczos, 1950). It is in this situation where tensor network methods can be employed to efficiently simulate quantum many-

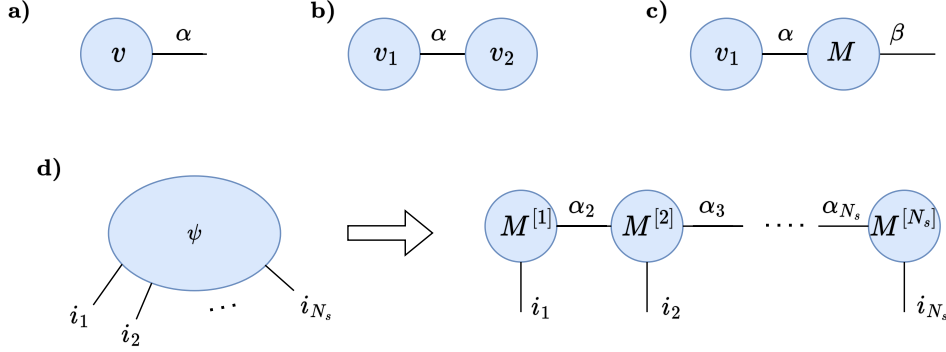


Figure 1.2: Diagrammatic representation for a vector v with components v_α in a). The vector product $\sum_\alpha (v_1)_\alpha (v_2)_\alpha$ is represented in b) and the vector-matrix multiplication $\sum_\alpha (v_1)_\alpha M_{\alpha\beta}$ is represented in c). A general quantum state Eq. (1.1) is expressed as an MPS Eq. (1.2) in d).

body systems with a scaling polynomial in the number of sites instead of being exponential. Numerous reviews on tensor network based algorithms can be found (Schollwöck, 2005; De Chiara et al., 2008; Schollwöck, 2011a; Biamonte and Bergholm, 2017; Montangelo, 2018; Bridgeman and Chubb, 2017; Orús, 2019; Ran et al., 2020; Bañuls, 2023) and we review the basics of tensor networks and different algorithms in this section and in App. A.

Any pure quantum state of a many-body system comprised of N_s sites can be written as,

$$|\psi\rangle = \sum_{i_1, i_2, \dots, i_{N_s}} \psi_{i_1, i_2, \dots, i_{N_s}} |i_1, i_2, \dots, i_{N_s}\rangle, \quad (1.1)$$

where $\psi_{i_1, i_2, \dots, i_{N_s}} = \langle i_1, i_2, \dots, i_{N_s} | \psi \rangle$ contains all the coefficients of the wavefunction and can be understood as a N_s -rank tensor. Tensor network methods are usually based on the matrix product state (MPS) ansatz, see Fig. 1.2 d), which expresses the original tensor $\psi_{i_1, i_2, \dots, i_{N_s}}$ as the product of N_s matrices (Fannes et al., 1992; Klümper et al., 1993; Östlund and Rommer, 1995; Rommer and Östlund, 1997; Vidal, 2003; Perez-Garcia et al., 2007),

$$\begin{aligned} |\psi\rangle &= \sum_{i_1, i_2, \dots, i_{N_s}} \sum_{\alpha_2, \dots, \alpha_{N_s}} M_{\alpha_1 \alpha_2}^{[1], i_1} M_{\alpha_2 \alpha_3}^{[2], i_2} \dots M_{\alpha_{N_s} \alpha_{N_s+1}}^{[N_s], i_{N_s}} |i_1, i_2, \dots, i_{N_s}\rangle, \\ &\equiv \sum_{i_1, i_2, \dots, i_{N_s}} M^{[1], i_1} M^{[2], i_2} \dots M^{[N_s], i_{N_s}} |i_1, i_2, \dots, i_{N_s}\rangle, \end{aligned} \quad (1.2)$$

where each $M_{\alpha_n \alpha_{n+1}}^{[n], i_n}$ is a tensor of order 3 with dimension $\chi_n \times d \times \chi_{n+1}$ but we can think of it as d matrices of dimension $\chi_n \times \chi_{n+1}$ in each site. The indexes α_n are usually called “virtual” or “bond” indexes since they do not affect the coefficient $\psi_{i_1, i_2, \dots, i_{N_s}}$ once the physical indexes i_n are fixed. Let us remark that the indexes at the boundaries are dummy ones since they can only take a single value $\alpha_1 = \alpha_{N_s+1} = 1$. They are introduced to lead to a more homogeneous equation. In practice, tensor network algorithms make us of a diagrammatic notation that we sketch in Fig. 1.2. In this notation a tensor with N_s indices is illustrated as a circle with N_s open legs. When two legs are joined we are

performing a tensor contraction over the index, see Fig. 1.2 b).

The power of the MPS ansatz Eq. (1.2) becomes clear when analyzing the number of free parameters that the ansatz possesses. In Eq. (1.2) we have the product of N_s tensors with finite dimension independent on the system size and therefore, the number of parameters scales polynomially with the system size. Thus, performing simulations within the family of MPS wavefunctions is efficient. However, the original state Eq. (1.1) represented by the tensor $\psi_{i_1, i_2, \dots, i_{N_s}}$ contains a number of free parameters that scales exponentially with the system size. By assuming an MPS representation of a general quantum state we are losing a lot of information about the original state. A way of quantifying this loss of information is by the entanglement entropy, see App. A for details on the entanglement entropy. If the entanglement entropy of a quantum state linearly scales with the volume of the partition (Page, 1993), it follows a “volume law”, then, we will need larger and larger matrices M as the system grows in size. Therefore, at some point we will run out of space in our computer and we will not be able to perform simulations in an efficient way. However, if the entanglement entropy linearly scales with the area of the partition (Eisert et al., 2010), it follows an “area law”, then, we can always find a suitable MPS representation of the original state with matrices of finite dimension. In general, most of the states in the Hilbert space exhibit a volume law and cannot be efficiently represented by an MPS. However, we are not interested in general quantum states but on physical ones. It has been formally proven in (Hastings, 2007) that ground states of one-dimensional (1D) local, gapped and frustration-free Hamiltonians follow an area law and therefore, they can be efficiently simulated by assuming an MPS ansatz. Even though this seems a very small subset of systems that can be simulated within the family of MPS wavefunctions, they have shown to be a very powerful technique for solving quantum many-body problems in many situations. Critical 1D systems can be efficiently simulated within the family of MPS and the study of the entanglement scaling has been used to characterize the universality of critical points (Calabrese and Cardy, 2004; Tagliacozzo et al., 2008; Calabrese and Lefevre, 2008; Pollmann et al., 2009). Topological systems can also be efficiently simulated and the characterization of entanglement has been used to classify topological phases (Levin and Wen, 2006; Kitaev and Preskill, 2006; Pollmann and Turner, 2012; Cincio and Vidal, 2013). Two-dimensional systems can be simulated using geometries such a cylinder that can be mapped to a 1D problem (Liang and Pang, 1994). Moreover, these techniques have been successfully applied to other areas of physics, such as quantum chemistry (Chan and Sharma, 2011) and lattice gauge theories (Banuls et al., 2019). Therefore, tensor network algorithms are one of the most powerful techniques for simulating low dimensional quantum systems.

The most prominent algorithm for obtaining ground states of strongly correlated quantum low dimensional systems is the density matrix renormalization group (DMRG) algorithm formulated in 1992 by S. White (White, 1992, 1993). While it was originally introduced as a numerical renormalization group algorithm, it was later found that it can be formulated as a variational optimization within the family of MPS wavefunctions (Östlund and Rommer, 1995; Rommer and Östlund, 1997; Schollwöck, 2011a). Therefore, it succeeds when the ground state of interest is slightly entangled. The MPS representation of DMRG has allowed to extend the algorithm and increase its efficiency. The inclusion of Abelian and non-Abelian symmetries speed up the simulations and allow to target ground states in

different symmetry sectors (McCulloch and Gulácsi, 2002; Singh et al., 2010, 2011; Singh and Vidal, 2012; Weichselbaum, 2012). Moreover, a hybrid real-momentum representation allows to target certain momentum states in cylindrical geometries (Motruk et al., 2016; Ehlers et al., 2017). The DMRG algorithm has also been extended to simulate translational invariant systems, a variant of the algorithm called infinite-DMRG (iDMRG) (White, 1992, 1993; McCulloch and Gulácsi, 2002). Therefore, the thermodynamic limit can be easily studied by performing iDMRG simulations. In addition, DMRG can also be used to simulate real-time evolution of quantum systems (Daley et al., 2004; White and Feiguin, 2004). However, the entanglement entropy increases linearly in time in a general quantum evolution and therefore, the simulations can only be trusted for relatively short times (Calabrese and Cardy, 2005). Nevertheless, these simulations have provided new insights into non-equilibrium systems. Other tensor network algorithms have been introduced to perform real and imaginary time evolutions, such as the time evolving decimation block (TEBD) algorithm (Vidal, 2004) and other algorithms based on the time dependent variational principle (TDVP) (Haegeman et al., 2011, 2016). The latter method enables real-time evolutions that conserve the charges of the Hamiltonian, resulting in more stable simulations. It can also be employed to simulate time-evolutions of quasi-1D systems and systems with long-range interactions (Zaletel et al., 2015b). In addition, the family of tensor networks has been extended beyond the MPS ansatz. For instance, the multi-scale entanglement renormalization ansatz (MERA) in an ansatz that allows to exactly simulate critical 1D systems and enables the extraction of their universal properties (Vidal, 2007a; Evenbly and Vidal, 2009). Additionally, they have revealed intriguing connections between entanglement and the emergence of geometry (Swingle, 2012; Evenbly and Vidal, 2011; Molina-Vilaplana, 2013). Projected entangled pair states (PEPS) generalize MPS wavefunctions to higher dimensions and have been successfully applied to simulate two-dimensional quantum systems (Nishio et al., 2004; Verstraete and Cirac, 2004; Verstraete et al., 2006; Schuch et al., 2007, 2008). Other techniques, such as the Corner Transfer Matrix (CTM) Renormalization Group Method (Nishino and Okunishi, 1996, 1997; Orús and Vidal, 2009; Orús, 2012), Tensor Renormalization Group (TRG) (Levin and Nave, 2007), and Tensor Network Renormalization (TNR) (Evenbly and Vidal, 2015), to name a few, can approximate the partition function of 2D classical systems. Furthermore, tensor network methods have been extended to deal with continuous systems and have proven successful in the simulation of one-dimensional quantum gases (Verstraete and Cirac, 2010; Haegeman et al., 2013).

In this Thesis we employ different tensor network algorithms to simulate the equilibrium and non-equilibrium properties of low dimensional quantum many-body systems. The reader who is interested in the implementation of different algorithms can consult App. A. In the beginning of this Thesis, we developed our own tensor network algorithms, including DMRG, iDMRG, TEBD, and iTEBD. However, we eventually made use of the TeNPy package due to its better efficiency and feasibility for simulating different many-body systems with various tensor network algorithms (Hauschild and Pollmann, 2018).

1.4 Outline of this Thesis

The content of this Thesis is divided into two parts. In Part I, we study ultracold atomic quantum liquid phases loaded in high 1D optical lattices. In Part II, we investigate the effects of kinetic frustration on ultracold atomic systems in frustrated geometries and TMD heterostructures with a triangular moiré pattern. Before Part I, we present two chapters, Chap. 2 and Chap. 3, where we introduce several introductory concepts so that the reader becomes familiar with the systems presented in the main part of this Thesis. In Chap. 2, we introduce the Bose-Hubbard model and how it can be obtained with ultracold atoms loaded in a high optical lattice. Moreover, we introduce the basics of the Bose-Hubbard model, such as its quantum phase transition and the two-body problem. In Chap. 3, we briefly introduce the physics of TMD materials and show how the Hubbard model can be obtained in a heterostructure TMD compound with a triangular moiré pattern. The reader who is already familiar with cold atoms in optical lattices or moiré materials can skip Chap. 2 or Chap. 3, respectively. We now briefly summarize the content of each chapter in the main part of this Thesis.

- In Chap. 4, we present a study of the quantum liquid phases present in the 1D two-component Bose-Hubbard model. We analyze the weakly-interacting regime by employing Bogoliubov's theory and the strongly-interacting regime by developing an effective theory of dimers. These two theories allow us to obtain the ground state properties of the Hamiltonian and predict a phase transition from a quantum gas to a quantum liquid. We compare our analytical predictions with large scale DMRG simulations and investigate the different phase transitions of the ground state as a function of the strength of the interactions.
- In Chap. 5, we investigate a 1D single-component bosonic system that interacts via attractive dipolar and repulsive s -wave interactions. We focus on the strongly s -wave interacting regime where the system fermionizes. We present an effective decoupling approach that allows us to capture the quantum many-body phases of the system. We show that superexchange processes lead to liquefaction and compare our analytical predictions with DMRG simulations. Additionally, we present the two-particle excitation spectrum of the system, obtained with TDVP simulations. We demonstrate that the excitation spectrum dramatically changes when moving from one phase to another.
- In Chap. 6, we study the universality of quantum fluids in one dimension and provide a self-consistent theory that describes quantum liquids with attractive two- and repulsive three-body forces. By matching different microscopic models, we investigate the universality of the equation of state of the respective many-body phases. We observe that quantum gases feature universal equation of states when the few-body problems are matched. However, quantum liquids are not universal since the equilibrium density of two models can differ even though the few-body energies are matched. We attribute this non-universality to the fact that the normalization constants of the few-body wavefunctions cannot be matched by just fixing the energy of the state. Additionally, we demonstrate that quantum droplets exhibit non-universal saturation densities, while their long-distance tails exhibit a universal decay.

- In Chap. 7, we introduce the concept of kinetic frustration and show how it leads to effective interactions in spin-1/2 systems. We focus on frustrated ladder geometries, including the zigzag ladder and square ladder with a perpendicular magnetic flux. We demonstrate that in the zigzag geometry, a fermionic (bosonic) spin-1/2 system exhibits an effective attractive (repulsive) interaction between holes and spin flips, leading to a strong spin-charge coupling. In the square ladder with magnetic flux, we observe attractive interactions for both fermionic and bosonic systems. We perform large scale DMRG simulations and present the phase diagram of multi-body composites induced by kinetic frustration. We study the many-body phases of the system and discuss different protocols in cold atom experiments to detect these exotic composites.
- In Chap. 8, we explore the magnetic properties of spin-1/2 fermions in a 2D triangular geometry at both finite and zero temperature, using tensor network techniques. We show that kinetic frustration experienced by the charge carriers induces a dramatic change in the magnetic correlations of the system as it is doped away from half-filling. Specifically, the system transitions from being antiferromagnetic below half-filling to ferromagnetic above half-filling. We also investigate the low-temperature magnetic many-body phases induced by kinetic frustration. Finally, we discuss the relevance of our findings for experiments with heterostructure TMDs and cold atom experiments with a quantum gas microscope.
- In Chap. 9, we present the conclusions of this Thesis and discuss possible future directions of research based on our work.

Chapter 2

PRELIMINARIES I: ULTRACOLD ATOMS IN AN OPTICAL LATTICE

The Hubbard model was originally introduced independently by Martin Gutzwiller ([Gutzwiller, 1963](#)), Junjiro Kanamori ([Kanamori, 1963](#)) and John Hubbard ([Hubbard, 1963](#)) to model the electronic correlations in a solid with a narrow energy band. In general, the model describes the interactions of particles moving in a periodic potential. In the case of solids, these particles correspond to the valence electrons which feel a periodic potential created by the ionic cores. The model goes beyond the naive band theory since it treats the electronic interactions and it is able to predict the appearance of strongly correlated phenomena. It has been successfully employed to study high-T superconductivity, magnetism, Mott insulators, spin liquids, among others ([Auerbach, 1998](#)). However, the Hubbard model has not only had a huge impact in the solid state theory but has also revolutionized the cold atom paradigm. In particular, cold atomic systems loaded in high optical lattices can be used as quantum simulators of the Hubbard model in its fermionic (Fermi-Hubbard) and bosonic (Bose-Hubbard) version, which has allowed to explore the physics of the Hubbard model in a very controlled way in the last decades ([Jaksch et al., 1998](#); [Bloch, 2005](#); [Lewenstein et al., 2012](#); [Bloch et al., 2008](#)). In this chapter we introduce the basic concepts and notations that underlie the part of this Thesis focused on cold atoms in optical lattices. In section 2.1 we present the main properties of cold atomic systems. Then, in section 2.2 we describe the problem of a single particle in an optical lattice and, in section 2.3 we derive the Bose-Hubbard Hamiltonian describing a bosonic system loaded in a high one-dimensional optical lattice. In section 2.4 we describe the basic physics of the Bose-Hubbard model and present its quantum phase transition from a superfluid to a Mott insulator phase. Finally, in section 2.5 we present the two-particle problem which plays a major role in many chapters of this Thesis.

2.1 Cold atomic systems

Cold atomic systems offer a high degree of tunability and control over the properties of a quantum many-body system. Since these systems are composed of neutral atoms, they are not sensitive to external electric fields. However, external laser beams offer the opportunity to produce different external potentials in which atoms can be trapped. For example, by producing a very anisotropic potential where the transverse $y-z$ coordinates are tightly confined, such as in a cigar-shaped configuration, the system can be effectively reduced to a 1D one described by a single coordinate x (Moritz et al., 2003; Kinoshita et al., 2004; Paredes et al., 2004). In this situation, the quantum many-body Hamiltonian describing N interacting bosonic atoms is given by,

$$\hat{H} = \int dx \hat{\psi}^\dagger(x) \left(\frac{-\hbar^2}{2m} \partial_x^2 + V_{\text{ext}}(x) \right) \hat{\psi}(x) + \frac{1}{2} \int dx dx' \hat{\psi}^\dagger(x) \hat{\psi}^\dagger(x') V_{\text{int}}(x-x') \hat{\psi}(x') \hat{\psi}(x), \quad (2.1)$$

where we introduce the mass of the atoms m , the 1D external potential $V_{\text{ext}}(x)$, the 1D atom-atom interaction $V_{\text{int}}(x-x')$ and the creation $\hat{\psi}^\dagger(x)$ and annihilation $\hat{\psi}(x)$ bosonic fields that create and destroy a particle at position x , respectively. Characterizing the interatomic potential $V_{\text{int}}(x-x')$ between a pair of atoms at arbitrary distances can be very complicated. However, in cold atomic systems, the exact shape of the interatomic potential is not relevant. In the situation where the thermal de Broglie wavelength,

$$\lambda_T = \frac{h}{\sqrt{2\pi m k_B T}}, \quad (2.2)$$

is much larger than the range of the potential, the only relevant scattering channel is the s -wave one. In such a situation, we can replace the full interatomic potential by a pseudo-potential (Bloch et al., 2008),

$$V_{\text{int}}(x-x') = g\delta(x-x'), \quad (2.3)$$

which is characterized by a single parameter: the 1D coupling constant g . The pseudo-potential approach was originally introduced in (Huang and Yang, 1957) to describe a hard-core sphere gas. The 1D coupling constant suffers a strong renormalization respect to the three-dimensional (3D) system due to a confinement-induced resonance. It can be related with the 3D scattering length a_s in the following way (Olshanii, 1998; Bergeman et al., 2003; Astrakharchik et al., 2004),

$$g = \frac{2\hbar^2 a_s}{m a_\perp^2} \frac{1}{1 - C a_s / a_\perp}, \quad (2.4)$$

where we introduce the dimensionless constant $C = |\zeta(1/2)|\sqrt{2}$ with $\zeta(\cdot)$ the Riemann zeta-function and the characteristic length of the transverse potential $a_\perp = \sqrt{\hbar/m\omega_\perp}$. Therefore, the strength and sign of the 1D coupling constant g can be tuned with the external potential. Moreover, Feshbach resonances can also be employed to directly tune the value of the 3D scattering lengths a_s (Inouye

et al., 1998; Courteille et al., 1998; Chin et al., 2010),

$$a_s = a^{\text{bg}} \left(1 - \frac{\Delta_s}{B - B_0} \right), \quad (2.5)$$

where a^{bg} is the background scattering length, B is the external magnetic field, and Δ_s and B_0 are the width and position of the resonance, respectively. These phenomena allow experimentalists to tune the value of the coupling constant g and to access the strongly interacting regime, where interaction energy dominates over kinetic energy.

Different 1D potentials $V_{\text{ext}}(x)$ can be realized in cold atom laboratories but we focus on a particular type of potentials which form a periodic structure in real space i.e. an optical lattice (Jaksch et al., 1998). These are created in laboratories when two counterpropagating fields with the same polarization interfere and create a periodic standing wave, which induces a periodic external potential that traps the atoms,

$$V_{\text{ext}}(x) = V_0 \sin^2(kx), \quad (2.6)$$

where we introduce the strength of the optical lattice V_0 , the momentum $k = \pi/a$ and the lattice spacing a . A characteristic kinetic energy associated with the lattice is the recoil energy $E_R = \pi^2 \hbar^2 / (2ma^2)$. The ratio V_0/E_R measures the competition between the potential energy and kinetic energy introduced by the lattice. At large values of the ratio V_0/E_R , atoms tend to localize in each local minimum of the potential given by Eq. (2.6), as we show below.

2.2 Single-particle problem

Before considering the quantum many-body problem described by the Hamiltonian (2.1), we first present the physics of a single particle moving in an optical lattice. The single-particle problem is characterized by the single-particle wavefunction $\phi(x)$, which obeys the standard Schrödinger equation,

$$\hat{H}\phi(x) = \left(\frac{\hat{p}^2}{2m} + V_{\text{ext}}(x) \right) \phi(x). \quad (2.7)$$

Since the optical potential has a periodicity $V(x+a) = V(x)$ our Hamiltonian commutes with the translation operator $\hat{T} = e^{-i\hat{p}a/\hbar}$. Therefore, we can find simultaneous eigenfunctions of the two operators \hat{T} and \hat{H} . According to Bloch's theorem (see e.g. (Ashcroft, 1976)),

$$\phi_q^{(n)} = e^{iqx/\hbar} u_q^{(n)}(x), \quad (2.8)$$

where $u_q^{(n)}(x) = u_q^{(n)}(x+a)$ are wavefunctions satisfying the same periodicity than the optical lattice. Here n denotes a quantum number characterizing the eigenstate (e.g. the band number) and q stands for the quasi-momentum of the particle which is unique up to a vector of the reciprocal lattice π/a . This allows to restrict q to the first Brillouin zone $q \in [-\pi/a, \pi/a)$. The Schrödinger equation (2.7)

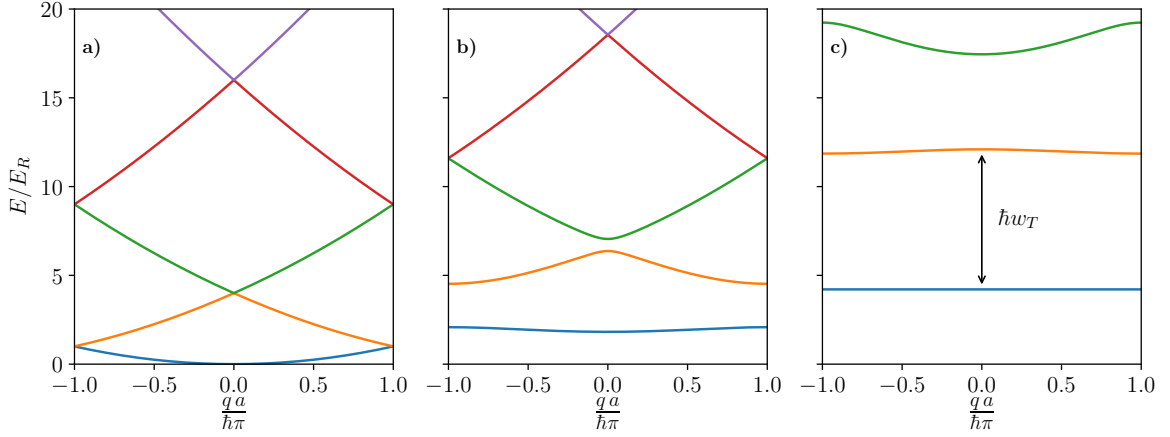


Figure 2.1: Dispersion relation of a particle trapped in a periodic potential, see Eq. (2.6), as a function of the quasi-momentum restricted to the first Brillouin zone for lattice depths $V_0/E_R = 0, 5, 20$ in panels a), b) and c), respectively. For large lattice depths $V_0/E_R \gg 1$, each band is separated by a band gap given by Eq. (2.12).

reduces to $\hat{H}\phi_q^{(n)} = E_q^{(n)}\phi_q^{(n)}$, which yields to an equation for the Bloch wavefunctions,

$$\left[\frac{(\hat{p} + \hbar q)^2}{2m} + V_{\text{ext}}(x) \right] u_q^{(n)}(x) = E_q^{(n)} u_q^{(n)}. \quad (2.9)$$

To solve Eq. (2.9) we decompose the Bloch wavefunctions and the external potential in a discrete Fourier transform,

$$u_q^{(n)}(x) = \sum_r e^{i2krx} c_r^{(n,q)}, \quad \text{and} \quad V(x) = -\frac{V_0}{4} (e^{i2kx} + e^{-i2kx} - 2). \quad (2.10)$$

By inserting the Fourier decomposition Eq. (2.10) into Bloch Hamiltonian (2.9) we obtain a matrix decomposition of the Schrödinger equation (Greiner, 2003),

$$\sum_r H_{r,r'} c_r^{(n,q)} = E_q^{(n)} c_r^{(n,q)}, \quad \text{with} \quad H_{r,r'} = \begin{cases} (2r + \frac{q}{\hbar k})^2 E_R & \text{if } |r - r'| = 0 \\ -\frac{V_0}{4} & \text{if } |r - r'| = 1 \\ 0 & \text{else} \end{cases} \quad (2.11)$$

By diagonalizing the matrix $H_{r,r'}$ we obtain the eigenenergies $E_q^{(n)}$ for a given quasi-momentum q and band index n . In practical purposes, the diagonalization is numerically performed by putting a cutoff on the index r . Restricting the size of the matrix is a good approximation if one focuses on the lowest energy bands.

The properties of the system depend on the dimensionless quantity V_0/E_R which measures the strength of the optical lattice compared with the typical kinetic energy. In Fig. 2.1 we represent the

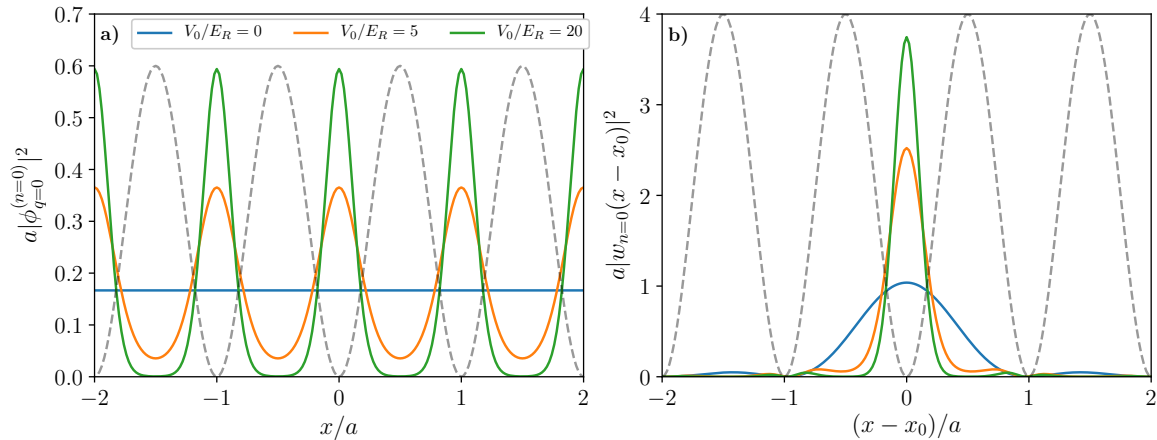


Figure 2.2: Panel a): Squared amplitude of the Bloch wavefunction $|\phi_q^{(n)}|^2$ in the lowest energy band $n = 0$ and at zero quasi-momentum $q = 0$ as a function of the position x for three different heights of the optical lattice. Panel b): Squared amplitude of the Wannier wavefunction $|w_n|^2$ in the lowest energy band $n = 0$ as a function of the position x for the same three values of V_0/E_R as in panel a). In both panels we schematically represent the optical lattice as a black dashed line.

band structure for different lattice depths V_0/E_R . For a vanishing optical lattice, the energy spectrum is continuous, and the bands fold as we are restricting the spectrum inside the first Brillouin zone. However, by increasing the lattice depth, gaps separating different bands start to appear. In the limit $V_0/E_R \rightarrow \infty$, each well of the optical lattice can be approximated by an harmonic oscillator. Therefore, the bands flatten and are separated by the characteristic energy $\hbar\omega_T$, which corresponds to the harmonic trapping frequency of each potential well, given by,

$$\hbar\omega_T = \sqrt{4V_0E_R}. \quad (2.12)$$

In Fig. 2.2 panel a) we represent the Bloch wavefunctions $\phi_q^{(n)}$ in the lowest band $n = 0$ at null quasi-momentum $q = 0$. When the optical lattice is absent $V_0/E_R = 0$, the Bloch wavefunction is constant over the entire system. However, as the height of the optical lattice increases, different maxima start to appear at the minima of the potential wells, indicating that atoms tend to occupy only the lattice positions. Note that Bloch wavefunctions are always distributed among different sites for any ratio of V_0/E_R .

2.3 Derivation of the Bose-Hubbard Hamiltonian

Once the problem of a single particle in an optical lattice is solved, we can focus on the many-body problem. First we expand the bosonic field operators,

$$\hat{\psi}(x) = \sum_n \phi_n(x) \hat{b}_n, \quad (2.13)$$

$$\hat{\psi}^\dagger(x) = \sum_n \phi_n^*(x) \hat{b}_n^\dagger, \quad (2.14)$$

where the coefficients $\phi_n(x)$ and $\phi_n^*(x)$ are single-particle wavefunctions corresponding to the n eigenstate and \hat{b}_n and \hat{b}_n^\dagger are the bosonic annihilation and creation operators for the n -state, respectively. If $\{\phi_n(x)\}$ form a complete basis, the bosonic field operators obey the bosonic commutation relations. As described in the previous section, a complete single-particle basis is formed by Bloch functions,

$$\hat{\psi}(x) = \sum_{n,q} e^{iqx/\hbar} u_q^{(n)}(x) \hat{b}_q^{(n)}. \quad (2.15)$$

However, this basis is not very convenient to describe the high optical lattice regime $V_0/E_R \gg 1$ since Bloch functions are always distributed among different sites, see Fig. 2.2 panel a). Another complete orthogonal basis is provided by the Wannier functions (Marzari et al., 2012),

$$w_n(x - x_j) = \frac{1}{\sqrt{\mathcal{N}}} \sum_j e^{-iqx_j/\hbar} \phi_q^{(n)}(x), \quad (2.16)$$

where \mathcal{N} is a normalization constant and $x_j = ja$ is the lattice position. Wannier functions are not uniquely defined since Bloch functions are defined up to a global phase, which can cause significant changes in the resulting Wannier functions. This freedom is often used to obtain highly localized functions centered at a point x_i , which rapidly decay away from it. In Fig. 2.2 panel b) we represent the lowest band Wannier function $n = 0$ for different ratios V_0/E_R . The Wannier function localizes in the potential well as the ratio V_0/E_R increases, being well approximated for $V_0/E_R \gg 1$ by a Gaussian function with width $\sigma = (E_R/V_0)^{1/4} a/\pi$. By employing the Wannier functions the field operator can be rewritten as,

$$\hat{\psi}(x) = \sum_{n,i} w_n(x - x_i) \hat{b}_i^{(n)}, \quad (2.17)$$

where $\hat{b}_i^{(n)}$ is the annihilation operator of a particle in the proper Wannier state $w_i^{(n)}(x)$ at site i and band n . Now we assume that all the energy scales of the system are much smaller than the typical band gap given by $\hbar w_T$ in the limit $V_0/E_R \gg 1$, see Fig. 2.1, which allows to neglect band transitions and consider only the lowest band $n = 0$. This approximation is usually called tight-binding approximation. Introducing the expansion (2.17) in the Hamiltonian (2.1) we obtain,

$$\begin{aligned} H = & \sum_{i,j} \hat{b}_i^\dagger \hat{b}_j \int d\mathbf{r} w^*(\mathbf{r} - \mathbf{r}_i) \left[-\frac{\hbar^2}{2m} \nabla^2 + V_{opt}(\mathbf{r}) \right] w(\mathbf{r} - \mathbf{r}_j) \\ & + \frac{g}{2} \sum_{i,j,i',j'} \hat{b}_i^\dagger \hat{b}_i^\dagger \hat{b}_j \hat{b}_{j'} w^*(\mathbf{r} - \mathbf{r}_i) w^*(\mathbf{r} - \mathbf{r}_{i'}) w(\mathbf{r} - \mathbf{r}_j) w(\mathbf{r} - \mathbf{r}_{j'}), \end{aligned} \quad (2.18)$$

where we have dropped the band index since we only consider the lowest one ($n = 0$). For the kinetic energy we can neglect contributions with $|i - j| > 2$ as the Wannier functions are localized at a particular site i and fall off rapidly away from it, which is equivalent to consider tunneling only between nearest neighbors. We can also neglect offsite interactions for the second integral and only

consider on-site interactions ($i = i' = j = j'$). With these assumptions we obtain the well-known 1D Bose-Hubbard Hamiltonian (Lewenstein et al., 2012),

$$H = - \sum_i t \left(\hat{b}_i^\dagger \hat{b}_{i+1} + \text{H.c.} \right) + \frac{U}{2} \sum_i \hat{n}_i (\hat{n}_i - 1) + \epsilon \sum_i \hat{n}_i, \quad (2.19)$$

where we identify the following parameters,

$$\begin{aligned} t &= \int dx w^*(x - x_i) \left[-\frac{\hbar^2}{2m} \partial_x^2 + V_{\text{ext}}(x) \right] w(x - x_{i+1}) \approx \frac{4}{\sqrt{\pi}} E_R \left(\frac{V_0}{E_R} \right)^{3/4} e^{-2\sqrt{V_0/E_R}}, \\ U &= g \int dx |w(x - x_i)|^4 \approx \sqrt{\frac{2}{\pi}} \hbar w_T \frac{a_s}{a}, \\ \epsilon &= \int dx w^*(x - x_i) \left[-\frac{\hbar^2}{2m} \partial_x^2 + V_{\text{ext}}(x) \right] w(x - x_i), \end{aligned} \quad (2.20)$$

which are the tunneling strength, on-site interaction and an on-site potential, respectively. Moreover, we have assumed that the optical lattice is homogeneous making the Hamiltonian parameters independent on the lattice site i . The on-site potential can be dropped ($\epsilon = 0$) when working in the canonical ensemble with a fixed number of particles. The approximate results given in Eq. (2.20) correspond to the limit $V_0/E_R \gg 1$, where the Wannier functions are approximated by Gaussian functions. In Fig. 2.4 panel b) we show the dependence of the on-site interaction U and tunneling strength t as a function of the ratio V_0/E_R . For a sufficiently high optical lattice the tunneling decays exponentially with the height of the lattice. Finally, let us emphasize that Hamiltonian (2.19) describes the physics of ultracold bosonic atoms in an optical lattice if the condition $U, t, T \ll \hbar w_T$ is fulfilled i.e. band transitions can be neglected. Moreover, the Hamiltonian parameters given by Eq. (2.20) can be tuned by controlling the ratio V_0/E_R giving an additional degree of control over the system by tuning the height of the optical lattice.

2.4 Physics of the Bose-Hubbard model

The experimental simulation of the Bose-Hubbard model, Eq. (2.19), using cold atoms loaded in a high optical lattice, was one of the big successes of cold atomic systems (Greiner et al., 2002; Stöferle et al., 2004; Spielman et al., 2007, 2008). This many-body quantum model displays very exotic phenomena due to the competition between two terms: the hopping t and the on-site interaction U . Note that these two terms do not commute $[\hat{H}_t, \hat{H}_U] \neq 0$, and therefore we cannot find a common eigenbasis that diagonalizes the full Hamiltonian. This has strong implications on the many-body ground state of the system when the number of particles N is commensurate with the number of sites N_s comprising the optical lattice $N/N_s \equiv n \in \mathbb{Z}$ (Fisher et al., 1989; Sachdev, 2011). If the hopping dominates over the interaction $t/U \gg 1$, then particles tend to delocalize over the optical lattice to minimize their kinetic energy, forming what is called a superfluid (SF) phase, see Fig. 2.3 b). However, if the interaction dominates over the hopping $t/U \ll 1$, then each potential well comprising the optical lattice is homogeneously filled with n particles, see Fig. 2.3 a). In such situation, particles completely localize

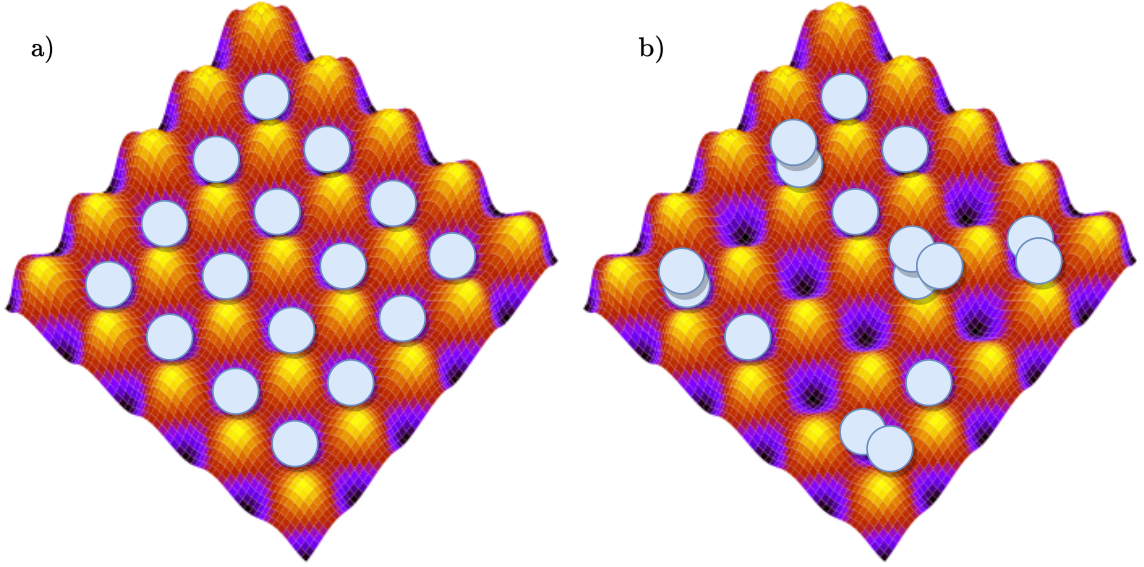


Figure 2.3: Schematic representation of a 2D square optical lattice where a commensurate number of bosons are loaded and a single snapshot of the particle configuration is taken for a) in the Mott-insulator phase and for b) in the superfluid phase.

to reduce their interaction energy forming what is called a Mott insulator (MI) phase. Therefore, the many-body ground state dramatically changes as a function of the ratio t/U . As we show below these two states cannot be continuously connected and a phase transition occurs between them. Note that this phase transition happens even at zero temperature and therefore it is called a quantum phase transition (Sachdev, 2011). In the following we describe these two quantum phases and the quantum phase transition between them in 1D.

2.4.1 Superfluid phase

When the on-site interaction is neglected $U/t = 0$, the Hamiltonian (2.19) can be diagonalized by performing the Fourier transform,

$$\hat{H} = \sum_k \epsilon_k \hat{b}_k^\dagger \hat{b}_k, \quad \text{with} \quad \hat{b}_k = \frac{1}{\sqrt{L}} \sum_{j=1}^{N_s} e^{ikx_j} \hat{b}_j, \quad (2.21)$$

where we introduce the single-particle dispersion relation $\epsilon_k = -2t \cos(ka)$ and the lattice length $L = aN_s$. The many-body ground state of the system $|\phi_t\rangle$ composed of N bosons is formed by populating the lowest point of the single-particle dispersion relation corresponding to $k = 0$,

$$|\phi_t\rangle = \frac{1}{\sqrt{N!}} \left(\hat{b}_{k=0}^\dagger \right)^N |0\rangle = \frac{1}{\sqrt{N!}} \left(\frac{1}{\sqrt{N_s}} \sum_{j=1}^{N_s} \hat{b}_j^\dagger \right)^N |0\rangle, \quad (2.22)$$

where we introduce the bosonic vacuum $\hat{b}_k|0\rangle = 0$. In the thermodynamic limit $N, N_s \rightarrow \infty$ with $N/N_s = n$ finite, we obtain,

$$|\phi_t\rangle = \frac{1}{\sqrt{\mathcal{N}}} \prod_j e^{\sqrt{n}\hat{b}_j^\dagger} |0\rangle, \quad (2.23)$$

with \mathcal{N} being a normalization constant. The state $|\phi_t\rangle$ corresponds to the direct product of each site being in a coherent state, i.e., an eigenstate of the local annihilation operator \hat{b}_i . Moreover, it is constructed as the direct product of single-particle eigenfunctions, which makes possible a description of the system via a macroscopic wavefunction with a well-defined global phase. At the same time, the system shows strong particle fluctuations in each lattice site following a Poissonian distribution with particle variance $\sigma(n_i) = \sqrt{n_i}$. Therefore, occupation numbers larger than the mean density n can be easily found. These configurations are dramatically disfavored in the limit $U/t \gg 1$.

The state $|\phi_t\rangle$ is not an eigenstate of the total particle number operator \hat{N} in the thermodynamic limit. Thus, it spontaneously breaks the underlying U(1) symmetry of the Bose-Hubbard Hamiltonian (2.19) associated with particle number conservation. To characterize the spontaneous breaking of the U(1) symmetry, we can compute the one-body correlation function $\langle \phi_t | \hat{b}_i^\dagger \hat{b}_j | \phi_t \rangle$, which shows long-range coherence,

$$\lim_{|i-j| \rightarrow \infty} \langle \phi_t | \hat{b}_i^\dagger \hat{b}_j | \phi_t \rangle = n, \quad (2.24)$$

which is a fundamental property of systems exhibiting Bose-Einstein condensation (Pitaevskii, 2003). In the weakly-interacting regime $t/U \ll 1$, the family of coherent states satisfying $\hat{a}_i |\phi_c\rangle = \sqrt{n_i} e^{i\phi_i} |\phi_c\rangle$, with a local density n_i and phase ϕ_i , is a good ansatz for describing the ground state properties of the bosonic system. This is called the mean-field approximation. The real part of the ground state energy can be easily determined,

$$\langle \phi_c | \hat{H} | \phi_c \rangle = -t \sum_i \cos(\phi_i - \phi_{i+1}) \sqrt{n_i n_{i+1}} + \frac{U}{2} \sum_i n_i^2, \quad (2.25)$$

which is minimized for a state exhibiting a global phase $\phi_i = \phi_{i+1} \equiv \phi$ in a homogeneous system $n_i \equiv n$. Therefore, we can expect a coherent type ground state in the weakly interacting regime $U/t \ll 1$.

In 1D systems spontaneous symmetry breaking is forbidden in the thermodynamic limit because of the Mermin-Wagner-Coleman theorem (Mermin and Wagner, 1966; Hohenberg, 1967; Mermin, 1968; Coleman, 1973) and, the true ground state of the system $|\psi_0\rangle$ for $U/t \ll 1$ does not exhibit long-range order. Therefore, the ground state $|\psi_0\rangle$ does not correspond to a coherent state. However, we can still expect quasi long-range order characterized by a power-law type decay of the correlation function (Giamarchi, 2003),

$$\lim_{|i-j| \rightarrow \infty} \langle \psi_0 | \hat{b}_i^\dagger \hat{b}_j | \psi_0 \rangle = \frac{C}{|x_i - x_j|^\alpha}, \quad (2.26)$$

where C is a non-universal constant and α depends on the low-energy properties of the system. This is one of the fundamental properties of the superfluid phase.

The superfluid phase is also characterized by its spectral properties. If we define the charge gap Δ_c as the energy cost of introducing a particle-hole in the system,

$$\Delta_c = E_{N+1} + E_{N-1} - 2E_N. \quad (2.27)$$

The gap closes in the thermodynamic limit $\Delta_c \propto 1/L$ for a state $|\phi_c\rangle$, indicating the appearance of gapless excitations. The charge gap can be understood as a discretized version of the incompressibility of the system $\kappa^{-1} = Ln^2 \partial^2 E / \partial N^2 \approx Ln^2 \Delta_c$. The incompressibility in the superfluid phase remains finite denoting that the system can be easily compressed.

It is also instructive to analyze the superfluid state given by Eq.(2.22) from a quantum information perspective. Consider a 1D optical lattice that we bipartite into two segments A and B of lengths L_A and L_B , respectively. We can perform a singular value decomposition (SVD) of the superfluid state, see Eq.(A.8) in Chap. A.1.1, with respect to this partition,

$$|\phi_t\rangle = \frac{L^{-N/2}}{\sqrt{N!}} \left(\sum_{j \in A} \hat{b}_j^\dagger + \sum_{j \in B} \hat{b}_j^\dagger \right)^N |0\rangle = \sum_{n=0}^N (L_A + L_B)^{-N/2} L_A^{n/2} L_B^{(N-n)/2} \sqrt{\binom{N}{n}} |n\rangle_A \otimes |N-n\rangle_B, \quad (2.28)$$

where we introduce the orthonormal states,

$$|n\rangle_A = \frac{L_A^{-n/2}}{\sqrt{n!}} \left(\sum_{j \in A} \hat{b}_j^\dagger \right)^n, \quad (2.29)$$

$$|n\rangle_B = \frac{L_B^{-n/2}}{\sqrt{n!}} \left(\sum_{j \in B} \hat{b}_j^\dagger \right)^n, \quad (2.30)$$

of segments A and B , respectively. From Eq. (2.28) we can read the Schmidt values of the superfluid state,

$$\lambda_n = (L_A + L_B)^{-N} L_A^n L_B^{N-n} \binom{N}{n}. \quad (2.31)$$

We now focus on an equal bipartition $L_A = L_B = L/2$ and consider the large particle number limit $N \rightarrow \infty$ in which we can approximate the binomial distribution as a continuum Gaussian one,

$$\lambda(n) \approx \frac{2}{N\pi} e^{-2\left(\frac{N}{2}-n\right)^2/N}. \quad (2.32)$$

The distribution of the Schmidt values is peaked at $n = N/2$, meaning that if we measure the particles in region A , we have the maximum probability of finding half of the particles in region A . The

entanglement entropy, see Eq. (A.11), is given by,

$$S_E = - \int_0^N dn \lambda(n) \log \lambda(n) \approx \frac{1}{2} \log N. \quad (2.33)$$

The entanglement entropy grows logarithmically with the number of particles. Such behavior is usually referred to as a weak violation of the area law since it is in between the area and the volume law. Critical phases in 1D usually exhibit this behavior (Calabrese and Cardy, 2004).

The appearance of quasi-long range order, the closing of the spectral gap and the divergence of the entanglement entropy define the superfluid phase. As we show below the state at $U/t \rightarrow \infty$ does not have these three properties.

2.4.2 Mott insulator phase

Particle number fluctuations are suppressed when the interaction energy dominates in the system $t/U = 0$. In this limit, the many-body wavefunction $|\phi_U\rangle$ has a well defined number of particles in each lattice site $\hat{n}_i|\phi_U\rangle = n|\phi_U\rangle$. When the number of particles is commensurate with the number of sites $n \in \mathbb{Z}$, the ground state of the system is given by,

$$|\phi_U\rangle = \frac{1}{n^{N_s}} \prod_{j=1}^{N_s} (\hat{b}_j^\dagger)^n |0\rangle, \quad (2.34)$$

which is a direct product of local Fock states in the local particle number basis. Therefore, the many-body state cannot be described by a macroscopic wavefunction due to strong particle correlations. These type of phases are called strongly correlated many-body phases. Moreover, the state $|\phi_U\rangle$ exhibits a vanishing one-body correlation function at any distance larger than the lattice spacing. In the strongly-interacting regime $U/t \gg 1$, atoms start to hop to gain kinetic energy, and the ground state of the system does not correspond to $|\phi_U\rangle$. However, if the gain in kinetic energy remains lower than the on-site interaction energy, then atoms remain localized. In this limit, short-range correlations appear, and an exponentially decaying correlation function is expected (Giamarchi, 2003),

$$\langle \psi_0 | \hat{b}_i^\dagger \hat{b}_j | \psi_0 \rangle = C e^{-|x_i - x_j|/\xi}, \quad (2.35)$$

where we introduce the constant C and the correlation length ξ measuring the characteristic distance at which coherence can be observed. Note that the superfluid phase is characterized by an infinite correlation length $\xi \rightarrow \infty$. Moreover, the Mott insulator phase is characterized by a finite charge gap which in the strongly interacting regime goes as $\Delta_c \propto U$, showing that the system becomes completely incompressible $\kappa = 0$ in the limit $t/U = 0$. Note that the Mott insulator phase can only exist at commensurate fillings $n \in \mathbb{Z}$. Therefore, the system undergoes a Mott insulator to superfluid transition as soon as some defects $n + \epsilon$ are introduced in a system with fixed total particle number, since these defects can delocalize on top of the frozen Mott insulator (Astrakharchik et al., 2017).

Moreover, the Mott-insulator state Eq. (2.34) is a product state, see discussion in Sec. 1.3, mean-

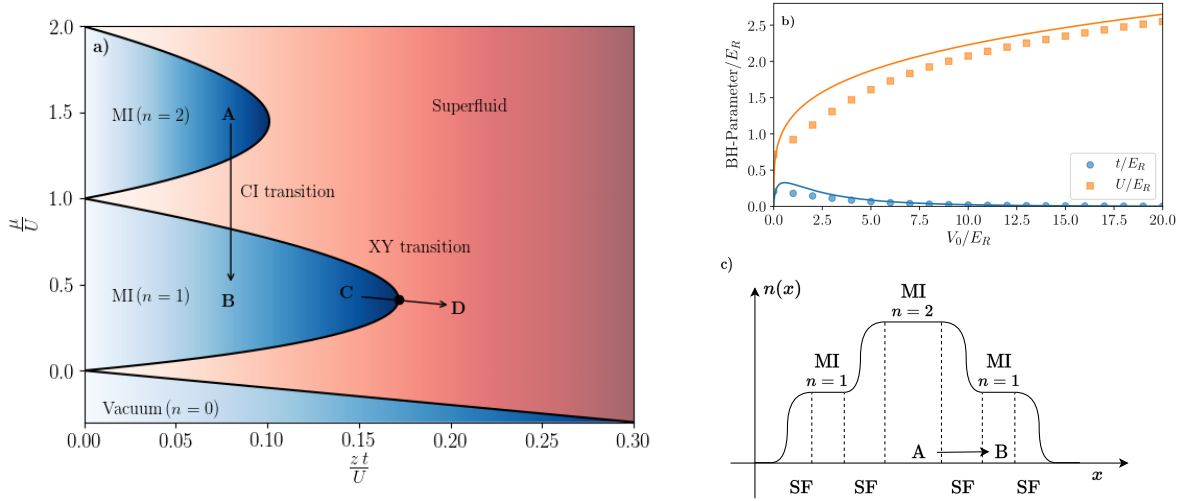


Figure 2.4: Mean-field Bose-Hubbard phase diagram at zero temperature in the $\mu/U - zt/U$ plane in panel a). The blue regions denote the different Mott lobes at densities $n = 1, 2, \dots$ and the vacuum region $n = 0$. The red region denotes the superfluid phase. The superfluid to Mott transition can be a commensurate to incommensurate (CI) transition $A \rightarrow B$ or a XY transition $C \rightarrow D$. In panel b) we show the dependence of the Bose-Hubbard parameters U and t as a function of the height of the optical lattice over the recoil energy V_0/E_R for $g = 1$. The continuous lines correspond to the approximate results assuming localized Gaussian functions at each lattice site, see Eq. (2.20). In panel c) we show a schematic density profile $n(x)$ of a bosonic system loaded in a high 1D optical lattice with a harmonic external confinement. The system shows a 'wedding-cake' structure where MI regions with a flat density plateau are connected by superfluid regions. The CI transition is crossed as a function of the spatial coordinate x .

ing that different subsystems are not entangled since the state has a vanishing correlation length. Therefore, the entanglement entropy of any bipartition is zero.

As we have seen, the ground state properties of the Bose-Hubbard model, Eq. (2.19), dramatically change as a function of t/U . A gap closes in the spectrum, the decay of the correlation functions changes, and the entanglement entropy diverges in the SF phase while it is constant in the MI one. Therefore, we expect a critical point $(t/U)_c$ where a phase transition occurs.

2.4.3 Quantum phase transition

The superfluid-to-Mott insulator quantum phase transition has been extensively studied theoretically, numerically and experimentally in the last few decades, see (Giamarchi, 2003; Lewenstein et al., 2012; Bloch et al., 2008; Sachdev, 2011) for a review. In this section we highlight its main properties.

In Fig. 2.4 panel a) we present the zero temperature Bose-Hubbard phase diagram in the $\mu/U - zt/U$ plane obtained with a mean-field approximation, where z is the coordination number of the lattice and μ is the chemical potential, see (Fisher et al., 1989; Sheshadri et al., 1993; van Oosten et al., 2001) for details on the calculation. In the strong coupling regime $U/t \gg 1$ we find different regions (Mott lobes) where a MI phase is stabilized at different commensurate densities. These regions are surrounded by a

superfluid phase with a real density $n \in \mathbb{R}$. The superfluid-to-Mott insulator transition can be crossed in two different ways (Fisher et al., 1989): the density of the system remains constant $n \in \mathbb{Z}$ while crossing the transition point, see C→D in Fig. 2.4 panel a), or the density exhibits a sudden jump at the transition point, see A→B in Fig. 2.4 panel a). Since the MI is an incompressible phase it cannot be smoothly connected with a superfluid phase at an incommensurate density. Therefore, a sudden jump of density has to occur at the critical point. This is called a commensurate-to-incommensurate (CI) type transition and it is characterized by having a finite correlation length at the transition point (Sachdev, 2011). The CI transition can also occur if a MI phase is doped with a small amount of defects $n + \epsilon$, which create a finite superfluid density. However, if we only change the ratio U/t then, the CI transition can only be crossed in the grandcanonical ensemble with a fixed chemical potential μ if the system is homogeneous. However, the total particle number is fixed in cold atoms experiments. Therefore, the CI transition can only be crossed by employing an external trap $V(x)$ such as a Gaussian one. In this situation, the chemical potential can be considered to be spatial dependent $\mu(x) = \mu(0) - V(x)$ and the phase transition can be crossed as a function of the spatial coordinate x , see Fig. 2.4 panels a) and c). For $U/t \gg 1$ the system develops flat density plateaus with $n \in \mathbb{Z}$ since the Mott insulator phase is completely incompressible $\partial n / \partial \mu(x) = 0$. Two Mott insulator regions are connected by a superfluid region where the density is smoothly connected between the two density plateaus, see Fig. 2.4 panel c). This is usually called a “wedding-cake” structure and it has been observed in cold atoms experiments (Gemelke et al., 2009; Bakr et al., 2010; Sherson et al., 2010).

The phase transition can also be crossed at fixed density $n \in \mathbb{Z}$, causing the properties of the transition to change drastically (Sachdev, 2011). In this situation the transition is in the $(D + 1)$ -XY universality class in D dimensions (Fisher et al., 1989), see Fig. 2.4 panel a). In a 1D system, it corresponds to a Berezinskii-Kosterlitz-Thouless (BKT) transition characterized by an exponential closing of the energy gap in the thermodynamic limit for $U > U_c$ (Giamarchi, 2003),

$$\Delta \propto e^{-C/\sqrt{U/t - U_c/t}}, \quad (2.36)$$

where C is some non-universal constant and U_c/t is the critical point at which the transition occurs. Therefore, the transition point becomes critical, and we observe a divergent correlation length $\xi \sim \Delta^{-1}$.

2.5 Two-particle problem

One of the main topics of this Thesis is the formation of bound states. Therefore, it is instructive to study the simplest lattice problem where a bound state appears: the two-particle problem of the BH model Eq. (2.19). For a detailed discussion on scattering theory on a lattice, see M. Valiente’s thesis (Cifuentes, 2010) and (Valiente and Petrosyan, 2008). We consider two-particles moving in a homogeneous high 1D optical lattice. We introduce the two-particle state $|i, j\rangle$,

$$|i, j\rangle = \begin{cases} \hat{b}_i^\dagger \hat{b}_j^\dagger |0\rangle & \text{if } |i - j| \geq 1, \\ \frac{1}{\sqrt{2}} \hat{b}_i^\dagger \hat{b}_i^\dagger |0\rangle & \text{otherwise,} \end{cases} \quad (2.37)$$

and separate the problem in center of mass $R/a = (i + j)/2$ and relative coordinates $z/a = i - j$,

$$|\psi\rangle = \frac{1}{\sqrt{L}} \sum_{i,j} e^{iQR} \psi_Q(z) |i, j\rangle, \quad (2.38)$$

where we introduce the total quasi-momentum $Q \in [-\pi/a, \pi/a)$ and the wavefunction of the relative motion $\psi_Q(z)$ which parametrically depends on the total quasi-momentum. By substituting the ansatz Eq (2.38) into Eq. (2.19), we obtain an equation of motion for $\psi_Q(z)$,

$$E_Q \psi_Q(z) = \sum_{e=\pm 1} -2t \cos(Qa/2) \psi_Q(z + e) + U \delta(z) \psi_Q(z). \quad (2.39)$$

The problem is reduced to a single-particle problem where the particle propagates with an effective hopping $t_Q = -2t \cos(Qa/2)$ and sees a potential corresponding to a delta-function of strength U located at the origin. The equation of motion Eq. (2.39) can be solved numerically performing exact diagonalization. However, to illustrate the different types of solutions we provide here an analytical solution which can be obtained for contact-like interactions. The equation of motion Eq. (2.39) has two types of solutions: scattering and bound states. Scattering states are states that are spread over the entire system and their energy in a large system for a local interaction potential is given by,

$$E_{Q,k} = -4t \cos(Qa/2) \cos(ka) \equiv -2t (\cos(k_1) + \cos(k_2)), \quad (2.40)$$

where the index k plays the role of the relative quasi-momentum. Eq. (2.40) defines the scattering continuum and we can obtain the associated density of states,

$$\rho(E_{Q,k}, Q) = \frac{L}{2\pi} \frac{\partial k}{\partial E_{Q,k}} = \frac{L}{2\pi a} \frac{1}{\sqrt{4t^2 \cos^2(Qa/2) - E_{Q,k}^2}}, \quad (2.41)$$

which exhibits a van Hove singularity at the upper and lower part of the scattering continuum and is minimum at the middle of the band ($Q \sim 0, E_Q \sim 0$), see Fig. 2.5.

The scattering state wavefunction $\psi_{Q,k}(z)$ can be obtained by solving the discrete Lippmann-Schwinger ([Lippmann and Schwinger, 1950](#)) equation,

$$\psi_{Q,k}(z) = \phi_{Q,k}(z) - \sum_m G_k(z - m) V(m) \phi_{Q,k}(m), \quad (2.42)$$

where we introduce the free-particle wavefunction $\phi_{Q,k}(z) = \cos(kz)$, the potential $V(m) = U \delta(m)$ and the lattice free Green's function $G_k(z)$ which obeys the equation,

$$\delta(z) = -2t \cos(Qa/2) \sum_{e=\pm 1} G_k(z + e) + E_{Q,k} G_k(z), \quad (2.43)$$

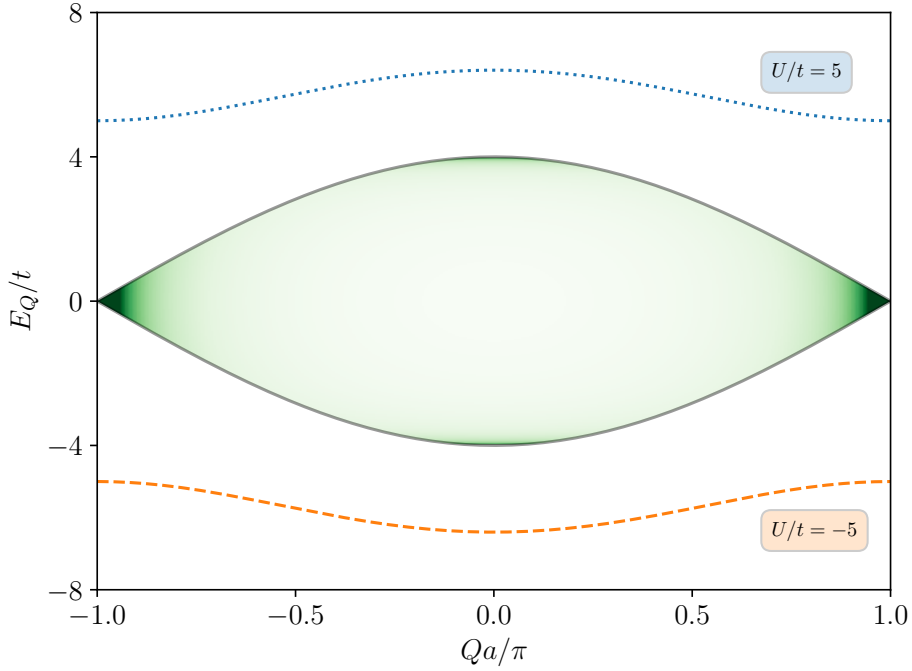


Figure 2.5: Energy spectrum as a function of the total quasi-momentum Q for the two-boson problem described by the Bose-Hubbard Hamiltonian, Eq. (2.19). The continuum region denotes the scattering continuum Eq. (2.40) where color is proportional to the density of states $\rho(Q, E_Q)$, see Eq. (2.41). The blue dotted (orange dashed) line represents the energy of the attractive (repulsive) bound state for attractive (repulsive) on-site interaction U/t .

with a symmetric solution,

$$G_k(z) = -\frac{\csc(ka)}{4t \cos(Qa/2)} \sin(k|z|). \quad (2.44)$$

Therefore, scattering states are given by,

$$\psi_{Q,k}(z) = \cos(kz) + \frac{U}{4t \cos(Qa/2)} \csc(ka) \sin(k|z|). \quad (2.45)$$

It is instructive to rewrite Eq. (2.45) as,

$$\psi_{Q,k}(z) = \sqrt{1 + \frac{U}{4t \cos(Qa/2)}} \cos(kz + \delta_{Q,k}), \quad (2.46)$$

for $z > 0$. We introduce the phase shift $\delta_{Q,k}$ which determines the phase shift of the wavefunction $\psi_{Q,k}(z)$ with respect to the free-particle wavefunction $\phi_{Q,k}(z)$ due to the presence of the interaction

potential. Its expression is given by,

$$\tan(\delta_{Q,k}) = -\frac{U}{4 \cos(Qa/2)} \csc(ka). \quad (2.47)$$

From the phase shift we can introduce the scattering length a_Q defined as the position of the pole closest to the origin of the wavefunction $\psi_{Q,k}(z)$ in the low relative quasi-momentum limit. The scattering length is related to the phase shift as,

$$a_Q = -\lim_{k \rightarrow 0} \frac{\partial \delta_{Q,k}}{\partial k} = -\frac{4ta \cos(Qa/2)}{U}. \quad (2.48)$$

Note that one could also introduce collisions close to the edge of the Brillouin zone and therefore, a scattering length for $k \rightarrow \pm\pi/a$. However, we focus on the low quasi-momentum limit. The scattering length is a very useful quantity, as low-energy collisions can be uniquely determined by it, regardless of the shape of the potential. This is a standard situation in ultracold atomic systems. The scattering length Eq. (2.48) exhibits a pole (from $a \rightarrow -\infty$ to $a \rightarrow \infty$) when the on-site interaction goes from repulsive to attractive, denoting the appearance of a bound state in the system. Contrary to scattering states, bound states exhibit an energy E_Q which lies outside the scattering continuum $|E_Q| > |E_{Q,k}|$. In this situation, the discrete Lippmann-Schwinger equation reads,

$$\psi_Q(z) = -\sum_m G_E(z-m)V(m)\psi_Q(m), \quad (2.49)$$

where the lattice Green's function $G_E(z-m)$ obeys,

$$\delta(z) = -2t \cos(Q/2) \sum_{e=\pm 1} G_k(z+e) + E_Q G_k(z). \quad (2.50)$$

To obtain the bound state energy we assume an ansatz for the relative wavefunction $\psi_Q(z)$, see (Cifuentes, 2010) for a detailed solution of the problem without assuming an ansatz. Bound states are localized within the range of the potential, and therefore, they exhibit an exponential decay away from it. In the lattice problem, we propose the exponential ansatz for $z \neq 0$,

$$\psi_Q(z) = \begin{cases} \beta_Q & \text{if } z = 0, \\ C_Q \alpha_Q^{|z|} & \text{otherwise,} \end{cases} \quad (2.51)$$

which inserting into Eq. (2.39) for $|z| > 1$ gives the relation,

$$E_Q = -2t \cos(Qa/2) \frac{1 + \alpha_Q^2}{\alpha_Q}, \quad (2.52)$$

which can be inverted to obtain,

$$\alpha_Q = -\frac{1}{2t \cos(Qa/2)} \left(E_Q + \text{sign}(E_Q) \sqrt{E_Q^2 - 16t^2 \cos^2(Qa/2)} \right), \quad (2.53)$$

where one solution of α_Q can be discarded by requiring the wavefunction $\psi_Q(z)$ to have a finite norm. By inserting these results into Eq. (2.39) for $z = 0$ and $|z| = 1$ we obtain $\beta_Q = C_Q$ and the expression for the bound state energy,

$$E_Q = \text{sign}(U) \sqrt{U^2 + 16t^2 \cos^2(Qa/2)}. \quad (2.54)$$

The bound state energy can lie either above ($U > 0$) or below ($U < 0$) the scattering continuum, see Fig. 2.5. Usually, bound states lying above (below) the scattering continuum are named repulsive (attractive) bound states. The existence of repulsive bound states is a unique property of a lattice system. Since the scattering continuum Eq. (2.40) is bounded from below and above, a very repulsive pair of particles localized in the same site with a leading energy $E_Q \sim U$ cannot dissociate into a free pair of particles. This process do not conserve the energy since the maximum scattering energy is given by $4t$. However, in a continuous system with a scattering continuum not bounded from above, a very repulsive pair can always dissociate into a free pair of particles with very large momenta. Repulsive bound states of cold atoms loaded in a high optical lattice have been experimentally observed in (Winkler et al., 2006).

The bound state energy Eq. (2.54) defines the effective mass of the bound pair,

$$M^* = \left(\frac{\partial E_Q}{\partial Q} \right)_{Q=0}^{-1} = -\text{sign}(U) \frac{\sqrt{U^2 + 16t^2}}{4t^2 a^2}, \quad (2.55)$$

which is positive (negative) for the attractive (repulsive) bound state. In the weakly-interacting regime $U/t \ll 1$, the effective mass of the pair is approximated by,

$$M^* \approx -\text{sign}(U) \frac{1}{ta^2} = -2\text{sign}(U)m^*, \quad (2.56)$$

corresponding to twice the effective mass of a single-particle described by the BH model. However, in the strongly interacting regime the effective mass becomes,

$$M^* \approx -\frac{U}{4ta^2} = \frac{1}{2Ja^2}, \quad (2.57)$$

where we define the effective hopping of a strongly bound pair $J = -2t^2/U$. Note that in the strongly interacting regime $U/t \gg 1$, the effective pair mass becomes very large, indicating a small tunneling rate $J/t \ll 1$. In this limit, the pair becomes strongly localized in a single site. As a result, its propagation requires a second-order process in tunneling, where the pair first breaks and then recombines in a neighboring site.

Bound states are usually characterized by their binding energy E_B , which is defined as the energy difference between the bound state energy and the energy at the lower (upper) part of the scattering band $E_{Q,k=0} = -4t$ ($E_{Q,k=\pi/a} = 4t$) for an attractive (repulsive) bound state,

$$\text{sign}(U)E_B = -4t \cos(Qa/2) + \sqrt{U^2 + 16t^2 \cos^2(Qa/2)}. \quad (2.58)$$

In the weakly interacting regime $U/t \ll 1$ and at vanishing quasi-momentum $Q = 0$ we obtain,

$$E_B(Q = 0) = \text{sign}(U) \frac{U^2}{8t} = \frac{\text{sign}(U)}{m^* a_{Q=0}^2}, \quad (2.59)$$

which fulfills the low-energy relation between the binding energy and the scattering length. In the strongly-interacting regime the binding energy approaches $E_B = U$ showing that the bosonic pair becomes strongly localized in a single site with a leading energy given by the on-site interaction.

We note that the bound state energy Eq. (2.54) fulfills the following relation,

$$E_Q(U) = -E_Q(-U), \quad (2.60)$$

which identifies a hidden symmetry of the BH model Eq. (2.19). Namely, for a given eigenfunction $|\psi(U)\rangle$ of the BH model $\hat{H}(U)$ with eigenenergy $E(U)$, there is an eigenfunction $|\psi(-U)\rangle = \hat{U}|\psi(U)\rangle$ of the Hamiltonian $\hat{H}(-U)$ with eigenenergy $E(-U) = -E(U)$. The unitary operator \hat{U} realizing this symmetry is given by (Sakmann et al., 2010; Deuchert et al., 2012),

$$\hat{U} \hat{b}_j = (-1)^j \hat{b}_j, \quad (2.61)$$

which changes the sign of the bosonic operator at every odd site of the lattice, therefore shifting the momentum of the system by π . By applying the unitary transformation to the Hamiltonian we obtain the relation,

$$\hat{U} \hat{H}(U) \hat{U}^{-1} = -\hat{H}(-U), \quad (2.62)$$

showing the hidden symmetry between repulsive and attractive interactions of the BH model Eq. (2.19).

PRELIMINARIES II: HUBBARD PHYSICS IN TRANSITION METAL DICALCOGENIDE MOIRÉ COMPOUNDS

3.1 Transition metal dichalcogenides

We start by discussing the physics of a monolayer transition metal dichalcogenide (TMD) ([Radisavljevic et al., 2011](#); [Manzeli et al., 2017](#)). We focus our discussion on MoS₂, but the results apply to the broad class of group-VI dichalcogenides MX_2 (with $M = \text{Mo, W}$ and $X = \text{S, Se, Te}$). When a bulk MoS₂ is exfoliated down to a monolayer, its properties dramatically change ([Radisavljevic et al., 2011](#); [Manzeli et al., 2017](#)). The monolayer of MoS₂ is three atoms thick, with the transition metal being in the middle surrounded by six chalcogenide atoms in a trigonal prismatic geometry, see Fig. 3.1 a). Moreover, the crystalline structure in the $x - y$ plane is a hexagonal one and therefore, the system possesses an additional C_3 symmetry, see Fig. 3.1 b). The band structure has been computed from first principle calculations ([Mattheiss, 1973](#)). The Mo atom is in a +4 oxidation state having two active electrons in the d orbital. The orbital degeneracy is broken due to the trigonal prismatic structure, and the orbitals are organized as d_{z^2} , $(d_{xy}, d_{x^2-y^2})$, (d_{xz}, d_{yz}) . The band structure is composed of a valence (conduction) band with edges at the K and $-K$ points composed primarily of the orbitals $d_{x^2-y^2} \pm id_{xy}$ (d_{z^2}). Here, we report a simple model based on symmetry considerations leading to the main features of the band structure, see ([Xiao et al., 2012](#)). Consider a simplified model describing the hopping of electrons from the chalcogen atoms to the transition metal ones. We can write the following tight-binding Hamiltonian,

$$H(\vec{k}) = \vec{d}(\vec{k}) \cdot \vec{\sigma}, \quad \text{with} \quad d_x(\vec{k}) = -t \sum_{i=1}^3 \cos(\vec{k} \cdot \vec{\delta}_i), \quad d_y(\vec{k}) = -t \sum_{i=1}^3 \sin(\vec{k} \cdot \vec{\delta}_i), \quad d_z(\vec{k}) = \frac{\Delta}{2}, \quad (3.1)$$

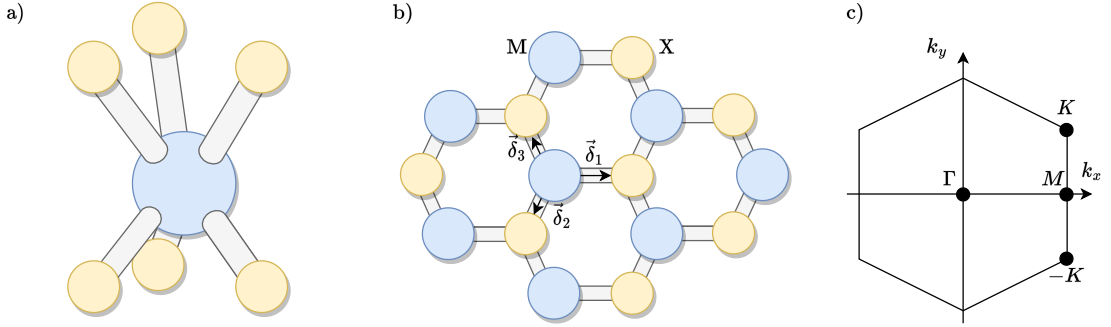


Figure 3.1: a) Side view of a monolayer TMD with a trigonal prismatic geometry. b) Top view of a monolayer TMD where the vectors $\vec{\delta}_i$ connect nearest neighbor atoms. c) First Brillouin zone of the hexagonal lattice.

where we introduce the Pauli matrices $\vec{\sigma}$, the hopping integral t , the band gap Δ and the vectors characterizing the hexagonal geometry $\vec{\delta}_i$, see Fig. 3.1 b). The Hamiltonian has a 2×2 structure since the hexagonal geometry is formed by two inequivalent sublattices containing the chalcogen X and transition metal M atoms, respectively, see Fig. 3.1 b). The spectrum of the system is given by,

$$E(\vec{k}) = \pm |\vec{d}(\vec{k})| = \pm \sqrt{d_x^2(\vec{k}) + d_y^2(\vec{k}) + d_z^2(\vec{k})}, \quad (3.2)$$

and it is characterized by having a direct gap Δ at the six corners of the Brillouin zone formed by the inequivalent points K and $-K$ which cannot be related by $2\pi/3$ rotations, see Fig. 3.2 a). Therefore, a monolayer TMD is a semiconductor with a direct gap making it very appealing since it can absorb photons with an energy equal or larger than the band gap which is on the order of $\Delta \sim 1.6$ eV (Qiu et al., 2013; Chernikov et al., 2014; Ye et al., 2014; Ugeda et al., 2014; Wang et al., 2015). Therefore, TMDs are sensitive to visible (nearly infrared) light, and their properties can be read out with light probes, making them promising platforms for optoelectronic applications. When an electron from the valence band is photoexcited to the conduction band, it leaves behind a quasi-particle of charge $+e$ which is usually called a hole. The photoexcited electron in the conduction band feels an attraction to the hole in the valence band due to Coulomb interaction, and they form a bound state called an exciton (Mueller and Malic, 2018). The exciton is a bosonic quasi-particle that has been extensively studied and appears in other semiconductors, such as GaAs (Fox, 2001). However, TMDs offer an exciting new opportunity for fundamental research since the binding energies of excitons are much larger than in traditional semiconductors. They can be on the order of several hundred meV (Ramasubramaniam, 2012). The two main reasons for the increased binding energy are the large effective mass of charge carriers in TMDs ($m_e \sim 0.5m_e$) and the reduced dielectric screening.

The appearance of a gap is a consequence of explicitly breaking inversion symmetry (Xiao et al., 2007). The two sublattices are inequivalent and therefore, we expect a different on-site energy for the chalcogen and the transition metal atom, giving the d_z component in Eq. (3.1) which leads to the opening of the gap at the K and $-K$ points. Let us remark that these two points are related

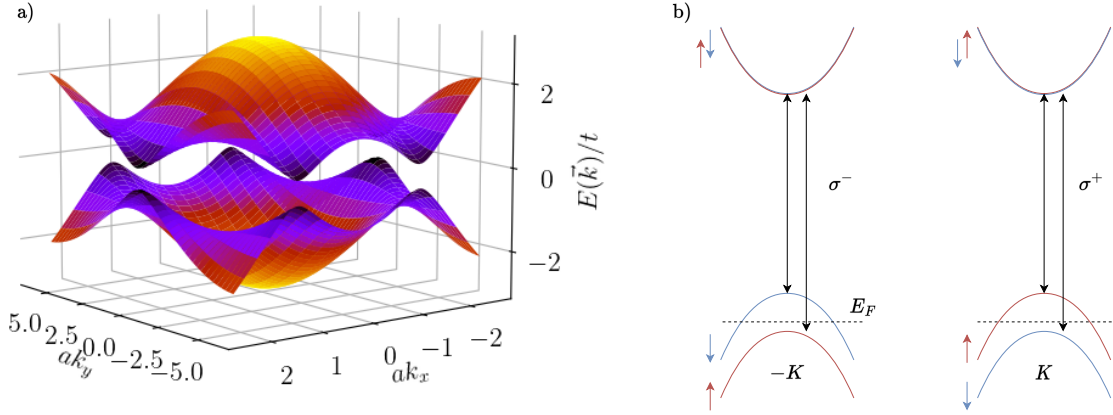


Figure 3.2: a) Dispersion relation associated with Hamiltonian Eq. (3.1) where direct gaps open at the K and $-K$ points. b) Schematic representation of the band structure close to the band edges when the spin is included. Different band transitions are allowed by coupling to circular polarized light depending on the spin and layer index. Each valley is locked with the electron spin when the Fermi energy lies between the two valence bands.

by the time reversal operator and time reversal symmetry remains a good symmetry of the system $E_{\uparrow}(\vec{k}) = E_{\downarrow}(-\vec{k})$, where we introduce the spin quantum number of the band (Haldane, 1988).

The coupling between the K and $-K$ valleys occurs via scattering with long wavelength phonons of the lattice. However, there is a large separation in momentum space between them that disfavors this coupling. Thus, the two valleys can be regarded as good quantum numbers of the system, and we can introduce the valley index $\tau = \pm 1$, for K and $-K$, respectively. The concept of utilizing the valley index as a sort of spin has opened a new field of research called valleytronics, based on the manipulation of the valley index similarly to the spin one (Xiao et al., 2007; Yao et al., 2008; Cao et al., 2012; Mak et al., 2012; Zeng et al., 2012). Therefore, it is interesting to expand the Hamiltonian Eq. (3.1) around the K and $-K$ points,

$$H(\vec{k}) = v_F (\tau k_x \sigma_x + k_y \sigma_y) + \frac{\Delta}{2} \sigma_z, \quad (3.3)$$

where we introduce the Fermi velocity $v_F = 3at/2$. That is, the low-energy theory around the corners of the Brillouin zone corresponds to massive Dirac fermions. It is important to remark that the same low-energy theory is obtained in monolayer graphene with a staggered potential since both systems exhibit the same symmetries (Xiao et al., 2007).

We have not yet introduced the most important ingredient in TMDs, the strong spin-orbit coupling (SOC) (Zhu et al., 2011; Xiao et al., 2012). The spin \vec{S} remains a good quantum number of the system even in the presence of SOC and therefore, we can write down an effective Hamiltonian depending on the valley and the spin number,

$$H(\vec{k}) = v_F (\tau k_x \sigma_x + k_y \sigma_y) + \frac{\Delta}{2} \sigma_z + \lambda_v \tau S_z \frac{1 - \sigma_z}{2} + \lambda_c \tau S_z \frac{1 + \sigma_z}{2}, \quad (3.4)$$

where we introduce the SOC strength for the valence λ_v and conduction band λ_c . Therefore, a spin splitting is produced in the valence and conduction bands. The spin splitting is several hundreds of meV in the valence band and a few meV in the conduction band (Zhu et al., 2011). Therefore, in the conduction band, we have almost degenerate spin bands ($\lambda_c \approx 0$), whereas in the valence band, the splitting is large. Moreover, the spin splitting is opposite depending on the valley index due to the intrinsic $\vec{L} \cdot \vec{S}$ nature of the SOC leading to a strong sin-valley coupling. Consider a system with a Fermi energy lying between the two spin-split valence bands. The electrons populating the K valley $\tau = +1$ have a spin index $S_z = +1$, and the electrons populating the $-K$ valley $\tau = -1$ have a spin index $S_z = -1$, as shown in Fig. 3.2 b). In this way, the spin and valley quantum numbers are locked, leading to the so-called spin-valley locking phenomenon.

To further illustrate the electronic properties of monolayer TMDs, consider now the coupling with circularly polarized optical fields σ^\pm (Xiao et al., 2012). As discussed above, an electron in the valence band can absorb a photon and be excited to the conduction band forming an exciton. The optical field only couples to the orbital part of the wavefunction and leaves the spin invariant. In particular, the valley $\pm K$ has an orbital angular momentum $m = 0$ at the top of the valence band and $m = \pm 1$ at the bottom of the conduction bands (Cao et al., 2012; Xiao et al., 2012). Therefore, the valley $\pm K$ only couples to σ^\pm polarized light, see Fig. 3.2 b). Moreover, due to the large spin splitting of the valence band we can photoexcite two different excitons in each valley, usually called A and B excitons. When the frequency of the σ^+ light equals $\Delta + \lambda_v$ ($\Delta - \lambda_v$) we photoexcite a spin- \downarrow (spin- \uparrow) electron of the K valley and with σ^- light of frequency $\Delta + \lambda_v$ ($\Delta - \lambda_v$) we photoexcite a spin- \uparrow (spin- \downarrow) electron of the $-K$ valley, see Fig. 3.2 b). In this way, the spin S_z and valley τ degrees of freedom are intrinsically locked and they can be probed by circularly polarized light σ^\pm allowing to probe spin properties with light.

3.2 Heterostructure transition metal dichalcogenide compounds

We have considered a single monolayer of TMDs so far, let us now study heterobilayer TMD materials WY_2/MoX_2 ($X, Y = \text{S, Se}$) (Geim and Grigorieva, 2013; Novoselov et al., 2016; Liu et al., 2016). Consider two monolayer TMDs with the same lattice spacing a_0 stacked one on top of each other such that the transition metal atoms are also stacked on top of each other, the so-called AA stacking. When the system is twisted with an angle θ , a moiré pattern is formed, as shown in Fig. 1.1 and Sec. 1.2. That is, a new lattice structure emerges with a triangular symmetry and a much larger lattice spacing $a_M = a_0/\theta$ (Lopes dos Santos et al., 2007; Shallock et al., 2008; Mele, 2010). There are symmetric points where the AA stacking is recovered and other symmetric points where an AB or BA stacking is formed, meaning that the transition metal of the top layer is on top of the chalcogens of the bottom layer or vice versa. Therefore, for small twisting angles, the scales of the problem change dramatically. The lattice spacing becomes ten times larger for a twisting angle of 6° , implying that the Brillouin zone is shrunk. Both TMD monolayers have degenerate K and $-K$ valleys, which can be independently accessed as aforementioned. In a homobilayer, we have to consider an extra quantum number corresponding to the layer index since the two monolayers have degenerate bands (Devakul

et al., 2021; Xu et al., 2022b). However, a moiré pattern is also formed in a heterostructure where the moiré lattice spacing is given by $a_M = a_0/\sqrt{\theta^2 + \delta^2}$, where δ is the lattice mismatch between the two monolayers (Yankowitz et al., 2012). Therefore, a moiré pattern is formed even without twisting the heterostructure. Moreover, a heterobilayer has a simpler description with respect to the homobilayer since the layer index can be discarded, and we can consider that only one of the two layers is active. That is, the valence band maxima located at the two inequivalent K and K' points of the WY_2 monolayer lie inside the band gap of the MoX_2 one (Zhang et al., 2016). In this situation, we can consider the WY_2 monolayer as active and the MoX_2 monolayer only creates an effective moiré potential $\Delta(\mathbf{r})$ which displaces the location of the valence band maxima of the WY_2 monolayer following the moiré periodicity a_M (Zhang et al., 2016; Wu et al., 2018b). The moiré potential has been computed from first-principles calculations employing relativistic density functional theory, see (Jung et al., 2014; Wu et al., 2017, 2018a,b). It has been shown that the potential is accurately approximated by a Fourier decomposition over the six moiré reciprocal vectors,

$$\Delta(\mathbf{r}) = \sum_{j=1}^6 V_j e^{i\mathbf{b}_j \cdot \mathbf{r}}, \quad (3.5)$$

where V_j are six coefficient to be determined and $\mathbf{b}_j \approx \theta \mathbf{G}_j \times \hat{z}$, with \mathbf{G}_j being the reciprocal lattice vectors of the WY_2 monolayer, $\mathbf{G}_1 = 4\pi/(\sqrt{3}a_0)\hat{x}$. Since the moiré potential has to obey three-fold rotational symmetry ($V_1 = V_3 = V_5$ and $V_2 = V_4 = V_6$) and is real ($V_1 = V_4^*$), the coefficients V_j are fixed by two parameters $V_1 = V e^{i\psi}$. By fitting to the *ab initio* calculated potentials one can find typical values of V and ψ for different heterostructures, see (Wu et al., 2018b). Moreover, we can consider an effective mass approximation for the WSe_2 monolayer when the local density approximation holds, leading to the Hamiltonian (Wu et al., 2018b),

$$H = -\frac{\hbar^2 \mathbf{q}^2}{2m^*} + \Delta(\mathbf{r}), \quad (3.6)$$

where we introduce the effective mass of the holes near the valence band maxima m^* . Therefore, charge carriers move in a periodic triangular potential and one can solve the effective Hamiltonian Eq. (3.6) as presented in Sec. (2.2). However, we consider a simplified model which already allows to derive the Fermi-Hubbard model description of a TMD heterostructure.

3.3 The Fermi-Hubbard model

To derive the Fermi-Hubbard model of a TMD heterostructure, we consider a double well potential instead of the periodic moiré one, see Fig. 3.3 a). Moreover, we focus on the case $\psi = 0$. We start our discussion by considering the single-electron problem moving in an external potential,

$$V(x, y) = V_M e^{-\bar{\Delta}(x-a_M/2, y) - \bar{\Delta}(x+a_M/2, y)}, \quad (3.7)$$

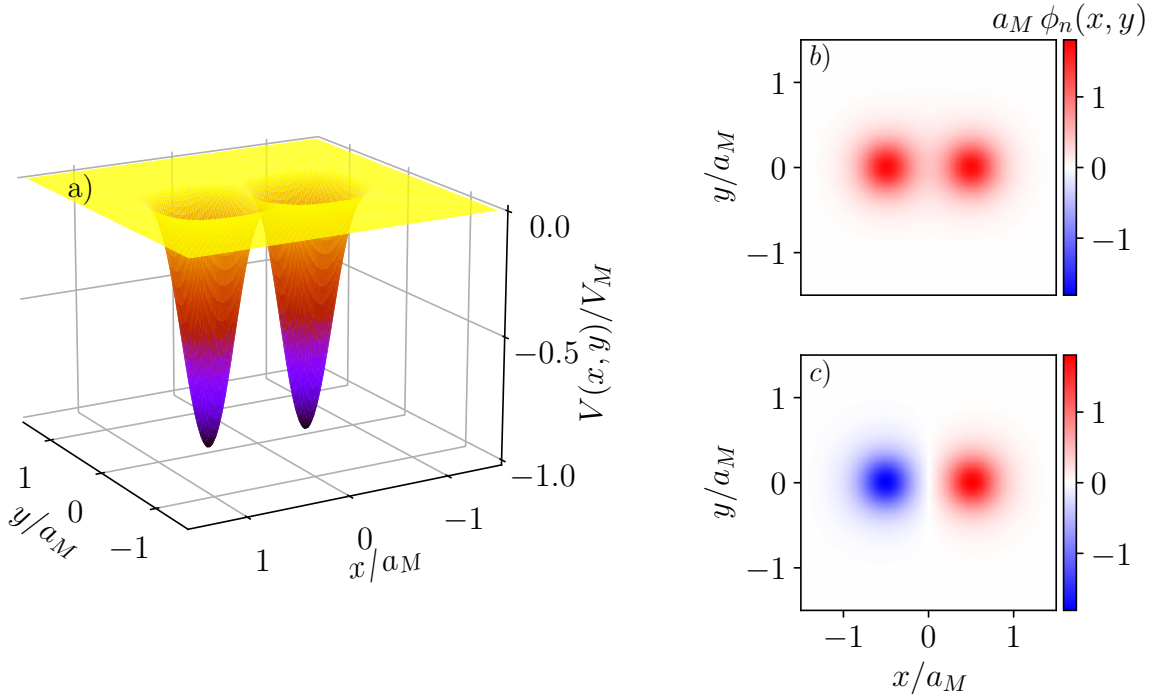


Figure 3.3: Double well potential a), see Eq. (3.7). Lowest b) and first excited c) wavefunctions of the double well potential for $a_M = 7$ nm, $V = 10$ meV and $m^* = 0.7m_e$.

where we introduce the height of the barrier V_M and the function,

$$\bar{\Delta}(x, y) = -\frac{\pi^2}{a_M^2} (x^2 + y^2) - \frac{\pi^4}{3a_M^4} (x^2 + y^2)^2. \quad (3.8)$$

The double-well potential Eq. (3.7) matches the original moiré one up to r^4 by setting the barrier height $V_M = 8V$. In this way, we are able to reproduce the characteristic frequency of each potential well and the barriers between them.

The 2D Schrödinger equation describing the single-electron problem is given by,

$$H\phi_n(\tilde{x}, \tilde{y}) = \tilde{E}_n\phi_n(\tilde{x}, \tilde{y}) = \frac{-\hbar^2}{2m^*a_M^2V_M}\tilde{\nabla}^2 + \frac{1}{V_M}V(\tilde{x}, \tilde{y}), \quad (3.9)$$

where we introduce the dimensionless eigenenergies $\tilde{E}_n = E_n/V_M$ and the dimensionless positions ($\tilde{x} = x/a_M, \tilde{y} = y/a_M$). We solve Eq. (3.9) by putting the system in a box of size $L_x \times L_y$ with $L_x = L_y = 3$ in units of a_M and finding the matrix representation of the Hamiltonian H using the

single-particle wavefunctions of a particle in a box $|\psi_n\rangle$,

$$\begin{aligned} \langle \psi_m | H | \psi_n \rangle &= \frac{1}{V_M} \int dx dy \psi_{m_x, m_y}^*(x, y) V(x, y) \psi_{n_x, n_y}(x, y) \\ &+ \delta_{n, m} \frac{\hbar^2 \pi^2}{2m^* a_M^2 V_M} \left[\left(\frac{n_x}{L_x} \right)^2 + \left(\frac{n_y}{L_y} \right)^2 \right], \end{aligned} \quad (3.10)$$

where $\psi_{n_x, n_y}(x, y) = \langle x, y | \psi_n \rangle = \frac{2}{\sqrt{L_x L_y}} \sin(\pi x / L_x) \sin(\pi y / L_y)$. The eigenenergies \tilde{E}_n are obtained by diagonalizing Hamiltonian Eq. (3.10) where the integrals are performed using a Simpson's rule in a $2^{10} \times 2^{10}$ grid and keeping 400 states of the single-particle eigenfunctions of a particle in a box. We find a set of localized states inside the double well $\tilde{E}_n < 0$ and delocalized ones $\tilde{E}_n > 0$. We can construct maximally localized Wannier wavefunctions in only one of the two wells by using the set of localized states. Consider the state $|\phi_0\rangle$ ($|\phi_1\rangle$) which corresponds to the symmetric (antisymmetric) superposition of having an electron localized in the left $|L\rangle$ and right well $|R\rangle$, see Fig. 3.3 b) and c). Then, we can obtain the Wannier wavefunction localized in one of the two wells by using the proper linear combinations,

$$w_0(x, y) = \frac{1}{\sqrt{2}} (\phi_0(x, y) + \phi_1(x, y)), \quad (3.11)$$

$$w_0(x - a_M, y) = \frac{1}{\sqrt{2}} (\phi_0(x, y) - \phi_1(x, y)), \quad (3.12)$$

where we shift the center of coordinates to the center of the left well. We are now in position of finding the effective Hubbard model describing the many-electron problem. Let us emphasize that we are focusing on a single-band Hubbard model. However, our theory can also be used to study the multi-band electron problem in an exact manner. We are not presenting the multi-orbital problem in this Thesis as it is a subject of current research. However, the multi-orbital extension may be crucial for a quantitative description of TMD heterostructures as Coulomb interaction can be comparable to the band gap, resulting in strong band hybridization.

The tunneling strength t of a single-electron is easily extracted from our diagonalization problem,

$$t = V_M \int dx dy w_0(x - a_M, y) H w_0(x, y) = \frac{1}{2} (E_1 - E_0). \quad (3.13)$$

To compute the on-site electron interaction U , we need to specify how two electrons interact in the 2D geometry. Coulomb interaction is strongly renormalized when the two electrons are confined in the 2D plane and the material is sandwiched between two dielectrics such as hexagonal boron-nitride (hBN) (Rytova, 1967; Keldysh, 1979; Cudazzo et al., 2011). The electron-electron interaction in this situation is properly captured by the Rytova-Keldysh potential (Rytova, 1967; Keldysh, 1979; Cudazzo et al., 2011),

$$V(r_{ij}) = \frac{e^2}{4\pi\kappa\epsilon_0\epsilon} \frac{\pi}{2r_0} \left[H_0 \left(\frac{r_{ij}}{r_0} \right) - Y_0 \left(\frac{r_{ij}}{r_0} \right) \right], \quad (3.14)$$

where $r_{ij} = |\mathbf{r}_i - \mathbf{r}_j|$, e is the electron charge, ϵ_0 is the vacuum permittivity, $\kappa = (\epsilon_t + \epsilon_b)/2$, with $\epsilon_{t(b)}$ the dielectric constant of the dielectric on top (bottom) of the TMD, H_0 and Y_0 are, respectively, the Struve function and the Bessel function of the second kind and $r_0 = \chi_{2D}/(2\kappa)$ is the screening length, with χ_{2D} the polarizability of the TMD (Cudazzo et al., 2011). For $r_{ij}/r_0 \rightarrow \infty$ the Rytova-Keldysh potential Eq. (3.14) reduces to the usual Coulomb interaction,

$$V(r_{ij} \rightarrow \infty) \approx \frac{e^2}{4\pi\kappa\epsilon_0 r_{ij}}. \quad (3.15)$$

However, Coulomb interaction is strongly renormalized at distances $r_{ij} < r_0$ and the Rytova-Keldysh potential leads to a drastic reduction of the short-range electron-electron interaction while keeping the long-range part unaffected. At short distances the electron-electron interaction diverges logarithmically,

$$V(r_{ij} \rightarrow 0) \approx \frac{e^2}{4\pi\kappa\epsilon_0 r_0} \ln\left(\frac{r_0}{r_{ij}}\right). \quad (3.16)$$

The on-site Hubbard interaction U is obtained by projecting the electron-electron interaction into the lowest Wannier orbital,

$$U = \int d\mathbf{r}_i^2 d\mathbf{r}_j^2 |w_0(x_j, y_j)|^2 V(r_{ij}) |w_0(x_i, y_i)|^2, \quad (3.17)$$

which involves performing a four-dimensional integral. The integral can be efficiently evaluated numerically by going to momentum space and utilizing the fast Fourier transform (FFT) routine,

$$U = \int \frac{d\mathbf{q}^2}{(2\pi)^2} |w_0(-q)|^2 V(q) |w_0(q)|^2, \quad (3.18)$$

where we introduce the Fourier transforms of the Wannier wavefunctions,

$$w_0(q) = \int d\mathbf{r}^2 w_0(x, y) e^{i\mathbf{q}\mathbf{r}} \quad (3.19)$$

and the Fourier transform of the Rytova-Keldysh potential,

$$V(q) = \int d\mathbf{r}^2 V(r) e^{i\mathbf{q}\mathbf{r}} = \frac{1}{2\kappa\epsilon_0(1+r_0q)} \frac{\tanh(Dq)}{q}, \quad (3.20)$$

where we introduce a short momentum cutoff D which is used to stabilize the numerical convergence of the integrals. In practice, we use a large value of the cutoff $D \approx 3.5a_M$ and check that the results do not depend on the value we choose. In Fig. 3.4 we present the dependence of the tunneling strength t and on-site interaction U on the moiré lattice spacing $a_M \approx a_0/\theta$ which can be tuned by changing the twist angle θ . The tunneling decays exponentially with the moiré lattice spacing, and the on-site interaction also decreases with it. These relations can be obtained from a Gaussian approximation of the lowest Wannier wavefunction which is valid in the limit $\sigma \ll a_m$ with $\sigma = \sqrt{\hbar/(m^*\omega)}$ and

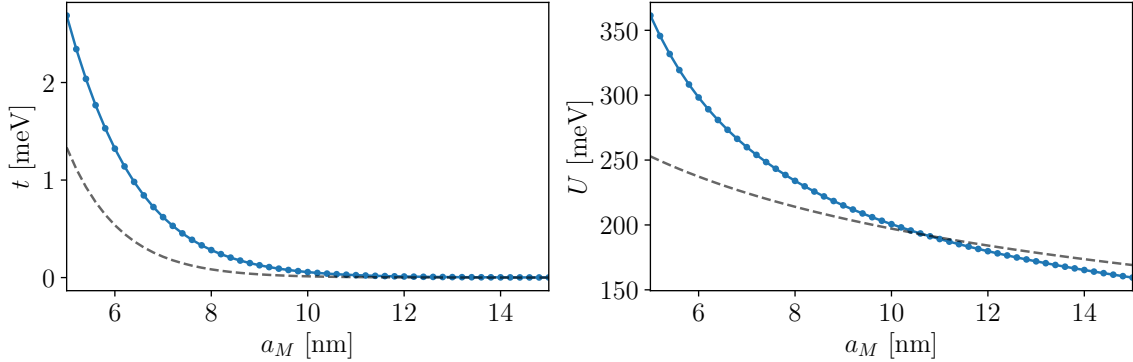


Figure 3.4: Hopping strength t and on-site interaction U as a function of the moiré lattice spacing a_M for $V = 10$ meV, $m^* = 0.7m_e$, $r_0 = 1$ nm and $\kappa = 4$. Dashed lines correspond to the Gaussian approximation Eq. (3.22) and Eq. (3.23).

$$\omega = 4\pi/a_M\sqrt{V/m^*},$$

$$w_0(r) = \frac{1}{\sqrt{\pi\sigma^2}}e^{-\frac{r^2}{2\sigma^2}}. \quad (3.21)$$

The Gaussian approximation gives,

$$t = \frac{\hbar^2}{2m^*\sigma^2} \left(\frac{a_M^2}{4\sigma^2} - 1 \right) e^{-\frac{a_M^2}{4\sigma^2}}, \quad (3.22)$$

$$U = \frac{1}{8\pi\kappa\epsilon_0 r_0} \left(\pi \operatorname{Erfi} \left(\frac{\sigma}{\sqrt{2}r_0} \right) - \operatorname{Ei} \left(\frac{\sigma^2}{2r_0^2} \right) \right) e^{-\frac{\sigma^2}{2r_0^2}}, \quad (3.23)$$

where $\operatorname{Erfi}(x)$ and $\operatorname{Ei}(x)$ are the imaginary error function and the exponential integral function, respectively.

We have assumed that the TMD heterostructure can be described by a Fermi-Hubbard model with hopping strength t and on-site interaction U in a 2D triangular geometry. However, since the Rytova-Keldysh potential is a long-range potential, we need to include interactions between nearest neighbors in the Hamiltonian to properly capture the effects of the electron-electron interaction (Morales-Durán et al., 2022). The general Fermi-Hubbard model is given by,

$$\hat{H} = -t \sum_{\langle ij \rangle, \sigma} \left(\hat{c}_{i, \sigma}^\dagger \hat{c}_{j, \sigma} + \text{H.c.} \right) + \sum_{i, j, k, l} V_{i, j, k, l}^{\sigma, \sigma'} \hat{c}_{i, \sigma}^\dagger \hat{c}_{j, \sigma'}^\dagger \hat{c}_{l, \sigma'} \hat{c}_{k, \sigma}, \quad (3.24)$$

where,

$$V_{i, j, k, l}^{\sigma, \sigma'} = \int d\mathbf{r}^2 d\mathbf{r}'^2 w_0^*(\mathbf{r} - \mathbf{R}_i) w_0^*(\mathbf{r} - \mathbf{R}_j) V(r - r') w_0(\mathbf{r}' - \mathbf{R}_k) w_0(\mathbf{r}' - \mathbf{R}_l), \quad (3.25)$$

and we can assume $\mathbf{R}_0 = 0$ and $\mathbf{R}_1 = (a_M, 0)$ because the system is invariant under global translations. The non-zero parameters are given by: $V_{0,0,0,0}^{\sigma, \sigma'} = U$ is the on-site interaction, $V_{0,1,0,1}^{\sigma, \sigma'} = V$ is the nearest-

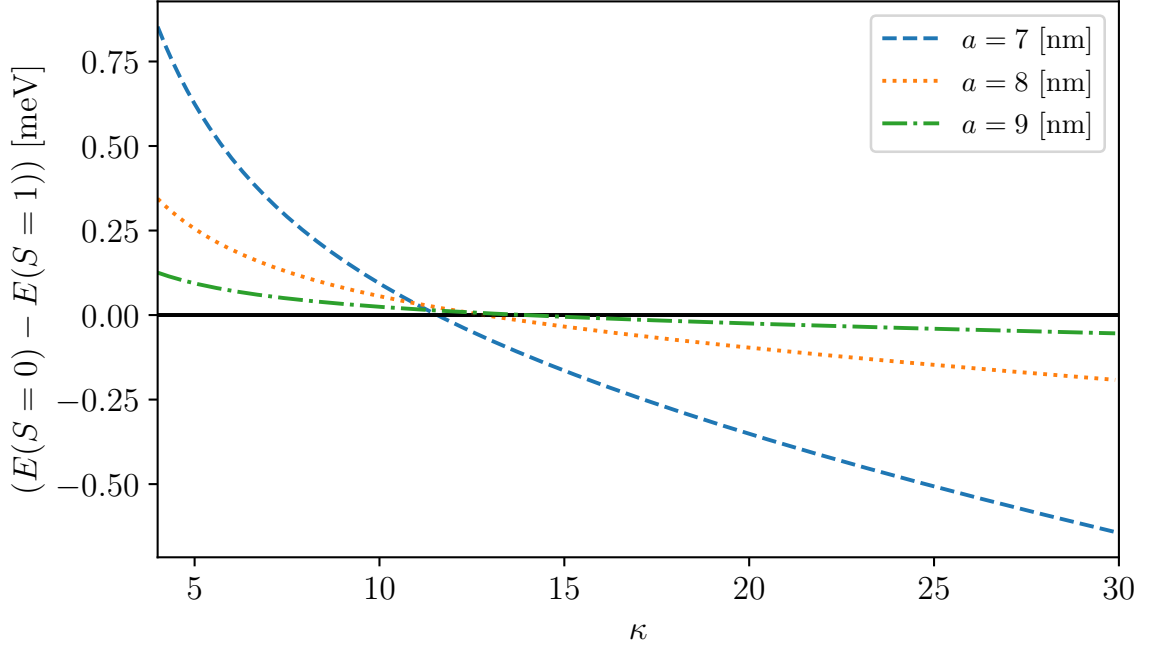


Figure 3.5: Energy difference between the singlet and triplet energies $E(S = 0) - E(S = 1)$ as a function of the dielectric constant κ for three values of the moiré lattice constant a_M and $V = 10$ meV, $m^* = 0.7m_e$, $r_0 = 1$ nm.

neighbor density-density interaction, $V_{0,0,0,1}^{\sigma,\sigma'} = t_c$ is the density correlated hopping, $V_{0,1,1,0}^{\sigma,\sigma'} = X$ is the direct exchange and $V_{0,0,1,1}^{\sigma,\sigma'} = P = X$ is the pair-hopping. The matrix representation of the Hamiltonian for the two-electron problem $N_\uparrow = N_\downarrow = 1$ using the left and right basis, reads,

$$H = \begin{bmatrix} U & t + t_c & -(t + t_c) & X \\ t + t_c & V & -X & t + t_c \\ -(t + t_c) & -X & V & -(t + t_c) \\ X & t + t_c & -(t + t_c) & U \end{bmatrix} \quad (3.26)$$

Interestingly, the inclusion of all the terms in the Fermi-Hubbard model leads to a competition of the magnetic interaction at half-filling $\nu = n_\uparrow + n_\downarrow = 1$. The magnetic interaction is given by,

$$J = \frac{4(t + t_c)^2}{U - V} - 2X, \quad (3.27)$$

and therefore, there is a competition between superexchange and direct exchange processes since they lead to antiferromagnetic and ferromagnetic interactions, respectively.

A way to self-consistently solve the multi-electron problem is to perform *ab initio* exact diagonalization calculations in the aforementioned double well potential. Moreover, by controlling the number of single-particle states N_{orb} utilized in the many-body problem, we can control the number of effective

bands of the Fermi-Hubbard model. We focus on $N_{\text{orb}} = 2$, which effectively describes a single-band Hubbard model characterized by the lowest Wannier function. However, our procedure can be easily extended to solve the multi-electron problem with a larger number of orbitals by changing N_{orb} , which describes a multi-band Fermi-Hubbard model. We solve the two-electron problem with $N_{\uparrow} = N_{\downarrow} = 1$ and compute the energy difference between the singlet and triplet energies $E(S = 0) - E(S = 1)$, as shown in Fig.3.5. By increasing the moir'e lattice spacing, the absolute value of the spin splitting is reduced. Moreover, by changing the dielectric environment, we observe a transition between ferromagnetism and antiferromagnetism. At small (large) dielectric constants, the system becomes ferromagnetic (antiferromagnetic)(Morales-Durán et al., 2022). By increasing the dielectric constant, we decrease the strength of the Coulomb interaction, which leads to a decrease of the on-site interaction U and the direct exchange X . Since the on-site interaction is reduced, superexchange processes become more dominant over direct exchange ones, and the system becomes antiferromagnetic.

We conclude that heterostructure TMD compounds can be used to simulate the Fermi-Hubbard model in a triangular geometry. However, the Fermi-Hubbard model must be extended to include the effects of non-local Coulomb interaction. We obtained a direct interaction between nearest neighbor sites, density-correlated hopping which leads to an asymmetry between the hopping below and above half-filling, and a change of the magnetic interactions at half-filling induced by the competition between superexchange and direct exchange processes. Therefore, heterostructure TMD compounds open a new and promising direction to simulate extensions of the Fermi-Hubbard model in 2D triangular geometries in a controlled way. The parameters of the model can be easily tuned by changing the twist angle or by choosing different dielectric environments.

Part I

Ultracold atomic quantum liquids induced by direct interactions in optical lattices

BOSE-BOSE MIXTURES IN A ONE-DIMENSIONAL OPTICAL LATTICE

Different cold atom laboratories in the world have produced mixtures of ultracold atoms, see the experimental works cited in (Lewenstein et al., 2012; Sowiński and Ángel García-March, 2019). In particular, binary mixtures can consist of: the same atomic species atoms but with different hyperfine states e.g. $|F = 1, m_F = 1\rangle$ and $|F = 1, m_F = 0\rangle$ of ^{39}K (see e.g. Cabrera et al. (2018)), different isotopes of the same atomic species e.g. ^{87}Rb - ^{85}Rb (see e.g. Papp et al. (2008)), or different atomic species e.g. ^{87}Rb - ^{40}K (see e.g. (Ospelkaus et al., 2006)). These internal degrees of freedom provide the system of an effective spin mimicking spin-1/2 particles. Furthermore, these binary systems exhibit different statistical properties depending on their constituent atoms. For example, they can be composed of fermionic atoms, bosonic atoms, or even a mixture of both, which are respectively referred to as Fermi-Fermi, Bose-Bose, and Bose-Fermi mixtures.

For decades, ultracold atomic systems have been classified as quantum gases, meaning that the system has no preferred density or chemical potential. Therefore, the system can always minimize its energy by expanding its volume, thereby reducing its density. However, this paradigm has recently been challenged by the theoretical investigation (Petrov, 2015; Baillie et al., 2016a; Wächtler and Santos, 2016; Kartashov et al., 2019) and experimental observation (Schmitt et al., 2016; Ferrier-Barbut et al., 2016; Chomaz et al., 2016; Ferrier-Barbut et al., 2018; Böttcher et al., 2019b; Cabrera et al., 2018; Semeghini et al., 2018; D’Errico et al., 2019) of ultra-dilute droplet-like quantum liquids. The appearance of quantum droplets indicates that the system transitions from a quantum gas to a quantum liquid, and therefore, has a preferred density at which it minimizes its energy per particle, known as the equilibrium density. Such quantum droplets are self-bound objects and can exist with no external trapping, similar to the case of helium droplets (Barranco et al., 2006). The crucial difference is that ultracold atoms provide unprecedented control over the tunability of interactions and geometry of the system. The droplets were first produced in Bose gases with dipolar interactions (Ferrier-Barbut et al., 2016; Schmitt et al., 2016; Chomaz et al., 2016) and afterwards in binary bosonic mixtures with

contact-like interactions (Cabrera et al., 2018; Semeghini et al., 2018; D’Errico et al., 2019). Moreover, the observed equilibrium density can be eight orders of magnitude smaller than in liquid water, making them a perfect platform to study quantum liquids with an unprecedented level of control.

A microscopic theory of liquids relies on the specific properties of the atom-atom interaction potential. In classical liquids the typical interaction potential has a van der Waals shape for which the long-range attraction is compensated by a short-range repulsion (Hansen and McDonald, 2013). In fermionic quantum fluids, e.g. electron gas, neutron stars, etc, the Pauli exclusion principle naturally provides a hard-core short-range repulsion (Fetter and Walecka, 2003). The classical picture carries over to the bosonic quantum realm where microscopic descriptions of very different systems, e.g. liquid helium, require strong short-range repulsive forces (Leggett, 2006). However, ultracold atomic quantum liquids seem to be stabilized due to a compensation between the mean-field interactions and quantum fluctuations (Petrov, 2015; Baillie et al., 2016b; Wächtler and Santos, 2016; Kartashov et al., 2019).

The dimensionality of the system has strong implications for the properties of these quantum droplets (Petrov and Astrakharchik, 2016). In 1D case, droplets get formed in the regime where at the mean-field level the system is on average repulsive. That is, the quantum fluctuations result in an effective attraction which is able to liquefy the system (Petrov and Astrakharchik, 2016). The properties of such one-dimensional liquids have been studied in the continuum (Parisi et al., 2019; Parisi and Giorgini, 2020; Ota and Astrakharchik, 2020). Moreover, in the 1D case the low-density regime corresponds to stronger correlations which makes the few-body problem very interesting.

In this chapter, we analyze the quantum many-body phases that appear in a 1D bosonic mixture loaded in a high optical lattice. Specifically, we study the competition between repulsive and attractive interactions and demonstrate the formation of different liquid phases. In Sec. 4.1, we present the model studied in this chapter. In Sec. 4.2, we focus on the weakly interacting regime and provide the lattice beyond mean-field equation of state compared with DMRG calculations. In Sec. 4.3, we study the strong coupling regime and provide an effective description in terms of new dimerized degrees of freedom, which allows us to capture the liquid to gas transition. In Sec. 4.4, we analyze the different phases that appear in the system employing DMRG, and finally, we present the phase diagram in Sec. 4.5. In Sec. 4.6, we present our conclusions and outlook.

4.1 Two-component Bose-Hubbard model

When a Bose-Bose mixture interacting with contact-line interactions is trapped in a high 1D optical lattice it can be described by a two-component Bose-Hubbard Hamiltonian (Lewenstein et al., 2012),

$$\hat{H} = - \sum_{i,\sigma} t_\sigma \left(\hat{b}_{i,\sigma}^\dagger \hat{b}_{i+1,\sigma} + \text{h.c.} \right) + \frac{1}{2} \sum_{i,\sigma} U_{\sigma\sigma} \hat{n}_{i,\sigma} (\hat{n}_{i,\sigma} - 1) + U_{\uparrow\downarrow} \sum_i \hat{n}_{i,\uparrow} \hat{n}_{i,\downarrow}, \quad (4.1)$$

where $\hat{b}_{i,\sigma}$ ($\hat{b}_{i,\sigma}^\dagger$) are the annihilation (creation) bosonic operators at site $i = 1, \dots, N_s$ for species $\sigma = \uparrow, \downarrow$, respectively, $\hat{n}_{i,\sigma} = \hat{b}_{i,\sigma}^\dagger \hat{b}_{i,\sigma}$ are their corresponding number operators and t_σ and $U_{\sigma\sigma'}$ are

the hopping and on-site interaction strengths, respectively. The derivation of the two-component Bose-Hubbard Hamiltonian is analogous to the single-component case presented in Chap. 2. The Hamiltonian (4.1) exhibits a plethora of quantum many-body effects and we examine a small subset of them in this chapter. In particular, we focus on the regime of parameters $U_{\sigma\sigma} > 0$, $t_\sigma > 0$ and $U_{\sigma\sigma'} < 0$, denoting that atoms of the same type repel each other while atoms of different type attract each other. Furthermore, to simplify the problem we consider a bosonic mixture of equal masses loaded in the same optical lattice $t_\uparrow = t_\downarrow \equiv t$. We also introduce the dimensionless parameter $r = 1 + U_{\uparrow\downarrow}/\sqrt{U_{\uparrow\uparrow}U_{\downarrow\downarrow}}$ characterizing the ratio between classical repulsion ($r > 0$) and attraction ($r < 0$) in the system.

4.2 Weak coupling regime

Introducing the dimensionless density $n = (N_\uparrow + N_\downarrow)/N_s$, being N_σ the number of particles with spin σ , the weakly interacting regime is defined as, $U/(nt), |U_{\uparrow\downarrow}|/(nt) \ll 1$. In this situation the kinetic energy dominates over the interaction energy and we can treat interactions perturbatively. Therefore, we assume that most of the atoms condense in the low-momentum state $k = 0$ and perform a Bogoliubov's decoupling. While it is known that true condensation cannot occur in a 1D system even at zero temperature, Bogoliubov's decoupling still provides a very good approximation of the system's energy. Moreover, we provide in Sec. 4.2.3 a comparison between the energy obtained with Bogoliubov's decoupling and full unbiased DMRG simulations.

4.2.1 Bogoliubov's decoupling

To perform a Bogoliubov's decoupling we first write the Hamiltonian (4.1) in momentum space,

$$\hat{H} = -2t(N_\uparrow + N_\downarrow) + \sum_{k,\sigma} \epsilon_k \hat{b}_{k,\sigma}^\dagger \hat{b}_{k,\sigma} + \frac{1}{2L} \sum_{k,k',q} \sum_{\sigma\sigma'} U_{\sigma\sigma'} \hat{b}_{k+q,\sigma}^\dagger \hat{b}_{k',\sigma'} \hat{b}_{k'-q,\sigma'}^\dagger \hat{b}_{k,\sigma}, \quad (4.2)$$

where we introduce the single particle dispersion relation $\epsilon_k = 4t^2 \sin(ka/2)^2$ and the bosonic operators in momentum space,

$$\hat{b}_{k,\sigma}^\dagger = \frac{1}{\sqrt{L}} \sum_j e^{ikja} \hat{b}_{j,\sigma}^\dagger, \quad (4.3)$$

where the sum over momenta runs over the first Brillouin zone $k \in [-\pi/a, \pi/a)$ and $L = aN_s$. We assume that both spin components condense in the $k = 0$ state and replace the bosonic operators by, $\hat{b}_{k,\sigma}^\dagger = \sqrt{N_\sigma} \delta_{k,0} + \hat{\delta}_{k,\sigma}^\dagger$, where we introduce the fluctuation field $\hat{\delta}_{k,\sigma}^\dagger$. We obtain the classical mean-field energy at zero order in fluctuations,

$$E_{\text{MF}} = -2t \sum_\sigma N_\sigma + \frac{1}{2L} \sum_{\sigma,\sigma'} U_{\sigma\sigma'} N_\sigma N_{\sigma'}. \quad (4.4)$$

The Eq. (4.4) provides the mean-field equation of state i.e. the energy dependence with the particle density. The equation of state gives information about the mechanical stability of the system. The

stability can be obtained by computing the Hessian matrix associated with the energy,

$$(\mathbf{H})_{\sigma\sigma'} \equiv \frac{\partial^2 E_{\text{MF}}}{\partial N_{\sigma} \partial N_{\sigma'}}. \quad (4.5)$$

A mechanically stable system is defined by a positive definite Hessian matrix. By requiring that both eigenvalues are positive, we obtain the stability condition at the mean-field level in the thermodynamic limit,

$$U_{\uparrow\uparrow}U_{\downarrow\downarrow} > U_{\uparrow\downarrow}^2. \quad (4.6)$$

In the situation $U_{\uparrow\downarrow} < 0$ and $U_{\uparrow\uparrow}, U_{\downarrow\downarrow} > 0$ the stability condition implies a positive dimensionless parameter $r = 1 + U_{\uparrow\downarrow}/\sqrt{U_{\uparrow\uparrow}U_{\downarrow\downarrow}} > 0$. Notice that the Hessian matrix Eq. (4.5) is independent of the particle densities $n_{\sigma} = N_{\sigma}/L$. Therefore, there is no homogeneous stable solution at any density when the stability condition Eq. (4.6) is not satisfied.

We now consider the quantum corrections to the mean-field energy, see (Tommasini et al., 2003; Oleś and Sacha, 2008; Sun and Pindzola, 2010; Abad and Recati, 2013; Ota and Astrakharchik, 2020) for a similar discussion. The Hamiltonian at second order in fluctuations is given by,

$$\begin{aligned} \hat{H} = E_{\text{MF}} &+ \sum_{k,\sigma} \epsilon_{\sigma,k} \hat{b}_{k,\sigma}^{\dagger} \hat{b}_{k,\sigma} + \frac{1}{2} \sum_{k,\sigma} U_{\sigma\sigma} n_{\sigma} \left(2\hat{b}_{k,\sigma}^{\dagger} \hat{b}_{k,\sigma} + \hat{b}_{k,\sigma}^{\dagger} \hat{b}_{-k,\sigma}^{\dagger} + \hat{b}_{k,\sigma} \hat{b}_{-k,\sigma} \right) \\ &+ \sum_k U_{\uparrow\downarrow} \sqrt{n_{\uparrow} n_{\downarrow}} \left(\hat{b}_{k,\uparrow}^{\dagger} \hat{b}_{k,\downarrow} + \hat{b}_{k,\downarrow}^{\dagger} \hat{b}_{k,\uparrow} + \hat{b}_{k,\uparrow}^{\dagger} \hat{b}_{-k,\downarrow}^{\dagger} + \hat{b}_{k,\uparrow} \hat{b}_{-k,\downarrow} \right). \end{aligned} \quad (4.7)$$

Note that the Bogoliubov's decoupling explicitly breaks the underlying $U(1) \otimes U(1)$ symmetry of the two-component Bose-Hubbard model (4.1). Moreover, terms mixing the two spin components appear in the effective description. To eliminate the spin mixing we perform the unitary rotation,

$$\begin{pmatrix} \hat{\mathbf{a}}_k \\ \hat{\mathbf{a}}_k^{\dagger} \end{pmatrix} = \begin{pmatrix} \mathcal{R}_{2 \times 2} & 0 \\ 0 & \mathcal{R}_{2 \times 2} \end{pmatrix} \begin{pmatrix} \hat{\mathbf{b}}_k \\ \hat{\mathbf{b}}_k^{\dagger} \end{pmatrix} \equiv \mathcal{R} \begin{pmatrix} \hat{\mathbf{b}}_k \\ \hat{\mathbf{b}}_k^{\dagger} \end{pmatrix}, \quad \text{with} \quad \mathcal{R}_{2 \times 2} = \begin{pmatrix} \cos(\theta) & -\sin(\theta) \\ \sin(\theta) & \cos(\theta) \end{pmatrix}, \quad (4.8)$$

where we introduce the 2×2 rotation matrix $\mathcal{R}_{2 \times 2}$ and the new spinor operators $\hat{\mathbf{a}}_k = (\hat{a}_{k,\uparrow}, \hat{a}_{k,\downarrow})^T$ and $\hat{\mathbf{a}}_k^{\dagger}$. The parameter θ characterizing the linear rotation is chosen such that the spin mixing is eliminated in the new spinor representation, leading to the condition,

$$\tan(2\theta) = \frac{2U_{\uparrow\downarrow}\sqrt{n_{\uparrow}n_{\downarrow}}}{U_{\uparrow\uparrow}n_{\uparrow} - U_{\downarrow\downarrow}n_{\downarrow}}, \quad (4.9)$$

which in the symmetric case $U_{\uparrow\uparrow} = U_{\downarrow\downarrow}$ and $n_{\uparrow} = n_{\downarrow}$ corresponds to $\theta = \pi/4$. Applying the linear rotation Eq. (4.8) into the Hamiltonian (4.7) together with the condition Eq. (4.9) leads to a Hamiltonian diagonal in the spin channel,

$$\hat{H} = E_{\text{MF}} + \frac{1}{2} \sum_{k \neq 0} \left[\mathbf{T}_k \mathbf{a}_k^{\dagger} \mathbf{a}_k + \mathbf{M}_k \left(\mathbf{a}_k^{\dagger} \mathbf{a}_{-k}^{\dagger} + \mathbf{a}_k \mathbf{a}_{-k} \right) \right] \quad (4.10)$$

where,

$$\mathbf{T}_k = \begin{pmatrix} \epsilon_k + A + B\sqrt{1 + 2\tan^2(2\theta)} & 0 \\ 0 & \epsilon_k + A - B\sqrt{1 + 2\tan^2(2\theta)} \end{pmatrix}, \quad (4.11)$$

$$\mathbf{M}_k = \begin{pmatrix} \frac{A}{2} + \frac{B}{2}\sqrt{1 + 2\tan^2(2\theta)} & 0 \\ 0 & \frac{A}{2} - \frac{B}{2}\sqrt{1 + 2\tan^2(2\theta)} \end{pmatrix}, \quad (4.12)$$

with $A = \frac{1}{2}(U_{\uparrow\uparrow}n_{\uparrow} + U_{\downarrow\downarrow}n_{\downarrow})$ and $B = \frac{1}{2}(U_{\uparrow\uparrow}n_{\uparrow} - U_{\downarrow\downarrow}n_{\downarrow})$. At this point we are in position of diagonalizing Hamiltonian (4.10) via a Bogoliubov transformation,

$$\begin{pmatrix} \hat{\mathbf{a}}_k \\ \hat{\mathbf{a}}_{-k}^\dagger \end{pmatrix} = \begin{pmatrix} \mathbf{U} & \mathbf{V} \\ \mathbf{V} & \mathbf{U} \end{pmatrix} \begin{pmatrix} \hat{\mathbf{c}}_k \\ \hat{\mathbf{c}}_k^\dagger \end{pmatrix} = \mathcal{S} \begin{pmatrix} \hat{\mathbf{c}}_k \\ \hat{\mathbf{c}}_{-k}^\dagger \end{pmatrix} = \mathcal{R} \begin{pmatrix} \hat{\mathbf{b}}_k \\ \hat{\mathbf{b}}_k^\dagger \end{pmatrix}. \quad (4.13)$$

To make the new spinor operators $\hat{\mathbf{c}}_k$ and $\hat{\mathbf{c}}_k^\dagger$ satisfy the Bosonic commutation rules we need to impose that the matrix transformation \mathcal{S} preserves the symplectic structure of the Hamiltonian,

$$\mathcal{S}^T \Omega \mathcal{S} = \Omega, \quad \text{with} \quad \Omega = \begin{pmatrix} 0 & -\mathbb{I}_{2 \times 2} \\ \mathbb{I}_{2 \times 2} & 0 \end{pmatrix}, \quad (4.14)$$

leading to the condition $U^\dagger U - V^\dagger V = \mathbb{I}_{2 \times 2}$. Notice that the Bogoliubov transformation is just the direct product of two independent Bogoliubov transformations because of the elimination of the spin mixing via the spin rotation introduced in Eq. (4.8). Therefore, the transformation lives in the space $S \in \text{Sp}(2, \mathbb{C}) \otimes \text{Sp}(2, \mathbb{C})$. In (Tommasini et al., 2003; Oleš and Sacha, 2008; Sun and Pindzola, 2010; Ota and Astrakharchik, 2020) one can find explicit expressions for the Bogoliubov modes.

4.2.2 Lee-Huang-Yang energy in the lattice

After performing the Bogoliubov's decoupling the energy is given by,

$$\frac{E}{L} = \frac{E_{\text{MF}}}{L} + \frac{1}{2L} \sum_{\pm} \sum_{\substack{k \in \text{1BZ} \\ k \neq 0}} (w_{\pm, k} - \epsilon_k - m^* c_{\pm}^2), \quad (4.15)$$

where we introduce the Bogoliubov modes $w_{\pm, k}^2 = \epsilon_k^2 + 2m^* c_{\pm}^2 \epsilon_k$, the effective mass $m^* = 1/(2ta^2)$ and the speed of sounds c_{\pm} that we have not yet specified their values.

The sum in Eq. (4.15) is restricted to the first Brilluoin zone $k \in [-\pi/a, \pi/a)$ without including the $k = 0$ state. Before solving the sum we exploit the parity symmetry of the system and rewrite the sum as,

$$\sum_{\substack{k \in \text{1BZ} \\ k \neq 0}} f_{\bar{k}, \pm} = 2 \sum_{\bar{k}=0}^{\pi} f_{\bar{k}, \pm} - 2f_{\bar{k}=0, \pm} - f_{\bar{k}=\pi, \pm}, \quad (4.16)$$

where f_k corresponds to the summand. In our case the summand is given by,

$$f_{k,\pm} = \sqrt{\alpha_{\pm}^2 \sin^2\left(\frac{k}{2}\right) + 2\alpha_{\pm} \sin\left(\frac{k}{2}\right) - \alpha_{\pm} \sin^2\left(\frac{k}{2}\right) - 1}, \quad (4.17)$$

where we introduce the dimensionless momentum $\bar{k} = ka$ and the dimensionless parameters $\alpha_{\pm} = 2/(m^*ac_{\pm})^2 = (2\xi_{\pm}/a)^2$ which corresponds to the ratio between the healing length $\xi_{\pm} = \sqrt{2}/(m^*c_{\pm})$ and the lattice spacing. Now we employ the Euler-Maclaurin formula (Whittaker and Watson, 1996),

$$\sum_{k=0}^{\pi} f_{k,\pm} = N_s \int_0^{\pi} \frac{dk}{2\pi} f_{\pm}(k) + \frac{f_{\pm}(0) + f_{\pm}(\pi)}{2} + \sum_{m=1}^{\lfloor \frac{p}{2} \rfloor} \left(\frac{2\pi}{N_s}\right)^{2m-1} \frac{B_{2m}}{(2m)!} f_{\pm}^{(2m-1)}(k) \Big|_0^{\pi} + R_p, \quad (4.18)$$

where we introduce the error term R_p and the Bernoulli numbers B_{2m} . Thus, we are left with the evaluation of an integral and the odd derivatives of the function at the two extrema. At this point the use of the parity symmetry in Eq. (4.16) becomes clear. The summand $f_{k,\pm}$ has a jump in its first derivative when crossing $k = 0$. By just computing the sum in half of the Brillouin zone we avoid the discontinuity improving the convergence of the Euler-Maclaurin formula. After some algebraic manipulations we obtain,

$$\int_0^{\pi} dk f_{\pm}(k) = \sqrt{2\alpha_{\pm}} - (2 + \alpha_{\pm}) \arcsin\left(\sqrt{\frac{2}{2 + \alpha_{\pm}}}\right). \quad (4.19)$$

We have not found a closed relation for the $f_{\pm}^{(2m-1)}$ derivative. However, higher-derivatives are suppressed by higher powers of the number of sites comprising the lattice, pointing to a convergence of the series at any value of α_{\pm} for a sufficiently large lattice. Moreover, we have checked that the product $\frac{B_{2m}}{(2m)!} f_{\pm}^{(2m-1)}(k) \Big|_0^{\pi}$ decays for large values of m . With these considerations, one can approximate the sum by the integral, cut to a finite value of p and neglect the error term R_p . This leads to the energy per length obtained at $p = 4$,

$$\begin{aligned} \frac{E}{L} &= \frac{E_{\text{MF}}}{L} \\ &+ \sum_{\pm} \frac{m^*c_{\pm}^2}{2\pi a} \left(\sqrt{2\alpha_{\pm}} - (2 + \alpha_{\pm}) \arcsin\left(\sqrt{\frac{2}{2 + \alpha_{\pm}}}\right) \right) \\ &+ \sum_{\pm} \left(\frac{m^*c_{\pm}^2}{2L} - \frac{\pi c_{\pm}}{3L^2} \right) - \frac{2\pi^3 a}{45L^4 m^*} \\ &+ \sum_{\pm} \frac{\pi^3 a}{90L^4 m^* \sqrt{1 + (m^*ac_{\pm})^2}} (2 + (m^*ac_{\pm})^2), \end{aligned} \quad (4.20)$$

where the first line represents the mean-field contribution, the second one corresponds to a Lee-Huang-Yang (LHY) correction in the lattice and the third and fourth ones represent finite size effects. By

taking the continuum limit $\xi_{\pm}/a \rightarrow \infty$ we obtain,

$$\frac{E}{L} = \frac{E_{\text{cont}}}{L} + \sum_{\pm} \frac{2}{15\pi} a^2 (m^* c_{\pm}^{5/4})^4 - \frac{a\pi^3}{45m^*L^4}, \quad (4.21)$$

$$\frac{E_{\text{cont}}}{L} = \frac{E_{\text{MF}}}{L} - \sum_{\pm} \frac{2}{3\pi} (m^* c_{\pm}^{3/2})^2 + \sum_{\pm} \left(\frac{m^* c_{\pm}^2}{2L} - \frac{\pi c_{\pm}}{3L^2} \right), \quad (4.22)$$

showing that the lattice leads to a repulsive contribution to the energy of the mixture in the thermodynamic limit. In this way we have recovered the result obtained in the continuum (Petrov and Astrakharchik, 2016) plus corrections which explicitly depend on the lattice spacing a .

Even though Bogoliubov's decoupling allows us to compute the energy of the system it still depends on the speed of sounds c_{\pm} which have to be determined. A mean-field calculation leads to,

$$2m^* c_{+}^2 = n(U + U_{\uparrow\downarrow}), \quad (4.23)$$

$$2m^* c_{-}^2 = n(U - U_{\uparrow\downarrow}), \quad (4.24)$$

with $n = n_{\uparrow} + n_{\downarrow}$ and we have considered the symmetric case $U_{\uparrow\uparrow} = U_{\uparrow\downarrow} \equiv U$. By plugging Eq. (4.24) into Eq. (4.20) we obtain the dependence of the energy of the system with the particle number.

4.2.3 Equation of state: quantum liquids

Before analyzing in full detail the results obtained within Bogoliubov's theory and provide a comparison with DMRG calculations, we discuss the concept of a quantum liquid. Let us consider the balanced case $N_{\uparrow} = N_{\downarrow} = N/2$, the continuum limit $\xi_{\pm}/a \rightarrow \infty$ and the thermodynamic one $n = (N_{\uparrow} + N_{\downarrow})/N_s$. In these limits, the energy per particle reduces to,

$$e(n) \equiv \frac{E}{N} = \frac{1}{4} (U + U_{\uparrow\downarrow}) n - \frac{1}{3\pi} \sqrt{\frac{nm^*a^2}{2}} \left[(U + U_{\uparrow\downarrow})^{3/2} + (U - U_{\uparrow\downarrow})^{3/2} \right]. \quad (4.25)$$

The dependence of the energy per particle with the density of the system at zero temperature is known as the equation of state and any thermodynamic property can be derived from it. Interestingly, the energy per particle has two contributions which scale with different powers of the total density. In the case $U > 0$, $U_{\uparrow\downarrow}$ and $U > |U_{\uparrow\downarrow}|$ we can express the energy per particle as,

$$e(n) = \alpha n - \beta \sqrt{n}, \quad (4.26)$$

with $\alpha, \beta > 0$, see Fig. (4.1) (a). The classical mean-field solution dictates the linear dependence of the energy per particle with the total density and therefore, dominates at large densities. Moreover, it comes with a positive sign denoting that the mixture is on average repulsive at the classical level $U > |U_{\uparrow\downarrow}|$. However, quantum fluctuations give rise to a new energy per particle contribution which scales with the square root of the total density and comes with a negative sign. Quantum fluctuations lead to an extra attraction in the system which dominates the energy per particle at small densities. Therefore, the system transitions from being on overall attractive at small densities to being repulsive at large

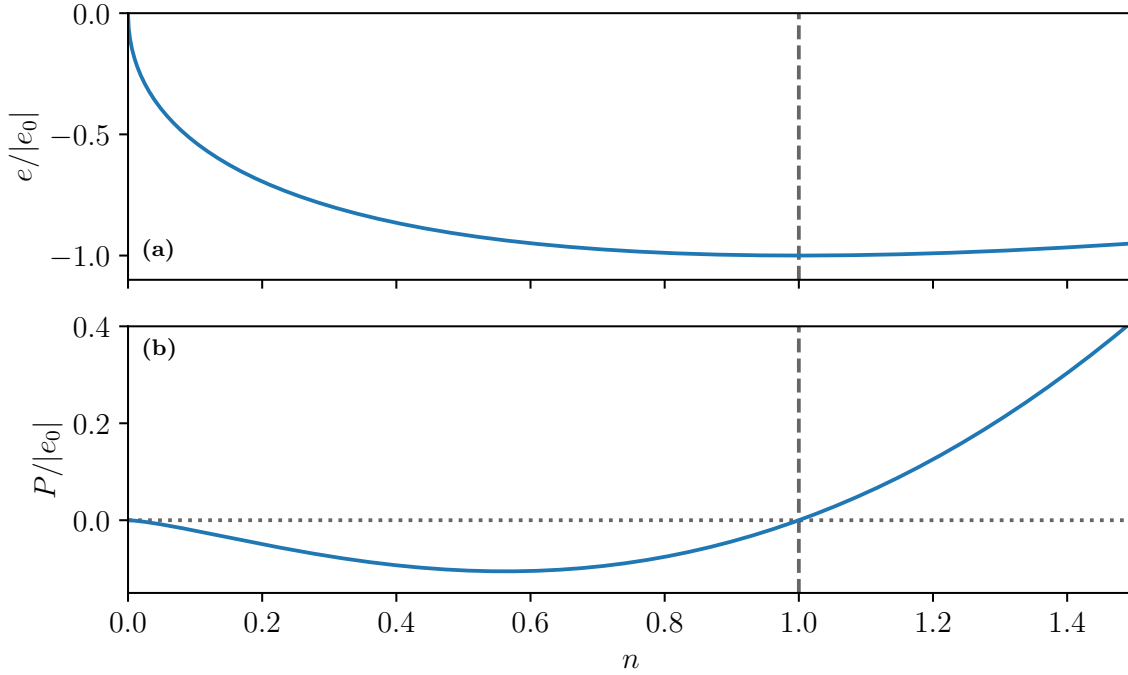


Figure 4.1: Energy per particle e , panel (a), and pressure P , panel (b), over the equilibrium energy $|e_0|$ as a function of the density for $\alpha = 1$ and $\beta = 2$ in Eq. (4.26). Dashed line denotes the equilibrium density characterized by a minimum in the energy per particle and a zero in pressure $P = 0$.

densities. The competition between classical and quantum contributions determines an equilibrium point i.e. a density n_0 for which the energy per particle is minimized,

$$\left. \frac{\partial e(n)}{\partial n} \right|_{n=n_0} = 0 \rightarrow n_0 = \frac{\beta^2}{4\alpha^2} = \frac{2m^* a^2}{9\pi^2} \frac{[(U + U_{\uparrow\downarrow})^{3/2} + (U - U_{\uparrow\downarrow})^{3/2}]^2}{(U + U_{\uparrow\downarrow})^2}. \quad (4.27)$$

The density which minimizes the energy per particle is called equilibrium density and it is the density at which the system will tend to go if it is not subjected to an external pressure, see Fig. 4.1 (a). That is, the main feature of a liquid (gas) at zero temperature is that the system exhibits a finite (zero) equilibrium density $n_0 > 0$ ($n_0 = 0$). Imagine opening a bottle of water in outer space. If the water is in the gaseous phase, it will escape and infinitely expand, reducing its density and minimizing energy per particle. However, if the water is in the liquid phase, it will form droplets that stabilize at a fixed density determined by the equilibrium density of liquid water. This configuration minimizes energy by reaching equilibrium in the bulk.

Another way to understand the equilibrium density is as the density at which the system experiences zero pressure. The pressure of the system at zero temperature is defined as,

$$P = -\frac{dE}{dL} = n^2 \frac{\partial e}{\partial n} = \alpha n^2 - \frac{1}{2} \beta n^{3/2}. \quad (4.28)$$

Therefore, there are two densities which are at zero pressure: the vacuum $n = 0$ and the equilibrium density $n = n_0$, see Fig. 4.1 (b). That is, in outer space, the water droplet is in equilibrium with the vacuum of particles and experiences zero pressure in the bulk. In a liquid, there are two densities at which zero pressure can be achieved: one is the trivial vacuum density, where $n = 0$, and the other is the non-trivial equilibrium density, given by n_0 . On the other hand, a gas has only one density at which zero pressure is attained, which is the trivial vacuum density, where $n = 0$.

To obtain a liquid, a competition between two mechanisms that contribute to the energy with different particle density scalings is necessary. In the classical van der Waals theory of liquids, this competition arises from the repulsive short-range core and attractive long-range tail of the van der Waals interaction (Hansen and McDonald, 2013). However, as mentioned earlier, ultracold atoms exist in an extremely dilute regime where the long-range tail of the van der Waals interaction can be neglected. This was the main reason why it was believed impossible to create a quantum liquid using ultracold atoms for many years. However, Bogoliubov's theory has shown us that the competition can arise from both classical and quantum contributions to the energy of the system, as was first demonstrated in (Petrov, 2015).

One may wonder why we need a mixture at all since a single-component system already exhibits a competition between classical and quantum contributions to the energy. The equilibrium density of the system for $U_{\uparrow\downarrow} = 0$ is given by,

$$n_0 = \frac{4}{9\pi^2 t} U \rightarrow \frac{U}{n_0 t} = \frac{9\pi^2}{4} \sim 22.2. \quad (4.29)$$

The equilibrium density appears in a regime where Bogoliubov's theory is not applicable. One may then question the appearance of a quantum liquid for a single-component Bose-Hubbard model. Indeed, full numerical simulations of the single-component Bose-Hubbard model exhibit only gaseous phases. Therefore, the mixture introduces an extra parameter that can be tuned, namely the intercomponent interaction $U_{\uparrow\downarrow}$, which allows independent control of the parameters α and β , making quantum fluctuations relevant in the regime where Bogoliubov's theory is applicable.

After exploring the main features of a quantum liquid at zero temperature, we now move on to a detailed analysis of the equation of state obtained via Bogoliubov's theory, and compare it with full numerical simulations obtained using DMRG and iDMRG algorithms, see Appendix A.1 for details on the numerical algorithms.

4.2.4 Comparison with DMRG simulations

To test our analytical theory we perform DMRG simulations of Hamiltonian (4.1). We impose a cutoff on the maximum number of bosons per site to make our simulations efficient. We choose a cutoff of $N_m = 4$ maximum bosons of each species per site. To check the convergence of our results we have performed simulations at particular values of parameters with $N_m = 5$. Moreover, we set a maximum bond dimension $\chi = 1024$ in our simulations. First, we compute the equation of state in the thermodynamic limit by employing iDMRG. The equation of state shows a minimum at a finite density denoting the formation of a liquid state in accordance with Bogoliubov's theory, see

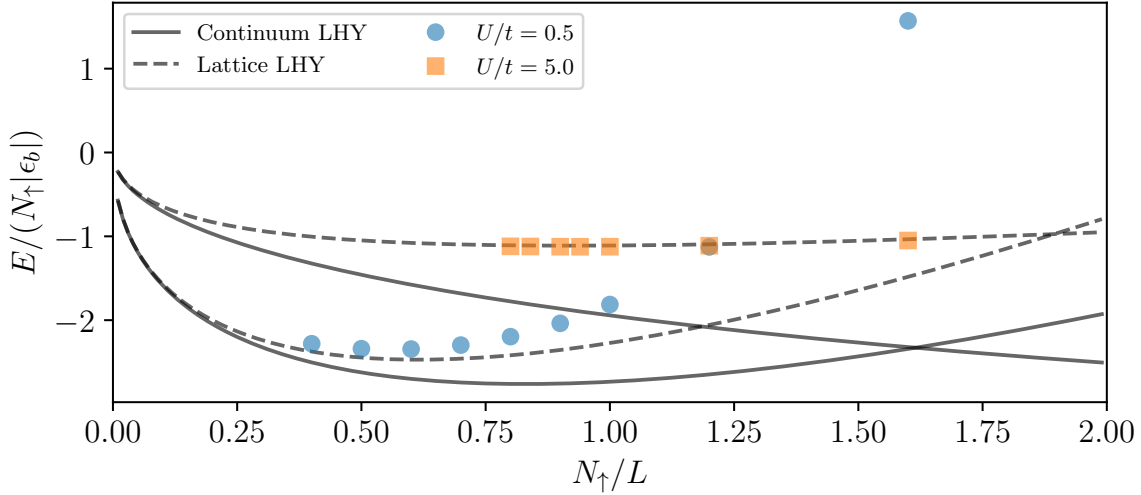


Figure 4.2: Energy per particle over the dimer binding energy as a function of the density for different values of the on-site interaction $U/t = 0.5, 5$ and fixed ratio $r = 0.15$ for a balanced mixture $N_{\uparrow} = N_{\downarrow}$. Filled symbols are obtained performing iDMRG simulations. Dashed (Continuous) line corresponds to the equation of state in the thermodynamic limit obtained with the lattice (continuum) LHY calculation, see Eq. (4.20) and Eq. (4.22).

Fig. 4.2. By comparing with the continuum energy Eq. (4.22) we observe that the lattice liquid is more repulsive than the continuum one. This can be understood from our analytical calculation in the lattice Eq. (4.20) which shows that the lattice introduces an effective repulsion into the system. The difference between the continuum and lattice liquids becomes more prominent for large values of the interaction U/t at fixed r . At the value $U/t = 5$ we observe a clear deviation of the continuum result with our iDMRG simulations while we find an excellent agreement between our simulations and the energy obtained via lattice Bogoliubov's theory Eq. (4.20). In our calculations we divide the energy per particle of the system over the dimer binding energy. The dimer is composed of two particles $N_{\uparrow} = N_{\downarrow} = 1$ and its binding energy is given by (Valiente and Petrosyan, 2008),

$$\epsilon_b = \text{sign}(U_{\uparrow\downarrow})\sqrt{U_{\uparrow\downarrow}^2 + 16t^2} + 4t, \quad (4.30)$$

see Sec. 2.5 for a detailed analysis of the two-particle problem. In the weakly interacting regime we observe that the many-body liquid has a more negative energy per particle than the dimer binding energy meaning that is strongly bound with respect to a repulsive gas of dimers. However, for increasing U/t the energy per particle approaches from below to the dimer binding energy meaning that the system is loosely bound with respect to the repulsive gas of dimers. At a critical U/t for fixed r we expect a transition from a liquid to a repulsive gas of dimers.

To properly understand the quantum liquid, we need to study how its equilibrium point depends on the interactions. In Fig. 4.3, we present the equilibrium energy per particle and density as a function of U/t for a fixed ratio $r = 0.15$. In the weakly interacting regime $U/t \ll 1$, the equilibrium

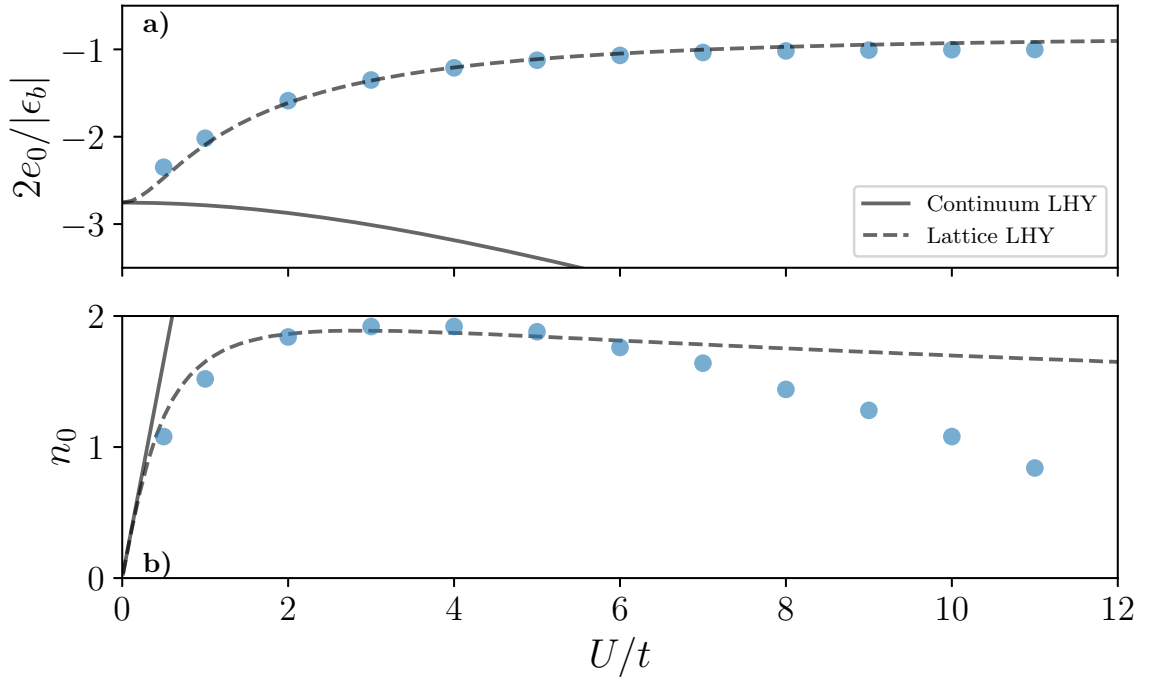


Figure 4.3: Equilibrium energy divided by the dimer binding energy (panel a)) and equilibrium density (panel b)) as a function of the on-site interaction U/t for the ratio $r = 0.15$. Filled symbols are obtained performing DMRG simulations. Continuous (dashed) line corresponds to the equilibrium density obtained with the continuum (lattice) LHY calculation, see the main text.

energy per particle over the dimer binding energy goes to a constant, in agreement with both the lattice Eq. (4.20) and continuum Eq. (4.22) equations of state obtained via Bogoliubov's theory. Moreover, the equilibrium density increases linearly with the interaction in the weakly interacting regime. However, we observe clear deviations between the continuum equation of state Eq. (4.22) and the lattice one Eq. (4.22). Moreover, the equilibrium density increases linearly with the interaction in the weakly interacting regime. However, we observe clear deviations between the continuum equation of state Eq. (4.22) and the lattice one Eq. (4.20). The continuum liquid exhibits a divergent equilibrium density for increasing on-site interaction at fixed r , $n_0 \propto U/r^2$, see Eq. (4.27), and its energy per particle becomes more negative by increasing U/t with respect to the dimer binding energy. However, in the lattice liquid, the equilibrium density saturates, and the energy per particle approaches the dimer binding energy for increasing interaction U/t . Therefore, clear differences between the two systems appear at large values of U/t . Our iDMRG simulations confirm the saturation of the equilibrium density with the on-site interaction U/t , see Fig. 4.3 b), indicating that the lattice liquid is more repulsive than the continuum one and therefore is stabilized at lower densities. Furthermore, the equilibrium energy per particle approaches the dimer binding energy for increasing U/t . Therefore, we find excellent agreement between our iDMRG results and the lattice equation of state Eq. (4.20). Even though the equilibrium density is not quantitatively reproduced by Eq. (4.20), the qualitative

features are well captured. On the other hand, the energy per particle is in astonishing agreement. The comparison of our full iDMRG simulations and the equation of state Eq. (4.20) shows the reliability of lattice Bogoliubov's theory to capture most of the main features of the lattice liquid state. In particular, the energy of the system can be obtained very accurately.

Let us remark on the main difference between the lattice equation of state Eq. (4.20) and our iDMRG results. The latter show that the system undergoes a phase transition from a liquid to a repulsive gas of dimers. This transition occurs at a critical U/t for each ratio r . Moreover, at the transition point, the equilibrium energy per particle of the liquid becomes $2e_0 = -|\epsilon_b|$ and the equilibrium density vanishes $n_0 = 0$, indicating that the transition is of second order. While the lattice equation of state Eq. (4.20) also exhibits a phase transition from a liquid to a repulsive gas of dimers, it does not accurately predict the critical value of the interaction at which the transition occurs. Furthermore, the transition predicted by Eq. (4.20) is of first order, since the equilibrium density at the critical point is non-zero. Therefore, lattice Bogoliubov's theory cannot fully capture the features of the liquid-to-gas phase transition, and we need an alternative theory to explain it. In the following, we present a theory in the strongly interacting regime that is able to capture the phase transition.

4.3 Strong coupling regime

4.3.1 Dimerized effective theory

A prominent feature of 1D geometry is that it facilitates the formation of $\uparrow\downarrow$ dimers for intercomponent attraction. For strong interactions, $U/t \gg 1$ and $|U_{ab}|/t \gg 1$, each dimer gets localized on a single site. Moreover when the attractive intercomponent interaction is close to the repulsive intracomponent one $r \equiv (U + U_{ab})/U \ll 1$ we can define the effective low-energy dimer subspace characterized by $n_{i,\uparrow} = n_{i,\downarrow}$ (Kuklov et al., 2004b,a; Trefzger et al., 2009). A similar approach has been employed to study the trimer problem in the single-component Bose-Hubbard model (Valiente et al., 2010) and the formation of localized states in a polar gas (Li et al., 2020). As well, the initial $(N_\uparrow + N_\downarrow)$ -body problem can be reduced to a N_D -body problem of dimers described by an effective Hamiltonian with $N_D = (N_\uparrow + N_\downarrow)/2$. Let us discuss in detail how the dimerized effective theory can be derived. First we study the symmetric problem of two bosons $N_\uparrow = N_\downarrow = 1$, described by Eq. (4.1), in an infinite lattice $N_s \rightarrow \infty$. In the strong interacting regime $U/t \gg 1$ and $r \equiv \frac{U+U_{AB}}{U} \ll 1$ we can work in the effective Hilbert subspace of dimers made of pairs of bosons \uparrow and \downarrow localized in the same site (Kuklov et al., 2004b,a; Trefzger et al., 2009). The number of these states is given by N_s and we use the notation $|D_n\rangle$ to denote a pair of bosons $|\uparrow\downarrow\rangle$ located at site n . The matrix elements of the effective Hamiltonian are given by,

$$\langle\alpha|H_{\text{eff}}|\beta\rangle = \langle\alpha|H_0|\beta\rangle - \frac{1}{2} \sum_{\gamma} \langle\alpha|H_t|\gamma\rangle \langle\gamma|H_t|\beta\rangle \left(\frac{1}{E_{\gamma}^0 - E_{\alpha}^0} + \frac{1}{E_{\gamma}^0 - E_{\beta}^0} \right), \quad (4.31)$$

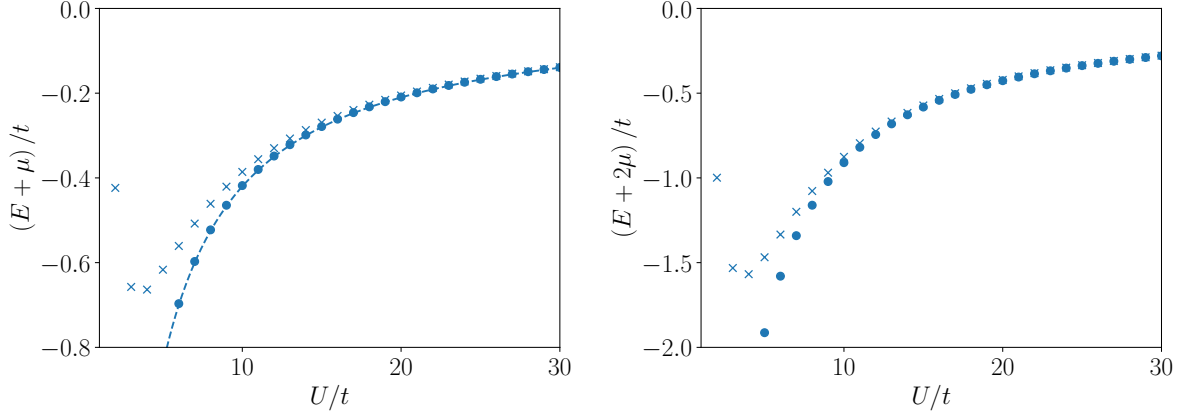


Figure 4.4: Energy obtained for two bosons $N_\uparrow = N_\downarrow = 1$ in left panel and four bosons $N_\uparrow = N_\downarrow = 2$ in right panel, using DMRG for the full Hamiltonian (crosses) and the effective one (dots) for $N_s = 32$ and $r = 0.05$. Dashed line represents the tight binding result $N_s \rightarrow \infty$ for a single dimer $E + \mu = 2J^{(2)}$.

where H_0 contains the interaction part and H_t the hopping one from the original Hamiltonian Eq. (4.1) and $|\gamma\rangle$ are the set of states outside of the effective Hilbert space which are connected with this one by hopping processes. In our situation these excited states consist of breaking the bosonic pair via moving one of the two bosons to an adjacent site and they have an energy $E_\gamma^0 = 0$. Given the interaction part of the subspace $\langle D_n | H_0 | D_m \rangle = \delta_{n,m} U_{AB}$ we obtain for the matrix elements of the effective Hamiltonian,

$$\langle D_n | H_{\text{eff}} | D_m \rangle = \delta_{n,m} \left(U_{AB} + \frac{4t^2}{U_{AB}} \right) + \frac{2t^2}{U_{AB}} \delta_{n+1,m} + \frac{2t^2}{U_{AB}} \delta_{n-1,m}. \quad (4.32)$$

These matrix elements can be identified with a single particle hopping between two adjacent sites with an effective hopping

$$J^{(2)} = 2t^2/U_{AB} \approx -2t^2(1+r)/U, \quad (4.33)$$

and an effective chemical potential

$$-\mu = U_{AB} + 4t^2/U_{AB} \approx U(r-1) - 4t^2(1+r)/U, \quad (4.34)$$

where we expand for $r \ll 1$.

In order to extract the effective interaction between dimers we study the symmetric problem of four bosons $N_\uparrow = N_\downarrow = 2$. The effective Hilbert subspace is spanned by the set of states $|D_n, D_m\rangle$, with interaction zero order energies

$$\langle D_n, D_m | H_0 | D_n, D_m \rangle = 2U_{AB} + 2\delta_{m,n} (U_{AB} + U). \quad (4.35)$$

The effective interaction is extracted from computing the diagonal matrix elements connected by

Eq. (4.31). By performing an expansion for $r \ll 1$ we obtain,

$$\begin{aligned}\langle D_n, D_n | H_{\text{eff}} | D_n, D_n \rangle &= 2U(2r - 1) - \frac{8t^2}{U}(1 + 2r), \\ \langle D_{n+1}, D_n | H_{\text{eff}} | D_{n+1}, D_n \rangle &= 2U(r - 1) - \frac{8t^2}{U} - \frac{4t^2}{U}(1 + r).\end{aligned}\quad (4.36)$$

In order to properly identify the interaction part of the effective Hamiltonian we have to remove the chemical potential contribution from these diagonal elements. The first matrix element in Eq. (4.37) corresponds to an on-site dimer interaction. The second one corresponds to a nearest-neighbor dimer interaction. By properly identifying the matrix elements we can write the effective Hamiltonian in an operational form

$$\hat{H}_{\text{eff}}^D + \mu \hat{N}^D = -J^{(2)} \sum_n (\hat{c}_n^\dagger \hat{c}_{n+1} + \text{h.c.}) + \frac{U^{(2)}}{2} \sum_n \hat{N}_n^D \hat{N}_n^D + V^{(2)} \sum_n \hat{N}_n^D \hat{N}_{n+1}^D, \quad (4.37)$$

where $\hat{N}_n^D |N_n^D\rangle = \frac{\hat{n}_{n,\uparrow} + \hat{n}_{n,\downarrow}}{2} |N_n^D\rangle = N_n^D |N_n^D\rangle$ is the dimer number operator and $\hat{c}_n^\dagger, \hat{c}_n$ are the respective dimer creation and annihilation operators which satisfy $[\hat{c}_n, \hat{c}_m^\dagger] = \delta_{n,m}$. The first term describes the hopping of the dimers with an strength $J^{(2)} = 2t^2(1+r)/U$. Finally, we have on-site interactions between two dimers with strength $U^{(2)} = Ur - 4t^2r/U$ and a nearest-neighbor interaction $V^{(2)} = -4t^2(1-r)/U$. Notice that we included the cross terms proportional to t^2r/U which play a major role in the formation of the liquid as we will show later and are usually ignored in the standard derivation of the effective Hamiltonian (Kuklov et al., 2004b,a; Trefzger et al., 2009). To test the reliability of the effective Hamiltonian Eq. (4.37) to describe the full Hamiltonian Eq. (4.1) we have performed DMRG simulations of both for two- and four-bosons, see Fig. 4.4. In the strongly interacting regime $U/t \gg 1$ we observe an excellent agreement between the ground state energy of both Hamiltonians.

4.3.2 Effective dimer-dimer interaction

The effective Hamiltonian Eq. (4.37) allows us to describe the strongly interacting regime ($U/t \gg 1$ and $r \ll 1$) of the two-component Bose-Hubbard model Eq. (4.1) in the reduced Hilbert space spanned by the dimer degrees of freedom. In particular, let us consider the few-body problem and consider four bosons $N_\uparrow = N_\downarrow = 2$ described by the Hamiltonian (4.1). Even though the full problem corresponds to a four-particle problem which cannot be described easily with analytical tools, the problem simplifies in the effective subspace spanned by the dimers where it corresponds to a two dimer problem which can be easily solved analytically.

The scattering problem of two particles described by the Hamiltonian (4.37) was solved in Ref. (Valiente and Petrosyan, 2009b), see Sec. 2.5 for a detailed analysis of the two-body problem described by a Bose-Hubbard Hamiltonian. The resulting s -wave scattering length is given by (Valiente and

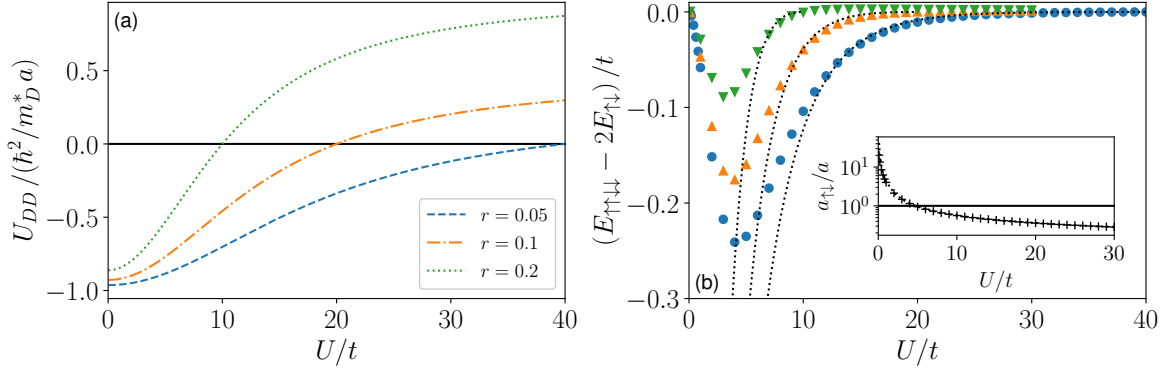


Figure 4.5: Panel (a): Strength of the effective dimer-dimer interaction as a function of the interaction U/t for different values of the ratio r . Panel (b): Main figure: Tetramer energy as a function of the interaction U/t for different ratios r . Analytical result (dotted lines) for the bound state energy, Eq. (4.42). Inset: Typical length scale a_{AB} associated with the two-particle bound state for $r = 0.1$. Dotted line shows the analytical result for this length, see Eq. (4.43).

Petrosyan, 2009b),

$$\frac{a_{DD}}{a} = \frac{U^{(2)}V^{(2)} - 4J^{(2)}(2J^{(2)} - V^{(2)})}{U^{(2)}V^{(2)} + 2J^{(2)}(2V^{(2)} + U^{(2)})} \quad (4.38)$$

with a the lattice spacing. In terms of characteristic parameters U, t, r of the problem, we express it as

$$\frac{a_{DD}}{a} = \frac{(r-1)rU^2/t^2 - 4(r^2 + 3r + 4)}{2r^2U^2/t^2 - 8}. \quad (4.39)$$

Increasing the interaction U/t for fixed r we find a special point where the scattering length diverges and changes sign, going from $a_{DD} \rightarrow +\infty$ to $a_{DD} \rightarrow -\infty$. The position of this threshold corresponds to a pole in a_{DD}/a indicating the formation of a two-dimer bound state, which results in the condition

$$V^{(2)} = -2J^{(2)} \frac{U^{(2)}}{4J^{(2)} + U^{(2)}} \Rightarrow r_c = \frac{2t}{U}. \quad (4.40)$$

The effective one-dimensional dimer-dimer coupling constant, defined as

$$U_{DD} = \frac{-2}{m_D^* a_{DD}}, \quad (4.41)$$

with $m_D^* = 1/(2J^{(2)}a^2)$ the effective mass of the dimer, crosses zero at the threshold. To the left (right) of this point, when $a_{DD} > 0$ ($a_{DD} < 0$) the effective dimer-dimer interactions are attractive (repulsive), see Fig. 4.5(a). In the attractive region a dimer-dimer bound state, i.e. tetramer, is formed and its energy vanishes when the threshold is reached. The binding energy of the tetramer in the vicinity of

the threshold can be estimated by

$$E_B \approx -\frac{\hbar^2}{m_D^* a_{DD}^2} = -\frac{1}{2J^{(2)}} \left(\frac{2J^{(2)}U^{(2)}}{4J^{(2)} + U^{(2)}} + V^{(2)} \right)^2 + \dots \quad (4.42)$$

Let us remark that the appearance of the threshold at a finite value of U/t is a direct consequence of the cross terms proportional to $t^2 r/U$ included in the effective Hamiltonian (4.37).

The exact tetramer energy of the full Hamiltonian (4.1) in the four-particle $N_\uparrow = N_\downarrow = 2$ and two-particle $N_\uparrow = N_\downarrow = 1$ cases is obtained by DMRG. In order to establish if a dimer-dimer bound state gets formed we compute the four-particle energy $E_{\uparrow\uparrow\downarrow\downarrow}$ and the two-particle one $E_{\uparrow\downarrow}$ and we define the tetramer binding energy $E_{\uparrow\uparrow\downarrow\downarrow} - 2E_{\uparrow\downarrow}$. Its negative value signals the formation of the bound state due to an effective attraction between dimers. Figure 4.5(b) shows the comparison of the exact tetramer energy with the analytical prediction given by the dimer model, Eq. (4.42). An excellent agreement is found when $U/t \gg 1$ and $r \ll 1$, i.e. for deep dimers. To get a further insight, we calculate the dimer size $a_{\uparrow\downarrow}$ by associating it with the exact dimer energy $E_{\uparrow\downarrow} - 2E_\uparrow = -2ta^2/a_{\uparrow\downarrow}^2$ and alternatively with their asymptotic values for $N_s \rightarrow \infty$, $E_{\uparrow\downarrow} - 2E_\uparrow = \epsilon_b$, see Eq. (4.30). This sets the relation,

$$\begin{aligned} E_{\uparrow\downarrow} - 2E_\uparrow &= \frac{-2t}{(a_{\uparrow\downarrow}/a)^2} \\ &= -U|r - 1| \sqrt{1 + \frac{16t^2}{U^2(1-r)^2}} + 4t. \end{aligned} \quad (4.43)$$

We compare the energy obtained in DMRG calculations and the asymptotic expression in the inset of Fig. 4.5(b). For $U/t \gg 1$ the dimer size is much smaller than the lattice spacing, $a_{\uparrow\downarrow} \ll a$. In this regime, it is possible to neglect the internal structure of dimers and treat them as composite bosons described by the effective Hamiltonian (4.37). At the same time, the four-particle bound state might be large $a_{DD} \gg a \gg a_{\uparrow\downarrow}$. Crucial differences appear in the opposite regime $U/t \ll 1$ where the effective composite boson model predicts a deeper bound state while exact results show that the bound state is shallower, see Fig. 4.5(b). In this regime we observe a dimer with an extension comparable to the four-body bound state $a_{DD} \sim a_{\uparrow\downarrow} \gg a$, which makes the assumption of localized dimers no longer applicable.

4.3.3 Liquid to gas transition

The dimer effective theory allows us to understand the liquid to gas transition as the point at which the effective dimer-dimer interaction passes from being attractive to repulsive. The phase diagram in the $(r, U/t)$ plane is reported in Fig. 4.6. We find a sizable region of parameters where a four-body bound state is formed. We discern two different regimes separated by the $a_{\uparrow\downarrow} = a$ condition shown with a dotted line. To its right, the dimer size is smaller than the lattice spacing and the interactions are strong, $|U_{\uparrow\downarrow}|/t \approx U/t \geq 10$. Here, the dimers are deeply bound and the effective dimer model is expected to be applicable. Indeed, it correctly predicts the boundary for tetramer formation, shown with a dashed line which is defined by a diverging dimer-dimer scattering length,

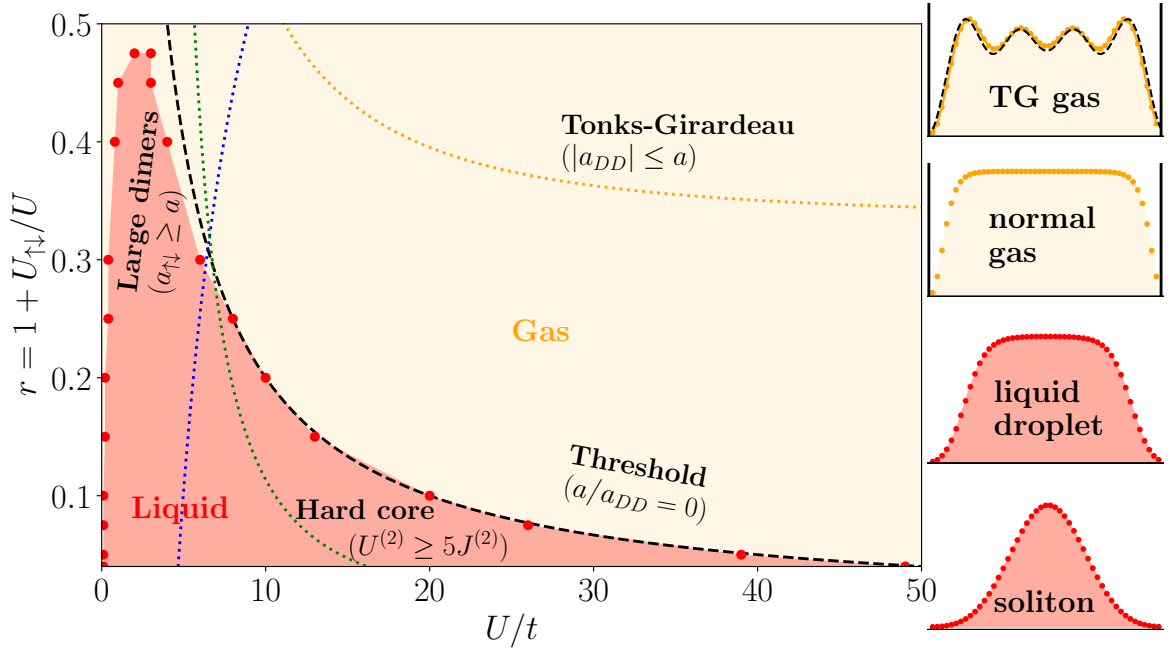


Figure 4.6: Phase diagram in the plane of interaction strength U/t and interaction imbalance r . The region where a tetramer bound state is formed is shown as a shaded (red) area. Its boundary, delimited by circles, is defined by a vanishing energy in the full Hamiltonian (4.1), $E_{\uparrow\uparrow\downarrow\downarrow} - 2E_{\uparrow\downarrow} = 0$. The boundary obtained within the effective dimer Hamiltonian is shown with a dashed line and corresponds to Eq. (4.40). The blue dotted line depicts the characteristic condition $a_{\uparrow\downarrow} = a$, e.g. to the left of the line, the dimer size is larger than the lattice spacing, see Eq. (4.43), and the effective Hamiltonian (4.37) does not apply. The green dotted line denotes the hard-core dimer condition $U^{(2)} \gg J^{(2)}$, to the right of this line the effective Hamiltonian (4.45) applies. To the right of the orange dotted line the Tonks-Girardeau regime is reached $|a_{DD}| \leq a$ and we recover the local properties of an ideal spinless fermionic gas. In the many-body problem the different regimes still persist and the threshold line denotes the phase transition between a gas-liquid/soliton phase. On the right we show the typical dimer density profiles for the Tonks-Girardeau gas together with the density of ideal spinless fermions (dashed line), the normal gas, the liquid droplet, and the soliton. Note that the atom density profiles are very similar.

$a_{DD} \rightarrow \infty$, Eq. (4.40). In the second region, $U/t < 10$ the effective dimer model breaks down, as the dimers are no longer localized on a single lattice site. The tetramer bound state completely disappears for interaction imbalance larger than $r \approx 0.475$, a slightly smaller value than $r \approx 0.53$ reported in the continuum (Pricoupenko and Petrov, 2018; Parisi et al., 2019). Let us remark that neither the Bogoliubov's theory presented in Sec. 4.2 and the effective dimer theory are able to capture the critical value of $r \approx 0.475$ at which the liquid disappears for all U/t . Probably a self-consistent Bogoliubov's theory could be able to capture such transition.

Once the threshold line is crossed, $a_{DD} < 0$, the effective dimer-dimer interaction becomes repulsive and tetramer formation does not happen. At the same time the dimers are still formed and repulsion between them becomes stronger as U/t is increased. Eventually, when $|a_{DD}| \ll a$, the Tonks-Girardeau regime is reached and the dimers fermionize. The strong repulsion between dimers does not allow them

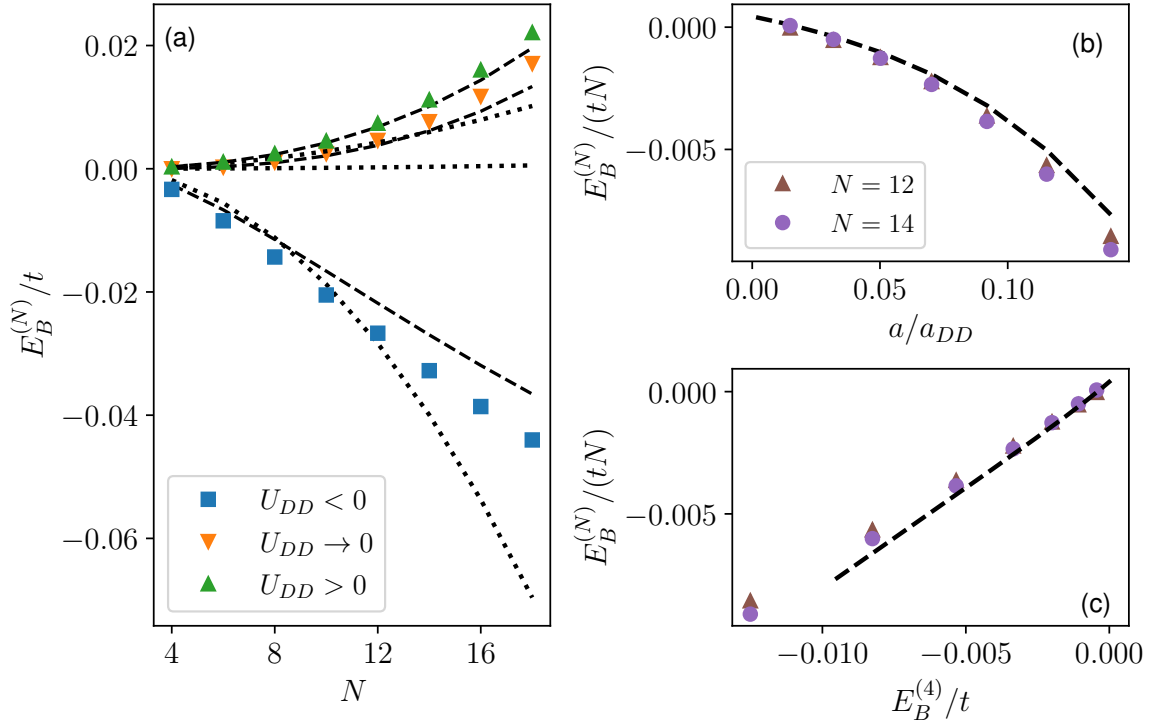


Figure 4.7: Panel (a): Energy of the N -body state $E_B^{(N)} = E^{(N)} - NE^{(2)}/2$ as a function of the total number of particles N for fixed ratio $r = 0.1$ and three characteristic interaction strengths, $U = 16, 19.95, 21$, corresponding to $U_{DD} < 0$, $U_{DD} \simeq 0$ and $U_{DD} > 0$, respectively. The results are obtained for the full Hamiltonian (4.1) (symbols), for the effective model of composite bosons matching the dimer-dimer scattering length (dotted line) and for the full effective dimer model, Eq. (4.37) (dashed line). Panels (b) and (c): Energy of the N -body state per particle for $U_{DD} < 0$ as a function of the inverse of the dimer-dimer scattering length (b) or the dimer-dimer bound energy (c) for the full Hamiltonian (symbols) and the effective dimer model (4.37) (dashed line).

to stay at the same lattice site, mimicking the Fermi exclusion principle. As a result, the energetic and local properties of dimers are expected to be similar to those of ideal fermions. In order to demonstrate that we compute the dimer density profile $n_i^D = \langle \hat{d}_i^\dagger \hat{d}_i \rangle$ with the bosonic dimer operator $\hat{d}_i = \hat{b}_{i,\uparrow} \hat{b}_{i,\downarrow}$ for different system with $N_A = N_B = N/2$ particles. The profiles obtained are almost equal to the ones corresponding to a system of ideal fermions, see Fig. 4.6 for an example with $N = 8$.

4.3.4 Many-dimer problem

As we have shown, in the regime of deeply bound dimers, the four-body problem can be interpreted in terms of composite bosons interacting via an effective potential. Here we show that a similar interpretation holds for any number of particles. To this end, we compute the binding energy of the N -body state $E_B^{(N)} = E^{(N)} - NE^{(2)}/2$ for the case where the dimer-dimer effective interaction is attractive, vanishing, and repulsive.

For repulsive dimer-dimer interactions, $U_{DD} > 0$, the energy of N -body state is positive and grows nearly quadratically with N , which can be interpreted as a linear increase of the chemical potential of a gas as the density is augmented, see Fig. 4.7(a). In the attractive dimer-dimer case, $U_{DD} < 0$, we observe a nearly constant negative energy per particle which signals the presence of a stable liquid phase, as shown in Fig. 4.7(a). This physics is fully captured by the effective dimer-dimer Hamiltonian of Eq. (4.37) as can be seen by comparing the dashed lines with the symbols in Fig. 4.7(a). The formation of a liquid in the attractive dimer-dimer regime is not trivial, as in principle the bosonic dimers could form a soliton and eventually condense on a single site. In the continuum, the interpretation of the stability provided in Refs. (Bulgac, 2002; Pricoupenko and Petrov, 2018) involves the introduction of microscopic repulsive three-dimer interactions which counterbalance the dimer-dimer attraction. In our case, the effective model correctly captures the formation of the liquid and thus it must incorporate a stabilization mechanism. Indeed we find that in our case the liquid is stabilized by the non-zero effective range of the dimer-dimer interaction stemming from Eq. (4.37). Close to the threshold, the effective range (Valiente and Petrosyan, 2009b)

$$\frac{r_e}{a} \simeq -\frac{V^{(2)}}{4J^{(2)}} \left(4 + \frac{V^{(2)}}{J^{(2)}} \right) = \frac{(1-r_c)(3r_c+1)}{(r_c+1)^2}, \quad (4.44)$$

changes smoothly contrarily to the resonant behavior of the effective dimer-dimer scattering length a_{DD} . In this regime, the effective range is proportional to the nearest-neighbor interaction $V^{(2)}$ and is of the order of the lattice spacing $r_e/a \approx 1 - 4r_c^2$ for $r_c \ll 1$. To elucidate the role of the effective range we perform calculations using a dimer-dimer model without the $V^{(2)}$ term, and with the effective interaction $U^{(2)}$ tuned such that the model reproduces the same scattering length as the full dimer-dimer Hamiltonian. In this case, the energy per particle is not constant and becomes more negative for increasing N . In this situation the energy follows the scaling $E \propto U_{DD}N_D(N_D - 1)/2$ which indicates the collapse of all dimers at one site thus creating a lattice soliton (Scott et al., 1994). Therefore, the on-site $U^{(2)}$ and nearest-neighbor $V^{(2)}$ interaction are both needed in order to explain the stabilization of the liquid phase, see below.

We verify that the effective dimer-dimer model describes correctly the energy of the liquid as a function of the interaction strength reported in Fig. 4.7(b) for a fixed number of particles. Close to the threshold, the energy of the N -body problem is linearly proportional to the energy of the two-dimer problem as shown in Fig. 4.7(c). This linear relation suggests a dimerized and universal nature of the self-bound liquid, i.e. the properties of the N -body liquid are directly expressed in terms of the dimer-dimer energy.

The liquid is very dilute in the vicinity of the threshold of its appearance. In particular, the probability of finding two dimers in the same site is extremely small. This suggests that an effective description in terms of hard-core dimers with a finite-range attraction could explain the liquid formation in the full Hamiltonian (4.1). The hard-core description applies when the local dimer effective interaction is much stronger than the effective hopping $U^{(2)} \gg J^{(2)}$ which leads to $(U/t)^2 r \gg 1$. Therefore, there is a window in the regime of validity of the effective dimer Hamiltonian $U/t \gg 1$ and $r \ll 1$ where the hard-core condition is satisfied. In order to impose the hard-core constrain on the

dimers, $(\hat{c}^\dagger)^2 |0\rangle = 0$, we write a new effective Hamiltonian at second order in $J^{(2)}$ (Cazalilla, 2003; Giuliano et al., 2013),

$$H_{\text{eff}}^{\text{HCD}} = -J_{\text{HC}}^{(2)} \sum_n (\hat{c}_n^\dagger \hat{c}_{n+1} + \text{h.c.}) + V_{\text{HC}}^{(2)} \sum_n \hat{N}_n^D \hat{N}_{n+1}^D, \quad (4.45)$$

with,

$$J_{\text{HC}}^{(2)} \approx J^{(2)} \left(1 + \left(4J^{(2)}/U^{(2)} \right)^2 \right), \quad (4.46)$$

$$V_{\text{HC}}^{(2)} = V^{(2)} - 8 \left(J^{(2)} \right)^2 / U^{(2)}. \quad (4.47)$$

This model has been extensively studied and presents a phase transition at $V_{\text{HC}}^{(2)} = -2J_{\text{HC}}^{(2)}$ (Cazalilla et al., 2011; Giamarchi, 2003) which leads to the condition,

$$V^{(2)} = -2J^{(2)} \frac{U^{(2)}}{4J^{(2)} + U^{(2)}}. \quad (4.48)$$

Strikingly, this is nothing else but the condition of finding a pole in the effective dimer-dimer scattering length Eq. (4.40) demonstrating that the N -particle quantum liquid problem can be understood by examining the four-particle problem in the strongly interacting regime. Therefore we conclude that the hard-core effective dimer model can explain the liquid formation of the complete Hamiltonian (4.1). First of all, the strong on-site repulsion $U^{(2)}$ avoids the collapse of the system. Then the attractive nearest-neighbor interaction, which sets the effective range of the dimer-dimer scattering problem, bounds the system and stabilizes the liquid phase. Fascinatingly, this mechanism resembles the classical one proposed by van der Waals to explain the emergence of classical liquids in terms of a compensation between repulsive short-range and attractive long-range forces. Within our effective theory we have been able to show that the quantum liquid phase of the two-component Bose-Hubbard model Eq. (4.1) falls into this class of liquids in the strongly interacting regime. In Sec. 5.1 we provide a simple theory demonstrating the appearance of a quantum liquid for the extended Bose-Hubbard model in the strongly interacting regime. Interestingly the two-component Bose-Hubbard model Eq. (4.1) is effectively described by a single-component extended Bose-Hubbard model Eq. (4.37) in the strongly interacting regime.

The quantum liquid in the weakly interacting regime is stabilized due to a competition between classical and quantum fluctuations, which contribute with opposite signs to the equation of state, see Eq. (4.20). However, the stabilization mechanism dramatically changes in the strongly interacting regime, where new effective degrees of freedom, i.e. dimers, arise, and the system is better understood in terms of them. In this regime, the stabilization of the quantum liquid comes from the competition between the repulsive short-range (on-site) and attractive long-range (nearest-neighbor) effective dimer-dimer interaction. One may wonder whether these two regimes can be continuously connected or whether a phase transition occurs between them. In the next section, we study in detail how the two regimes are connected with iDMRG.

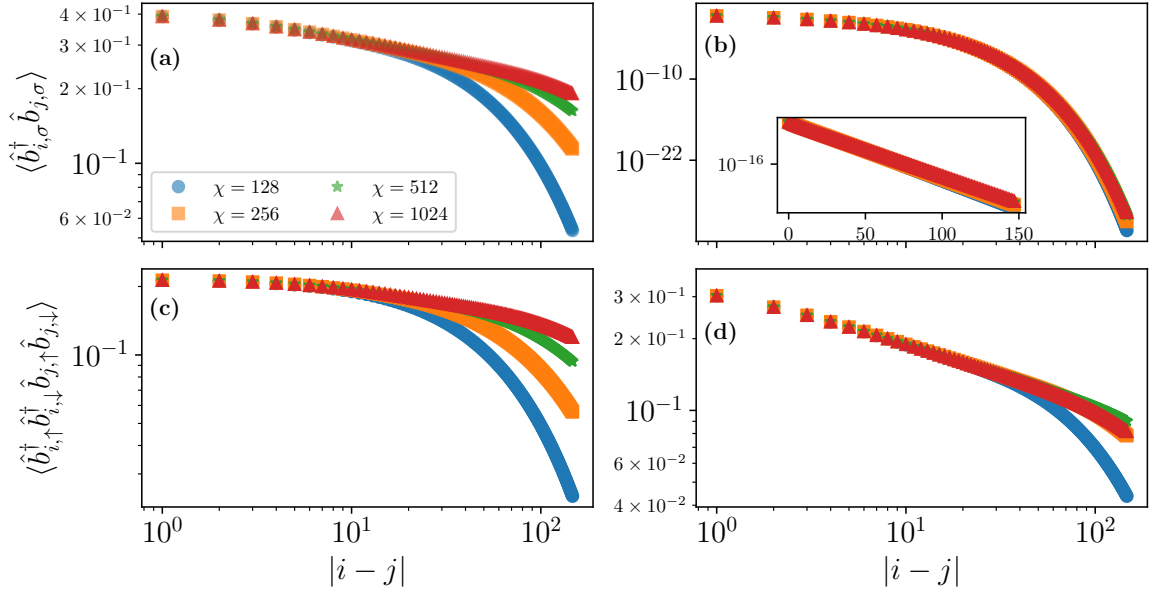


Figure 4.8: One-body $\langle \hat{b}_{i,\sigma}^\dagger \hat{b}_{j,\sigma} \rangle$ and two-body $\langle \hat{b}_{i,\uparrow}^\dagger \hat{b}_{i,\downarrow} \hat{b}_{j,\uparrow} \hat{b}_{j,\downarrow} \rangle$ correlation functions at $U/t = 1$ (a)-(c) and $U/t = 9$ (b)-(d), respectively, as a function of the distance $|i - j|$ for an infinite system with density $n_\uparrow = n_\downarrow = 2/5$, $r = 0.3$ and different bond dimensions. The inset panel in (b) shows the same plot but in a log-y and linear-x scale.

4.4 Quantum correlations

We now focus on the study of quantum correlations as one moves from the weakly interacting regime ($U/t \ll 1$) to the strongly interacting one ($U/t \gg 1$). Let us remark that we consider non-commensurate filling factors, so Mott physics is not relevant. We perform iDMRG simulations at a fixed density $n_\uparrow = n_\downarrow = 2/5$ and study the ground state dependence with the interactions U/t and r . In particular, we compute the ground state off-diagonal correlators which indicate the tendency of the system to exhibit phase coherence. In the 1D geometry truly long-range phase coherence is forbidden because of the Mermin-Wagner-Coleman theorem (Mermin and Wagner, 1966; Hohenberg, 1967; Mermin, 1968; Coleman, 1973). However, we can still expect quasi-long-range coherence, which is seen as a slow power-law decay of the correlation function with distance. We interpret the presence of quasi-long-range phase coherence as the formation of superfluid states. In the two-component Bose-Hubbard model, we can have up to two different superfluids since the system can be decomposed into two channels, namely density and spin (Giamarchi, 2003). Therefore, we can have superfluidity in both channels, which is called the two-superfluid (2SF) phase. Alternatively, we can lose superfluidity in one channel while maintaining it in the other, such as density in our case, which is called the pair superfluid (PSF) phase (Kuklov et al., 2004b; Hu et al., 2009; Kuklov et al., 2004a; Radzihovsky et al., 2004; Astrakharchik et al., 2016). The PSF is characterized by the formation of pairs of atoms (dimers) that exhibit long-range (Kuklov et al., 2004b; Hu et al., 2009; Kuklov et al., 2004a; Radzihovsky et al., 2004) or quasi long-range phase coherence in our 1D geometry. To distinguish between these two phases, we

can compute the one-body $\langle \hat{b}_{i,\sigma}^\dagger \hat{b}_{j,\sigma} \rangle$ and two-body correlation functions $\langle \hat{b}_{i,\uparrow}^\dagger \hat{b}_{i,\downarrow}^\dagger \hat{b}_{j,\uparrow} \hat{b}_{j,\downarrow} \rangle = \langle \hat{d}_i^\dagger \hat{d}_j \rangle$ and study their dependence on the distance $|i - j|$. The following behaviors are expected at long distances in the two phases,

$$\text{2SF: } \langle \hat{b}_{i,\sigma}^\dagger \hat{b}_{j,\sigma} \rangle \propto \frac{1}{|i - j|^{\alpha_1}}, \quad \langle \hat{b}_{i,\uparrow}^\dagger \hat{b}_{i,\downarrow}^\dagger \hat{b}_{j,\uparrow} \hat{b}_{j,\downarrow} \rangle \propto \frac{1}{|i - j|^{\alpha_2}}, \quad (4.49)$$

$$\text{PSF: } \langle \hat{b}_{i,\sigma}^\dagger \hat{b}_{j,\sigma} \rangle \propto e^{-|i-j|a/\xi}, \quad \langle \hat{b}_{i,\uparrow}^\dagger \hat{b}_{i,\downarrow}^\dagger \hat{b}_{j,\uparrow} \hat{b}_{j,\downarrow} \rangle \propto \frac{1}{|i - j|^{\alpha_2}}. \quad (4.50)$$

$$(4.51)$$

The 2SF phase is gapless in both the density and spin sectors, and therefore, all correlation functions decay with a power-law, as shown in Fig.4.8 (a) and (c). However, the PSF exhibits a gap in the spin sector associated with the breaking of a dimer, and therefore, the single-body correlation function decays exponentially fast, as it is associated with the breaking of a dimer, as shown in Fig.4.8 (b). The density sector remains gapless, and the two-body correlation function decays as a power-law, as shown in Fig.4.8 (d). Thus, the PSF is characterized by: (i) absence of quasi long-range phase coherence in the one-body correlator, (ii) appearance of quasi long-range phase coherence in the two-body correlator, and (iii) a finite gap associated with spin excitations. In addition, we have verified for several selected points that the PSF phase possesses a finite gap in the spin sector $\Delta = E(N + 1, N) - 2E(N, N) + E(N - 1, N) > 0$, which is absent in the 2SF phase (Astrakharchik et al., 2016), where $E(N_\uparrow, N_\downarrow)$ characterizes the energy of a finite system with N_\uparrow and N_\downarrow particles.

Our iDMRG simulations allow us to obtain the correlation functions directly in the thermodynamic limit at a fixed density. However, a dependence of the correlation function with the bond dimension χ of our MPS can be observed at very long distances, see Fig. 4.8. That is, a finite bond dimension always sets an artificial finite correlation length $\xi(\chi)$ making our correlation functions start to fall exponentially fast when the distance surpasses the artificial correlation length, see Fig. 4.8 (a),(c) and (d). If the system has a true physical correlation length ξ it can be obtained in the limit of infinite bond dimension $\xi = \xi(\chi \rightarrow \infty)$. Simulations with relatively small bond dimension can already be converged if the physical correlation length is small, see Fig. 4.8 (b). However, if the correlation function decays as a power-law, then, the physical correlation length goes to infinite and we need to perform a finite entanglement scaling (Tagliacozzo et al., 2008; Pollmann et al., 2009), namely study the dependence of our observables with the bond dimension. We can extract the correlation length at a given bond dimension by performing an analysis of the transfer matrix (Schollwöck, 2011b). Moreover, we can extract the correlation length associated with the one-body $\langle \hat{b}_{i,\sigma}^\dagger \hat{b}_{j,\sigma} \rangle$ correlation function $\xi_{1,0}(\chi) = \xi_{0,1}(\chi)$ and the two-body $\langle \hat{b}_{i,\uparrow}^\dagger \hat{b}_{i,\downarrow}^\dagger \hat{b}_{j,\uparrow} \hat{b}_{j,\downarrow} \rangle$ correlation function $\xi_{1,1}(\chi)$. In Fig. 4.9 we present the dependence of the inverse of the correlation lengths with the bond dimension for different values of U/t . In the 2SF phase we observe that both correlation lengths tend to infinite $\xi_{1,0}, \xi_{1,1} \rightarrow \infty$ in the limit $\chi \rightarrow \infty$, indicating that both correlation functions decay as a power-law, see $U/t = 1$ case. However, in the PSF phase we observe that the correlation length $\xi_{1,1}$ tends to infinite in the limit $\chi \rightarrow \infty$ but the correlation length $\xi_{1,0}$ associated with the one-body correlation function tends to a constant in the same limit, see $U/t = 5, 9$ cases. By iterating this procedure we can obtain the

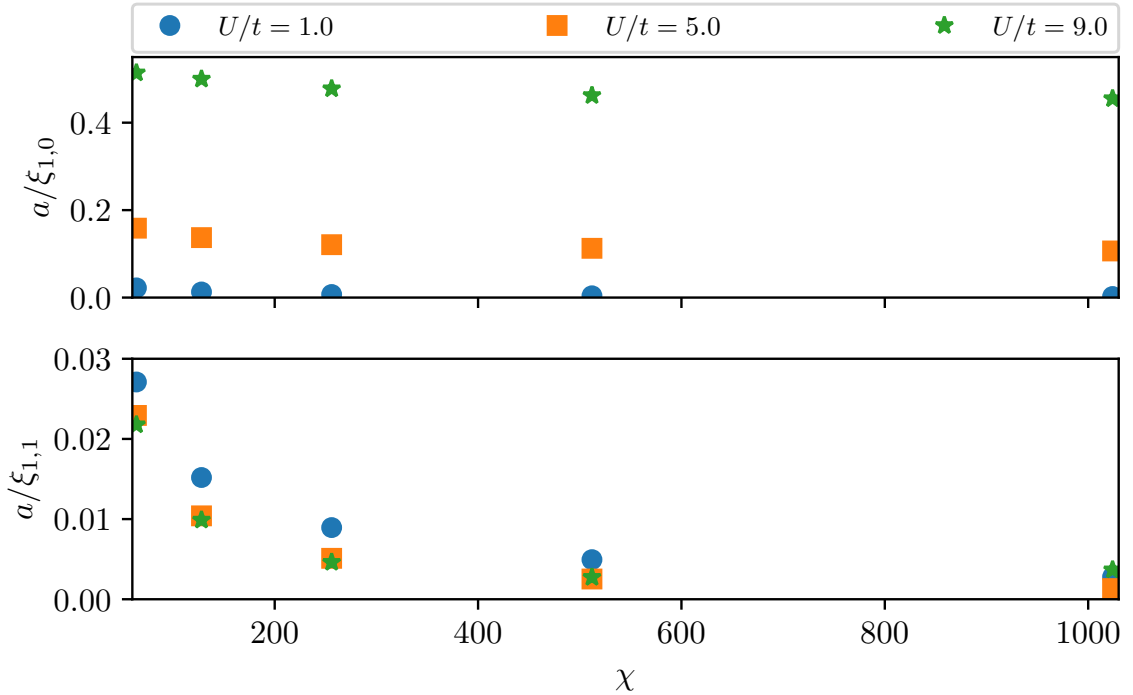


Figure 4.9: Inverse correlation lengths $a/\xi_{1,0}$ and $a/\xi_{1,1}$ associated with the one-body $\langle \hat{b}_{i,\sigma}^\dagger \hat{b}_{j,\sigma} \rangle$ and two-body $\langle \hat{b}_{i,\uparrow}^\dagger \hat{b}_{i,\downarrow}^\dagger \hat{b}_{j,\uparrow} \hat{b}_{j,\downarrow} \rangle$ correlation functions, respectively, as a function of the bond dimension χ for an infinite system with density $n_\uparrow = n_\downarrow = 2/5$, $r = 0.3$ and lattice spacing a .

true physical correlation length of the system as a function of U/t and r , see Fig. 4.10. At a critical interaction U/t the correlation length $\xi_{1,0}$ ceases to be infinite and becomes finite denoting the opening of a gap in the spin sector $\Delta \propto a/\xi_{1,0}$. The opening of a gap in the spin sector characterizes the phase transition from a 2SF to a PSF. That is, the weakly-interacting regime and the strongly-interacting one are not continuously connected and a 2SF-PSF phase transition occurs between them characterized by the opening of a gap in the spin sector. Importantly, one expects that Andreev-Bashkin drag (Andreev and Bashkin, 1976) is maximal in the 2SF phase in the vicinity of the transition to PSF (Nespolo et al., 2017; Parisi et al., 2018). In this case, a superflow imposed on one component induces a supercurrent in the second component which is dragged without any energy dissipation.

4.5 Phase diagram

Let us discuss the implications of the results presented in Fig. 4.6 and Fig. 4.10 together. The two-component Bose-Hubbard model Eq. (4.1) presents a liquid-to-gas transition at a critical $r_c = 2t/U$ for sufficiently large U/t and the liquid phase completely disappears at $r \approx 0.475$ for all U/t , see Fig. 4.6. The homogeneous quantum liquid can either behave as a 2SF in the weakly-interacting limit or as a PSF in the strongly-interacting one. The same applies for the quantum gas phase. The PSF phase is

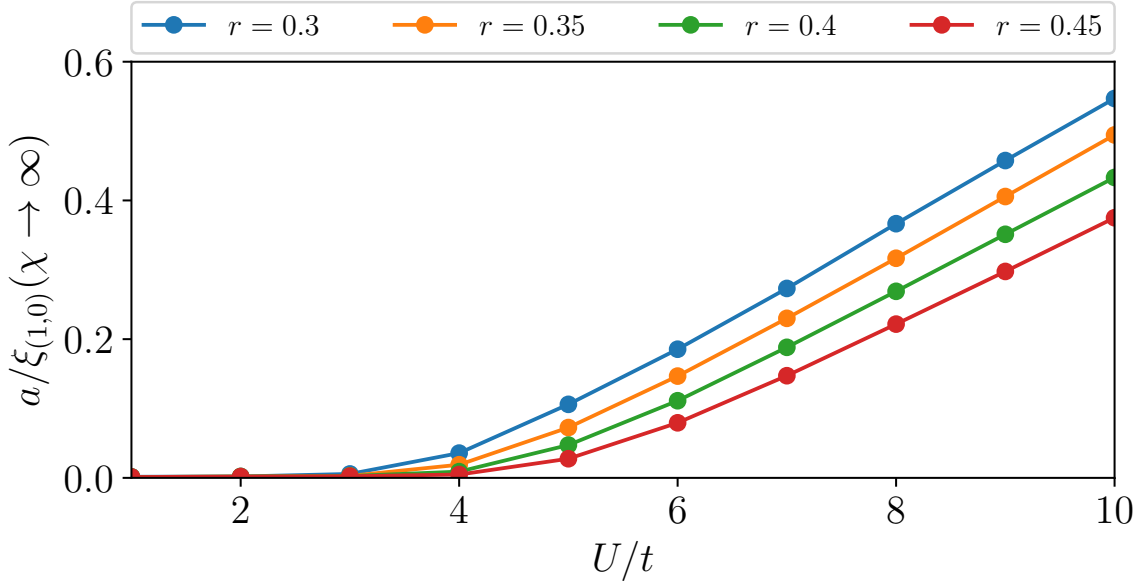


Figure 4.10: Inverse correlation length $a/\xi_{1,0}$ associated with the one-body correlation function $\langle \hat{b}_{i,\sigma}^\dagger \hat{b}_{j,\sigma} \rangle$ obtained in the limit $\chi \rightarrow \infty$ as a function of U/t for an infinite system with density $n_\uparrow = n_\downarrow = 2/5$, lattice spacing a and different values of r .

characterized by the opening of a gap in the spin sector, see Fig. 4.10. The spin gap also decreases with increasing r since we expect that the PSF phase is not present in the $r = 1$ limit where the mixture is completely decoupled $U_{\uparrow\downarrow} = 0$. Let us remark that we have discussed the 2SF to PSF transition in a small range of values of r and at a fixed density $n_\uparrow = n_\downarrow = 2/5$. Understanding the complete phase diagram is a subject of current study and goes beyond the scope of this Thesis.

4.6 Conclusions and outlook

In conclusion, we have demonstrated the existence of quantum liquids in the two-component Bose-Hubbard model describing a bosonic mixture loaded in a high one-dimensional optical lattice. By employing Bogoliubov's theory in the weakly-interacting regime we have obtained the equation of state and have determined the appearance of a quantum liquid in the lattice when the mixture is on overall repulsive at the mean-field level. We have observed that the lattice quantum liquid displays quantitative differences with respect its continuum counterpart. Moreover, we have compared our analytical theory with full iDMRG simulations and have shown an excellent agreement between both in the weakly interacting regime. Moreover, Bogoliubov's theory predicts a transition from a quantum liquid to a dimerized gas which we have confirmed with our iDMRG simulations. In the strongly interacting regime we have derived an effective theory describing the dimer-dimer interaction which captures the four-atom problem and correctly describes the liquid-gas phase transition when the system is formed by deeply bound dimers. This phase transition is marked by the resonance of the dimer-

dimer scattering length. Moreover, the liquid state exhibits a universal behavior since it only depends on the parameters of the two-dimer scattering problem, namely the scattering length and the effective range. These ingredients are enough to predict the existence of self-bound objects. In the vicinity of the resonance, the liquid is very dilute and can be described in terms of hard-core dimers with an attractive nearest-neighbor interaction. For strong repulsive dimer-dimer interactions bosonic dimers experience fermionization thus reaching the Tonks-Girardeau regime. We have studied the transition between the weakly and strongly interacting regime by performing iDMRG simulations. Exploring the long-range decay of one- and two-body correlation functions we have been able to identify a quantum superfluid with atomic or dimer quasi long-range phase coherence. By performing an extensive study with the bond dimension of our MPS we have been able to determine the quantum phase transition between the two superfluid and the pair superfluid phases.

The applicability of our results goes beyond the study of bosonic mixtures and the universal liquid phase could also be observed in other systems such as dipolar bosons in optical lattices ([Lahaye et al., 2009](#); [Trefzger et al., 2011](#)). Specifically, in Chapter 5 we study this system in detail. In addition, the predicted phases are directly accessible with current techniques used in ultracold quantum gases laboratories ([Schmitt et al., 2016](#); [Cabrera et al., 2018](#); [D’Errico et al., 2019](#); [Jepsen et al., 2020b](#)). Moreover, it could be interesting to extend Bogoliubov’s theory to include the dimer degrees of freedom which dominate the physics in the strongly interacting regime. Similar attempts have been performed in the continuum ([Hu and Liu, 2020](#)). A full self-consistent Gaussian solution of the two-component Bose-Hubbard model could be the way of obtaining a self-consistent theory incorporating all these ingredients ([Shi et al., 2018](#); [Pan et al., 2022](#)). Additionally, we plan to explore the dependence of the 2SF to PSF transition point with the total density and the imbalance of the system.

DIPOLAR BOSONS IN A ONE-DIMENSIONAL OPTICAL LATTICE

The interactions between neutral alkaline atoms loaded in a high 1D optical lattice have an exponentially decay with their relative distance, allowing a description of the system in terms of local interactions, as we have shown in Chapter 2. However, recent advances in the manipulation of cold atomic systems have lead to the development of systems composed of atoms, molecules or ions which feature strong non-local interactions (Lahaye et al., 2009; Lewenstein et al., 2012; Trefzger et al., 2011). In particular, the constituents which have permanent electric or magnetic dipolar moment interact through the dipole-dipole interaction,

$$V_{\text{dip}}(\mathbf{r}) = \frac{C_{dd}}{4\pi} \frac{(\mathbf{e}_1 \cdot \mathbf{e}_1)r^2 - 3(\mathbf{e}_1 \cdot \mathbf{r})(\mathbf{e}_1 \cdot \mathbf{r})}{r^5}, \quad (5.1)$$

where \mathbf{e}_1 and \mathbf{e}_2 are the dipole unit vectors and \mathbf{r} is the relative distance between two dipoles, see Fig. 5.1. We introduce the strength of the dipolar interaction: $C_{dd} = \mu_0\mu$ for particles having a permanent magnetic moment (being μ_0 the vacuum permeability) and, $C_{dd} = \mu_e^2/\epsilon_0$ for particles having a permanent electric moment μ (being ϵ_0 the vacuum permittivity). The dipolar interaction Eq. (5.1) decays at large distances as $1/r^3$ and, therefore, it is a long-range interaction in $D \geq 3$ dimensions since there is not a well defined thermodynamic limit (Lahaye et al., 2009). Although the dipolar interaction in $D = 1$ dimensions has a well-defined thermodynamic limit, it leads to striking effects compared to systems interacting through contact interactions, as we show in this chapter. Another relevant property of the dipolar interaction Eq. (5.1) is its anisotropic character. Depending on the relative angle between two dipoles the interaction can be repulsive or attractive. Typically, in ultracold systems the sample of particles is polarized in a given direction and Eq. (5.1) simplifies to,

$$V_{\text{dip}}(\mathbf{r}) = \frac{C_{dd}}{4\pi} \frac{1 - 3 \cos^2 \theta}{r^3}, \quad (5.2)$$

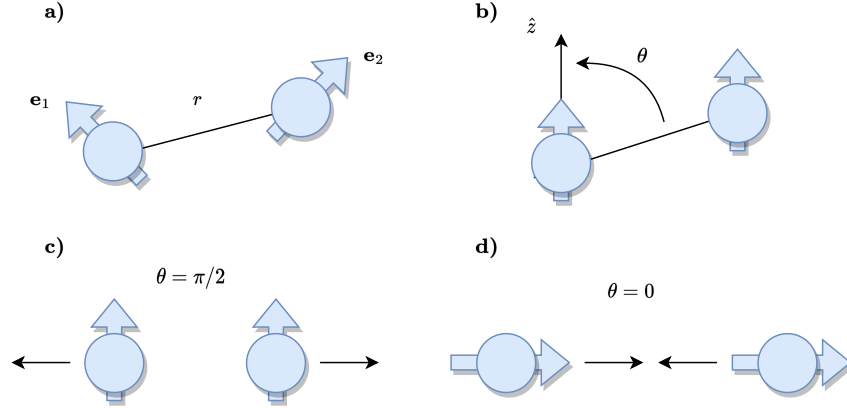


Figure 5.1: Two particles at a relative distance r with large permanent dipoles oriented in \mathbf{e}_1 and \mathbf{e}_2 directions, respectively, interact through the dipolar interaction Eq. (5.1), see panel a). When the sample is oriented in a given axis e.g. $\mathbf{e}_1 = \mathbf{e}_2 = \hat{z}$, particles interact through the dipolar interaction Eq. (5.2) characterized by the polarization angle θ , see panel b). Two dipoles repel each other when they are parallel $\theta = \pi/2$, see panel c), and attract each other in a head-to-tail configuration $\theta = 0$, see panel d).

where θ is the angle between the polarization axis and the relative position between two dipoles, see Fig. 5.1 b). Therefore, two dipoles repel each other when they are parallel ($\theta = \pi/2$) see Fig. 5.1 c), and attract to each other in a “head-to-tail” configuration ($\theta = 0$), see Fig. 5.1 d). Interestingly, there is a “magic-angle” ($\theta = \arccos(1/\sqrt{3})$) at which the dipolar interaction vanishes.

A very interesting platform for studying many-body systems with a strong dipolar interaction is magnetic atoms such as dysprosium, erbium, chromium, etc, which have a large magnetic moment of several Bohr magnetons (μ_B). While the dipolar interaction of these systems is weaker compared to the electric dipolar interaction, incredible advances have been produced in the last decade, including the observation of supersolids (Tanzi et al., 2019a; Böttcher et al., 2019a; Chomaz et al., 2019; Guo et al., 2019; Natale et al., 2019; Tanzi et al., 2019b; Norcia et al., 2021), quantum droplets (Schmitt et al., 2016; Ferrier-Barbut et al., 2016; Chomaz et al., 2016; Ferrier-Barbut et al., 2018), rotonic spectrum (Natale et al., 2019), among others. In combination with optical lattices they have been used to quantum simulate the extended Bose-Hubbard model (Baier et al., 2016). Importantly, it is possible to tune the local and non-local interactions separately in experiments (Kao et al., 2021), e.g. by using Feshbach resonances and adjusting the polarization angle of the magnetic moment in the system.

Heteronuclear polar molecules can exhibit large electric dipoles which can surpass the strength of the s -wave contact-like interactions by two orders of magnitude (Lewenstein et al., 2012). Recent advances in the cooling and trapping techniques have allowed to assess the many rotational, vibrational and electronic degrees of freedom present in molecules (Ni et al., 2008, 2010; Ospelkaus et al., 2010b,a; de Miranda et al., 2011; Neyenhuis et al., 2012; Chotia et al., 2012; Hazzard et al., 2014).

Another interesting platform for realizing electric dipolar systems are neutral Rydberg atoms (Zeiher et al., 2016; Guardado-Sanchez et al., 2018; Lienhard et al., 2018; Browaeys and Lahaye, 2020).

These ones exhibit an electric dipolar moment scaling as n^2 , being n the main quantum number of the atom, and, the interaction between two Rydberg atoms can be a dipolar one $V(r) \propto 1/r^3$ at relatively short distances or a van der Waals one $V(r) \propto 1/r^6$ at larger distances (Walker and Saffman, 2008). In addition, a Rydberg atom features a “Rydberg blockade radius” r_b , which is a forbidden region in which a second atom cannot be excited to the high- n state (Lukin et al., 2001). Therefore, the interaction between two Rydberg atoms is decomposed by a short-range hard-core potential with a typical radius $r_b \sim 5 - 10 \mu\text{m}$ and a non-local dipolar or van der Waals interaction at larger distances. The Rydberg blockade effect has been employed to design two-qubit states and therefore, it is a building block for doing quantum computation with Rydberg atoms (Saffman et al., 2010). These ideas have given rise to QuEra, a company selling quantum computers based on Rydberg atom architectures. However, one of the main limitations of coupled Rydberg atoms is their relatively short lifetime, which can be partially overcome by weakly dressing the system (Henkel et al., 2010; Pupillo et al., 2010).

Ionic systems also offer an interesting platform where non-local interactions can be studied since ions possess a net electric charge leading to strong Coulomb forces. Moreover, cold ions are one of the possible architectures to build a quantum computer (Cirac and Zoller, 1995; Monz et al., 2011; Friis et al., 2018; Pogorelov et al., 2021). Ensembles of hundreds of ions can be cooled down at ultra-low temperatures $\sim \text{mK}$ forming a crystalline structure (Britton et al., 2012) which can be confined in 1D or 2D geometries by employing Paul (Paul, 1990) or Penning traps (Mitchell et al., 1998; Itano et al., 1998). By coupling the vibrational modes of the crystal with the internal electronic structure of the ions an effective non-local spin-spin exchange interaction between ions can be engineered with a power-law decay $1/r^\alpha$ (Porras and Cirac, 2006; Britton et al., 2012), where $0 \leq \alpha \leq 3$. Therefore, ensembles of ions are a promising source for quantum computation and quantum simulation (Cirac and Zoller, 2000; Lanyon et al., 2011).

Non-local interactions can also be produced by the exchange of a photon between a pair of neutral atoms. However, these interactions are usually weak given the typical interparticle spacing of ultracold systems. Recently, photonic nanocrystals (Douglas et al., 2015; González-Tudela et al., 2015; Chang et al., 2018) and optical cavities (Münstermann et al., 2000; Baumann et al., 2010; Mottl et al., 2012; Ritsch et al., 2013; Vaidya et al., 2018) have been proposed to enhance the photon-mediated interaction. A different approach is to consider the exchange of a different atomic species between a pair of atoms which has allowed to quantum simulate lattice gauge theories with ultracold atoms (Zohar et al., 2015; Bañuls et al., 2020).

In this chapter we analyze the many-body physics of attractive dipolar systems loaded in a high 1D optical lattice. In particular, we study the interplay between the short-range repulsive core, the attractive non-local tail of the dipolar interaction and the kinetic energy. This interplay leads to exotic many-body phases including: a self-bound Mott-insulator, a gas phase and a strongly interacting quantum liquid. In Sec. 5.1 we present the extended Bose-Hubbard model and its main properties: we describe the self-bound Mott-insulator phase and present the novel mechanism leading to the formation of strongly-correlated quantum liquids. Then, in Sec. 5.2 we present the Hamiltonian describing dipolar bosons in a high 1D optical lattice and we discuss the numerical techniques employed to study the properties of the system. We study the equilibrium properties of dipolar bosons in a high 1D optical

lattice in Sec. 5.3 and Sec. 5.4. In Sec. 5.5 we present the non-equilibrium properties, including the dynamic structure factor and the speed of sound. Finally, in Sec. 5.6 we present our conclusions and outlook.

5.1 Extended Bose-Hubbard model

In order to treat non-local interactions among particles loaded in a high 1D optical lattice we first study the case where the interaction is cut at distances larger than the lattice spacing, leading to the following extended Bose-Hubbard model,

$$\hat{H} = -t \sum_i \left(\hat{b}_i^\dagger \hat{b}_{i+1} + \text{H.c.} \right) + \frac{U}{2} \sum_i \hat{n}_i (\hat{n}_i - 1) + V \sum_i \hat{n}_i \hat{n}_{i+1}, \quad (5.3)$$

where V is the strength of the non-local interaction projected in the lowest Wannier orbitals. Note that we have neglected a term, $T \hat{b}_i^\dagger \hat{n}_i \hat{b}_{i+1}$, called density-correlated hopping, which usually is a subleading term when the dipolar interaction is weak enough (Aramthottil et al., 2023). In this chapter we focus on the strongly-correlated regime corresponding to $U \gg t, |V|$.

5.1.1 Self-bound Mott-insulator

To understand the many-body phases appearing in the strongly interacting limit $U/t \gg 1$ we first consider the limit $t/U = 0$ where a Bose-Fermi mapping can be employed by performing a Jordan-Wigner transformation,

$$\hat{b}_i^\dagger = e^{i\pi \sum_{j<i} \hat{c}_j^\dagger \hat{c}_j} \hat{c}_i^\dagger, \quad (5.4)$$

where \hat{c}_i^\dagger is the creation spinless fermionic operator and \hat{b}_i^\dagger is the creation hard-core bosonic operator, meaning that $(\hat{b}_i^\dagger)^2 |\psi\rangle = 0$ for any state $|\psi\rangle$. For vanishing non-local interaction $V = 0$ this leads to the well-known Tonks-Girardeau (TG) gas state in a 1D optical lattice (Cazalilla, 2003, 2004b; Paredes et al., 2004). The Hamiltonian of the resulting fermionic model is given by,

$$\hat{H} = -t \sum_i \left(\hat{c}_i^\dagger \hat{c}_{i+1} + \text{H.c.} \right) + V \sum_i \hat{n}_i \hat{n}_{i+1}, \quad (5.5)$$

where \hat{c}_i and \hat{c}_i^\dagger correspond to annihilation and creation fermionic operators, respectively. The ground state of Hamiltonian (5.5) can be obtained through Bethe ansatz procedure and the phase diagram is well known (Cazalilla et al., 2011; Petrosyan et al., 2007; Giuliano et al., 2013). We focus our discussion on the attractive regime $V < 0$. At $V = -2t$ there is a quantum phase transition from a gas phase ($V > -2t$) to a phase separated phase ($V < -2t$).

The phase separated phase is characterized by having no stable homogeneous ground state in a finite system. For large number of particles, the system is spatially decomposed into two regions: a particle-rich region where the density is fixed at $n = 1$ and a hole-rich region which essentially is a

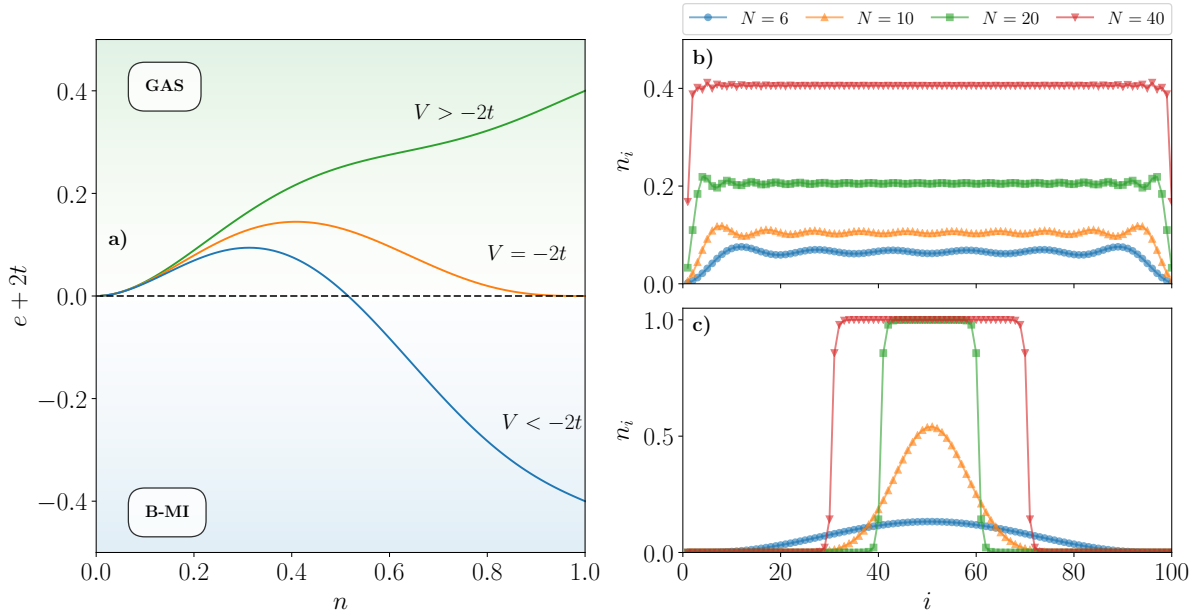


Figure 5.2: Equation of state of the fermionic extended Hubbard model, see Eq. (5.8), in the gas phase $V > -2t$, at the critical point $V = -2t$ and in the B-MI phase $V < -2t$, see panel a). Density profiles obtained performing DMRG simulations with $\chi = 128$ in finite boxes of $N_s = 100$ sites with different number of particles N and different values of the non-local strength: $V/t = -1$ in panel b) and $V/t = -3$ in panel c).

vacuum state $n = 0$. The quantum phase transition can be understood by performing a restricted Hartree-Fock decoupling where the anomalous average is neglected ($\langle \hat{c}_i \hat{c}_j \rangle = 0$). Notice that a Hartree-Fock decoupling in the superconducting channel ($\langle \hat{c}_i \hat{c}_j \rangle = \Delta_i$, $\langle \hat{c}_i^\dagger \hat{c}_j \rangle = 0$) explicitly breaking the U(1) symmetry leads to the appearance of a p-wave superconductor with unpaired Majorana fermions at the edges of the system (Kitaev, 2001).

By perturbatively adding an attractive non-local interaction to the non-interacting lattice Fermi gas we can estimate the energy as,

$$E = E_t + E_V = -\frac{2tN_s}{\pi} \sin(n\pi) + V \sum_i \langle \hat{n}_i \hat{n}_{i+1} \rangle. \quad (5.6)$$

The first term represents the kinetic energy of the lattice Fermi gas that we obtain in the thermodynamic limit $N, N_s \rightarrow \infty$ for a fixed particle density $n = N/N_s$. The second term is the non-local energy, which can be computed in a perturbative manner by employing Wick's theorem,

$$\frac{\langle \hat{n}_i \hat{n}_j \rangle}{n^2} \approx \frac{\langle \hat{n}_i \rangle \langle \hat{n}_j \rangle - \langle \hat{c}_i^\dagger \hat{c}_i \rangle \langle \hat{c}_j^\dagger \hat{c}_j \rangle}{n^2} = 1 - \frac{\sin^2(k_F |i - j|)}{k_F^2 |i - j|^2}, \quad (5.7)$$

where we introduce the Fermi momentum $k_F = \pi n$, and we employ $\langle \hat{c}_i^\dagger \hat{c}_j \rangle = \sin(k_F |i - j|) / (\pi |i - j|)$.

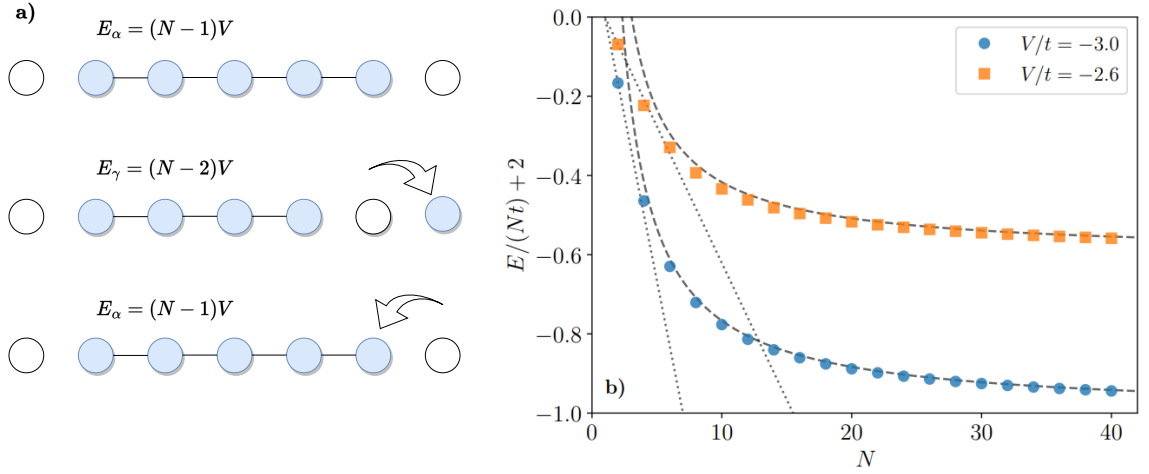


Figure 5.3: Schematic representation of second order tunneling processes occurring at the surface of the B-MI state, see panel a). In panel b) we represent the ground state energy obtained performing DMRG simulations with $\chi = 128$ in finite boxes of $N_s = 100$ sites at two ratios of V/t as a function of the particle number. Dashed lines correspond to the energy of the drop model, see Eq. (5.9), and dotted ones represent the energy of the lattice soliton, see Eq. (5.10).

The decoupling allows us to obtain the EoS of the system,

$$e \equiv \frac{E}{N} = -2t \frac{\sin(n\pi)}{n\pi} + V \left(n - \frac{\sin^2(n\pi)}{n\pi^2} \right). \quad (5.8)$$

At the critical value of $V = -2t$, the global minimum of the EoS jumps to unit density $n_0 = 1$, signaling a first-order transition to an insulator state, as shown in Fig. 5.2 panel a). Furthermore, the insulator state has a lower energy per particle than the free particle energy $-2t$. Therefore, it is a self-bound state which we name self-bound Mott insulator (B-MI). The threshold of the B-MI state is defined by the condition that the energy per particle at unit filling equals the free energy per particle $e(n=1) = -2t$ giving the critical value of the non-local interaction $V_{\text{B-MI}}/t = -2$. B-MI states feature complete incompressibility. Thus, in finite systems, they become completely localized, exhibiting compact density profiles with a saturated density corresponding to strictly one particle per site $n = 1$, as shown in Fig. 5.2, panel c). This corresponds to the phase-separated state. Although the density profile for these states bears similarity to quantum droplets, quantum correlations are completely suppressed in the B-MI case, as discussed in Sec. 5.4. Therefore, one should not consider this phase as a quantum liquid.

It is also interesting to examine the problem for a finite number of particles in a finite system. The energy of the B-MI can be decomposed into a bulk and a surface contribution, similar to the liquid drop model of the nucleus. The bulk energy E_B corresponds to the thermodynamic energy per particle at unit filling $E_B = Ne(n=1) = VN$. It represents the binding energy of putting all fermions on a line. Moreover, the surface energy can be obtained in the limit $|V| \gg t$, where the B-MI is a strongly self-bound object. In this limit, second-order tunneling processes occur at the surface of the B-MI,

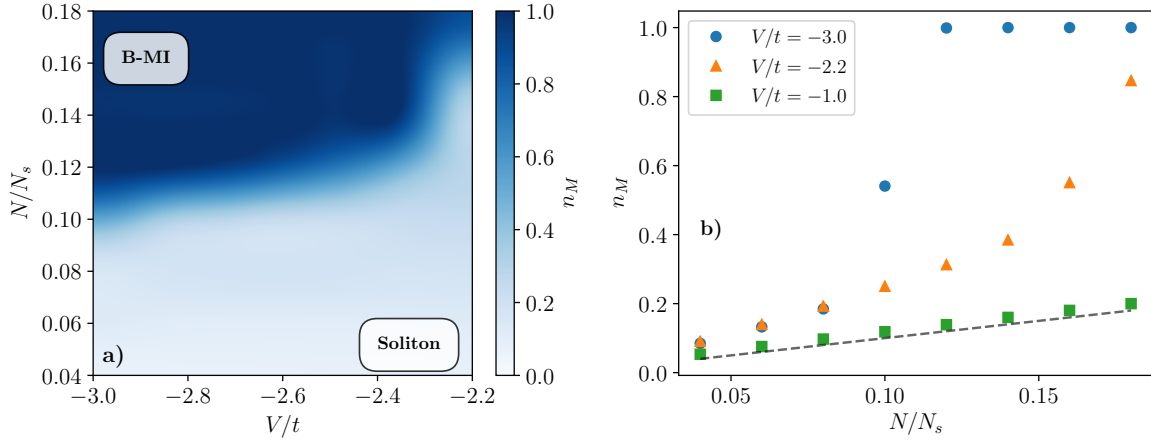


Figure 5.4: Maximum density n_M of the density profiles obtained in finite boxes of N_s sites with N particles as a function of the ratio N/N_s and the non-local strength V/t , see panel a). In panel b) we show three cuts at constant $V/t = -3, -2.2, -1$ as a function of N/N_s . Dashed line represent the linear behaviour expected in the gas phase.

where a fermionic pair is first broken and then recombines, see Fig. 5.3 panel a). Taking into account these processes, we obtain the dependence of the energy with the particle number in the B-MI phase,

$$\frac{E}{N} = E_B + \frac{2\sigma}{N} = V - \frac{V - 2t^2/V}{N}. \quad (5.9)$$

The negative bulk energy is compensated by an effective repulsive surface energy which stabilizes the object, see Fig. 5.3 panel b) for a comparison with DMRG simulations. However, for small particle number the system is surface dominated. In this situation a flat density profile is not formed and we find a lattice soliton solution, see Fig. 5.2 panel c) $N = 10$ result. In this limit the energy of the system is given by,

$$\frac{E}{N} + 2t = \frac{N - 1}{2} \epsilon_b, \quad (5.10)$$

where ϵ_b corresponds to the two-particle binding energy. The soliton to B-MI crossover can be studied by computing the ground state density profile in a finite box. We define the maximum particle density n_M of the density profile and study its dependence with the particle number N and the non-local interaction strength V , see Fig. 5.4. At a critical particle number N_c the maximum density reaches unit filling $n_M(N_c) = 1$ and the system enters in the B-MI phase. The critical particle number N_c decreases by increasing the non-local strength V in absolute value. Therefore, the soliton to B-MI crossover can be reached faster as a function of the particle number for stronger attractive non-local interaction. This behavior can be contrasted with what occurs in the gas phase where the maximum density simply follows the average density of the system $n_M = N/N_s$ regardless of the non-local interaction, see Fig. 5.4 panel b) ($V/t = -1$ results).

Let us also remark that lattice physics significantly differs from what one expects to find in a

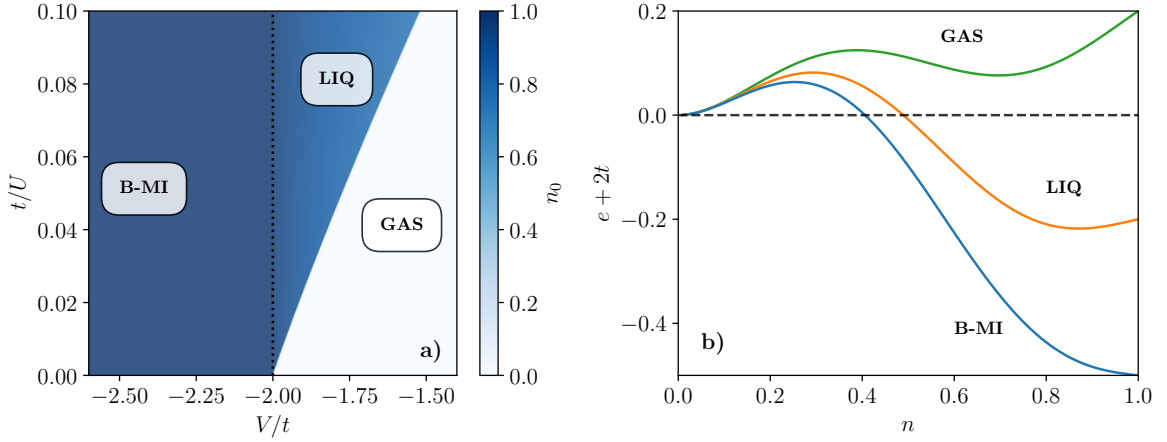


Figure 5.5: Phase diagram of penetrable bosons with a large on-site interaction U/t and a non-local nearest-neighbor attraction V/t in panel a). The different phases can be distinguished by the equilibrium density n_0 which minimizes the energy per particle of the system. The different phases correspond to: $n_0 = 0$ for GAS phase, $0 < n_0 < 1$ for LIQ phase and $n_0 = 1$ for B-MI phase. In panel b) we show the characteristic energy per particle as a function of density for the three different phases.

continuous analogue of the described system. In the 1D continuum, the addition of attractive dipolar interaction to the free Fermi gas leads to the collapse of the system as the quantum fluctuations cannot compensate for the diverging dipolar attraction. The feature of a lattice is that it provides a natural regularization of the problem since, for hard-core particles, the maximum density allowed is fixed by the lattice spacing ($n \leq 1$). This holds in the regime of applicability of the single-band eBH. For very strong attractive dipolar interactions, one may need to include higher bands into consideration.

5.1.2 Superexchange liquefaction

The mechanism lying behind B-MI formation is based on a near cancellation between the effective repulsion coming from the kinetic energy of lattice hard-core particles and the dipolar attraction. In the following, we study the effects of relaxing the hard-core condition in our system.

We consider penetrable bosons with large but finite on-site interaction $U/J \gg 1$. We thus move away from the TG limit that opens the possibility of next-to-nearest neighbor hopping through a virtual intermediate process of two bosons occupying the same site — the so-called superexchange process. This effect can be taken into account at second order in degenerate perturbation theory in U/J (Cazalilla, 2003, 2004b), leading to the effective Hamiltonian,

$$\hat{H} = -t \sum_{i=1} \left(\hat{c}_i^\dagger \hat{c}_{i+1} + \text{H.c.} \right) + \frac{2t^2}{U} \sum_{i=1} \left(\hat{c}_{i-1}^\dagger \hat{n}_i \hat{c}_{i+1} + \text{H.c.} \right) + \left(V - \frac{4t^2}{U} \right) \sum_{i=1} \hat{n}_i \hat{n}_{i+1}. \quad (5.11)$$

The energy of the system is given by, $E = E_t + E_V + E_U$, where E_t and E_V are given by Eq. (5.8)

and the on-site energy can be similarly computed as in Sec. 5.1.1, leading to,

$$e_U \equiv E_U/N = -\frac{4t^2}{U}n \left(1 - \frac{\sin(2\pi n)}{2\pi n}\right). \quad (5.12)$$

Note that the superexchange correction effectively introduces additional attraction of order $J^2/U \ll 1$ in the system for all densities. Remarkably, by inspecting the modified EoS of the ground state, we encounter a gas-to-liquid transition close to the B-MI boundary by reducing the on-site interaction, owing entirely to the emerging superexchange process. The found liquid phase is characterized by a negative energy per particle smaller than for the free case $E/N < -2t$ and a finite equilibrium density $0 < n_0 < 1$, see Fig. 5.5. By increasing the attractive non-local coupling, the density saturates with one particle per site, and consequently, the system enters the B-MI state. Notice that the equilibrium density exhibits a jump at the gas-to-liq transition line denoting a first order type transition. The nature of the transition is studied in Sec. 5.5.1 by performing DMRG simulations, going beyond the analytical decoupling introduced in this section.

Notably, the discovered mechanism of liquefaction in the strongly-correlated regime bears certain similarities with the one vastly studied in the opposite limit of weak interactions, see Sec.4.2.3. As therein, quantum liquids appear due to the subleading terms when dominating contributions of opposite signs cancel each other (Petrov, 2015). Nonetheless, contrary to the LHY term as a small beyond mean-field effect, the superexchange correlations occur for strongly interacting systems well beyond the Bogoliubov theory applicability.

5.2 Dipolar bosons loaded in a high 1D optical lattice

The competition between the attractive non-local interaction and the superexchange processes leads to a liquefaction of ultracold bosons in a high 1D optical lattice, as shown in Sec. 5.1. Therefore, we explore now a more realistic realization of these quantum liquids by considering a 1D system of ultracold dipolar bosons loaded to a high optical lattice. The system is described by the following Hamiltonian,

$$\hat{H} = -t \sum_i \left(\hat{b}_i^\dagger \hat{b}_{i+1} + \text{H.c.} \right) + \frac{U}{2} \sum_i \hat{n}_i (\hat{n}_i - 1) + V \sum_{i < j} \frac{\hat{n}_i \hat{n}_j}{|i - j|^3}, \quad (5.13)$$

where we do not cut the dipolar interaction to nearest-neighbors.

In the following, we study the two-particle problem of Hamiltonian (5.13), its many-body ground state in Sec. 5.4 and its non-equilibrium properties in Sec. 5.5. We develop a perturbative theory as in Sec. 5.1 and perform unbiased tensor network simulations focusing on the strongly-correlated regime $U/t \gg 1$ and $|V| \sim t$. We focus on the large particle number limit, so that solitonic solutions can be discarded. For a discussion on the soliton solution see Sec. 5.1.1. For obtaining the ground state we employ the DMRG algorithm and for performing real-time evolution we make use of the TDVP algorithm, see App. A for details on the algorithms.

5.2.1 Experimental considerations

Before moving to our theoretical calculations we discuss the experimental implementation of the above Hamiltonian (5.13). A recent experiment with ^{162}Dy atoms (Kao et al., 2021) has been able to confine the system in a quasi-1D geometry by employing a very high transverse optical lattice and tune independently the s -wave and the dipolar interaction by employing Feshbach resonances and adjusting the polarization angle, respectively. Therefore, Hamiltonian (5.13) could be realized by including a high 1D optical lattice in the longitudinal direction. Moreover, the typical transverse length of the trapping potential $\sigma_{\perp} \approx 50$ nm (Kao et al., 2021) is much smaller than the typical lattice spacing $a_x \approx 500$ nm, allowing us to consider pure dipolar interaction $1/r^3$ in 1D instead of the effective interaction for quasi-1D geometries, which includes corrections at distances of the order of σ_{\perp} (Deuretzbacher et al., 2010). In this situation the dipolar strength V is related to the experimental parameters by,

$$V = \frac{C_{dd}}{4\pi} \frac{1 - 3\cos^2(\theta)}{a_x^3}, \quad (5.14)$$

being C_{dd} the dipolar coupling. Considering the experimental parameters for ^{162}Dy atoms (Kao et al., 2021) ($C_{dd} \approx (9.93\mu_B)^2\mu_0$) with $\sigma_{\perp} = 952a_0$, a_0 being the Bohr radius, $V_{\perp} = 30E_{\perp}$ and $E_{\perp}/\hbar = 2\pi \times 2.24\text{kHz}$ and a longitudinal optical lattice of lattice spacing $a_x = 532\text{nm}$ with a height $V_x = 14E_x$, one can cross all the phases encountered in this section by changing the polarization angle θ .

5.2.2 Numerical details

We employ the two-site update DMRG and iDMRG algorithms in order to find the ground state of Hamiltonian (5.13). To calculate various properties of different phases exhibited by the considered system, we performed simulations with $N_s = 100 - 800$ lattice sites and $N = 50 - 100$ particles. To obtain the density dependence, we imposed the periodic boundary conditions on Hamiltonian (5.13) and employed DMRG. We find an excellent agreement between these results and the ones obtained with the iDMRG method where the homogeneous solution is mechanically stable. To obtain the quantum droplets we used open boundary conditions ensuring that the system size does not affect the profiles. We perform simulations making sure that the number of particles is large enough to be in the saturated regime where solitonic solutions can be discarded. In our code, to go beyond the nearest-neighbor interaction and couple two arbitrary distant dipolar bosons, we fit the power-law decaying dipolar interaction with a sum of ten exponential functions (Pirvu et al., 2010), when having open boundary conditions. Thus, we are not cutting the range of the interaction in the numerical implementation of our model. For systems with periodic boundary conditions we define the distance between two particles as the arc of the respective ring. To test the MPS representation of the ground state, we have checked the convergence in terms of the bond dimension χ up to $\chi = 800$. The equilibrium properties of the system, such as the energy or particle variance, show a fast convergence with the bond dimension. At the same time, we have implemented a cutoff in the maximum number of bosons per site N_m . Our perturbative theory hints that doublons play a crucial role in the formation

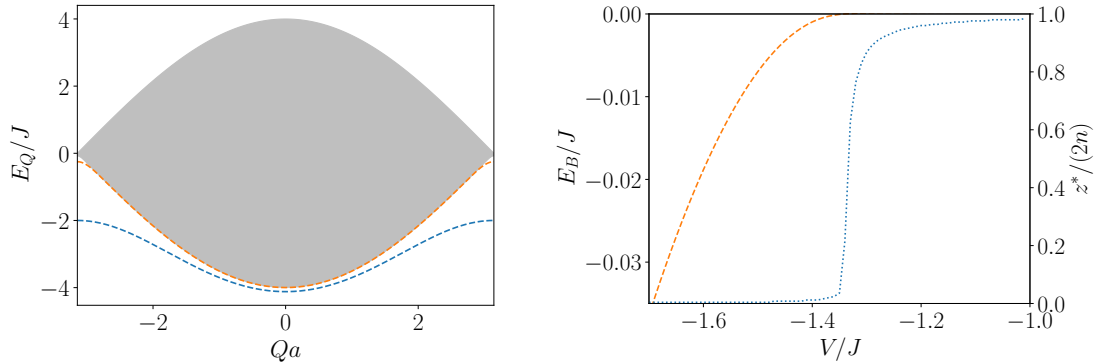


Figure 5.6: In panel a) we represent the energy of two dipolar bosons in a 1D optical lattice as a function of the total quasi-momentum Qa of the pair. The on-site interaction is $U/J = 20$ and the dipolar strength $V/J = -10$. The filled gray region represents the scattering continuum and dashed lines depict bound state solutions.

of the liquid state. We thus also checked the convergence for the varying cutoff N_m . For the case $U = 20$ and $V = -1.5$, which shows the maximum particle variance, see Sec. 5.5.1, we observe an excellent convergence already obtained for $N_m = 3$. The energy and entanglement entropy difference with respect to $N_m = 4$ are $\Delta E = 10^{-7}$ and $\Delta S = 10^{-7}$. Therefore, all the results presented in the following sections are performed at $N_m = 3$.

5.3 Equilibrium properties of two dipolar bosons

Similar to Sec. 2.5 we solve the problem of two dipolar bosons in a one-dimensional lattice by separating the center of mass and relative motion. We obtain the equation of motion for the relative wavefunction,

$$E_Q \psi_Q(z) = \sum_{e=\pm 1} -2t \cos(Q/2) \psi_Q(z+e) + U \delta(z) \psi_Q(z) + 2V \sum_{n=1}^{N_s} \frac{\delta(|z|-n)}{n^3} \psi_Q(z). \quad (5.15)$$

By performing exact diagonalization of Eq. (5.15), we get the spectrum of the system as a function of the pair quasi-momentum, see Fig. 5.6. We notice that for large values of the on-site interaction $U \gg t$, there is a critical negative value of the dipolar strength V_c/t , for which a bound state appears in the spectrum. This bound state appears below the two-particle scattering continuum and its energy has a minimum at $Qa = 0$. It is characterized by a negative binding energy E_B/t defined as a difference between the energy of the lowest-energy state and the minimum of the scattering band. For larger negative values of the dipolar strength, more bound states can be found. For the deepest bound state in the system, we compute a typical relative distance between the two particles z^* as a function of the dipolar strength. For large values of the on-site interaction $U/t \gg 1$ we observe that the bound state has a large probability of having both particles in adjacent sites $z^* \sim a$ at large values of the dipolar interaction in absolute value. This indicates the local nature of the bound state even though the presence of a non-local dipolar interaction.

5.4 Many-body equilibrium properties of dipolar bosons

We start investigating the many-body phases of Hamiltonian (5.13) by employing the perturbative theory developed in Sec. 5.2. After some algebraic manipulations we obtain the perturbative energy per particle in the thermodynamic limit,

$$\begin{aligned}
 e &= e_t + e_V + e_U, \\
 e_t &= -2t \frac{\sin(n\pi)}{n\pi}, \\
 e_V &= V \left(\zeta(3)n - \frac{\zeta(5)}{2n\pi^2} + \frac{1}{4n\pi^2} [\text{Li}_5(e^{2i\pi n}) + \text{Li}_5(e^{-2i\pi n})] \right), \\
 e_U &= -\frac{4t^2}{U} n \left(1 - \frac{\sin(2\pi n)}{2\pi n} \right),
 \end{aligned} \tag{5.16}$$

where we introduce the polylogarithm function $\text{Li}_\beta(n)$ of order β . The presence of the non-local dipolar tail effectively introduces additional attraction in the system as compared to Eq. (5.8), where the dipolar interaction is cut at nearest-neighbors. From the EoS (5.16) we can obtain the thermodynamic many-body phases characterized by their equilibrium density n_0 , which correspond to the ones presented in Sec. 5.2: a gas phase ($n_0 = 0$), a liquid phase ($0 < n_0 < 1$) and a self-bound Mott-insulator ($n_0 = 1$). The main difference with respect to Eq. (5.8) is that the transition points occur at smaller values of the dipolar strength V in absolute value. In particular, at the critical value,

$$V_{\text{B-MI}}/t = -2/\zeta(3), \tag{5.17}$$

we have a phase transition to a B-MI phase in the strongly interacting regime $U/t \gg 1$. One can easily generalize this result for a general attractive non-local interaction decaying as $1/|r|^\alpha$, obtaining a transition point $V_{\text{B-MI}}/t = -2/\zeta(\alpha)$. Therefore, we recover the transition point $V_{\text{B-MI}}/t = -2$ when the non-local interaction decays very fast $\alpha \rightarrow \infty$ by using the mathematical property $\lim_{s \rightarrow \infty} \zeta(s) = 1$.

To benchmark the perturbative EoS (5.16), we calculate the ground-state energy of Hamiltonian (5.13) using the DMRG algorithm, see Sec. 5.2.2. We compute the ground state for different strengths of the dipolar interaction V/t keeping fixed a large but finite on-site interaction U/t , see Fig. 5.7. In the case of larger densities ($n \gtrsim 0.8$), an excellent agreement is found for any value of the dipolar interaction, especially when approaching the unit filling limit $n = 1$ owing to suppressed quantum correlations, see Fig. 5.7 panel a). For smaller densities ($n \lesssim 0.5$), the effective EoS (5.16) deviates significantly, as it does not include the presence of few-body bound states. In the few-body limit, the equation of state is well approximated by a lattice soliton solution, see Eq. (5.10).

The equilibrium properties differ dramatically among the various phases, as shown in Fig. 5.7. The equilibrium density ranges from $0 < n_0 < 1$ in the liquid phase and saturates to $n_0 = 1$ in the B-MI phase. DMRG simulations result in density profiles that do not fill the entire lattice for these phases, contrary to the gaseous state, see Fig. 5.7 panels b), c) and d). Moreover, the value of the saturated density agrees excellently with the equilibrium density found from the EoS. Its value increases almost

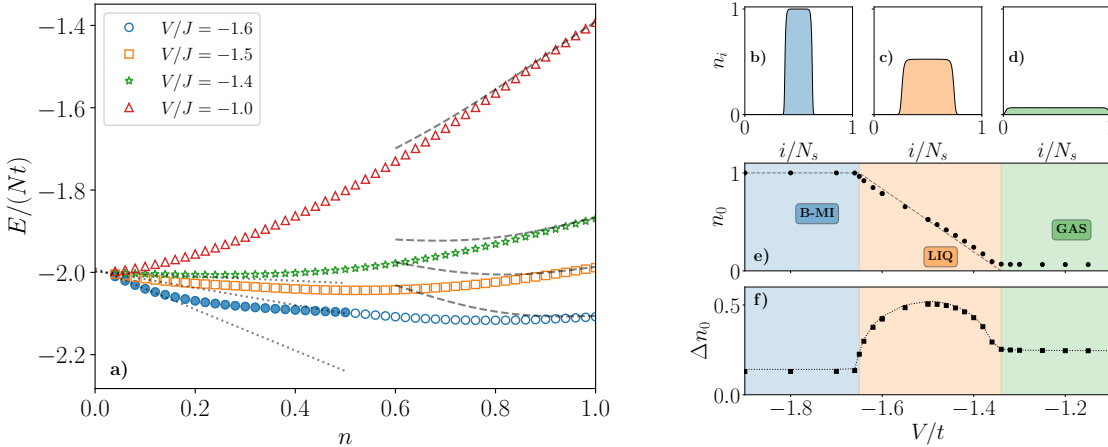


Figure 5.7: In panel a) we show the equation of state of dipolar bosons in a one-dimensional optical lattice for different dipolar strength V/J and fixed on-site repulsion $U/J = 20$. Filled symbols denote inhomogeneous solutions. Dashed lines show the perturbative result Eq. (5.16). The dotted line shows the behavior expected for a lattice soliton solution Eq. (5.10). Liquid forms when the equation of state shows a minimum at some finite value of density n_0 with the energy per particle $E/(N_s n_0) < -2J$, see $V/J = -1.4, -1.5, -1.6$ curves. A gas occurs when the minimum is located at zero density with the energy per particle $E/N > -2J$, see the $V/J = -1.0$ curve. Panels b), c) and d) correspond to typical density profiles in finite boxes for the three many-body phases at $U/t = 20$: B-MI ($V/t = -1.7$, $N = 100$, $N_s = 400$), LIQ ($V/t = -1.5$, $N = 100$, $N_s = 400$) and GAS ($V/t = -1.3$, $N = 50$, $N_s = 800$) phase, respectively. In panel e) we present the saturation density n_0 (circles), defined as the maximum density obtained in the density profiles, as a function of V/J for a fixed $U/J = 20$. Dashed line corresponds to: unit filling, $n_0 = 1$ (B-MI); zero filling, $n_0 = 0$ (GAS); linear interpolation (LIQ). We have performed o.b.c numerical simulations up to a density $n = 50/800$ to obtain the density profiles. In panel f) we show the particle number variance $\Delta n_0^2 = \langle \hat{n}_0^2 \rangle - \langle \hat{n}_0 \rangle^2$ (squares) at equilibrium for the same parameters as panel e). The dotted line denotes the particle number variance obtained in a TG-like state, see Eq. (5.20).

linearly for the growing attractive dipolar interaction in the liquid phase. Upon reaching the B-MI phase, the equilibrium density saturates to $n_0 = 1$ and becomes independent of the dipolar coupling. Another important observable pertains to the particle variance $\Delta n_0 = \sqrt{\langle \hat{n}_0^2 \rangle - n_0^2}$, as it quantifies the fluctuations of density and probes the structure of pair correlations. Particularly, it vanishes in the gas phase (due to vanishing equilibrium density) and in the B-MI phase becomes of order J/\sqrt{U} . We find that the maximal value of Δn_0 is reached in the liquid phase close to half-filling $n_0 \sim 1/2$, see Fig. 5.7 panel f). The behavior of the particle variance can be understood from our perturbative theory. The local particle variance can be directly related with the local pair-correlation function $g_2 = \langle \hat{b}_i^\dagger \hat{b}_i^\dagger \hat{b}_i \hat{b}_i \rangle / n^2$,

$$\Delta n \equiv \sqrt{\langle \hat{n}^2 \rangle - n^2} = \sqrt{g_2 n^2 + n - n^2}. \quad (5.18)$$

By employing the Hellmann-Feynman theorem, the local pair-correlation function can be written as,

$$g_2 = \frac{2}{n^2} \frac{\partial}{\partial U} \left(\frac{E_U}{N_s} \right) = \frac{8J^2}{U^2 n^2} \left(1 - \frac{\sin(2\pi n)}{2\pi n} \right), \quad (5.19)$$

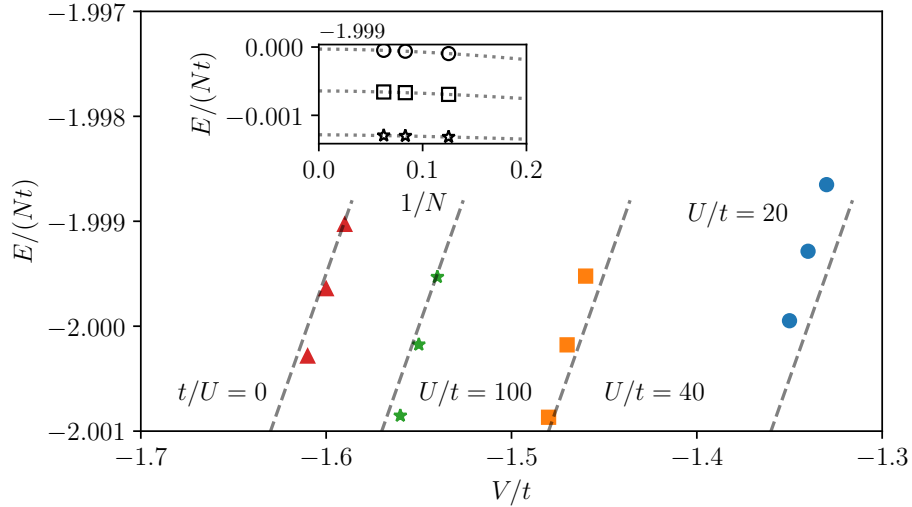


Figure 5.8: Main panel: Energy per particle in the thermodynamic limit for a system density $n = 1/10$ as a function of the dipolar strength V/t for different values of on-site interaction U/t . The gas-to-liquid phase transition occurs when $E/(Nt) = -2$. Dashed lines indicate a two-body decoupling, see the main text. Inset panel: Energy per particle dependence with the number of particles at fixed density for the case of hard-core bosons.

which leads to particle variance,

$$\Delta n \equiv \sqrt{n - n^2 + \frac{8J^2}{U^2} \left(1 - \frac{\sin(2\pi n)}{2\pi n}\right)}. \quad (5.20)$$

Fascinatingly, the perturbative calculation Eq. (5.20) captures well the DMRG results and provides a precise analytic description, see Fig. 5.7 panel f). Moreover, the particle variance can be used to detect the different phases present in the system. The gas-to-liquid phase transition is characterized by a discontinuity in the first derivative of the local particle variance at equilibrium $\Delta n_0 \sim \sqrt{n_0}$. On the other hand, when crossing the transition from liquid to self-bound Mott-insulator, the particle variance is an analytic differentiable function $\Delta n_0 \sim 2\sqrt{2}J/\sqrt{U} - (n_0 - 1)\frac{8J^2+U}{4\sqrt{2}J\sqrt{U}}$ for any value of finite on-site interaction $U/J \gg 1$. However, it shows a kink at the transition point owing to the presence of a discontinuity of the first derivative of the equilibrium density. In the Tonks-Girardeau limit $U/J \rightarrow \infty$, the particle variance also exhibits a discontinuity in its first derivative $\Delta n_0 \sim \sqrt{1 - n_0}$.

5.4.1 Gas to liquid transition

Our DMRG simulations in finite boxes do not show a sudden jump of the equilibrium density at the critical gas-to-liquid transition line, in contrast to the perturbative EoS, see Eq. (5.16). Moreover, the equilibrium density seems to increase linearly at the critical line denoting a second order phase transition, see Fig. 5.7 panel e). The failure of the perturbative theory close to the gas-to-liquid transition can be understood by comparing the perturbative EoS with the one obtained from DMRG

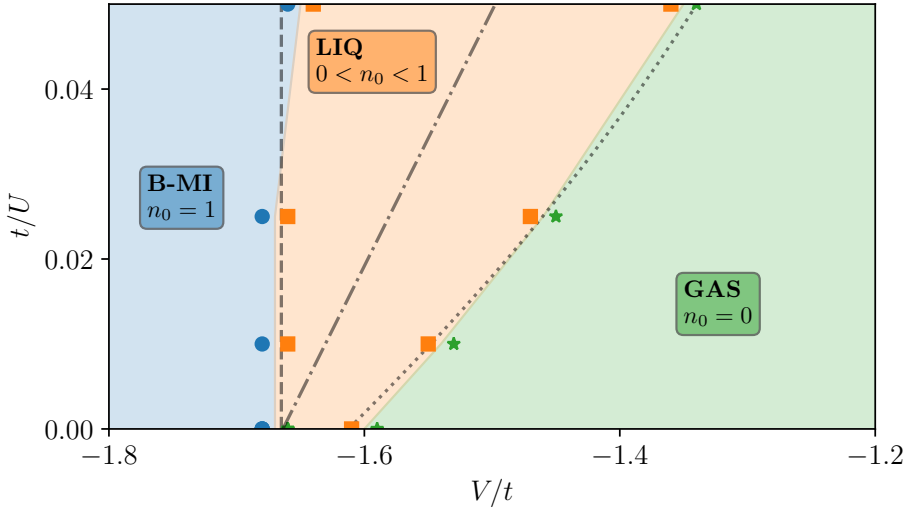


Figure 5.9: Phase diagram for dipolar bosons in a one-dimensional optical lattice. Different phases can be characterized by their respective equilibrium densities n_0 . We encounter a gaseous phase (GAS), a liquid one (LIQ), and a self-bound Mott-insulator (B-MI). Dashed and dotted-dashed lines denote respectively LIQ-to-B-MI and GAS-to-LIQ transitions obtained in perturbation theory. The dotted line indicates the threshold for a bound state (dimer) in the two-body problem, see Sec. 5.3.

simulations, see Fig. 5.7 panel a). The perturbative EoS does not capture well the behavior of the system at low densities, as we have anticipated. Therefore, it is unable to capture the gas-to-liquid transition since close to the transition the equilibrium density vanishes.

The numerical identification of the gas-to-liquid transition line in the thermodynamic limit is a complicated task since one has to reach the thermodynamic limit at arbitrary low densities close to the critical line. However, we have managed to study the stability of the homogeneous thermodynamic gas as a function of the interactions for a very small density $n = 0.1$. For increasing dipolar interaction, the many-body gas state becomes self-bound $E/N < -2J$ and a transition to a liquid phase occurs, see Fig. 5.8. To ensure the many-body transition, we study the dependence of the energy per particle with the number of particles for fixed density $n = 1/10$. This allows us to extrapolate the observables to the thermodynamic limit.

The energy per particle depends almost linearly on the strength of dipolar interaction. This points to a two-body decoupling. All interaction effects can be absorbed in a two-body coupling strength $g_0 = (V - V_0)$, V_0 being the point at which a two-body bound state appears, see Sec. 5.3. The energy per particle can be thus estimated as $E/N = \frac{1}{2}g_0n$. Remarkably, this gives a good estimation of the energy per particle close to the liquid-to-gas transition, see Fig. 5.8.

5.4.2 Phase diagram

Having explored the different equilibrium properties of the system and identified the critical observables at the transition lines allows us to construct the phase diagram of the system, see Fig. 5.9. The phase

diagram resembles the one presented for the extended BH model with nearest-neighbor attraction, see Fig. 5.5. However, one of the qualitative differences between the two models is the presence of a narrow liquid phase in the TG limit $t/U = 0$ for the model in which the dipolar interaction is not cut off at any distance. Moreover, our perturbative theory does not capture the presence of this liquid phase either. This liquid state is sandwiched between the gas and B-MI phases for $V_{\text{MI}} < V < -1.61t$, see Fig. 5.9. The weakest attraction, for which the liquid forms, is defined by the existence of a two-body bound state. Remarkably, for the dipolar interaction, the formation of a two-body bound state does not coincide with the formation of a self-bound MI state in the many-body problem for $t/U = 0$, in contrast to faster decaying potentials. We thus relate the presence of the liquid phase to the non-local tail of the dipolar interaction. In DMRG simulations, we always observe that the appearance of the liquid phase coincides with the formation of a two-body bound state in the system, see Fig. 5.9.

5.5 Non-equilibrium properties of dipolar bosons

The equilibrium properties of dipolar bosons in a high 1D optical lattice have allowed us to identify the formation of different quantum many-body phases in the system. In this section we explore how the interplay between the dipolar interaction and superexchange processes affects the non-equilibrium properties of the system. In particular, we focus on the dynamic structure factor $S(k, \omega)$ which measures the time-dependent density response of the system and, therefore, it contains information about the two-particle excitations of the system. From the dynamic structure factor we are able to identify a phononic branch and extract the speed of sound of the system. We study the dependence of the speed of sound on the dipolar interaction and density. Different experiments with ultracold atoms have been able to measure the excitation spectrum of the system by employing RF-spectroscopy, two-photon Bragg spectroscopy and lattice modulation. The effects of the dipolar interaction on the excitation spectrum have been experimentally studied in [Cheneau et al., 2012], where the softening of a rotonic mode has been observed. Moreover, the speed of sound could be directly accessed by studying holon propagation (Cheneau et al., 2012). Therefore, our theoretical calculations are relevant for current experiments with ultracold atoms.

5.5.1 Dynamic structure factor and lattice sum rules

To unravel the excitation spectrum of the system, we compute the dynamic structure factor $S(K, \omega)$. To this end, we calculate the space and time-dependent density-density correlation function in terms of (x, T) variables and perform a Fourier transform in order to express it in conjugate (k, ω) variables,

$$S(k, \omega) = \int_{-\infty}^{\infty} dt \sum_j \langle 0 | \delta n_j(T) \delta n_0(0) | 0 \rangle e^{ikx_j - i\omega T}, \quad (5.21)$$

where 0 index indicates the reference lattice site taken at the center of the system, $\delta n_i = n_i - n$, $x_j = ja$ with $a = 1$ and $|0\rangle$ is the ground state of the system. To perform the time evolution, we employ the two-site TDVP algorithm (Haegeman et al., 2011, 2016). We choose a time step $dT = 0.1$

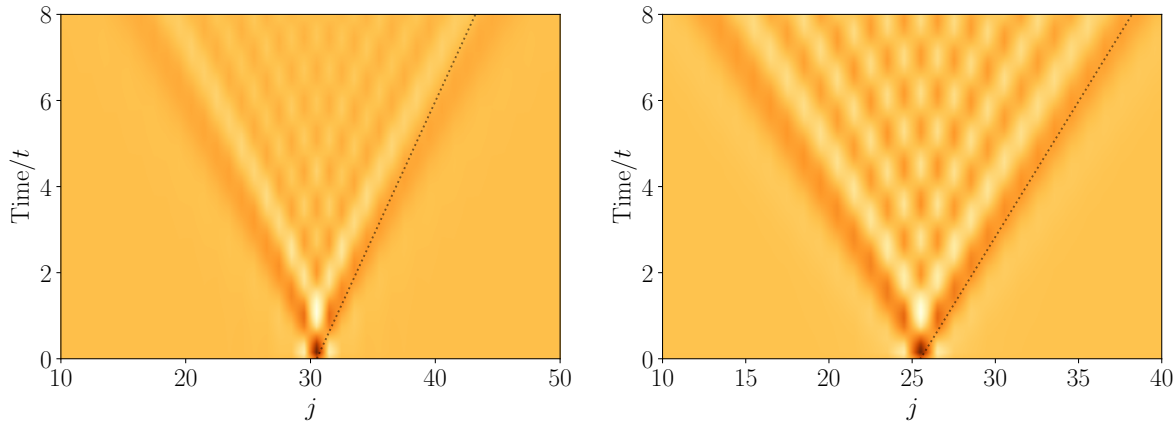


Figure 5.10: Characteristic examples of the space and time dependence of the correlation function $\langle \delta n_j(T) \delta n_0(T=0) \rangle$ in the GAS phase ($U/t = 20$, $V/t = -0.5$, $N = 30$, $N_s = 60$) for the left panel and in the LIQ phase ($U/t = 20$, $V/t = -1.4$, $N = 25$, $N_s = 50$) for the right panel. Dotted lines show the slope given by the speed of sound extracted from the static structure factor according to Eq. (5.44).

and a bond dimension $\chi = 800$. Since time evolution is not accurate at very long times, we employ the linear predictor to extrapolate our data to longer times (Pereira et al., 2008; Barthel et al., 2009), see App. B for details on the algorithm. Then, we use a Gaussian envelope to reduce numerical artifacts introduced by the linear predictor. In Fig. 5.10, we show typical time evolutions obtained in the gas and liquid phases for the full model with dipolar interaction Eq. (5.13). We observe the formation of a sound cone in our simulations denoting a notion of causality in the system. Moreover, the speed of sound decreases by increasing the strength of the dipolar interaction in absolute value pointing to a softening of the phononic mode.

Before presenting the numerical results of the dynamic structure factor we introduce an useful concept for obtaining analytical estimations of the dynamic structure factor: the sum rules. In particular, we present the sum rules for the Bose-Hubbard model which we name lattice sum rules, see (Roth and Burnett, 2004; Krutitsky, 2016) for a similar discussion. Sum rules are simply the frequency n -moments of the dynamic structure factor,

$$m_n(k) = \int d\omega S(k, \omega) \omega^n. \quad (5.22)$$

In particular, we focus on the relations between the plus one m_1 , zeroth m_0 and minus one moments m_{-1} . To compute these moments it is useful to express the dynamic structure factor using a Källén–Lehmann representation,

$$S(k, \omega) = \sum_m \langle 0 | \delta \hat{n}_{-k} | m \rangle \langle m | \delta \hat{n}_k | 0 \rangle \delta(\omega - (E_m - E_0)), \quad (5.23)$$

where we introduce the Fourier transform of the operator $\delta \hat{n}_j$, the set of eigenstates $|m\rangle$ and their

eigenenergies E_m . The Källén–Lehmann representation allows us to write the first moment as,

$$m_1(k) = \langle 0 | [\delta\hat{n}_{-k}, [\delta\hat{n}_k, \hat{H}]] | 0 \rangle = \frac{\epsilon(k)}{2} \sum_j \langle 0 | \hat{b}_j^\dagger \hat{b}_{j+1} + \hat{b}_{j+1}^\dagger \hat{b}_j | 0 \rangle, \quad (5.24)$$

where $\epsilon(k) = 4J \sin(ka/2)^2$ is the single-particle dispersion relation in the lattice. The zeroth moment is simply given by,

$$m_0(k) = \int d\omega S(k, \omega) = \langle 0 | \delta\hat{n}_{-k} \delta\hat{n}_k | 0 \rangle = NS(k), \quad (5.25)$$

where we introduce the static structure factor $S(k)$,

$$S(k) = 1 + n \sum_j e^{ikj} (g - 1), \quad (5.26)$$

related to the pair correlation function,

$$g = 1 + \frac{1}{n^2} \langle \delta n_i \delta n_j \rangle. \quad (5.27)$$

Finally, the minus one sum rule can be obtained by computing the linear response of the system to a constant chemical potential shift $\delta\mu$. The density response of the system is given by,

$$\frac{\delta n}{\delta\mu} = \chi(0, 0), \quad (5.28)$$

where we introduce the retarded propagator,

$$\chi(q, \nu) = \int d\nu S(k, \nu) \left[\frac{1}{w + \nu + i\epsilon} - \frac{1}{w - \nu + i\epsilon} \right]. \quad (5.29)$$

Leading to the relation,

$$\lim_{k \rightarrow 0} m_{-1}(k) = \frac{\delta n}{\delta\mu} \approx \frac{N^2 \kappa_s}{N_s 2}, \quad (5.30)$$

which is usually called compressibility sum rule. Therefore, Eqs. (5.24), (5.25) and (5.30) form the lattice sum rules and allow us to determine the behavior of the dynamic structure factor in terms of static properties. Assuming the energy spreading of the dynamic structure factor is small $\delta\omega = \omega_+ - \omega_- \ll \omega$ and the dynamic structure factor is almost constant in that interval gives,

$$S(k, \omega) \omega \delta\omega = N_s \langle \hat{b}_i^\dagger \hat{b}_{i+1} \rangle \epsilon(k), \quad (5.31)$$

$$S(k, \omega) \delta\omega = NS(k), \quad (5.32)$$

$$S(k, \omega) \frac{\delta\omega}{\omega} = \frac{N^2 \kappa_s}{N_s 2}. \quad (5.33)$$

The above relations allow us to extract two possible Feynman relations by either using the zeroth and

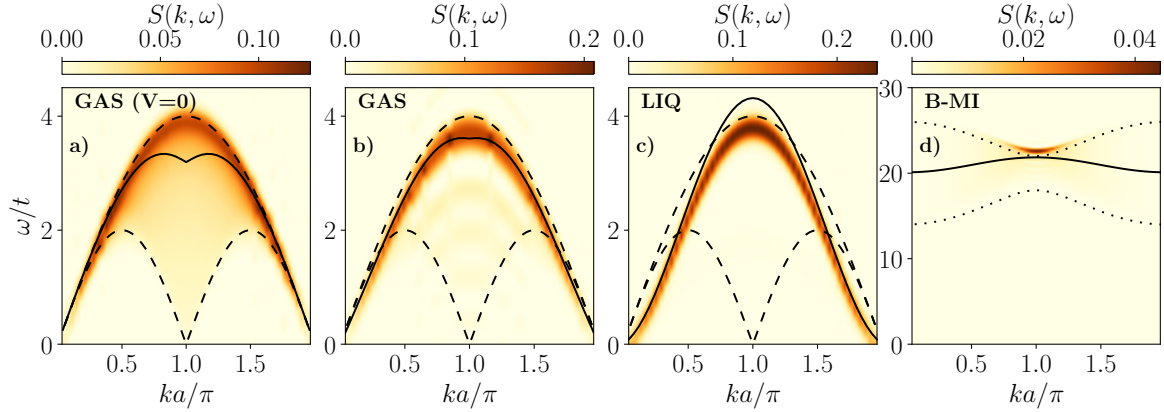


Figure 5.11: (a-d) Dynamic structure factor for (a) the GAS phase ($V/t = 0$, $U/t = 20$ and $n = 25/50$), (b) the GAS phase ($V/t = -0.5$, $U/t = 20$ and $n = 25/50$), (c) the LIQ phase ($V/t = -1.4$, $U/J = 20$ and $n = 25/50$) and (d) the B-MI phase ($V/t = -1.4$, $U/t = 20$ and $n = 50/50$). Upper and lower bounds to the excitation energies for $V/t = 0$ are obtained from Bethe ansatz Eq. (5.36) (dashed lines) for GAS and LIQ and from first-order perturbation theory Eq. (5.37) (dotted lines) for B-MI. Continuous lines represent the lattice Feynman relation Eq. (5.34).

plus one (f -sum rule) or zeroth and minus one (compressibility) sum rules,

$$\omega(k) = \frac{\langle \hat{b}_i^\dagger \hat{b}_{i+1} \rangle \epsilon(k)}{n S(k)}, \quad (5.34)$$

$$\omega(k) = \frac{2}{n\kappa_s} S(k). \quad (5.35)$$

The first one can be applied to either compressible and incompressible phases. While the second one assumes a finite compressibility. The two Feynman relations Eq. (5.34) and Eq. (5.35) provide an upper bound to the lower branch of the excitation spectrum $w_-(k)$. The bound becomes exact when excitations are exhausted by a single mode. It happens, for example, at low momenta in compressible phases where linear phonons are strongly populated, that is in the regime in which the Luttinger Liquid description applies. Moreover, it is important to remark that Eq. (5.35) is the lattice analogue of the original Feynman relation in continuum when a phononic branch appears at low momenta $w(k) = v_s k$.

In Figs. 5.11(a-d), we provide characteristic examples of $S(k, \omega)$ in different phases. At vanishing dipolar interaction the spectrum at half-filling is bounded by a lower and an upper branch representing spinon-like excitations, see dashed lines in Figs. 5.11(a-c). These ones can be obtained from the Bethe ansatz solution at $t/U = 0$ (des Cloizeaux and Pearson, 1962; Yamada, 1969),

$$w_+(k) = 4t \left| \sin\left(\frac{ka}{2}\right) \right|, \quad w_-(k) = 2t |\sin(ka)|. \quad (5.36)$$

However, the weight of the dynamic structure factor profoundly varies from that of a spinon-like spectrum (des Cloizeaux and Pearson, 1962; Yamada, 1969), in which modes are populated from the lower

(one-particle or -hole excitation) up to upper (two-particle excitation) branches. The presence of a finite but large on-site interaction $U/t \gg 1$ and an attractive dipolar interaction strongly affect the excitations, creating a dominant mode located close to the upper branch. Such a behavior is typical of systems that are softer than the TG gas and possess larger values of the Luttinger parameter, $K > 1$ (Caux and Calabrese, 2006). In particular, the dynamic structure factor is completely exhausted by a single-mode in the LIQ phase, see Fig. 5.11 panel c). This validates the use of the lattice Feynman relation Eq. (5.34), see continuous lines. Moreover, the GAS and LIQ phases are characterized by a phononic branch at low momenta which is also captured by the lattice Feynman relation Eq. (5.34). Importantly, the attractive dipolar interaction strongly affects the energy of the low momentum excitations of the system and it leads to a softening of the phononic branch. However, the energy of the high momentum excitations is almost not altered by the attractive dipolar interaction. Therefore, we conclude that, although the attractive dipolar interaction affects the low- k or long-distance physics it does not alter the high- k or short-distance physics. The decoupling of scales supports the validity of the perturbative theory introduced in Sec. 5.1 and Sec. 5.2 where the local correlations are of TG type regardless of the dipolar interaction.

The structure of excitations differs dramatically in the B-MI phase, wherein a gap Δ opens, see Fig. 5.11 panel d). In absence of dipolar interactions, the upper and lower bounds are no longer given by one- or two-particle excitations but rather by doublon-holon excitations. Using first-order perturbation theory the lower and upper bounds of the excitation spectrum in the insulating phase are given by (Iucci et al., 2006; Tokuno and Giamarchi, 2011; Ejima et al., 2012a,b),

$$w_{\pm}(k) = U \pm 2t\sqrt{5 + 4\cos(ka)}, \quad (5.37)$$

which capture well the bound of the excitation spectrum even in presence of a dipolar interaction $|V| \sim t$. However, we observe that the attractive dipolar interaction enhances the weight of the upper branch. The dependence of the dynamic structure factor with momentum can be obtained by employing the lattice sum rules. By using Eq. (5.31) in the B-MI phase $\omega(k) \sim \Delta$, we obtain,

$$S(k, \omega) \sim N_s \frac{\langle \hat{b}_i^\dagger \hat{b}_{i+1} \rangle}{\delta w \Delta} \epsilon(k). \quad (5.38)$$

Moreover, in the gapped phase, the kinetic energy can be estimated $\langle \hat{b}_i^\dagger \hat{b}_{i+1} \rangle \sim n(n+1)/\Delta$ giving,

$$S(k, \omega) \sim \frac{N_s n(n+1)}{\Delta^2} \frac{\sin^2\left(\frac{ka}{2}\right)}{\sqrt{5 + 4\cos(ka)}}. \quad (5.39)$$

Therefore, we infer that the spectral weight vanishes at small momenta, $S(k, \Delta) \propto k^2$ for $k \rightarrow 0$. Instead, the edge of the Brillouin zone, $k_{BZ} = \pi/a$, gets strongly populated, and a sharp peak is formed in $S(k_{BZ}, \omega)$ so that the lattice Feynman relation Eq. (5.34) captures well the value of the gap. This result is compatible with our numerical results, see Fig. 5.11 panel d).

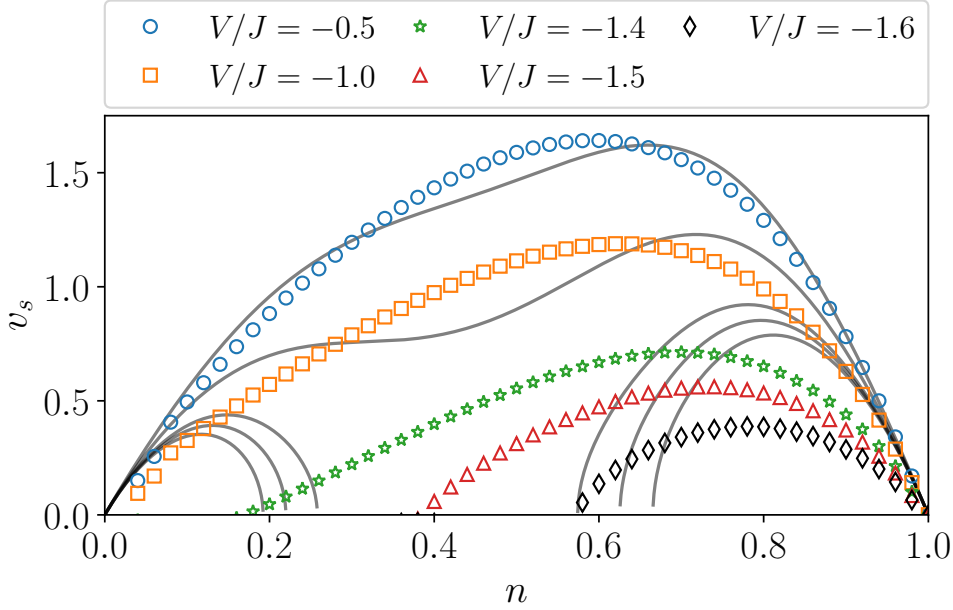


Figure 5.12: Speed of sound as a function of the density for different values of V/t and a fixed $U/t = 20$. Symbols from lattice Feynman relation, see the main text; lines from perturbative results; black diamonds extracted from the dynamic structure factor.

5.5.2 Speed of sound

Having studied the dynamic structure factor in the three phases, we focus now on the speed of sound. The presence of a lattice has strong consequences on sound propagation (Cazalilla, 2004a,b) and other transport properties (Anderson et al., 2019), as can be traced to the loss of Galilean invariance in the lattice. Galilean invariance does not hold for the BH model since the particle current is not a conserved quantity in any two-particle collision even though the total quasi-momentum is conserved. This produces a non-trivial dependence of the sound on the density. To obtain the speed of sound v_s , we employ the lattice Feynman relation Eq. (5.35) applicable for small momenta as we have shown. In Fig. 5.12 panel d), we present the sound velocity as a function of the density for different values of the long-range coupling. For weak dipolar attraction, the speed of sound decreases above half-filling and reaches zero at unit filling, signaling the transition to a MI state. As the dipolar strength increases, a liquid state forms, and the sound velocity also vanishes at spinodal density $n_s \leq 1$. Finally, when approaching the B-MI phase, the sound velocity nears zero for any value of density showing no stable homogeneous solution exists for $|V| > |V_{\text{B-MI}}|$.

For an analytical estimation of the speed of sound, we employ the non-Galilean invariant Luttinger liquid theory (Cazalilla, 2004a,b). The lack of Galilean invariance implies that the low-energy Luttinger theory cannot be described by a single parameter but rather needs two distinct phenomenologic parameters (Cazalilla, 2004a,b). These two parameters can be introduced by measuring the response

of the system to a change in particle number and to a phase shift,

$$v_N = \frac{N_s a}{\pi} \frac{\partial^2 E}{\partial N^2} \Big|_{N=N_0}, \quad v_J = \pi N_s a \frac{\partial^2 E}{\partial \phi^2} \Big|_{\phi=0}. \quad (5.40)$$

Notice that for a Galilean invariant system, one parameter is immediately reduced to the Fermi velocity $v_J = v_F$, which is fully fixed by the linear density $v_F = \pi n$. In that case, the low-energy properties are entirely characterized by the adiabatic compressibility. Instead, for a lattice system, one has to compute both parameters in a microscopic calculation. The low-energy properties of the fluid can be expressed in terms of these parameters,

$$K = \sqrt{\frac{v_J}{v_N}}, \quad v_s = \sqrt{v_J v_N}, \quad (5.41)$$

v_s being the speed of sound of the low-energy phonons and K the Luttinger parameter determining the long-range correlations in the fluid. The velocity v_N is inversely proportional to the compressibility of the system showing that the more incompressible the fluid, the larger the velocity v_N . On the other hand, the speed of sound v_s is also affected by the response to phase fluctuations and both v_J and v_N have an effect on it. This has to be contrasted with the continuum Galilean invariant system where one has a direct relationship between compressibility and the speed of sound. Namely, when a system becomes less compressible, its speed of sound increases. Let us also remark that non-Galilean Luttinger liquid theory can be employed to derive the lattice Feynman relation Eq. (5.35). By using the thermodynamic relation for the compressibility κ and using Eq. (5.41), we obtain the following relations,

$$\kappa_s^{-1} = n^2 \frac{\partial \mu}{\partial n} = \pi v_N n^2 = \frac{\pi v_s n^2}{K}, \quad (5.42)$$

between the inverse compressibility κ_s^{-1} , the speed of sound v_s and the Luttinger parameter K . By inserting these relations into the low-momentum expansion of the static structure factor,

$$S(k) = \frac{K}{2n\pi} k, \quad |k| \rightarrow 0. \quad (5.43)$$

we obtain,

$$S(k) = \frac{\kappa_s v_s n}{2} k, \quad (5.44)$$

which is nothing else than the second lattice Feynman relation Eq. (5.35) derived using lattice sum rules.

By employing our perturbative theory developed in Sec. 5.4 we compute the density and phase response of the system. The compressibility can already be computed from Eq. (5.16) leading to the density response,

$$v_N = 2J \sin(\pi n) + \frac{8J^2}{\pi U} (\cos(2\pi n) - n \sin(2\pi n) - 1) + \frac{V}{\pi} [2\xi(3) + \text{Li}_3(e^{-2i\pi n}) + \text{Li}_3(e^{2i\pi n})]. \quad (5.45)$$

To compute the response to phase fluctuations, we also performed a perturbative calculation imposing

twisted boundary conditions $\hat{c}_{i+N_s} = e^{i\phi}\hat{c}_i$. In the thermodynamic limit, this leads to a phase shift in the correlation function $\langle \hat{c}_i^\dagger \hat{c}_j \rangle = e^{i\phi|i-j|/N_s} \sin(k_F|i-j|)/(\pi|i-j|)$. By employing Wick's theorem, we can again obtain perturbatively the dependence of the energy on the phase ϕ . After some manipulations, the phase response is given by,

$$v_J = 2J \sin(\pi n) + \frac{8J^2}{\pi U} [2 \sin^2(\pi n) - \pi n \sin(2\pi n)] \quad (5.46)$$

In our perturbative calculation, we observe that the dipolar interaction does not lead to any modification of the phase response v_J .

Combining our calculations, we are able to perturbatively calculate the speed of sound,

$$v_s = 2J \sin(\pi n) - \frac{16J^2}{U} n \sin(\pi n) \cos(\pi n) + \frac{V}{2\pi} [2\xi(3) + \text{Li}_3(e^{-2i\pi n}) + \text{Li}_3(e^{2i\pi n})]. \quad (5.47)$$

For weak dipolar attraction, we note an agreement between the perturbative theory and exact numerical analysis, see Fig. 5.12. For the increased strength of attraction, the analytical approach predicts the appearance of a spinodal point, albeit at an incorrect density value. Additionally, we report a qualitative difference at small densities where perturbative theory predicts a finite value of the speed of sound, in stark contrast with numerical results where no stable homogeneous solution exists for $n \leq n_s$. We associate this discrepancy with the formation of molecules at small densities, which is overlooked in the perturbative description.

5.6 Conclusions and outlook

In this chapter we have shown an unconventional mechanism for liquid formation in strongly correlated one-dimensional lattice systems. Specifically, liquefaction arises due to an interplay between non-local attraction and the superexchange processes originating from short-range repulsion. Our work presents a non-trivial extension of the quantum van der Waals theory to lattice systems described by one-dimensional extended BH Hamiltonians. We have presented the equilibrium and non-equilibrium properties of the system. Moreover, we have shown that non-equilibrium probes reveal relevant information about the nature of excitations of the different quantum fluids which could be ultimately employed to determine the quantum phase of the system. Extended BH Hamiltonians could be realized experimentally in different ultracold atomic platforms like dipolar bosons (Kao et al., 2021; Natale et al., 2022), Rydberg atoms (Labuhn et al., 2016; Browaeys and Lahaye, 2020) or even excitonic systems (Lagoïn et al., 2022). Recently, one-dimensional dipolar bosonic systems were produced experimentally (Kao et al., 2021) and loaded into corresponding optical lattices (Natale et al., 2022). Interestingly, our predictions can be easily extended to fermionic systems with attractive dipolar interactions, which could pave the way for the production of fully polarized fermionic droplets. In that direction it would be interesting to improve our perturbative theory by making it self-consistent and see if it can predict the appearance of a liquid phase for fermionic particles with an attractive dipolar interaction.

Chapter 6

UNIVERSALITY OF QUANTUM FLUIDS IN ONE DIMENSION

In previous chapters we investigate the physics of 1D quantum fluids focusing on the description of quantum liquids. We study different physical realizations including bosonic mixtures and dipolar systems, that can be produced in ultracold atomic laboratories. Therefore, making them promising platforms to realize highly controllable strongly interacting droplets and liquids. Furthermore, we note that, despite considering very different physical systems, similar phenomena can be obtained. As explained in Chapter 2 one of the marvels of cold atoms systems is the universal low-energy description that is independent of the short-distance details of the relevant interactions (Bloch et al., 2008). This situation must be contrasted with that of the only other known quantum liquid observed so far, liquid helium. With traditional quantum helium, interatomic potentials that reproduce essentially all of the experimental measurable properties are known accurately (Kunitski et al., 2021). In deep contrast, the underlying interactions in ultracold atomic systems are highly dependent on the particular atomic species and are subject to magnetic Feshbach resonances (Inouye et al., 1998; Courteille et al., 1998; Chin et al., 2010) and confinement-induced resonances (Olshanii, 1998; Bergeman et al., 2003; Astrakharchik et al., 2004). Hence, it is impractical, if not impossible, to attempt as accurate a description as in liquid helium for each realization of an ultracold atomic liquid. Therefore, a universal low-energy description of these systems, within the effective field theory (EFT) paradigm (Bedaque and van Kolck, 2002; Hammer et al., 2013), is highly desirable. In particular, in this chapter we try to establish an equivalence between quantum liquids described only by two-body forces and quantum liquids described by three-body forces. This equivalence has long been the subject of debate in the nuclear and atomic physics community (Hammer et al., 2013).

Three-body interactions are always present in a many-atom system, and can be genuine or emergent from the off-shell structure of the two-body interactions (Valiente, 2019; Pricoupenko and Petrov, 2021; Hammer et al., 2013). In general, these are a combination of genuine and emergent. For repulsive one-dimensional systems, two-body effective range (on-shell) effects are typically negligible

for low densities (Astrakharchik et al., 2010). However, the effects of a non-zero physical range (off-shell) are important for three-body processes, especially for large scattering lengths (Valiente, 2019; Pricoupenko and Petrov, 2021), which can be rigorously modelled by simple three-body forces. This can also be explained qualitatively using field redefinitions (Hammer et al., 2013) that trade off-shell low-energy interactions in favour of simpler, on-shell three-particle forces. Since, in this case, the low-energy two- and three-body amplitudes are essentially identical, the S -matrix formulation of statistical mechanics (Dashen et al., 1969) implies thermodynamic equivalence in the gas phase. At zero temperature this is the case for overall repulsive interactions. However, when a quantum phase transition from a gas to a liquid phase occurs the results of Ref. (Dashen et al., 1969) do not apply and, as we shall see, there is no such equivalence.

In this chapter, we investigate the zero temperature universality of one-dimensional quantum fluids including quantum gases, liquids and droplets. We investigate two low-energy theories: One includes a zero-range two-body interaction as well as an effective range and the other one features zero-range two- and three-body interactions. In Sec. 6.1 we present the two low-energy theories and the procedure to match the coupling constants between them, such that few-body properties are equivalent. Then, in Sec. 6.2 we develop highly non-perturbative, analytical approximations to describe the quantum liquid phase present in the low-energy theory with two- and three-body interactions. Then, we move to investigate the universality of both theories. In Sec. 6.3 we show that the EoS in the quantum gas phase is equivalent for both low-energy theories after matching the coupling strengths. However, we demonstrate the non-universality of phases with overall attraction. In Sec. 6.4 we show that the quantum droplet profiles differ between the two theories even though presenting the same energy per particle. We find universality in the long-distance asymptotics of the droplet tails. In Sec. 6.5 we demonstrate the non-universality of the EoS in the quantum liquid phase. Finally, in Sec. 6.6 we present our conclusions and outlook.

6.1 Effective low-energy theories

The effective low-energy theories that are investigated in this chapter correspond to,

$$\hat{H}_c^{3B} = \int dx - \frac{\hbar^2}{2m} \hat{\phi}^\dagger(x) \partial_x^2 \hat{\phi}(x) + \frac{g_0}{2} \hat{\phi}^\dagger(x)^2 \hat{\phi}(x)^2 + \frac{g_3}{6} \hat{\phi}^\dagger(x)^3 \hat{\phi}(x)^3, \quad (6.1)$$

$$\hat{H}_c^{NL} = \int dx - \frac{\hbar^2}{2m} \hat{\phi}^\dagger(x) \partial_x^2 \hat{\phi}(x) + \frac{g'_0}{2} \hat{\phi}^\dagger(x)^2 \hat{\phi}(x)^2 - g_2 \hat{\rho}(x) \partial_x^2 \hat{\rho}(x). \quad (6.2)$$

where m is the mass of the particles, $g_0 = -2\hbar^2/ma_s$ and $g'_0 = -2\hbar^2/ma'_s$ are the Lieb-Liniger coupling constants, with a_s and a'_s the respective scattering lengths, g_3 is the bare three-body coupling constant and g_2 sets the effective range. We introduce the bosonic annihilation (creation) field operator $\hat{\phi}$ ($\hat{\phi}^\dagger$) and the density operator $\hat{\rho}(x) = \hat{\phi}^\dagger(x)\hat{\phi}(x)$. The low-energy theory Eq. (6.1) includes two- and three-body zero-range interactions. However, the low-energy theory Eq. (6.2) only includes two-body interactions but they present a finite range term. The coupling constants of the zero-range two-body interaction are chosen to be different in the two theories ($g_0 \neq g'_0$). This freedom will allow us to

ensure that the on-shell amplitudes in the two-body sector coincide, to a very good approximation, in both theories.

To study the equivalence between the two low-energy theories Eq. (6.1) and Eq. (6.2) we first need to define a procedure to match the coupling strengths such that the respective ground state energies agree well with each other. In this section we explain the details of such procedure.

6.1.1 Discretization of the continuum models

First of all, we perform a direct discretization of the low-energy theories (6.1) and (6.2) resulting in the following generalized Bose-Hubbard Hamiltonians,

$$\hat{H}_d^{3B} = -J \sum_j (\hat{b}_{j+1}^\dagger \hat{b}_j + \text{H.c.}) + \frac{U_2}{2} \sum_j \hat{n}_j (\hat{n}_j - 1) + \frac{W}{6} \sum_j \hat{n}_j (\hat{n}_j - 1) (\hat{n}_j - 2) + 2J \sum_j \hat{n}_j, \quad (6.3)$$

$$\hat{H}_d^{NL} = -J \sum_j (\hat{b}_{j+1}^\dagger \hat{b}_j + \text{H.c.}) + \frac{U}{2} \sum_j \hat{n}_j (\hat{n}_j - 1) + V \sum_j \hat{n}_j \hat{n}_{j+1} + 2J \sum_j \hat{n}_j, \quad (6.4)$$

where we introduce the hopping strength $J = \hbar^2/(2ma^2)$, with a the lattice spacing, the on-site two-body interaction strengths $U_2 = g_0/a$ and $U = g'_0/a + 2g_2/a^3$, three-body coupling constant $W > 0$ that has to be determined and the coupling $V = -g_2/a^3$ that sets the off-shell part of the two-body interaction in the discretized model. Moreover, the discretized bosonic operator $\hat{b}_j = a\hat{\phi}(ja)$ ($\hat{b}_j^\dagger = a\hat{\phi}^\dagger(ja)$) annihilates (creates) a boson at site $j \in \mathbb{Z}$, and $\hat{n}_j = \hat{b}_j^\dagger \hat{b}_j$ is the local number operator.

The discrete theories Eq. (6.3) and Eq. (6.4) can be employed to simulate the low-energy theories Eq. (6.1) and Eq. (6.2) by matching the low-energy scattering properties (Valiente and Zimmer, 2015; Valiente, 2018). The low-energy two-body collisions are described by the respective scattering lengths,

$$\frac{a_s}{a} = \frac{4J}{U_2}, \quad \frac{a'_s}{a} = -\frac{UV - 4J(2J - V)}{UV + 2J(U + 2V)}, \quad (6.5)$$

which set the binding energy of shallow two-body bound states when the scattering lengths are much larger than the effective ranges.

We show now that the discrete theory Eq. (6.3) can be faithfully employed to simulate the continuum three-body theory Eq. (6.1). To show this equivalence in the three-body sector we need first to explain the main features of the three-body problem in one spatial dimension. This problem has been recently solved in (Pastukhov, 2019; Valiente, 2019; Valiente and Pastukhov, 2019; Valiente, 2021, 2020; Sekino and Nishida, 2018; Hou and Drut, 2020; Czejdo et al., 2020; Hou et al., 2019; Drut et al., 2018; Pricoupenko and Petrov, 2019, 2021; Guijarro et al., 2018; Nishida, 2018; Pricoupenko, 2018, 2019). To establish an explicit analytical relation between the continuum and discrete theory we focus on the situation where the two-body interaction is absent and we have a system interacting with pure three-body interactions. The three-body T -matrix for the low-energy theory Eq. (6.1) is defined as,

$$\langle k'_1, k'_2, k'_3 | \hat{T}_3(z) | k_1, k_2, k_3 \rangle = 2\pi\delta(K - K')t_3(z), \quad (6.6)$$

where $z = E + i\epsilon$ is the complex collision energy, $K = k_1 + k_2 + k_3$ and $K' = k'_1 + k'_2 + k'_3$ are the total incoming and outgoing momentum. When no two-body interactions are present we do not need a Faddeev decomposition and the Lippmann-Schwinger equation can be directly employed to obtain the three-body amplitude at null total momentum (Valiente, 2019; Valiente and Pastukhov, 2019),

$$t_3(z) = \frac{1}{\frac{1}{g_3} - \mathcal{I}(z)}, \quad \text{with,} \quad \mathcal{I}(z) = -\frac{m}{2\pi\sqrt{3}\hbar^2} \left(\ln \left| \frac{\Lambda^2}{2mE/\hbar^2} \right| + i\pi \right), \quad (6.7)$$

where a UV-cutoff Λ is introduced. The renormalization of the bare three-body coupling constant can be obtained by locating the position of the three-body amplitude pole denoting the appearance of a bound state with energy $E_B = -|E| = \hbar^2 Q_*^2/2m$ in the attractive case (Valiente and Pastukhov, 2019),

$$\frac{1}{g_3(\Lambda)} = \frac{m}{\sqrt{3}\pi\hbar^2} \ln \left| \frac{Q_*}{\Lambda} \right|, \quad (6.8)$$

making the three-body amplitude finite and cutoff independent,

$$t_3(-|E|) = \frac{2\sqrt{3}\pi\hbar^2/m}{\ln |\hbar^2 Q_*^2/2mE| + i\pi}. \quad (6.9)$$

The relation between the momentum scale Q_* and the three-body scattering length a_3 can be obtained by comparing the binding energy obtained in (Guijarro et al., 2018) $E_B = -4e^{-2\gamma}\hbar^2/ma_3^2$, leading to the relation,

$$(Q_* a_3)^2 = 8\sqrt{2}e^{-2\gamma}, \quad (6.10)$$

where γ is the Euler's gamma constant. Let us remark that even in the repulsive case a bound state appears in the system as can be seen in Eq. (6.7). Even though the bare three-body coupling constant is repulsive at low-energies, attractive logarithmic quantum corrections dominate the behavior of the scattering amplitude at high energies. However, the position of the bound state $E_B = -|E|$ coincides with the position of the Landau pole at which the three-body coupling constant diverges. Therefore, such state appears to be unphysical since lies in the energy range where the low-energy effective description should break down (Valiente, 2019) as happens in the repulsive 2D case (Beane, 2010, 2018).

To relate the three-body coupling constant W to the three-body scale Q_* , we need to solve the lattice three-body problem in the absence of two-body interactions ($U_2 = 0$). Setting the total momentum to zero, the lattice three-body amplitude $t_3^l(z)$ is given by,

$$t_3^l(z) = \frac{a^2}{W^{-1} - \mathcal{I}(z)}, \quad \text{with,} \quad \mathcal{I}(z) = \frac{1}{(2\pi)^2} \int_{\text{BZ}} d^2k \frac{1}{z - \epsilon(k_1, k_2, k_1 + k_2)}, \quad (6.11)$$

where $\epsilon(k_1, k_2, k_3) = -2J \sum_{i=1}^3 \cos(k_i a) + 6J$ and $\text{BZ} = [-\pi/a, \pi/a) \times [\pi/a, \pi/a)$. The lattice problem exhibits a bound state for attractive three-body interaction $W < 0$. The bound state energy can be

obtained by locating the pole position of the lattice three-body amplitude,

$$\frac{1}{W} = \frac{1}{(2\pi)^2} \int_{\text{BZ}} d^2k \frac{1}{E - \epsilon(k_1, k_2, k_1 + k_2)}, \quad (6.12)$$

which in the weakly-interacting limit $W/J \rightarrow 0^-$ leads to an exponential small binding energy $E_B = -|E|$ (Sekino and Nishida, 2018),

$$E_B/J \approx -72e^{-4\sqrt{3}\pi J/|W|}. \quad (6.13)$$

The analogy of W with the momentum scale Q_* in the continuum limit can be drawn by matching the exponential small binding energy of the lattice theory with the continuum one, leading to the relation,

$$\frac{W}{J} = \frac{2\sqrt{3}\pi}{\ln|Q_*d| + \frac{1}{2}\ln(72)}, \quad (6.14)$$

Therefore, the discretized version of the three-body low-energy theory Eq. (6.3) can be used to simulate a continuum repulsive three-body force – thereby avoiding unphysical bound states – at low densities with a finite lattice spacing, provided that $W/J > 0$, i.e., for $|Q_*d| > 6\sqrt{2} \approx 8.5$. These values correspond to the weak to moderate coupling regime for the three-body interaction (Pastukhov, 2019; Valiente, 2019; Valiente and Pastukhov, 2019; Valiente, 2021, 2020; Sekino and Nishida, 2018; Hou and Drut, 2020; Czejdo et al., 2020; Hou et al., 2019; Drut et al., 2018; Pricoupenko and Petrov, 2019, 2021; Guijarro et al., 2018; Nishida, 2018; Pricoupenko, 2018, 2019).

6.1.2 Setting the coupling strengths

The discretized low-energy theories (6.3) and (6.4) allow us to numerically obtain the ground-state of the respective Hamiltonians by performing DMRG simulations. To match the low-energy N -body amplitudes of both models we consider the finite-size ground state energy of their respective Hamiltonians. Given the parameters (U, V) of Hamiltonian (6.4) we adjust the parameters (U_2, W) of Hamiltonian (6.3) to find the best match between the corresponding energies of both models for $2 \leq N \leq 6$, a well-established method in lattice and finite-size simulations (Lüscher, 1986a; Valiente, 2019). With (U, V) fixed, we increase the particle number N , and calculate the ground state N -boson ($3 \leq N \leq 6$) binding energies for Hamiltonians (6.3) and (6.4) in a large box with open boundary conditions using the DMRG algorithm. We first set U_2 given the couplings (U, V) by matching the two-body binding energies of both Hamiltonians. Then, we calculate W such that the ground state energies with $3 \leq N \leq 6$, for Hamiltonian (6.3), best match (in mean-squared error) those of Hamiltonian (6.4). In Fig. 6.1 left panel, we plot the calculated W/J as a function of U_2/J for $V/J = -1.6$ and varying U/J , corresponding to the values of U_2/J in the abscissa as explained above. The small relative errors obtained for W/J indicate that the procedure is robust and the best fit of W/J does not significantly change for varying particle number. This conclusion is further strengthened by comparing N -body binding energies for the two models with corresponding parameters as has just been discussed. In Fig. 6.1 right panel, we clearly observe excellent agreement in the N -body binding energies for large

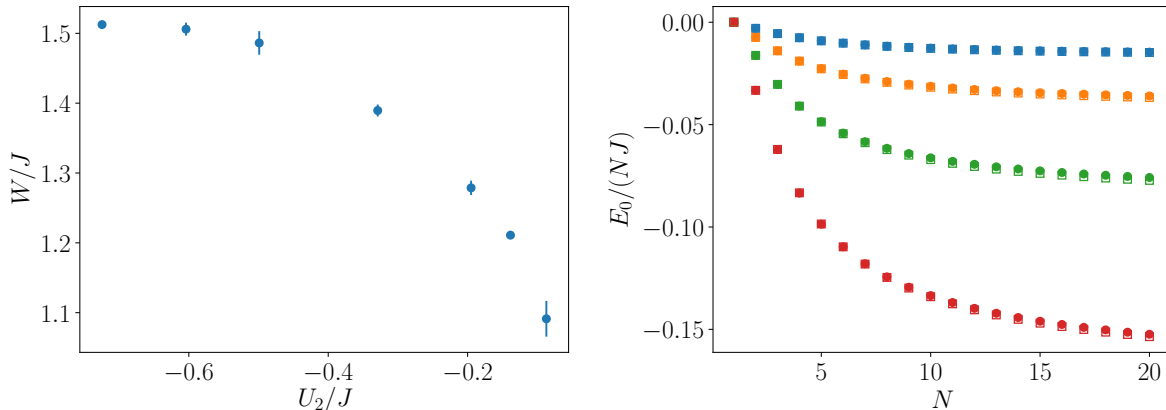


Figure 6.1: Left panel: calculated value of the lattice three-body coupling W/J as a function of the two-body coupling U_2/J in Hamiltonian (6.3) to match the results for Hamiltonian (6.4) with $V/J = -8/5$ and varying U/J . Right panel: ground state energy per particle of Hamiltonian (6.4) (open squares), with $V/J = -8/5$ and varying U/J , and of Hamiltonian (6.3) (filled dots). From top to bottom, $U/J = 12, 10, 8, 6$, and $(U_2/J, W/J) = (-0.2, 1.28), (-0.33, 1.40), (-0.5, 1.49)$ and $(-0.73, 1.51)$. In both panels the size of the system is $L/a = 100$ and the bond dimension of DMRG simulations corresponds to $\chi = 256$.

N , especially for large scattering lengths (small binding energies). All binding energies agree within 2%.

6.2 Quantum gases and liquids with three-body interactions

Before studying the universality of the quantum fluids described by the two models with Hamiltonian (6.1) and Hamiltonian (6.2), we present two different non-perturbative theories explaining the formation of quantum liquids in a system with attractive two-body forces $g_0 < 0$ and repulsive three-body ones $g_3 > 0$. The original idea of creating a quantum liquid from the compensation of two- and three-body forces was proposed in (Bulgac, 2002), where a restricted mean-field theory was employed, which we review here. A mean-field decoupling in the dilute limit at fixed density ρ leads to the energy per particle,

$$e(\rho) = \frac{1}{2}g_0\rho + \frac{1}{6}g_3\rho^2. \quad (6.15)$$

The energy per particle presents a minimum at a finite density ρ_{eq} defining the equilibrium point. The equilibrium energy e_{eq} and equilibrium density ρ_{eq} are given by,

$$e_{\text{eq}} = -\frac{3}{8}\frac{g_0^2}{g_3}, \quad \rho_{\text{eq}} = -\frac{3}{2}\frac{g_0}{g_3}, \quad (6.16)$$

and therefore, one can obtain an equilibrium relation not involving the three-body coupling constant,

$$e_{\text{eq}} = \frac{1}{4}g_0\rho_{\text{eq}}. \quad (6.17)$$

As we show in Sec. 6.2.1 and Sec. 6.2.2 mean-field equilibrium relations do not correctly describe the many-body liquid phase and non-perturbative effects must be taken into account to capture the properties of the quantum liquid.

6.2.1 Self-consistent decoupling

To show the appearance of quantum liquids beyond the restricted mean-field theory we present a self-consistent decoupling solution of the N -boson problem with an attractive two-body interaction and a repulsive three-body one. The Hamiltonian in first quantization becomes,

$$H = -\frac{\hbar^2}{2m} \sum_i \nabla_i^2 + g_0 \sum_{i<j} \delta(x_i - x_j) + g_3 \sum_{i<j<k} \delta(x_i - x_j)\delta(x_j - x_k). \quad (6.18)$$

Our decoupling approximation consists of decomposing the three-body interaction into a state-dependent two-body interaction by replacing the two delta product as,

$$\delta(x_i - x_j)\delta(x_j - x_k) \approx \Gamma\delta(x_i - x_j) + \Gamma\delta(x_j - x_k) + \Gamma\delta(x_i - x_k) - 2\Gamma^2, \quad (6.19)$$

where we assume N -identical bosons such that $\Gamma = \langle \delta(x_i - x_j) \rangle = \langle \delta(x_{i'} - x_{j'}) \rangle$, for all $i \neq j$ and $i' \neq j'$. The decoupling Eq. (6.19) leads to the effective Hamiltonian,

$$H = -\frac{\hbar^2}{2m} \sum_i \nabla_i^2 + G_N \sum_{i<j} \delta(x_i - x_j) + C_N, \quad (6.20)$$

with coupling constant $G_N = g_0 + (N-2)g_3\Gamma$ and $C_N = -\Gamma^2 g_3 N(N-1)(N-2)/3$. The Hamiltonian (6.20) corresponds to the Lieb-Liniger model (Lieb and Liniger, 1963) with coupling constant $G_N(\Gamma)$ and an energy shift C_N . The Lieb-Liniger model is an integrable system and an exact solution was provided by MacGuire (McGuire, 1966) in the attractive case $G_N < 0$. The ground state energy $E_0(N)$ is given by,

$$E_0(N) = -\frac{mG_N^2}{24\hbar^2} N(N+1)(N-1) + C_N(\Gamma). \quad (6.21)$$

To self-consistently obtain Γ we can employ the celebrated Hellmann-Feynman theorem,

$$G_N = -|g_0| \left[1 - \frac{1}{1 + \frac{6\hbar^2}{mg_3} [(N+1)(N-2)]^{-1}} \right], \quad (6.22)$$

$$\Gamma = -\frac{mG_N}{6\hbar^2} (N+1). \quad (6.23)$$

Therefore, in the large particle number limit $N \rightarrow \infty$ the effective coupling constant G_N and the expectation value Γ decay as,

$$G_N \approx -\frac{6\hbar^2|g_0|}{mg_3} \frac{1}{N^2}, \quad (6.24)$$

$$\Gamma \approx \frac{|g_0|}{g_3} \frac{1}{N}. \quad (6.25)$$

To understand the nature of the ground state described by Hamiltonian (6.20) we compute the density profile $\rho_N(x)$. As described in (Calogero and Degasperis, 1975), the translational invariant N -particle symmetric ground state wavefunction is given by,

$$\psi_N = C_N \exp\left(\frac{mG_N}{2\hbar^2} \sum_{i < j} |x_i - x_j|\right), \quad (6.26)$$

with $|C_N| = N! \sqrt{(N-1)!(mG_N/\hbar^2)^{N-1}}$. The density profile $\rho(x)$ is measured respect to the position of the center of mass,

$$\rho_N(x) = \int dx_1 \dots dx_N \delta(X_N) \delta(x_N - x) |\psi_N|^2, \quad \text{with,} \quad X_N = \frac{1}{N} \sum_{i=1}^N x_i. \quad (6.27)$$

After an explicit evaluation of the multi-dimensional integral, see (Calogero and Degasperis, 1975), we obtain the density profile,

$$\rho_N(x) = -\frac{mG_N}{\hbar^2} \sum_{n=1}^{N-1} (-1)^{n+1} \frac{n(N!)^2}{(N+n-1)!(N-n-1)!} e^{mG_N n |x|/\hbar^2}. \quad (6.28)$$

The density profile Eq. (6.28) exhibits a solitonic shape for small number of particles and saturates to a droplet shape at large number of particles. To understand the saturation of the density profile we compute the density profile at the center of mass position $x = 0$,

$$\rho_N(0) = -\frac{mG_N}{2\hbar^2} N^2 \frac{N-1}{2N-3}, \quad (6.29)$$

which saturates to a constant in the large particle number limit defining the equilibrium density ρ_0 ,

$$\lim_{N \rightarrow \infty} \rho_N(0) = \frac{3}{2} \frac{|g_0|}{g_3} \equiv \rho_{\text{eq}}. \quad (6.30)$$

The saturation of the density profile is a consequence of the particle number scaling of the effective coupling constant, see Eq. (6.24). While the MacGuire's soliton does not have a well defined thermodynamic limit, the self-consistent solution of the coupling constant G_N makes the state well defined in the thermodynamic limit and a quantum liquid appears with an equilibrium energy,

$$e_{\text{eq}} \equiv \lim_{N \rightarrow \infty} \frac{E_0(N)}{N} = -\frac{|g_0|^2}{3g_3}. \quad (6.31)$$

Interestingly, the thermodynamic equilibrium energy comes from the energy shift C_N of the effective Hamiltonian (6.20).

The predictive power of the self-consistent decoupling approximation is limited since the three-body coupling constant g_3 ceases to be a bare coupling constant and it depends on the state of the system. However, the self-consistent decoupling approximation leads to,

$$e_{\text{eq}} = \frac{2}{9}g_0\rho_{\text{eq}}. \quad (6.32)$$

Our theory, although approximate, is highly non-perturbative. It predicts a strongly constrained, linear relation between the equilibrium energy per particle and density for fixed two-body interaction strength $g_0 < 0$. This relation resembles the mean-field equilibrium relation Eq. (6.17) but the numerical factor is different. In Sec. 6.5 we employ the DMRG algorithm to obtain the equilibrium density and energy and show that relation Eq. (6.32) is in excellent agreement with the numerical results.

6.2.2 Improved mean-field theory

Even though our self-consistent decoupling theory is able to predict the existence of a liquid phase and the constrained Eq. (6.32), it does not have a predictive power for the EoS of the quantum liquid. To gain some analytical insight into the EoS with two- and three-body interactions, we present an improved version of the mean-field theory (iMF), by allowing the three-body coupling constant g_3 to depend logarithmically on the density,

$$g_3(\rho) = \frac{g_3^{\text{eq}}}{\lambda \ln \left| \frac{\rho}{\rho_{\text{eq}}} \right| + 1}, \quad (6.33)$$

so that it can account for the logarithmic anomaly non-perturbatively. The value g_3^{eq} is chosen such that the equilibrium properties of the system are reproduced, namely the equilibrium energy e_{eq} . Moreover, we introduce the dimensionless parameter λ that is fixed by the equilibrium density ρ_{eq} , given e_{eq} . The coupling constant g_3 within this improved mean-field theory is renormalized by the equilibrium energy and density, and mean-field theory for the chemical potential,

$$\mu(\rho) = g_0\rho + \frac{1}{2}g_3(\rho)\rho^2, \quad (6.34)$$

is used to predict the properties of the system in the thermodynamic limit at all available densities. By integrating the chemical potential we obtain the energy per particle of the system,

$$e_{\text{iMF}}(\rho) = \frac{1}{\rho} \int_0^\rho d\rho' \mu(\rho') = \frac{1}{2}g_0\rho + \frac{g_3^{\text{eq}}}{2\lambda\rho} \left(\frac{e^{1/\lambda}}{\rho_{\text{eq}}} \right)^3 \text{Ei}[3(\ln |\rho/\rho_{\text{eq}}| + 1/\lambda)], \quad (6.35)$$

where $\text{Ei}(x)$ is the exponential integral function. To lowest order $\rho \rightarrow \infty$, we obtain,

$$e_{\text{iMF}}(\rho) \approx \frac{1}{2}g_0\rho + \frac{1}{6}g_3(\rho)\rho^2. \quad (6.36)$$

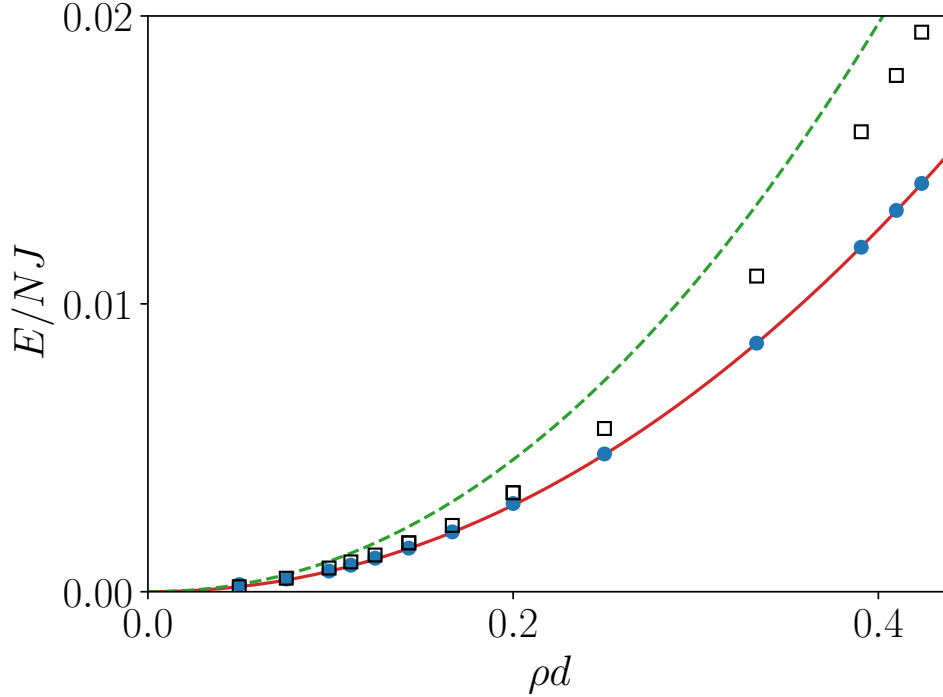


Figure 6.2: Zero-temperature equation of state for Hamiltonian (6.3) with $U_2 = 0$ and $W/J = 1.1$ (filled blue dots) and Hamiltonian (6.4) at its two-body resonance (open black squares) with $(U/J, V/J) = (16, -8/5)$. Weak-coupling EoS (6.38), at scale $\mu = \exp(\gamma)Q_*^2/\sqrt{8\rho}$, corresponding to Pastukhov's scale (Pastukhov, 2019) (green dashed line), and at the renormalization scale $\mu = 188.464/\rho d^2$ (red solid line).

Given the freedom of scale in logarithmic running of the coupling constant, the above approximation is sufficient. The relation between the equilibrium energy and density can also be obtained,

$$e_{\text{iMF}}(\rho_{\text{eq}}) = \frac{1}{2} \frac{1 - \lambda}{2 - \lambda} g_0 \rho_{\text{eq}}, \quad (6.37)$$

allowing an elimination of g_3^{eq} . Even though the dimensionless parameter λ should depend on the properties of the state, we find that there is a unique value $\lambda = 1/5$ which fulfills the relation Eq. (6.32) obtained within a self-consistent decoupling theory. Therefore, if such relation holds, there is a single parameter characterizing the EoS of the system, namely the value of g_3^{eq} . A comparison between the iMF theory and numerical results obtained with DMRG is presented in Sec. 6.5.

6.3 Universality of quantum gases

We begin by demonstrating that the discretized low-energy theories (6.3) and (6.4) reproduce continuum physics, and showing that universality is present in the gas phase. To do the first, we numerically study the ground state quantum gas with pure three-body interactions, i.e., $U_2 = 0$ (s -wave scattering

length $a_s \rightarrow \infty$) and $W > 0$ by employing the DMRG algorithm. In this special limit explicit relations between the continuum and discrete three-body parameters can be obtained, see Sec. 6.1.1. We compare our numerical results with the weak-coupling expansion of the EoS of Hamiltonian (6.1) with $g_0 = 0$, due to Pastukhov (Pastukhov, 2019),

$$\frac{E}{N} = \frac{\hbar^2 \rho^2}{6m} g(\mu) \left\{ 1 - \frac{4}{\pi} \sqrt{g(\mu)} + \frac{g(\mu)}{\sqrt{3}\pi} \left[\frac{1}{2} \ln \left| \frac{\sqrt{3}\pi}{g(\mu)} \right| - C \right] \right\}, \quad (6.38)$$

where $\mu = \mu(\rho) = \xi/\rho$ is a renormalization scale with the same ambiguity of choice, in perturbation theory, as that in the 2D Bose gas (Beane, 2010, 2018), ξ is a numerical constant, $g(\mu) = -\sqrt{3}\pi/\ln|Q_*/\mu|$ is a dimensionless coupling constant (Pastukhov, 2019), and $C = -9.863\dots$ is a numerical constant. At the scale $\mu = \sqrt{8} \exp(-\gamma)/\rho a_3^2$, which is the one chosen in (Pastukhov, 2019), the green dashed line in Fig. 6.2 is obtained. We can use the ambiguity of scale to our advantage, and choosing a different scale to best match the EoS at a particular value of the density (at $\rho a = 0.333$), we obtain the red solid line, which is in excellent agreement with the entire EoS at all ranges of density.

Having demonstrated the ability of the discretized model to reproduce continuum physics, we now study the universality of the quantum gas for Hamiltonian (6.3) and Hamiltonian (6.4) close to the two-body resonance $a_s \rightarrow \infty$. For Hamiltonian (6.4), imposing a two-body resonance $a_s \rightarrow \infty$ implies a relation between U and V given by (Valiente and Petrosyan, 2009a),

$$\frac{U}{J} = -4 \frac{V/J}{2 + V/J}. \quad (6.39)$$

To show the low-density equivalence of these two quantum gases we obtain the EoS for both models using DMRG under the set of conditions just mentioned. In Fig. 6.2, we clearly observe that for low densities the two models give the same EoS showing the universality of the quantum gas. This result was expected since for repulsive gases it is known that two models will have identical thermodynamic properties if their (N -body) S -matrices are identical (Dashen et al., 1969). This is the case at low densities where N -body scattering processes with $N > 3$ are suppressed. Thus, fixing the two- and three-body low-energy amplitudes yield similar EoS for the two models studied.

6.4 Universality of quantum droplets

We focus now on the universality properties of a quantum fluid where a many-body bound state is formed i.e. a quantum droplet. In particular, we focus on the regime ($U/J \gg 1, V < 0$) for Hamiltonian (6.4) and ($U_2 < 0, W > 0$) for Hamiltonian (6.3). As shown in Fig. 6.1 right panel, one can perform a matching between the two sets of parameters such that the energy per particle in both models is very well approximated for any number of particles. One could be tempted to claim universality in such case since the energies of both models are well reproduced. However, striking differences appear in the ground state of the respective Hamiltonians as we show below.

We start by considering the two-body bound state of both Hamiltonians. The bound state wave-

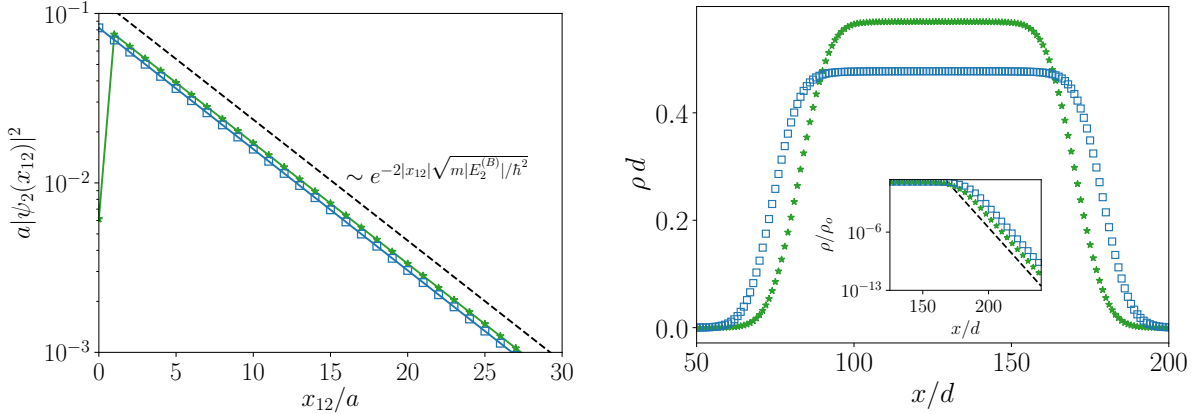


Figure 6.3: Left panel: amplitude of the two-body wavefunction $|\psi_2(x_{12})|^2$ in the relative space coordinate x_{12} for Hamiltonian (6.3) with $U_2/J = -0.33$ and $W/J = 1.39$ (open squares) and Hamiltonian (6.4) with $U/J = 10$ and $V/J = -1.6$ (stars). Dashed line indicates the asymptotic behavior, see Eq. (6.40). Right panel: density profiles with $N = 50$ particles for Hamiltonian (6.3) with $U_2/J = -0.33$ and $W/J = 1.39$ (open squares) and Hamiltonian (6.4) with $U/J = 10$ and $V/J = -1.6$ (stars). In the inset panel we show the density tails, rescaled by their respective saturation densities. Dashed line indicates the analytical result Eq. (6.43).

function in the relative coordinate space $x_{12} = x_1 - x_2$ at large distances $x_{12} \rightarrow \infty$ is given by, see Sec. 2.5,

$$\psi_2(x_{12}) = |\gamma_2| e^{-\sqrt{m|E_2^{(B)}|/\hbar^2}|x_{12}|}, \quad (6.40)$$

where γ_2 is the asymptotic normalization constant (ANC) (Taylor, 1972; Lüscher, 1986b; König et al., 2012) in the two-body sector and $E_2^{(B)}$ is the binding energy. For large and positive s -wave scattering length a_s in comparison with the effective range r_e ($a/|r_e| \gg 1$), the two-body binding energies obtained with and without including the effective range agree well with each other $E_2^{(B)} = -\hbar^2/(2ma_s^2)$. For the case studied in Fig. 6.3 we obtain $E_2^{(B)}/J \approx -0.0135$ for both models within a 1% error. Therefore, by fixing the two-body binding energies of the two models Eq. (6.3) and Eq. (6.4) the exponential decay of the relative wavefunction is reproduced for both wavefunctions, see Fig. 6.3 left panel. However, the ANCs γ_2 remain unfixed. For the two models considered we obtain the relation between the ANC in each model,

$$\left| \frac{\gamma_2^{\text{NL}}}{\gamma_2^{\text{3B}}} \right|^2 \approx 1 + \frac{|U_2|}{4J} \left[1 - \frac{1}{(1 + \frac{U}{4J})^2} \right], \quad (6.41)$$

where γ_2^{NL} and γ_2^{3B} are, respectively, the two-body ANC of Hamiltonians (6.4) and (6.3) with identical scattering lengths i.e. identical binding energies. For the case studied in Fig. 6.3, we have $|\gamma_2^{\text{NL}}/\gamma_2^{\text{3B}}|^2 \approx 1.07$, which shows a small yet non-negligible deviation from unity as shown in Fig. 6.3 left panel.

For an attractive system, which features N -body bound states for all N , it is possible to fix the

locations of the poles of the S -matrix (bound state energies) rather accurately in both models, but not the residues at the poles without further parametrization that determine the ANC γ_N for an N -body bound state (Taylor, 1972; Lüscher, 1986b; König et al., 2012). The disagreement between two models in the ANC γ_N leads to dramatic differences in their respective many-body limits. To show the impact of the ANC constant on the many-body properties let us consider the limit in which one of the particles (e.g. particle N) is asymptotically far from the rest of the system, the ground state wave function ψ_N factorizes as (König et al., 2012),

$$\lim_{x_N \rightarrow \infty} \psi_N(x_1, \dots, x_N) = \gamma_N e^{-\kappa_{1,N}|x_N - X_{N-1}|} \psi_{N-1}(x_1, \dots, x_{N-1}), \quad (6.42)$$

where we introduce the asymptotic normalization coefficient in the $N \leftrightarrow (N-1) + 1$ breakup channel γ_N , the binding energy with respect to the ground state with one fewer particle $\hbar^2 \kappa_{1,N}^2 / 2m = |E_N - E_{N-1}|(N-1)/N$, the center of mass coordinate of the $(N-1)$ -body subsystem $X_{N-1} = \sum_{i=2}^N x_i / (N-1)$, and the ground state wave function of the subsystem ψ_{N-1} . The density profile $\rho_N(x)$ of the bound state is given by Eq. (6.27). At long distances away from the bulk of the $N-1$ subsystem, we can introduce Eq. (6.42) into Eq. (6.27), obtaining,

$$\rho_N(x) \sim |\gamma_N|^2 A_{N-1} e^{-2\kappa_{1,N}|x|}, \quad (6.43)$$

for $|x| \rightarrow \infty$ and $N \rightarrow \infty$, where $A_{N-1} = \int d^{N-2}z |\psi_{N-1}|^2$ is a model-independent normalization factor. Collectively, \mathbf{z} is an $(N-2)$ -dimensional vector containing all degrees of freedom of the $(N-1)$ -particle system except for the center-of-mass coordinate. When two models have the same energy per particle for all number of particles there is a relation between the density profiles at large distances given by Eq. (6.43),

$$\lim_{|x| \rightarrow \infty} \frac{\rho_N^{\text{NL}}(x)}{\rho_N^{\text{3B}}(x)} = \left| \frac{\gamma_N^{\text{NL}}}{\gamma_N^{\text{3B}}} \right|^2, \quad (6.44)$$

that allows us to determine the scaling of the ANCs with the number of particles N . We assume that the asymptotic normalization coefficients for the two models are different for all N , since they already are for two particles as shown above. If an N -body bound state is a quantum droplet, then most of the particle content lies within the bulk of the droplet, with a density we may consider constant. The radius R of the droplet is then $R \approx N/2\rho_N(0)$. One may approximate the exponential tails for large N and $|x| \rightarrow \infty$ as,

$$\rho_N(x) \sim \rho_N(0) \exp(-2\kappa_{1,N}|x - R|), \quad (6.45)$$

that combined together with relation Eq. (6.44) gives,

$$\left| \frac{\gamma_N^{\text{NL}}}{\gamma_N^{\text{3B}}} \right|^2 \sim \frac{\rho_N^{\text{NL}}(0)}{\rho_N^{\text{3B}}(0)} \exp \left[\kappa_{1,N} N \left(\frac{1}{\rho_N^{\text{NL}}(0)} - \frac{1}{\rho_N^{\text{3B}}(0)} \right) \right], \quad (6.46)$$

showing that the ratio between the ANC's of both theories increases exponentially with the number of particles. The above relation indicates that we require algebraically small ($O(N^{-1/2-|\epsilon|})$) differences between the ANC's in order to achieve algebraically ($O(N^{-1-|\delta|})$) small differences in the equilibrium densities of quantum droplets. A finite difference in the large- N densities of the two models immediately implies an exponential disagreement between the ANC's, and therefore the residues at the poles of the S -matrix. Equation (6.46) shows that to match the equilibrium densities of two models displaying an N -body bound state one cannot only match the binding energies but also the residues at these energies must be matched, and that the matching must have algebraic precision.

To benchmark our theoretical considerations we have numerically obtained the quantum droplets of the two models Eq. (6.3) and Eq. (6.4) for the same number of particles using DMRG, see Fig. 6.3 right panel. For the regime of parameters chosen both models display the same energy per particle within a 2% error. However, the droplet saturation density does not agree between the two models. This implies that droplets in the two models with equal particle number have different sizes, see Fig. 6.3 right panel, a direct consequence of the ANC's γ_N , Eq. (6.46). On the other hand, the decay of the density far away from the center of the droplet has to be identical in both models if the energy per particle is the same, as predicted by Eq. (6.43). In the inset panel of Fig. 6.3 we show that both droplets exhibit the same exponential density decay far away from the respective centers. Moreover the decay is dictated by Eq. (6.43) which shows that it is directly related to the chemical potential at equilibrium for large number of particles. Therefore, the tails of quantum droplets are universal for different models with identical binding energies (in free space), as opposed to the saturation density which are model dependent and therefore non-universal.

6.5 Universality of quantum liquids

We now turn our attention to the liquid phases of the low-energy theories. In particular, we show the non-universality of the EoS. As shown above, the saturation density of the quantum droplets is a non-universal quantity. Therefore, the equilibrium density minimizing the EoS is a non-universal property even though we match the binding energies of both theories for all N , see Fig. 6.4 left panel. By performing DMRG simulations we observe that the equilibrium energy is very similar for both theories but the equilibrium densities are in clear disagreement, making the two EoS very different at a particular value of the coupling strengths. Therefore, we can claim that the equilibrium density of quantum liquids is a highly non-universal property and, therefore, so is the EoS. Moreover, we compare our numerical results to the iMF theory developed in Sec. 6.2.2. The iMF Eq. (6.37) turns out to be a very accurate description of the exact EoS. In Fig. 6.4 left panel, we plot the EoS at zero temperature for Hamiltonian (6.3), together with the iMF, Eq. (6.36). We choose a value of g_3^{eq} and λ to reproduce the equilibrium energy and density. Given such input the iMF theory is able to reproduce the EoS at all values of the density, well beyond the low-density limit. Moreover, we observe that the numerical value of λ is in very good agreement with $\lambda = 1/5$ fulfilling the self-consistent relation Eq. (6.32).

Finally, we demonstrate the inequivalence between the EoS of the low-energy theories at any value of the coupling strengths. In Fig. 6.4 right panel we present the ratio of the equilibrium energy and

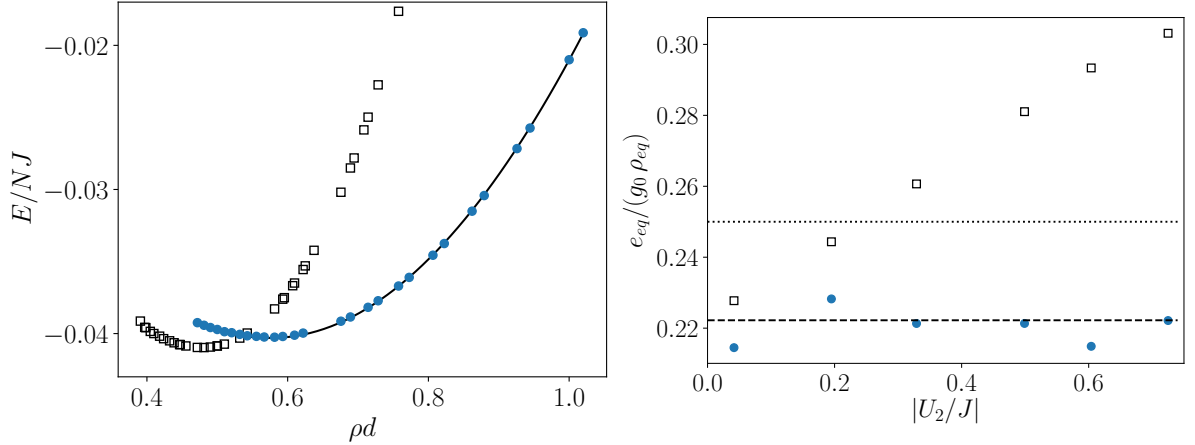


Figure 6.4: Left panel: Exact zero-temperature equation of state for Hamiltonian (6.3) with $U_2/J = -0.33$ and $W/J = 1.39$ (blue dots), and for Hamiltonian (6.4) with $U/J = 10$ and $V/J = -8/5$ (open black squares). Improved mean-field approximation, Eq. (6.36), (solid black line) with $\rho_{\text{eq}}d = 0.576$, $mg_3^{\text{eq}}/\hbar^2 = 0.9899$ and $\lambda = 0.2645$ (see text). Right panel: ratio $e_{\text{eq}}/g_0\rho_{\text{eq}}$ calculated numerically for Hamiltonian (6.3) as function of two-body interaction strength (blue dots). The three-body interaction strengths for points labelled with $U_2/J = -0.195, -0.329, -0.499, -0.604$ and -0.725 are given by $W/J = 1.28, 1.4, 1.48625, 1.506$ and 1.508 , respectively. Open black squares correspond to the same ratio but for Hamiltonian (6.4), with $V/J = -8/5$. From left to right, $U/J = 12, 10, 8, 7$ and 6 . Dashed line ($2/9 = 0.222\dots$) is the prediction from Eq. (6.32), and dotted line ($1/4$) is the standard mean field prediction, see text.

equilibrium density for different values of the coupling constants. We observe that this ratio does not coincide in both theories at any value of the couplings. In fact, the three-body theory (6.3) shows an approximately constant ratio while the theory with non-zero range (6.4) shows a nearly linear relation. Therefore, the thermodynamic properties of both models do not coincide for any value of the coupling strengths and therefore, we observe a non-universal behavior of the respective EoS.

Finally, let us remark that the self-consistent theory developed in Sec. 6.2.1 is able to correctly capture the relation between the equilibrium properties of the liquid with three-body forces. Our theory, although approximate, is highly non-perturbative. In Fig. 6.4 right panel we show that the DMRG results of the discrete three-body model (6.3) are in excellent agreement with our prediction given by Eq. (6.32). Moreover the mean-field relation $e_{\text{eq}}/g_0\rho_{\text{eq}} = 1/4$ can be discarded, demonstrating the higher predictive power of our self-consistent theory respect to the restricted mean-field approximation.

6.6 Conclusions and outlook

In this chapter we have investigated interacting one-dimensional bosons in the universal low-energy regime at zero temperature. We have considered two particular low-energy theories: one including zero-range two- and three-body forces and another one including finite range two-body forces. We have matched the two- and three-body scattering amplitudes of both theories and explore the universality of the many-body phases. We have found that for the quantum gas phase the two models display

identical low-density equation of states and therefore, the thermodynamics is universal in the gas phase. However, in the quantum liquid phase the equation of states differ for all densities. We have developed an analytical theory showing that small deviations in densities in the few-particle sector grow exponentially in the many-body limit for droplets and liquids implying the lack of equivalence of the zero-temperature thermodynamics. Moreover, we have developed highly non-perturbative theories yielding quantitative predictions for the quantum liquid phase with repulsive three-body forces, when compared to exact results obtained with DMRG.

From the perspective of utilizing lattice theories to simulate continuum physics it would be interesting to explore the renormalization of many-body properties when the theory is discretized. Moreover, the lack of universality in the quantum liquid phase points to a possible transformation relating two quantum liquids with identical binding energies. Such transformation would be highly desirable since it will allow to relate the thermodynamics of two quantum liquids described by different microscopic models.

Part II

Binding induced by kinetic frustration: applications to cold atoms and moiré systems

ATTRACTION FROM FRUSTRATION IN LADDER SYSTEMS

In the first part of this Thesis, we have demonstrated how the interplay between attractive and repulsive interactions results in the formation of exotic phases of matter in one-dimensional optical lattices. Specifically, we have examined the formation of quantum liquids, a new type of quantum fluid that has already been produced in ultracold atomic systems. Quantum liquids are better understood as the self-organization of bound states that arise from the few-body problem, which suggests the appearance of stronger multi-body correlations compared to repulsive quantum gases. In the second part of this Thesis, we present a novel mechanism that induces binding in the system, relying on the kinetic energy of particles rather than interactions between them. Normally, particles in free space can only form a bound state when an attractive interaction between them is present. However, we introduce an additional factor in this picture: the lattice geometry in which particles propagate. The geometry plays a critical role in dictating the possible propagation paths that a particle can follow. By selecting appropriate geometrical configurations, we can induce binding between two particles even in the presence of repulsive interactions.

The lattice geometry plays a fundamental role in condensed matter systems as it governs the possible configurations of states in the system. Hence, it is important to note that not only the Hamiltonian terms dictate the lowest energy configurations, but these configurations must also be consistent with the underlying geometry. This introduces the concept of frustration. A system becomes frustrated when its lowest energy configuration dictated by the Hamiltonian terms is incompatible with the lattice geometry. The classical example of geometrical frustration corresponds to an antiferromagnetic Ising Hamiltonian placed in a three-site triangular plaquette ([Wannier, 1950](#)),

$$H = J \sum_{\langle ij \rangle} S_i^z S_j^z, \quad (7.1)$$

with $J > 0$. Naively, one would be tempted to argue that the lowest energy configuration of Hamil-

tonian (7.1) is given by the Neel state $|\uparrow, \downarrow, \uparrow\rangle$. However, this spin configuration is not the lowest energy configuration since it has a ferromagnetic link between two spins no matter the order of the Neel state. The lowest energy configuration turns out to be a 120° spiral order with an energy $E_0 = -3J/2$ (Wannier, 1950). Interestingly, one would argue that Hamiltonian (7.1) always has a lowest energy configuration with an energy density given by $-zJ$, corresponding to the local energy minimization of every couple of spins. This is true whenever frustration is absent. For systems with geometrical frustration, the lowest energy configuration appears to be higher in energy $E_0 > -zJ$ since the energy cannot be minimized locally. The term frustration has originally coined by J. Vannimenus and G. Toulouse and it was shown to be essential for the description of spin glasses (Toulouse et al., 1977; Vannimenus and Toulouse, 1977). Moreover, it was formalized that frustration appears when a closed loop of the lattice geometry contains an odd number of links (Mezard et al., 1987). In this chapter we show that the concept of geometric frustration can be promoted to the quantum world and lead to the appearance of exotic phenomena.

In this chapter we consider two component (spin-1/2) mixtures of fermionic or bosonic particles on ladders with frustrated kinetic energy in the regime of light doping relative to insulating states at half-filling, spin polarization close to 100%, and repulsive SU(2) symmetric interactions. We demonstrate that such systems exhibit a common tendency to form multi-particle bound states with effective attraction between particles arising from kinetic frustration. In many cases we find that the ground state of such systems is best understood as resulting from self-organization of multi-particle clusters. The systems under consideration can be realized using ultracold Bose and Fermi atoms in optical lattices with the currently available experimental techniques (Bakr et al., 2009; Sherson et al., 2010; Parsons et al., 2015; Cheuk et al., 2015; Omran et al., 2015; Haller et al., 2015; Edge et al., 2015; Greif et al., 2016; Brown et al., 2017; Weitenberg et al., 2011; Yang et al., 2021; Sørensen et al., 2005; Dalibard et al., 2011; Atala et al., 2014; Fukuhara et al., 2013b; Struck et al., 2012; Cooper and Dalibard, 2013; Aidelsburger et al., 2013; Miyake et al., 2013; Jotzu et al., 2014; Celi et al., 2014; Goldman et al., 2016; An et al., 2017). Specifically, quantum gas microscopes offer the possibility of imaging atoms with a single site resolution (Bakr et al., 2009; Sherson et al., 2010; Parsons et al., 2015; Cheuk et al., 2015; Omran et al., 2015; Haller et al., 2015; Edge et al., 2015; Greif et al., 2016; Brown et al., 2017; Weitenberg et al., 2011; Yang et al., 2021). This will allow a direct measurement of the kinetically induced multi-particle clusters found in our system. At the same time, ladder systems have been produced in different cold atom laboratories and kinetic frustration can be introduced by adding a synthetic static gauge field in the system (Sørensen et al., 2005; Dalibard et al., 2011; Atala et al., 2014; Fukuhara et al., 2013b; Struck et al., 2012; Cooper and Dalibard, 2013; Aidelsburger et al., 2013; Miyake et al., 2013; Jotzu et al., 2014; Celi et al., 2014; Goldman et al., 2016; An et al., 2017). Ultracold atomic systems also offer the possibility to study these systems at a fixed number of particles of each internal state (spin) and to directly image the two internal states, see e.g. (Boll et al., 2016). This can be achieved by using different atomic species or different hyperfine states of the same type of atom. Thus, physics close to the fully polarized state can be accessed even though the underlying magnetic interactions are antiferromagnetic. This motivates us to study the ground state of the system in each sector of fixed magnetization and total number of particles. In addition, in Chap. 8 we show the importance of

kinetic frustration for TMD heterostructures, which has also been discussed in Refs. (Davydova et al., 2022; Lee et al., 2022; Zhang and Fu, 2022). We employ a strong external magnetic field to polarize the system since the magnetization cannot be fixed by setting the total number of electrons. Another interesting platform where kinetically induced pairing may also be relevant is twisted bilayer graphene close to ferromagnetic insulating states (Sharpe et al., 2019).

The central objective of our work is understanding the interplay of few- and many-body phenomena. Many-body systems are usually understood from the perspective of two-body correlations, such as the pairing amplitude in superconductors that arises due to formation of Cooper pairs. Traditional mean-field approaches rely on the order parameters defined to describe two particle correlations (superconductivity, magnetism, spin and charge density wave states). We show that kinetically frustrated systems present many-body phases where multi-body correlations are dominant. Thus, they go beyond the simple mean-field picture. On the other hand, powerful theoretical methods have been developed for analyzing few-body states in vacuum, such as the celebrated Skorniakov-Ter-Martirosian (STM) equation (Braaten and Hammer, 2006; Greene et al., 2017). However, understanding the implications of multi-particle composites on the many-body physics remains an open problem in many areas of physics. For example, the primary objective of quantum chromodynamics (QCD) is developing accurate models of triplets of quarks binding into nucleons, which in turn combine to form nuclei. Intriguingly, we find many analogies between our system and the “bag model” of QCD (Hasenfratz and Kuti, 1978). While in QCD gluons provide a “bag” that holds quarks together, in the ladder systems discussed in this chapter, magnons provide a “bag” which traps one or several holes, and in turn holes are holding the magnons together.

This chapter is devoted to the study of binding induced by kinetic frustration in ladder systems. In Sec. 7.1 we present the concept of kinetic frustration and show how binding between a charge (hole) and a single spin flip (magnon) can be induced by this type of frustration. We present the microscopic model studied in this chapter in Sec. 7.2 and the numerical techniques employed to find our results in Sec. 7.3. In Sec. 7.4 we present a study of spin-1/2 fermions loaded in the zigzag ladder. We solve the two-particle hole-magnon problem and show the appearance of a bound state. Then, we study multi-body composites formed by multiple holes and magnons. We present a study of dynamical probes and demonstrate how they can be employed to detect the appearance of hole-magnon bound states. Finally, we study the many-body problem of multiple holes and magnons and study many-body phases induced by the self-organization of multi-body composites. In Sec. 7.5 we focus on spin-1/2 hardcore bosons loaded in the same zigzag ladder geometry. We present a mapping between the fermionic and bosonic problem which allows us to show the appearance of anti-bound hole-magnon states in the bosonic case. In Sec. 7.6 we present a study of the square ladder with a static perpendicular magnetic flux for spin-1/2 fermions and hardcore bosons. The magnetic flux induces kinetic frustration in the system creating hole-magnon bound states for both fermionic and bosonic systems. Finally, in Sec. 7.7 we present our conclusions and outlook.

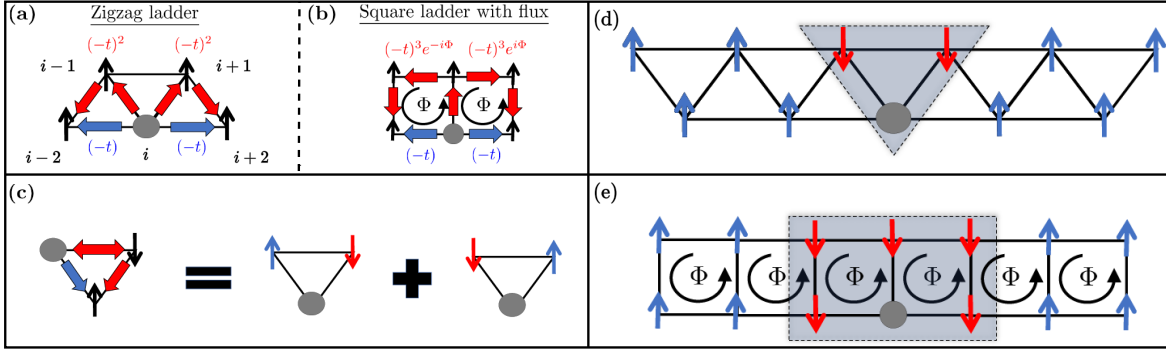


Figure 7.1: A single hole injected into a fully polarized insulating state exhibits kinetic frustration arising from destructive interference of different paths. This occurs for non-bipartite geometries such as the zigzag ladder (a) or for bipartite ones in the presence of magnetic flux (b). When a flipped spin is added into the system (c), the two different paths cannot interfere since they lead to different final states. These two final states correspond to the permutation of the two spins. In the right panel we show a schematic representation of multi-particle bound states of a single hole and one or several flipped spins (magnons) on top of a fully polarized insulating state. (d) corresponds to the non-bipartite zigzag ladder and (e) to the square ladder with a perpendicular magnetic flux Φ .

7.1 Kinetic frustration

In this chapter we consider two specific lattice geometries: zigzag ladders and square ladders with flux (see Fig. 7.1), but we expect that our conclusions apply to broader classes of systems. Our starting “vacuum” is an insulating state with one fermion per site on a frustrated ladder (zigzag or regular ladder with a flux) and full spin polarization. When one of the spins is flipped, we call it a magnon. To describe the concept of kinetic frustration we consider the case of a single hole immersed in the fully polarized insulating background in the zigzag ladder. This problem is better described by performing a charge conjugation transformation,

$$c_{i,\uparrow} \rightarrow h_i^\dagger, \quad (7.2)$$

where we assume the system to be polarized along the z -axis. The propagation of the single-hole is described by the Hamiltonian,

$$\hat{H}_{1H} = \pm t \sum_{\langle i,j \rangle} \left(\hat{h}_i^\dagger \hat{h}_j + \text{h.c.} \right), \quad (7.3)$$

where $+$ ($-$) corresponds to the fermionic (bosonic) case. The change of sign is a consequence of the anticommutation relations for the fermionic case. Therefore, the bosonic case can be studied by just changing the sign of t . In the fermionic case we observe that propagation paths of different lengths interfere partially destructively. There is a relative minus sign difference depending on whether the length of the path is even or odd, see Fig. 7.1 (a). Therefore, the hole cannot completely minimize its kinetic energy since different paths interfere destructively (Barford and Kim, 1991; Merino et al., 2006). This phenomenon is called kinetic frustration in analogy with the classical geometric frustration. However, if the sign of t is changed, the relative minus sign disappears and all paths interfere

constructively (Barford and Kim, 1991; Merino et al., 2006). This case corresponds to the bosonic one for which the hole can completely minimize its kinetic energy and becomes non-frustrated. The same argument applies to the square ladder with a perpendicular magnetic flux which creates a pattern of interference between paths of different length either for bosons and fermions. Notice that for null perpendicular magnetic flux the propagation paths always interfere constructively since paths of length odd are not present in the square ladder. Therefore, the square ladder without magnetic flux is non-frustrated in accordance with the classical criterion of frustration.

7.1.1 Imaginary time picture

The picture of kinetic frustration based on the interference pattern of different propagation paths can be formalized in a path integral perspective or an imaginary time propagation. Let us start by considering an initial state at zero imaginary time $\tau = 0$, which has the hole localized in an arbitrary site i ,

$$|\psi(\tau = 0)\rangle = h_i^\dagger |0\rangle. \quad (7.4)$$

The ground state of the system $|\psi_0\rangle$ is reached in the long imaginary time limit after proper normalization,

$$|\psi_0\rangle = \lim_{\tau \rightarrow \infty} \frac{e^{-\tau \hat{H}} |\psi(\tau = 0)\rangle}{\|e^{-\tau \hat{H}} |\psi(\tau = 0)\rangle\|}. \quad (7.5)$$

At short times $\tau|t| \ll 1$, we can expand the exponential factors and perform a short imaginary time expansion. The energy of the system at a given value of the imaginary time is given by,

$$E(\tau) = \frac{\langle \psi(\tau = 0) | e^{-\tau \hat{H}} \hat{H} e^{-\tau \hat{H}} | \psi(\tau = 0) \rangle}{\|e^{-\tau \hat{H}} |\psi(\tau = 0)\rangle\|^2}, \quad (7.6)$$

which we compute up to order $\mathcal{O}(\tau^4|t|^4)$,

$$E(\tau) = \frac{-8\tau t^2 + 12\tau^2 t^3 - 48\tau^3 t^4 + \frac{200}{3}\tau^4 t^5}{1 + 8\tau^2 t^2 - 8\tau^3 t^3 + 24\tau^4 t^4}. \quad (7.7)$$

The pattern of interference becomes clear in the expression of the energy. When the tunneling is positive $t > 0$ (fermionic case) relative minus signs appear at different orders of the short imaginary time expansion, leading to a partially destructive pattern of interference. However, when the tunneling is negative $t < 0$ (bosonic case) all orders contribute with the same sign and therefore, the propagation paths constructively interfere.

The small imaginary time expansion provides some intuition about the pattern of interference between different propagation paths. However, the imaginary time problem can be solved in a more elegant way. By expanding the exponential factors in Eq. (7.6) we can write the energy as $E = \frac{\bar{E}}{N}$

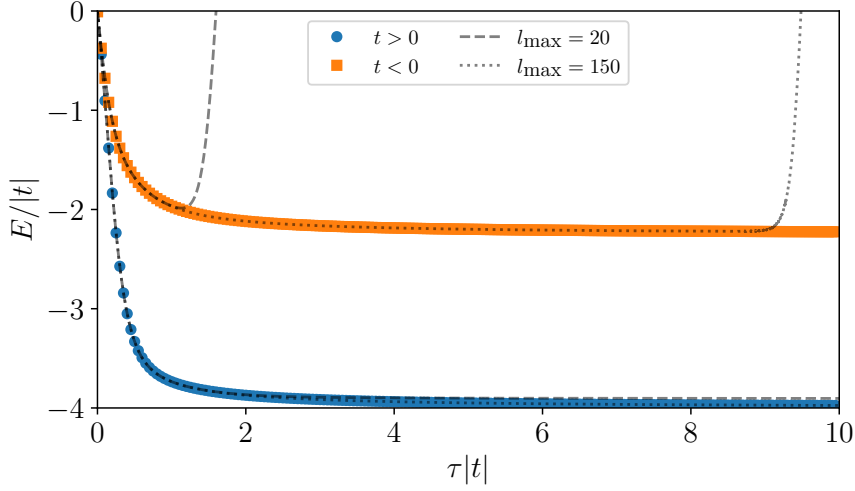


Figure 7.2: Imaginary time evolution of the energy of a single fermionic hole propagating in a fully polarized insulator with hopping t in the zigzag ladder with 2×50 sites. Blue dots (orange squares) correspond to the positive (negative) hopping case for which a constructive (partially destructive) pattern of interference appears. Lines represent the imaginary time expansion obtained at order l_{\max} following the expansion developed in the main text.

with,

$$\bar{E} = \sum_n \frac{(-2\tau)^n}{n!} t^{n+1} \langle \psi(\tau=0) | \hat{H}^{n+1} | \psi(\tau=0) \rangle, \quad N = \sum_n \frac{(-2\tau t)^n}{n!} \langle \psi(\tau=0) | \hat{H}^n | \psi(\tau=0) \rangle. \quad (7.8)$$

Therefore, we just need to evaluate the expectation value of the n -power of the Hamiltonian over the initial state. The expectation value just counts the number of paths of length n that start and end at the initial site i . This problem can be formalized by employing graph theory, where the matrix representation of the Hamiltonian (7.3) corresponds to the adjacency matrix of the network corresponding to the zigzag ladder. To compute the expectation value we just need to count the number of closed paths of length n of the zigzag geometry. We attack this problem by mapping the zigzag geometry to a one-dimensional chain where we can perform hops of length ± 1 and ± 2 , see Fig. 7.1 (a). A given propagation path is specified by the number of hops of length ± 1 ($N_{\pm 1}$) and length ± 2 ($N_{\pm 2}$). Since we want to restrict ourselves to paths of length n that start and end at the same point we need to impose the following conditions,

$$N_{+1} + N_{-1} + N_{+2} + N_{-2} = n, \quad \text{and,} \quad N_{+1} + 2N_{+2} = N_{-1} + 2N_{-2}. \quad (7.9)$$

Then, the vacuum expectation value is set by the combinations and permutations of the possible

propagation paths of length n which are given by,

$$\langle \psi(\tau = 0) | \hat{H}^n | \psi(\tau = 0) \rangle = \sum_{N_{+2}=0}^{n/2} \sum_{N_{-2}=0}^{n/2} \binom{n}{N_{+1} + N_{-1}} \binom{N_{+1} + N_{-1}}{N_{+1}} \binom{n - N_{+1} - N_{-1}}{N_{+2} + N_{-2}} \binom{N_{+2} + N_{-2}}{N_{+2}}. \quad (7.10)$$

Finally, by inserting the conditions Eq. (7.9) into Eq. (7.11) we obtain,

$$\langle \psi(\tau = 0) | \hat{H}^n | \psi(\tau = 0) \rangle = \sum_{N_{+2}=0}^{n/2} \frac{n!}{N_{+2}!} \sum_{N_{-2}=0}^{n/2} \frac{1}{\left(\frac{n}{2} + \frac{N_{-2} - 3N_{+2}}{2}\right)! \left(\frac{n}{2} + \frac{N_{+2} - 3N_{-2}}{2}\right)! N_{-2}!}. \quad (7.11)$$

Moreover, we notice that given a path of length n not all combinations of $N_{\pm 2}$ satisfy the condition that $N_{\pm 1}$ must be an integer. These combinations have to be discarded leading to an extra rule. If the total length of the path is even then N_{+2} and N_{-2} must have the same parity, meaning that if one is even the other is even and vice versa. However, if the total length of the path is odd then N_{+2} and N_{-2} must have opposite parities. While we have not been able to obtain a closed analytical expression after carrying out the sums in Eq. (7.11), the sums can be evaluated numerically in an efficient way. Therefore, Eq. (7.11) together with Eq. (7.8) are a generalization of the short imaginary time expansion which can be evaluated at any order.

In Fig. (7.2) we show the imaginary time evolution of a hole initially localized in the center of a zigzag ladder. This result is obtained by performing exact diagonalization of Hamiltonian (7.3). For negative values of the hopping we obtain a lower value of the ground state energy with respect to the positive hopping case. Therefore, the positive hopping case suffers from a partially destructive pattern of interference, as expected. Moreover, we show the analytical exact solution of the imaginary time evolution given by Eq. (7.11) and Eq. (7.8). To numerically evaluate the expression we put a cutoff on the maximum length of the paths l_{\max} . The negative hopping case converges rapidly with the cutoff, suggesting that the non-frustrated case can be treated perturbatively since all paths contribute with the same sign. However, our analytical solution for the positive hopping case shows an instability at a critical imaginary time τ_c fixed by the cutoff l_{\max} . We obtain a divergence of the energy for longer imaginary times $\tau > \tau_c$ and a good comparison with respect to the exact diagonalization result for shorter times $\tau < \tau_c$. The instability of our analytical solution hints at the partially destructive pattern of interference by showing that the frustrated case cannot be treated perturbatively.

7.1.2 Attraction from frustration

We have shown that a single fermionic hole suffers from kinetic frustration in the two geometries considered. We now introduce an additional ingredient: spin degrees of freedom. Specifically, we consider the case of having a single hole and a single magnon in the system. Now different propagation paths of the fermionic hole become distinguishable if the position of the magnon is changed during the propagation of the hole, see Fig. 7.1 (c). Therefore, the destructive pattern of interference can be avoided when the hole exchanges its position with the magnon. In this way, the hole alleviates the

kinetic frustration and reduces its energy. We conclude that the hole wants to be near the vicinity of the flipped spin and a hole-magnon bound state is formed solely induced by kinetic frustration. Interestingly, when particles suffer from kinetic frustration they seem to want to cluster and propagate together to release the kinetic frustration. A mechanism that seems to apply even in human behavior. In this chapter we formalize the concept of attraction from frustration in both fermionic and bosonic systems. Moreover we characterize the formation of multi-body composites formed by a single hole and multiple magnons, see Fig. 7.1 (d) and (e). While a previous study has already shown the formation of kinetically induced bound states in the triangular lattice (Zhang et al., 2018b), we extend this analysis to ladder systems and explore in detail the formation of multi-particle composites and their implications on the many-body physics.

7.2 Microscopic model

In this chapter we focus on Fermi-Hubbard and Bose-Hubbard models of spin-1/2 particles in the strongly interacting regime $U \gg t$ with $SU(2)$ interactions. Both models can be mapped to effective $t - J$ models below half-filling in an exact way up to order $\mathcal{O}(t^2/U)$, see e.g. (Auerbach, 1998). We consider a simplified version of the $t - J$ model given by,

$$\hat{H}_{t-J} = -t\hat{\mathcal{P}} \left[\sum_{\langle i,j \rangle, \sigma} \left(\hat{c}_{i\sigma}^\dagger \hat{c}_{j\sigma} + \text{h.c.} \right) \right] \hat{\mathcal{P}} + J \sum_{\langle i,j \rangle} \mathbf{S}_i \mathbf{S}_j, \quad (7.12)$$

where $\hat{c}_{i\sigma}^\dagger$ creates a fermion or a hardcore boson at site i with spin $\sigma = \uparrow, \downarrow$ and $\hat{\mathcal{P}}$ project onto the subspace of no double occupancies. The spin operators are defined by $S_i^\gamma = \frac{1}{2} \sum_{\alpha, \beta} \hat{c}_{i\alpha}^\dagger \sigma_{\alpha, \beta}^\gamma \hat{c}_{i\beta}$ where σ^γ are the Pauli matrices with $\gamma = x, y, z$. The sum $\sum_{\langle i,j \rangle}$ is taken over first neighbors and we set the lattice spacing $a = 1$.

The $t - J$ model contains two energy scales: the quantum tunneling (hopping) of particles t and the superexchange J . The hopping t gives rise to the kinetic energy of holes, and the superexchange term describes propagation and interaction of magnons. The $t - J$ model (7.12) is an effective low energy model for the Hubbard model at very strong Hubbard interaction $U \gg t$ with $J = \pm 4t^2/U$, where $+$ ($-$) corresponds to the fermionic (bosonic) case (Duan et al., 2003; Trotzky et al., 2008a; Brown et al., 2015; Nichols et al., 2019; Jepsen et al., 2020a).

The $t - J$ model (7.12) presents an underlying $U(1) \otimes SU(2)$ symmetry associated with the conservation of the total number of particles and the spin rotational invariance. In our simulations we exploit the subgroup $U(1) \otimes U(1)$ associated with the conservation of the number of particles in each spin (component) N_\uparrow and N_\downarrow . This is achieved by performing simulations in the canonical ensemble fixing the total number of particles $N = N_\uparrow + N_\downarrow$ and the magnetization measured respect to the z -axis $S^z = (N_\uparrow - N_\downarrow)/2$. We focus our study on the physics close to the fully polarized Mott state $N \approx N_s$ and $S^z \approx N_s/2$, where N_s is the total number of sites in the system. For convenience we define the number of holes and the number of magnons $N_h = N_s - N \ll N_s$ and $N_m = N_s - M \ll N_s$, respectively.

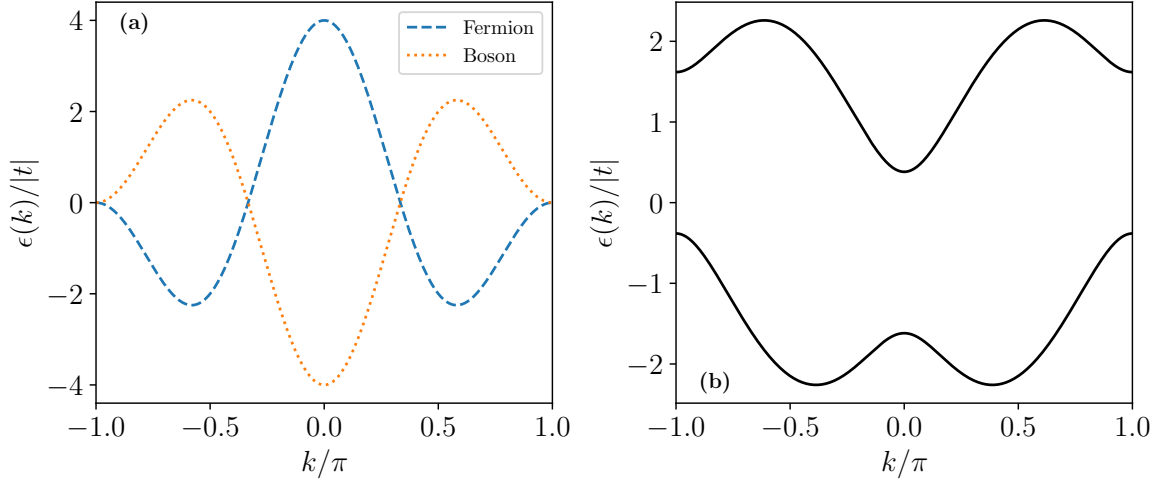


Figure 7.3: Dispersion relation of a single hole in a fully polarized background in (a) the zigzag ladder and in (b) the square ladder with a transverse perpendicular flux $\phi = 0.8\pi$. Dashed and dotted lines in (a) correspond to the fermionic and bosonic case, respectively.

In order to study kinetic frustration in the $t - J$ model (7.12) we have to specify the underlying lattice. Kinetic frustration can be easily achieved for fermions in lattice geometries where the number of legs enclosed in a minimal closed loop is odd. Therefore ladders are promising candidates where this condition can be satisfied. The minimal lattice fulfilling that condition is a zigzag ladder, in which a unit cell corresponds to two stacked triangles, see Fig. 7.1 (a). Another promising platform for realizing a one-dimensional model with kinetic frustration is flux ladder systems, which have been recently realized in experiments with ultracold atoms (Atala et al., 2014; Tai et al., 2017). In this system a static synthetic gauge field is used to provide the analogue of the Aharonov-Bohm flux of the ordinary magnetic field in condensed matter systems. A particularly attractive feature of such systems is the possibility of reaching high flux density per unit cell.

7.2.1 Single particle dispersion for the zigzag ladder

The single hole problem described by Eq. (7.3) can be easily solved by going to momentum space. For the zigzag ladder we obtain the following hole dispersion relation

$$\epsilon_h(k) = \pm 2t\{\cos(k) + \cos(2k)\}. \quad (7.13)$$

For fermions kinetic frustration manifests in the ground state of the hole since its ground state energy is given by $\epsilon_h(k_0) = -2.25t$ and $k_0 = \arccos(-1/4)$, which agrees with the value of the energy obtained at long imaginary times, see Fig. 7.2. This ground state energy is higher than the kinetic energy we would expect from counting the number of nearest neighbors $-4t$, see Fig. 7.3 (a). For bosons kinetic frustration appears not in the ground state but for the highest energy single particle states. In this situation the highest energy obtained $2.25t$ is lower than the expected value of $4t$. To understand this

effect, one can change the sign of hopping $t \rightarrow -t$, so that the highest energy states of the positive t model correspond to the lowest energy states of the negative t model. Then one observes that in the negative t case there is a relative minus sign between the two trajectories around a single triangle (blue and red paths in Fig. 7.1), which implies a destructive interference and thus a reduction of the kinetic energy gain due to hopping. This plays a crucial role when studying bound states of holes and magnons for the fermionic and bosonic systems.

7.2.2 Single particle dispersion for the square ladder with a flux

For a square flux ladder we consider propagation of a single hole on top of a fully polarized insulating state. In this situation the dispersion relation of the hole reads,

$$\epsilon_{\pm}(k) = -2t \cos(\phi/2) \cos(k) \pm \sqrt{t^2 + 4t^2 \sin(\phi/2)^2 \sin(k)^2}, \quad (7.14)$$

where ϕ corresponds to the magnetic flux per plaquette (see e.g. (Tai et al., 2017)). The minimum of the band (-) is at $k_m = 0$ ($k_m = \pm \sin(\phi/2) \sqrt{1 - \cos(\phi/2)/(4 \sin(\phi/2)^4)}$) for $\phi < \phi_c$ ($\phi > \phi_c$) where $\phi_c \approx 0.43\pi$, respectively. In this case two different bands are present (\pm) because the system can be thought of as two coupled 1D systems. It is easy to check that the kinetic energy is always higher than the non-frustrated situation $\epsilon_{\pm}(k) > -3t$ for all momenta when the magnetic flux is turned on, see Fig. 7.3 (b). Moreover, the spectrum is symmetric with respect to a change of sign of t , shifting the momentum by π , and exchanging the two bands (\pm). This symmetry shows that in this case frustration does not arise from the sign of the bare t (recall that hole hopping has different signs for the bosonic and fermionic systems) but originates from the magnetic flux ϕ and appears for both lowest and highest energy single particle states. As a consequence, the dispersion of a single hole is the same for bosonic and fermionic systems.

7.3 Numerical techniques

To verify the presence of kinetically induced bound states we have employed a combination of numerical techniques. To obtain the ground state of the system with a single hole and a single magnon we have numerically solved the two-body problem and study its finite size scaling, see Sec. 7.4.1 for details. To obtain the unitary time evolution presented in Sec. 7.4.5 we have performed an exact diagonalization of the Hamiltonian (7.12) and then successively applied the time evolution operator with a discretized time step $dt/J = 0.05$ to an initial state with a hole and magnon in adjacent sites. The time evolution runs until the wavefunction starts to exhibit probability at the edges of the system. In this way, we ensure that it does not suffer from finite size effects and the chosen boundary conditions. Simulations with larger number of holes and magnons $N_h, N_m > 1$ are performed using the DMRG algorithm and are presented in Sec. 7.4.4 and Sec. 7.4.6. We study systems with open boundary conditions and analyze the dependence of the energy on the system size. This allows us to identify the presence of different bound states by examining the binding energies of different decomposition channels. Moreover, we also explore different correlation functions to verify the presence of bound states. We perform system

simulations with up to 150×2 sites for the largest composites and we limit the bond dimension of the DMRG calculations up to $\chi = 512$.

7.4 Spin-1/2 fermions in the zigzag ladder

7.4.1 Hole-magnon bound states

In order to solve the hole-magnon problem of the fermionic $t - J$ model Eq. (7.12) in a zigzag ladder we first map the ladder to a one-dimensional system in which the sites are indexed as shown in Fig. 7.11. Then we pass from the original particle operators to operators of holes and magnons. In this way we reduce the problem to a one-dimensional two-body problem. This procedure can be formalized by introducing the hole and magnon operators

$$\hat{c}_{\uparrow i} = \hat{h}_i^\dagger \quad \text{and} \quad \hat{c}_{\downarrow i} = \hat{h}_i^\dagger S_i^+. \quad (7.15)$$

In this way the original $2L - N_h$ particles problem can be reduced to a problem of N_h holes and N_m magnons, being $2L$ the total number of sites in the ladder. Using these operators the $t - J$ Hamiltonian becomes,

$$\hat{H}_{t-J} = \pm t \sum_{i,e} \left(\hat{h}_{i+e}^\dagger \hat{h}_i + \text{h.c.} \right) + J \sum_{i,e} \mathbf{S}_i \mathbf{S}_{i+e} \pm t \sum_{i,e} \left(\hat{h}_{i+e}^\dagger \hat{h}_i S_i^- S_{i+e}^+ + \text{h.c.} \right), \quad (7.16)$$

where $e = a, 2a$ being a the lattice spacing and the $+$ and $-$ signs correspond to the fermionic and bosonic case, respectively. They appear because of the anticommutation and commutation relations satisfied by the hole operators in each case. Under these transformations the fully polarized insulating state $|\text{FP}\rangle$ becomes the vacuum of holes and magnons. Holes and magnons can be created by applying the respective creation operators. In particular the hole-magnon state is defined as $\hat{h}_i^\dagger S_j^- |\text{FP}\rangle \equiv |ij\rangle$. We can solve this two-particle problem by separating the center $R/a = (i+j)/2$ and relative $z/a = i-j$ motion using the set of states

$$|\psi\rangle = \sum_{ij} e^{iQR} \psi_Q(z) |ij\rangle, \quad (7.17)$$

where we introduce the total quasi-momentum Q of the pair and the wavefunction in relative position space $\psi_Q(z)$. Since the interaction part of the Hamiltonian (7.16) does not couple states with different quasi-momentum Q we can obtain the equation of motion for the relative part,

$$\begin{aligned} E_Q \psi_Q(z) &= \sum_{e=\pm a, \pm 2a} \left(\pm t e^{iQe/2} + \frac{J}{2} e^{-iQe/2} \right) \psi_Q(z+e) \\ &+ \sum_{e=\pm a, \pm 2a} \delta(z-e) \left(\pm t \psi_Q(-e) + \frac{J}{2} \psi_Q(e) \right), \end{aligned} \quad (7.18)$$

where the energy of the pair E_Q depends parametrically on the total quasi-momentum. We measure the hole-magnon energy E_Q with respect to the energy of the ferromagnetic background. The hole-

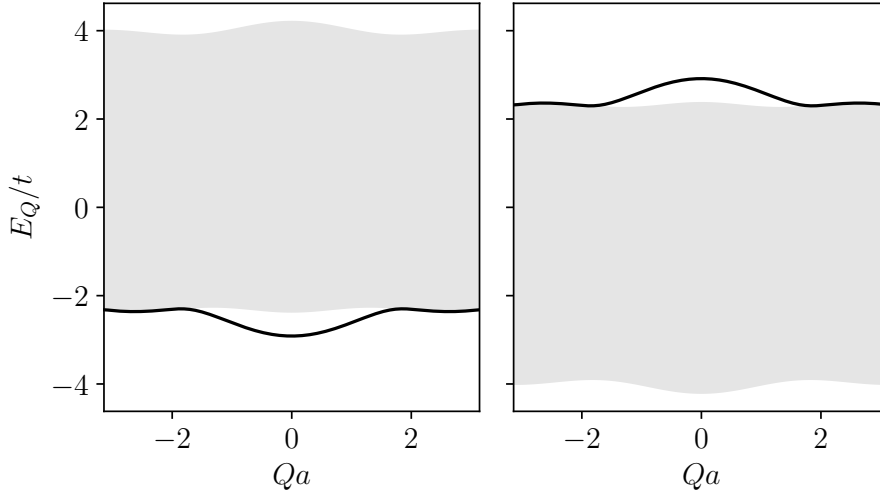


Figure 7.4: Band structure of the hole-magnon problem on the zigzag ladder as a function of the total quasimomentum Q for $J/t = 0.1$. The grey area marks the hole-magnon scattering continuum and the continuous line the bound state band. The left (right) panel corresponds to the fermionic (bosonic) case $t > 0, J > 0$ ($t < 0, J < 0$).

magnon interaction contains an exchange term of strength t and a bare nearest-neighbor interaction of strength $J/2$. For fermions (bosons) the nearest-neighbor interaction $J > 0$ ($J < 0$) has a repulsive (attractive) effect on the pair. The effect of the exchange interaction, last term of Eq. (7.16), becomes clear at null total quasi-momentum $Q = 0$. In this situation the relative wavefunction has the property $\psi_{Q=0}(-e) = \pm\psi_{Q=0}(e)$ for a symmetric or antisymmetric state with respect to the hole-magnon exchange. In this way, we notice that the exchange interaction has an attractive (repulsive) effect for the antisymmetric (symmetric) solution in the fermionic model. In the bosonic model we observe the opposite. Finally, since by definition we cannot have a hole and a magnon in the same position we impose a hard-core constrain in the solution $\psi_Q(0) = 0$ by including a very strong on-site repulsion.

After these manipulations the equation of motion Eq. (7.18) describes a single-particle problem which parametrically depends on the total quasi-momentum Q . Therefore, we numerically diagonalize the respective Hamiltonian and obtain the dispersion relation as a function of Q . We find a hole-magnon bound state for the fermionic model and an antibound state in the bosonic one, see Fig. 7.4. The bound and antibound states are antisymmetric with respect to the exchange of the hole and magnon positions. Thus we do not observe binding when the solution is symmetric. The appearance of an antisymmetric bound (antibound) state can be explained by the presence of the interexchange interaction which leads to an effective attraction (repulsion) between the hole and the magnon in the fermionic (bosonic) model.

The minimum of the binding energy appears at $Q = 0$ for any value of J/t . Therefore we define the binding energy at this quasi-momentum $E_B = E_{1H1M} - E_{1H} - E_{1M}$ where E_{1H1M} , E_{1H} and E_{1M} are the groundstate energies for the hole-magnon, the single hole, and the single magnon states respectively. We find the largest binding energy when $J/t = 0$, see Fig. 7.5 (a). This demonstrates that kinetic frustration provides an effective attraction between a hole and a magnon. At the same

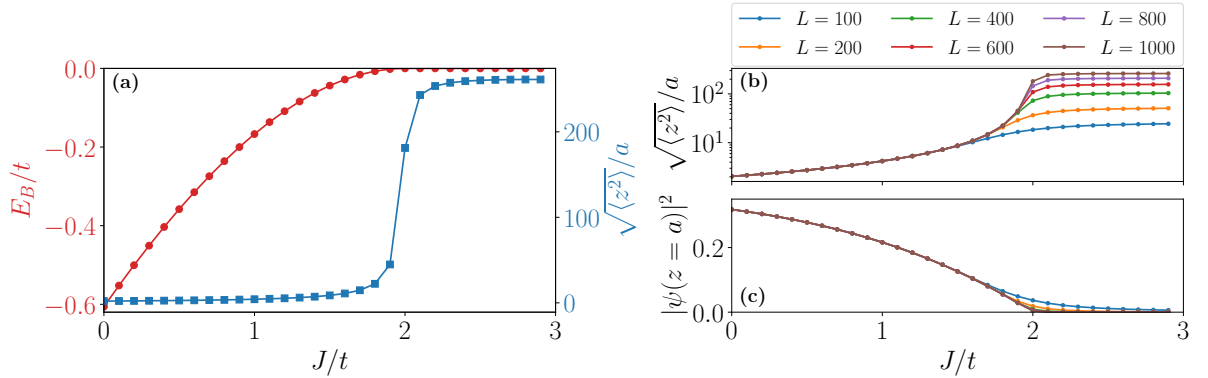


Figure 7.5: Binding energy E_B/t (a) of the hole-magnon pair (red dots) on the fermionic zigzag ladder obtained in the limit of having an infinite ladder by performing a finite size scaling and the hole-magnon pair extension (blue squares) $\sqrt{\langle z^2 \rangle}/a$ for a ladder of 2×500 sites. Extension of the hole-magnon pair $\sqrt{\langle z^2 \rangle}/a$ (b) as a function of J/t for different system sizes. Probability of finding a hole and a flipped spin at a distance equal to the lattice spacing a (c) as a function of J/t for different system sizes.

time the superexchange interaction J provides an effective repulsion between them. To see this effect one can consider the difference of superexchange energies of having a hole and a magnon at adjacent sites relative to the case of being at larger distances, $E_{J,\text{adjacent}} - E_{J,\text{separated}} = J/2$. This shows that in the fermionic system with $J > 0$ having a hole and a magnon on adjacent sites increases the exchange energy. At $J/t = 2$ the repulsion exactly cancels the attraction and the hole-magnon pair vanishes. Moreover, we observe that the dispersion relation at $J/t = 0$ can be well approximated by $E_Q/t = E_B + \sin(Qa/2)^2$. Therefore, the effective mass of the composite object is much larger than the one of a single hole $m_{\text{H-M}}^* \approx 15m_H^*$, being $m_H^* = 2\hbar^2/(15ta^2)$ the effective mass of a single hole in the zigzag ladder.

7.4.2 Finite size scaling

In order to ensure the bound state nature of the hole-magnon pair for a range of J/t we have performed a finite size scaling. We have obtained the binding energy, the extension of the pair and the probability of finding the hole and the magnon in nearest sites, by performing exact diagonalization of the Hamiltonian associated with Eq. (7.16) for large systems sizes. Then we have extrapolated to the infinite size limit, see Fig. 7.5 (b) and (c). The binding energy in the infinite size limit becomes negative for $J/t < 2$ and the probability $a|\psi(z=a)|^2$ becomes zero for $J/t > 2$ as shown in Fig. 7.5 (c). This signals a transition from bound to non-bound pair in the infinite size limit at $J/t = 2$. Moreover the size of the pair is independent of the system size for $J/t < 2$ in the large size limit and it is strongly dependent on it for $J/t > 2$. This also supports the appearance of a hole-magnon bound state at $J/t < 2$ with a characteristic size independent of the system size.

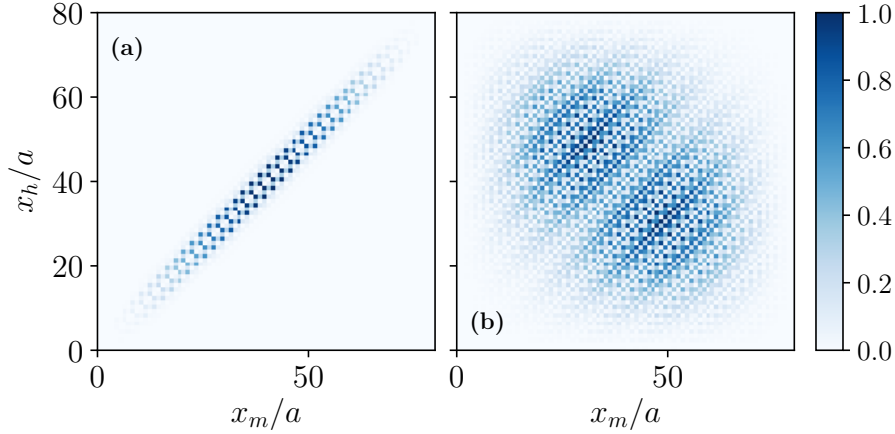


Figure 7.6: Hole-magnon correlation function on the fermionic zigzag ladder for the case of $N_h = N_m = 1$ and different values of the superexchange interaction $J/t = 0.1, 2.2$ for (a) and (b), respectively.

7.4.3 Correlation function

The hole-magnon bound state is characterized by having the two particles close to each other in real space. By construction they are hardcore particles because they cannot occupy the same site. We compute the size of the bound state relative to the lattice spacing $\sqrt{\langle z^2 \rangle}/a$. In the regime of strongest binding, $J/t \rightarrow 0$, the size of the bound state is comparable to the lattice spacing and in fact, it is independent of the system size. With increasing J and decreasing binding energy, the bound state expands, see Fig. 7.5 (a). At $J/t = 2$ the binding energy goes to zero and the size of the bound state reaches the system size. Beyond that it becomes proportional to the system size, indicating a transition from a bound to a non-bound state, see Fig. 7.5 (b). The hole-magnon correlation function $\langle n_i^h n_j^m \rangle$ can be used to see the real space structure of this bound state. To simplify the notation we define the hole and magnon positions x_h and x_m in different figures. They denote the sites at which a hole or a magnon operator acts, such as n_i^h and n_j^m , respectively. For small values of J/t we see that the positions of the magnon and the hole are staying close to each other, see Fig. 7.6. Moreover the correlation function has a peak on adjacent sites which also indicates a small spatial extent of the bound state. With increasing J/t the distance between the hole and the magnon begins to increase and positions of the hole and the magnon become less correlated. These results indicate that analysis of the hole-magnon correlation function should provide direct experimental evidence of the bound state formation.

7.4.4 Multi-body composites

Having demonstrated the formation of a hole-magnon bound state induced by kinetic frustration, we now focus on the formation of multi-body composites. We present the phase diagram of multi-particle bound states in the fermionic zigzag ladder in Fig. 7.7. We note that we perform calculations at fixed ratios of the hole to magnon densities, and with system sizes that are much larger than the number of holes and magnons. Thus the phase diagram shown in Fig. 7.7 should be understood as corresponding

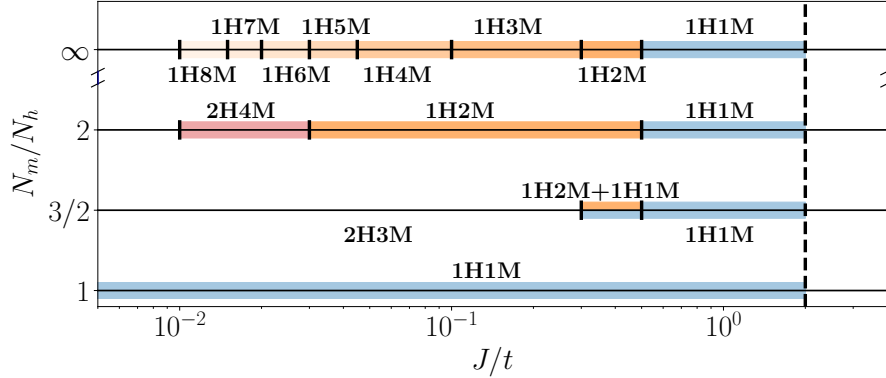


Figure 7.7: Phase diagram of the multi-particle bound states in the fermionic zigzag ladder for different J/t and different ratios of the magnon to hole densities. The vertical dashed line represents the point $J/t \sim 2$ at which the hole-magnon bound states disappears. The ∞ line represents the case of a single hole with an arbitrary number of magnons.

to the limit of vanishingly small concentrations of holes and magnons, with tuning parameters being J/t and the ratio between the densities of holes and magnons. Going to finite density of dopants may result in stabilization of other phases, which we plan to address in future work. The fermionic $t - J$ model in a zigzag ladder exhibits a large zoo of bound states with different numbers of holes and magnons as can be seen in Fig. 7.7. To obtain the transition points between different types of bound states as a function of J/t we have followed a procedure based on the binding energies associated to different decomposition channels. Our first step was to compute binding energies defined previously for different numbers of the holes and magnons. We use this procedure to identify the lowest energy bound states for different values of J/t and different ratios of the hole to magnon densities. Then we double the number of particles and compute the respective binding energy $E_{2N} - 2E_N$. A negative binding energy denotes an effective attraction and particles will cluster and create a larger bound state. Instead a positive binding energy indicates an effective repulsive interaction and two separated bound states appear. This means that we have found the largest possible bound state for this ratio of number of magnons and holes at this value of J/t . Iterating this procedure for different values of N_m/N_h and J/t we obtain the phase diagram presented in Fig. 7.7.

To understand the results presented in Fig. 7.7 it is useful to consider cuts through the phase diagram at fixed N_m/N_h as we vary J/t . We find that generally large J/t favors the decomposition of hole-magnon bound states into free holes and magnons as we have explicitly shown in the single hole-magnon problem. By contrast, for small J/t we find stabilization of large composite objects. For the case $N_m/N_h = 1$ we find that the bound hole-magnon state appears only when $J/t < 2$ in accordance with the two-body problem. Moreover, we do not find formation of larger composites, which suggests that hole-magnon pairs repel each other for equal and small densities of holes and magnons. In Sec. 7.4.4.2 we study different correlations functions showing the effective repulsion between hole-magnon pairs.

For $N_m/N_h = 3/2$ we observe that at $J/t \sim 0.5$ a trimer bound states 1H2M is formed, see Sec. 7.4.4.1 for details on the correlation functions. Between $J/t \sim 0.3$ and $J/t \sim 0.5$ we find that hole-

magnon pairs and trimers coexist, which suggests repulsive interaction between trimers and pairs. For smaller values $J/t < 0.3$ a pentamer 2H3M composed of two holes and three magnons is formed. This indicates that the attraction between holes and magnons induces an effective attraction between two holes. This is the smallest bound state that we have found which includes a pair of holes. In Sec. 7.4.4.3 we show that the pair hole-hole correlation function is peaked at small distances demonstrating hole attraction. For $N_m/N_h = 2$ we find a similar scenario but the hole-magnon trimer appears for a wider range of J/t and an hexamer 2H4M, which includes a pair of holes, appears for a narrow range of J/t . In Sec. 7.4.6 we discuss the many-body phases associated with the pentamer and the hole-magnon pair.

Finally we study a single hole immersed in a fluid of magnons: this is the $N_m/N_h = \infty$ line in Fig. 7.7. By lowering the superexchange interaction J/t we observe that the number of magnons bound to the hole increases. Magnons bound to the hole form a finite size cloud around the hole, a phenomenon that we will refer to as formation of a “spinbag”. Within the spinbag region we observe strong antiferromagnetic correlations of the XY spin components between the two legs of the ladder as shown in Fig. 7.11. This feature is a counterpart of the ferromagnetic spinbag (Nagaoka polaron) found in bipartite lattices (Nagaev, 1992; Alexandrov, 2007; Auerbach, 1998; White and Affleck, 2001). Furthermore, similar to the Nagaoka polaron in the limit $J/t \rightarrow 0$ the bag size becomes of the order of the system size, which in our case indicates that the full system will exhibit antiferromagnetic correlations of the transverse spin components. Antiferromagnetic correlations surrounding the hole alleviate its kinetic frustration by making all possible paths distinguishable, thus lowering the energy. In this way, hole-magnon binding provides an explanation to the origin of antiferromagnetism in non-bipartite lattices (Haerter and Shastry, 2005; Sposetti et al., 2014). In Sec. 7.4.4.4 we present a detailed study of the antiferromagnetic spin bag.

7.4.4.1 Analysis of the 1H2M trimer

In the previous section we discussed that superexchange interaction gives rise to an effective repulsion between a hole and a magnon, which competes with attraction arising from kinetic frustration. The relative strength of these opposing interactions determines the transition between trionic and pair binding on the $N_m/N_h = 2$ line. For small values of J/t the ground state of the system has 1H2M trimers. As J/t increases, the system undergoes a transition in which trimers dissociate into 1H1M pairs and free magnons. Numerically we identify this transition by computing $E_B = E_{1H2M} - E_{1H1M} - E_{1M}$. When the binding energy E_B is negative, a trimer state is stable. When E_B is positive, trimers become unstable to dissociating into hole-magnon pairs and free magnons. We observe that this transition occurs around $J/t \sim 0.5$. Correlation functions can also be used to detect the formation of a trimer. Since these trimers contain two magnons, these bound states can be revealed by observing two magnon bunching in the correlation function $\langle n_i^m n_j^m \rangle$. On the other hand, for large values of J/t , when the system decomposes in a pair and a free magnon, the magnon-magnon correlation function shows that the two magnons are separated by a large distance comparable to the system size, see Fig. 7.8 lower row. Moreover the hole-magnon correlation function always shows that there is a magnon close to a hole (see the enhanced probability close to the diagonal $i_h = j_m$ line in Fig. 7.8 upper row). This can

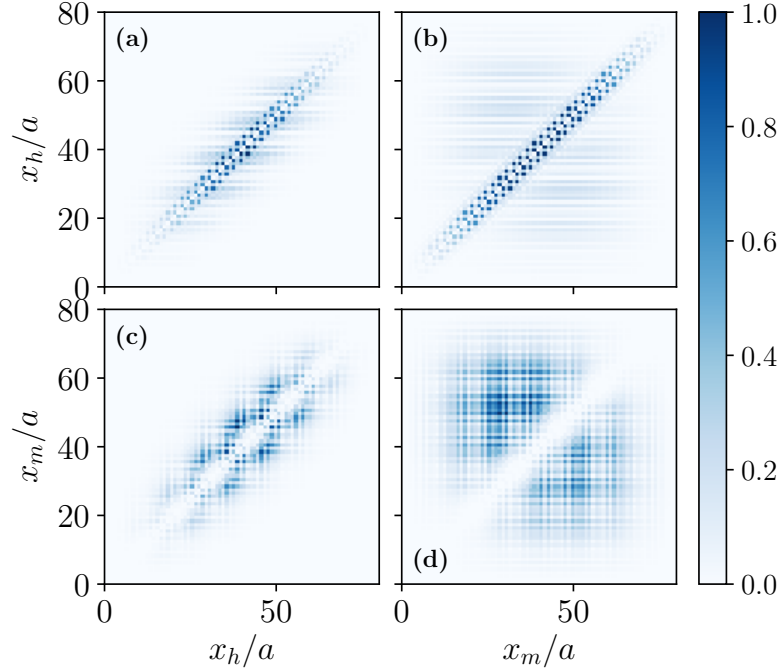


Figure 7.8: Hole-magnon, (a) and (b), correlation function and magnon-magnon correlation function, (c) and (d), on the fermionic zigzag ladder for $N_h = 1$, $N_m = 2$ and two values of the superexchange interaction $J/t = 0.2, 0.6$.

be understood from the observation that for both trimers and 1H1M pairs, we should find a hole and a magnon close to each other.

7.4.4.2 2H2M: Effective repulsive interactions

When multiple hole-magnon pairs are present in the system effective interactions between them appear. In particular, magnons can mediate effective interactions between holes. We analyze whether these effective interactions are enough to bind a pair of holes in zigzag ladders with nearly full spin polarization. Surprisingly we do not find hole pairs for the cases of 2H1M and 2H2M. In the case of two holes and two magnons we observe that the system decomposes into two hole-magnon pairs. The binding energy $E_{2H2M} - 2E_{1H1M}$ approaches zero when we increase the system size for any value of J/t . This indicates that there is an effective repulsive force between hole-magnon pairs. By computing the hole-hole and magnon-magnon correlation we observe that the two holes and the two magnons are separated in space, see Fig. 7.9. On the other hand, the hole-magnon correlation still shows that a hole and a magnon sit close together. This indicates that the system forms two pairs which then stay away from each other.

7.4.4.3 2H3M: Hole pairing

In the zigzag ladder the smallest bound state containing a pair of holes is a pentamer formed by two holes and three magnons. We checked that the binding energy of the pentamer is negative with

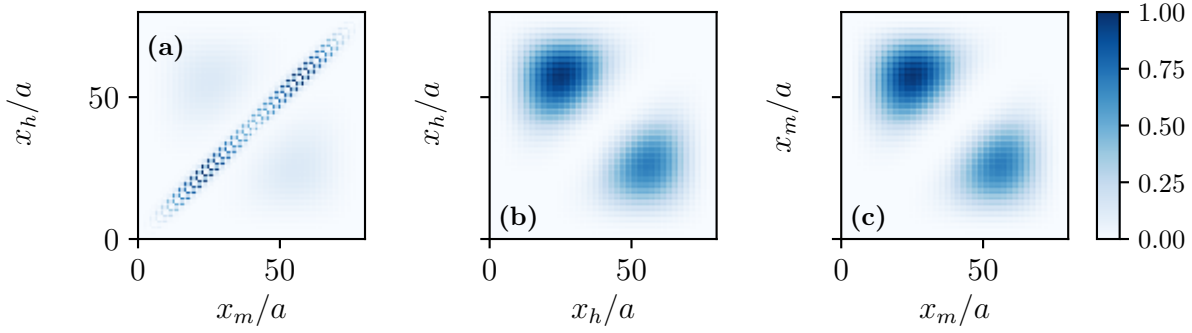


Figure 7.9: (a) Hole-magnon, (b) hole-hole and (c) magnon-magnon correlation functions on the fermionic zigzag ladder for $N_h = 2$, $N_m = 2$ and $J/t = 0.1$.

respect to all possible decompositions into smaller objects when $J/t < 0.3$. We observe however that the binding energy with respect to the decomposition into a trimer and a pair is small. Therefore, although the pentamer is the groundstate of the system, already small temperatures will lead to the breaking of a pentamer into a 1H1M pair and a 1H2M trimer. In the remainder of this subsection we will focus on the properties of the ground state of the system. In order to detect the formation of hole pairs we measure the hole density, see Fig. 7.10. For large values of J/t the hole density exhibits two humps indicating that the holes are separated by a large distance. With decreasing J/t the two humps begin to approach to each other and finally fuse into a single one. After the fusion the two holes share the same region of space forming the pentamer together with three magnons. In order to quantify how far apart the two holes are, we fix the position of the first hole and compute the spatial distribution of the probability density of the second hole. Technically this is done by first projecting the groundstate wavefunction into the state which contains a hole in the center of the lattice (White and Scalapino, 1997),

$$|\psi_h\rangle \equiv \hat{P}_L^h |\psi\rangle = \hat{c}_{L\uparrow} \hat{c}_{L\uparrow}^\dagger \hat{c}_{L\downarrow} \hat{c}_{L\downarrow}^\dagger |\psi\rangle, \quad (7.19)$$

and then computing the density of the second hole defined by,

$$\langle \psi_h | \hat{P}_i^h | \psi_h \rangle. \quad (7.20)$$

We also normalize the state $\langle \psi_h | \psi_h \rangle = 1$. For large values of J/t this probability has maxima at the positions $L/4$ and $3L/4$, which is the expected result for two hardcore particles. When reducing J/t the positions of the two maxima start to approach the center of the lattice. This shows that the two holes start approaching each other, which indicates effective attraction between them and formation of a bound state. As a function of J/t the distance between the two maxima exhibits a minimum value of 2×10 sites at $J/t \sim 0.05$, see Fig. 7.10. We conclude that the pentamer exists but it is a loosely bound object with a relatively large size.

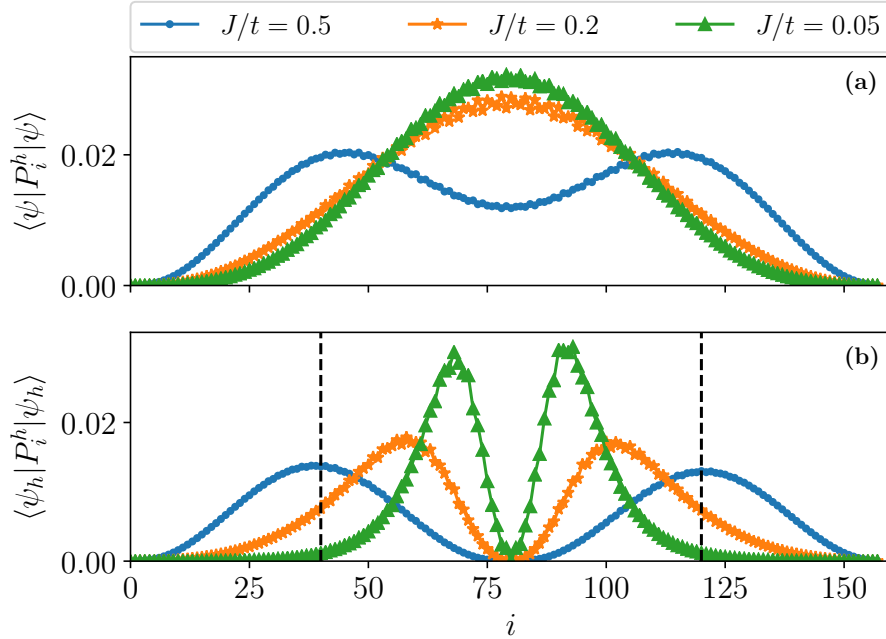


Figure 7.10: Hole density (a) for the case of $N_h = 2$, $N_m = 3$ and different values of the superexchange interaction on the fermionic zigzag ladder. Hole density of the projected state $|\psi_h\rangle$ (b) which has a fixed hole in the middle of the lattice, see main text. We removed the central point to improve visibility.

7.4.4.4 1HNM: Antiferromagnetic spinbag

We now discuss the character of a magnetic polaron when a single hole makes a bound state with several magnons. With this goal in mind we studied systems that consist of a single hole and up to eight magnons. We define the binding energy $E_B^{(N)} \equiv E_{1HNM} - E_{1H} - NE_{1M}$ and then compute the difference $\mu_{mN} \equiv E_B^{(N)} - E_B^{(N-1)}$. This quantity plays the role of a magnonic affinity energy. We present its dependence on the superexchange interaction for different number of magnons in Fig. 7.12 panel (a). The negative value of this quantity indicates that when the N -th magnon is added to the system, it is energetically favorable to attach it to the 1H(N-1)M bound state as an extra bound particle. Addition of magnons will continue to increase the size of the cluster bound to the hole as long as the magnon affinity remains negative. We refer to such clusters of bound magnons as a “spinbag”, see Fig. 7.11. When the magnon affinity becomes positive, the excess magnons are pushed away from the bag. The point at which the magnonic affinity energy changes sign indicates the optimal number of magnons forming a spinbag N_m^* . For small values of J/t the number of magnons inside the spinbag increases which also results in the expansion of its size, see Fig. 7.12 panel (b). A simple scaling analysis can be used to understand the dependence of N_m^* on the ratio J/t . For small values of J/t the antiferromagnetic spinbag is frozen and it acts as an effective potential trapping the hole inside it. Therefore the kinetic energy of the hole decreases for larger spinbags t/N_m^2 . On the other hand, creating the antiferromagnetic spinbag costs an extra magnetic energy JN_m . This competition between kinetic and magnetic energy gives the optimal number of magnons present in the spinbag

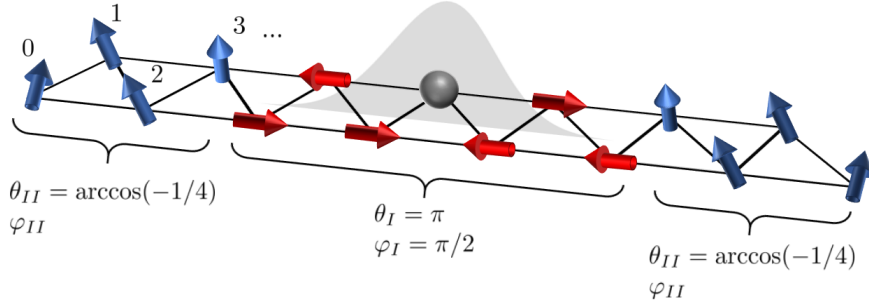


Figure 7.11: Schematic picture of the antiferromagnetic spin bag surrounding a single hole. Inside the spinbag z -components of the spins are suppressed, while the xy components exhibit antiferromagnetic correlations between two sites of different legs. For clarity of presentation, in the figure we oriented transverse components to point along the y axis. Outside the spinbag, we find spiral winding of the xy components of the spins and z -magnetization approaching its asymptotic value. The two angles θ and φ characterize the magnetic orders present in the system. They correspond to the angles between two adjacent spins in different legs in the xy plane and with respect to the z axis, respectively. We define two regions: Region (I) inside the spinbag and region (II) outside of it. In order to perform numerical calculations we map the ladder to a one-dimensional system in which the sites are indexed following the zigzag pattern specified by the numbers.

$N_m^* \propto (t/J)^{1/3}$. Similar scalings have been found for the magnetic polaron in a two-dimensional square lattice (Shraiman and Siggia, 1988a; White and Affleck, 2001; Grusdt et al., 2018a). Let us present a semiclassical theory quantifying the antiferromagnetic spinbag.

An analytical treatment of the spinbag problem using the Hamiltonian (7.16) is very hard since the hole hopping disturbs the spin background. Therefore we change to a representation where the hole lives in the links of a new lattice with $2L - 1$ sites i.e. the squeezed space (Ogata and Shiba, 1990; Ren and Anderson, 1993; Zaanen et al., 2001; Kruis et al., 2004; Hilker et al., 2017; Bohrdt et al., 2018). In this way the hole hopping between the two legs of the ladder simply becomes $(t \sum_i \hat{h}_{i+1}^\dagger \hat{h}_i + \text{h.c.})$ since it does not disturb the spin order in squeezed space. On the other hand, for the hole hopping between two sites of the same leg we have to take into account that two spins are exchanged in squeezed space. The operator doing such process is $(\hat{h}_{i+2}^\dagger \hat{h}_i + \hat{h}_i^\dagger \hat{h}_{i+2}) (\frac{1}{2} + 2 \mathbf{S}_i \mathbf{S}_{i+1})$. Concerning the spin interaction we have to take into account that two spins will not interact if a hole was occupying one of the two sites in the original lattice, giving the term $J \mathbf{S}_i \mathbf{S}_{i+1} (1 - \hat{h}_i^\dagger \hat{h}_i)$ and $J \mathbf{S}_i \mathbf{S}_{i+2} (1 - \hat{h}_i^\dagger \hat{h}_i) (1 - \hat{h}_{i+1}^\dagger \hat{h}_{i+1})$. Moreover if a hole is present in the original lattice between two spins these two will be nearest neighbor in squeezed space and they will interact through the superexchange coupling $J \mathbf{S}_i \mathbf{S}_{i+1} \hat{h}_i^\dagger \hat{h}_i$. Therefore the Hamiltonian in squeezed space becomes,

$$\begin{aligned}
\hat{H}_{t,J} &= t \sum_i (\hat{h}_{i+1}^\dagger \hat{h}_i + \text{h.c.}) + J \sum_i \mathbf{S}_i \mathbf{S}_{i+1} \\
&+ t \sum_i (\hat{h}_{i+2}^\dagger \hat{h}_i + \hat{h}_i^\dagger \hat{h}_{i+2}) \left(\frac{1}{2} + 2 \mathbf{S}_i \mathbf{S}_{i+1} \right) \\
&+ J \sum_i \mathbf{S}_i \mathbf{S}_{i+2} (1 - \hat{h}_i^\dagger \hat{h}_i) (1 - \hat{h}_{i+1}^\dagger \hat{h}_{i+1}).
\end{aligned} \tag{7.21}$$

We notice that the Hamiltonian in squeezed space presents terms which explicitly couple the hole movement and the spin environment, see the second and third line of Hamiltonian (7.22). These terms are absent in the pure one-dimensional case being the reason for spin-charge separation in one-dimension (Ogata and Shiba, 1990; Ren and Anderson, 1993; Zaanen et al., 2001; Kruis et al., 2004; Hilker et al., 2017; Bohrdt et al., 2018). Therefore, we conclude that the original frustration of the hole inducing an intrinsic spin-charge coupling is transformed into explicit terms coupling the two degrees of freedom in the squeezed space. It is also important to remark that the coupling with strength t induces strong antiferromagnetic correlations between the two legs even though the original Ising interaction is not present for $J/t = 0$. This explains the origin of antiferromagnetic correlations of strength t in the zigzag ladder when the system is doped with holes. These antiferromagnetic correlations between the two legs will appear when a hole is present and the direct hopping dominates over the superexchange interaction $t/J \gg 1$. The original superexchange interaction presents magnetic frustration and at the semiclassical level it favours the formation of a spiral order of angle $\theta = \arccos(-1/4)$. Since we work at a fixed total magnetization (i.e. a fixed number of magnons) we expect that the system can be understood as consisting of two regions: Region (I) is adjacent to the hole and has spins in the XY plane with antiferromagnetic correlations between the legs. Region (II) extends outside of region (I), has nearly full S^z polarization and spiral winding of the small XY components of the spins, see Fig. 8.6.

To obtain qualitative expressions for the size and energy of the antiferromagnetic spinbag we consider a semiclassical approximation of the spin part of the wavefunction $\mathbf{S}_i \mathbf{S}_{i+1} = \tilde{S}^2 (\sin(\varphi)^2 \cos(\theta) + \cos(\varphi)^2)$ with $\tilde{S}^2 = S(S+1) = 3/4$. The angles θ and φ determine the spin orientation in the XY plane and the angle respect to the z axis, respectively, see Fig. 8.6. Therefore we can relate the total number of magnons N_m and the size of the antiferromagnetic spinbag $2R$ using the angle φ_{II} ,

$$\cos(\varphi_{II}) (L - R) = L - N_m. \quad (7.22)$$

By considering the limit $J/t \ll 1$ we assume a frozen magnetic order and solve the equation of motion for the hole with a fixed spin background along the lines of the Born-Oppenheimer approximation. The hole equation of motion in each region is given by,

$$\begin{aligned} (I) : E_h h_i &= t(h_{i+1} + h_{i-1}) - \frac{3J}{4}(h_i + h_{i+1}) \\ &- t(h_{i-2} + h_{i+2}), \end{aligned} \quad (7.23)$$

$$\begin{aligned} (II) : E_h h_i &= t(h_{i+1} + h_{i-1}) \\ &+ \frac{3J}{32}(15 \cos(\varphi_{II})^2 - 7)(h_i + h_{i+1}) \\ &+ \frac{t}{8}(15 \cos(\varphi_{II})^2 + 1)(h_{i-2} + h_{i+2}). \end{aligned} \quad (7.24)$$

These equations show that the hole energy is reduced when it is localized inside the antiferromagnetic region (I). Thus the antiferromagnetic background acts as an effective square well potential to the hole. In order to obtain an analytical expression for the hole energy E_h we solve the hole equation of motion by taking the continuum limit and proposing a wavefunction localized in the antiferromagnetic

region $h_i = \exp\{-x_i^2/(R^2)\}/\sqrt{R\sqrt{\pi/2}}$, where we choose an optimal width of the hole wavefunction. Moreover Eq. (7.22) establishes the relation between the size of the bag R and the angle φ_{II} when the total number of magnons is specified. Taking the limit $L \ll R \sim N_m \ll 1$ we obtain a hole energy that scales with the number of magnons as,

$$E_h \propto 4.28 \frac{t}{N_m^2} - 0.04 \frac{J}{N_m}. \quad (7.25)$$

We now consider the magnetic energy cost of creating an antiferromagnetic spinbag. We compare the magnetic energies with the same number of magnons when there is an antiferromagnetic spinbag and when there is not. In the first case the antiferromagnetic region has zero magnetic energy and the spiral region has an energy E_{M1} which is determined by the angle φ_{II} (see Eq. (7.22)) and the size of the spinbag R . In the second case the full ladder presents a spiral order with energy E_{M2} and an angle satisfying $\cos(\varphi)L = L - N_m$. The difference between these two magnetic energies in the limit $L \gg R \gg 1$ is,

$$E_{M1} - E_{M2} \propto \frac{51}{8} JN_m. \quad (7.26)$$

The magnetic energy increases when creating an antiferromagnetic spinbag because the angle φ of the spiral order is reduced. The total energy of the antiferromagnetic spinbag is given by,

$$E_{ASB} = 4.28 \frac{t}{N_m^2} - 0.04 \frac{J}{N_m} + \frac{51}{8} JN_m, \quad (7.27)$$

where we discard the constant terms with respect to the number of magnons. From Eq. (7.27) we observe that increasing the size of the antiferromagnetic spinbag reduces the hole kinetic energy but increases the magnetic one. Therefore there is an optimal number of magnons forming the antiferromagnetic spinbag N_m^* . Considering the situation of a small antiferromagnetic region compared with the spiral region $L \gg R \sim N_m \gg 1$ we can estimate the number of magnons,

$$N_m^* \propto 1.10 (t/J)^{1/3}, \quad (7.28)$$

considering the condition $(J/t) \ll 1$.

The semiclassical spinbag theory predicts that under doping the fermionic zigzag ladder with a single hole and magnons, a certain number of magnons, given by Eq. (7.28), accumulate around the hole with an antiferromagnetic ordering and the remaining ones are pushed away from this region forming a spiral order with a net magnetization pointing in the z axis, see Fig. 8.6. In order to benchmark our theory we have performed DMRG simulations of the fermionic zigzag ladder with a single hole and different number of magnons. We observe that for small values of J/t , the hole density accumulates in a certain region of the lattice, see panel (d) of Fig. 7.12. This can be attributed to the large effective mass of the antiferromagnetic spinbag and the fact that we are working with open boundary conditions thus explicitly breaking the translational invariance of the system. By computing the projected wavefunction $\hat{P}_L^h |\psi\rangle = |\psi_h\rangle$ which has a hole fixed at the center of the lattice we obtain the spin ordering surrounding the hole (White and Scalapino, 1997). Around the hole

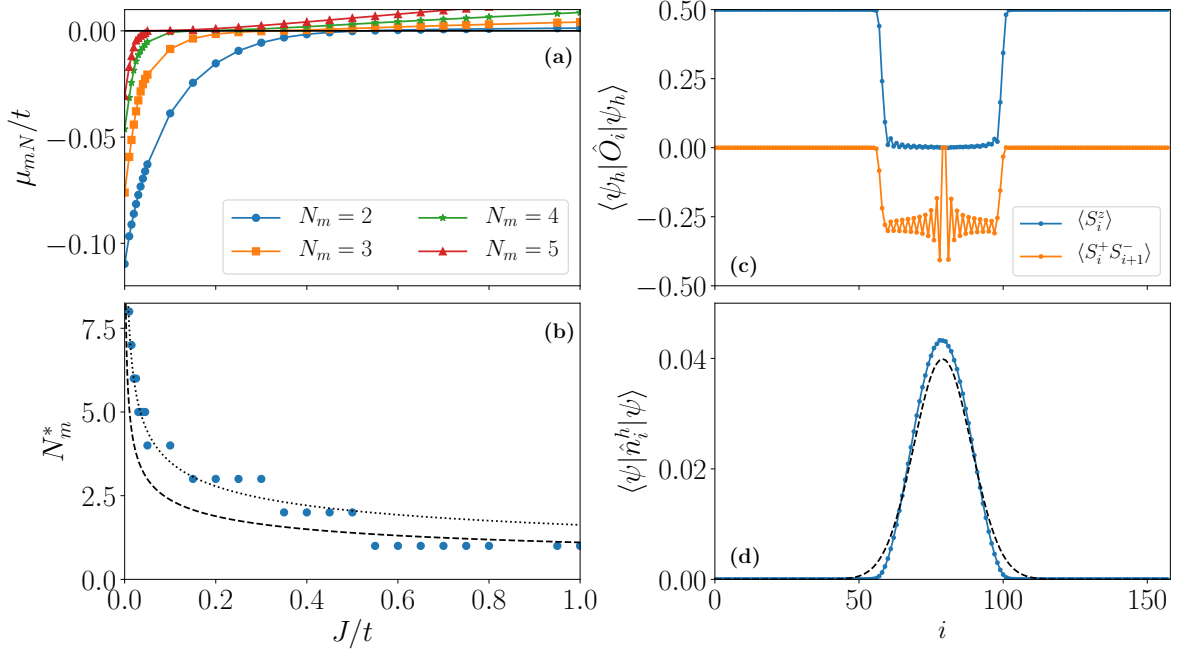


Figure 7.12: Panel (a): Magnonic affinity energy μ_{mN}/t on the fermionic zigzag ladder as a function of the superexchange interaction for the cases with $N_h = 1$ and different numbers of magnons. Panel (b): Number of magnons forming the antiferromagnetic spinbag N_m^* as a function of the superexchange interaction J/t . Dashed line represents the analytical result for the antiferromagnetic spinbag $N_m^* \propto 1.10(t/J)^{1/3}$. Dotted line is the fit to numerical data which gives $N_m^* \propto 1.63(t/J)^{1/3}$. Panel (c): Magnetization and in-plane spin-spin correlations computed over the projected wavefunction $|\psi_h\rangle$ for which we fix the hole position to be at the center of the lattice. Panel (d): Hole density of the groundstate obtained from DMRG (blue dots) and from the variational calculation (dashed line). Both panels correspond to a computation of the fermionic zigzag ladder with a single hole and 20 magnons for $J/t = 0$.

the magnetization suddenly decays indicating that the spins tilt to the XY plane. Moreover the in-plane spin-spin correlations show an antiferromagnetic order inside this region. Outside this region we recover a perfect ferromagnetic spin order, see panel (c) of Fig. 7.12. This confirms the formation of an antiferromagnetic spinbag for small values of J/t . Notice that the simulation is performed at $J/t = 0$. Therefore all the magnons are contained in the antiferromagnetic spinbag and the spiral order simply becomes a ferromagnetic order since $\varphi = 0$.

7.4.5 Dynamical probes

So far we discussed hole-magnon and other composites at zero temperature. We expect that at temperature smaller than the binding energies our conclusions will remain accurate. However, when temperature exceeds the binding energy, we expect composites to dissociate. Thus one of the practical challenges for experimental observation of the bound states that we discussed in previous sections is the requirement of cooling systems to temperatures below the binding energies. This difficulty is exacerbated by the requirement of having strongly polarized Fermi mixtures for which Pauli principle

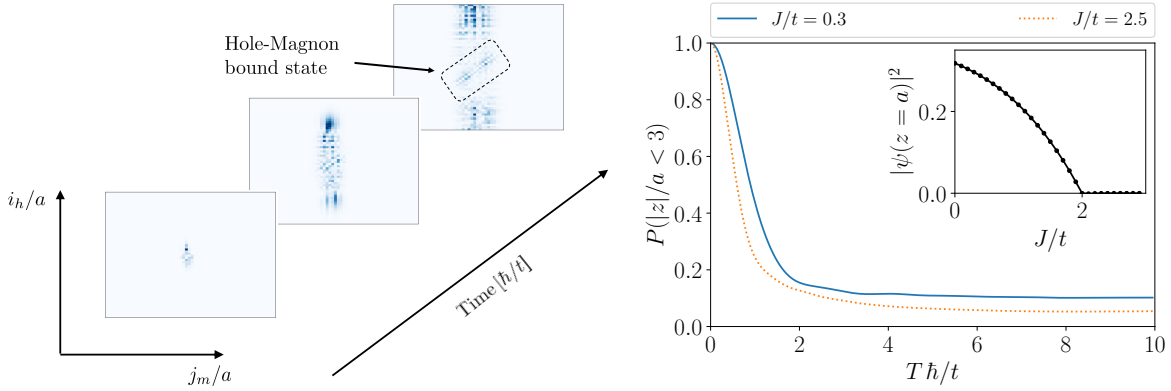


Figure 7.13: Left panel: Dynamics of a hole-magnon pair in the zigzag ladder. Hole-magnon correlation function $\langle \hat{n}_i^h \hat{n}_j^m \rangle$ computed at different times for $J/t = 0$. The initial state corresponds to putting a hole and a flipped spin in adjacent sites in the middle of the lattice. At long times a diagonal part can be discerned showing the correlated expansion of the hole and the magnon bound together. Right panel: Probability of finding a hole and a flipped spin at a relative distance less than three lattice sites $P(|z|/a < 3)$ as a function of time for a fermionic zigzag lattice of 2×50 sites for two values of J/t . Inset panel: Probability of finding the hole and magnon at a relative distance $z = a$ as a function of J/t obtained in the limit of having an infinite ladder by performing a finite size scaling.

cuts off contact interactions and suppresses thermalization. An alternative is to perform dynamical experiments. To be concrete we consider the case of a 1H1M pair, however, this discussion can be generalized to arbitrary nHmM composites. The idea is as follows: use external local potential and/or local optical spin control to prepare an initial state in which a hole and a magnon are localized on neighboring sites. Switch off the localizing potential and let the system evolve under the many-body Hamiltonian. When there are no bound (antibound) states, the two particles will spread out essentially independently and the probability to find them next to each other should eventually decrease to zero (in a finite system it will saturate to a finite value set by inverse of the system size). On the other hand, when there is a bound (or antibound) state in the spectrum, we will find a finite probability that the magnon and the hole spread out together. In Fig. 7.13 we show dynamics in the zigzag ladder starting from the initial state in which one hole and one magnon have been prepared on neighboring sites. We observe that the joint probability distribution function remains peaked where the two particles are close to each other. The probability to find the two particles together after a long evolution time is given by the overlap between the bound state wavefunction and the initial state. In the inset of Fig. 7.13 we present the probability of finding the hole and the magnon at nearest sites as a function of the superexchange coupling J/t . The overlap between the initial state of the time evolution and the hole-magnon bound state is around 0.3 for $J/t = 0$. The finite overlap of the initial state with the bound state ensures that during the coherent evolution there is a finite probability for the hole and the magnon to stay close to each other as shown in Fig. 7.13. In order to avoid finite size effects we have performed dynamical simulations up to the point where the hole or magnon touches the ends of the system. These finite time and finite size simulations make the probability to always saturate to a finite value even if no bound state is present. To dynamically discern the formation of a

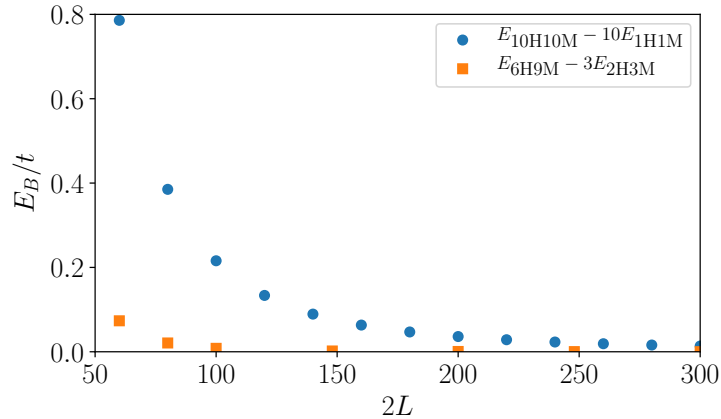


Figure 7.14: Binding energies relative to the hole-magnon pair 1H1M $E_B = E_{10H10M} - 10E_{1H1M}$ (blue dots) and the pentamer 2H3M $E_B = E_{6H9M} - 3E_{2H3M}$ (orange squares) for the fermionic zigzag ladder as a function of the lattice length $2L$.

hole-magnon bound state we require to have saturation values much larger than one over the system size. For small values of J/t we observe saturation values that can be ten times larger than one over the system size. Hence such “quantum walk” like dynamics (Preiss et al., 2015) starting from the adjacent hole-magnon configuration can reveal the existence of the bound state. The dynamical observation of hole-magnon bound states could be addressed in current ultracold atom experiments with a quantum gas microscope (Bakr et al., 2009; Sherson et al., 2010; Parsons et al., 2015; Cheuk et al., 2015; Omran et al., 2015; Haller et al., 2015; Edge et al., 2015; Greif et al., 2016; Brown et al., 2017; Weitenberg et al., 2011; Yang et al., 2021). A similar experimental technique has been used previously in the Mott insulating regime of two component bosons to demonstrate the existence of two magnon bound states in the Heisenberg model in one-dimension (Fukuhara et al., 2013b).

7.4.6 Many-body phases

In this section we review many-body states that emerge in systems with many bound states. More formally we analyze zigzag ladders as we increase the number of holes and magnons while keeping the ratio N_m/N_h fixed. After identifying “optimal” multi-particle bound states, we do not find further clustering. This suggest that optimal composites of holes and magnons exhibit repulsive interactions with each other. We begin by discussing the situation of small densities, when the interaction between different bound states is much smaller than the binding energy. In this regime the system can be understood as a dilute fluid of weakly interacting bound states, and the total energy of the system E_{NB} should be equal to $N_B E_{1B}$, where E_{1B} is the energy of a single bound state and N_B is the number of bound states (see Fig. 7.14). We present results of these calculations for the cases of 10H10M and 6H9M where the energy of the system converges to $10E_{1H1M}$ and $3E_{2H3M}$, respectively. In the first case the energy converges slowly with the system size. In the second case the energy converges to the asymptotic value already for small sizes. This indicates strong repulsive interactions between pentamers which forces them to avoid spatial overlap.

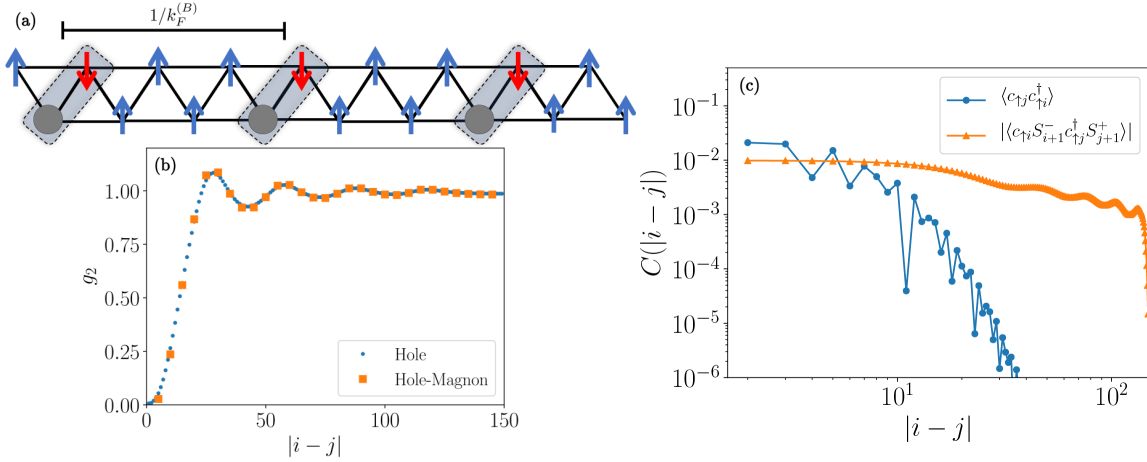


Figure 7.15: Panel (a): Schematic representation of a self-organization of hole-magnon pairs in the fermionic zigzag ladder. Hole-magnon pairs form a Luttinger liquid with a characteristic Fermi momentum $k_F^{(B)} = \pi n_B$ given by the density of pairs n_B . Panel (b): Pair correlation function of single holes and hole-magnon pairs in the fermionic zigzag ladder for $J/t = 0$ and $N_h = N_m = 10$. Panel (c): Correlation functions of holes (dots) and hole-magnon pairs (upper triangles) on the fermionic zigzag ladder for $N_h = 10$, $N_m = 10$ and $J/t = 0$. We note that operators c_σ denote the original fermionic operators.

7.4.6.1 Luttinger liquid of composite fermions

Our next step is to establish the best physical picture of the quantum fluids of bound states. As our first example we analyze a system in which we increase the densities of holes and magnons but fix the ratio $N_m/N_h = 1$. 1H1M pairs exhibit strong binding with the scale of the binding energy set by t and effective repulsive interaction between pairs. This suggests that the many-body state can be understood as a Luttinger liquid of 1H1M pairs. In order to show the paired nature of the liquid we define the pair correlation function of hole-magnon pairs for $i > j$,

$$g_2 = \frac{\langle n_i^c n_j^c \rangle}{\langle n_i^c \rangle \langle n_j^c \rangle}, \quad \text{with,} \quad n_i^c = n_i^h n_{i+1}^m + n_i^m n_{i+1}^h, \quad (7.29)$$

being n_i^h and n_i^m the hole and magnon density on site i , respectively. This correlator shows that every hole in the system is accompanied by a magnon on an adjacent site, see Fig. 7.15 panel (b). This result strongly supports the hypothesis of the liquid of pairs, but we need to provide additional verification that the long range part of correlations is consistent with the Luttinger liquid phase.

The Luttinger liquid of bare holes and the Luttinger liquid of hole-magnon composites can be rigorously distinguished by identifying the operators that decay most slowly in space. To this end we compute two types of correlation functions: the correlation function of bare holes $\langle \hat{c}_{\uparrow i} \hat{c}_{\uparrow j}^\dagger \rangle$ and the correlation function of pairs $\langle \hat{c}_{\uparrow i} S_i^+ \hat{c}_{\uparrow j}^\dagger S_j^- \rangle$ (see Fig. 7.15 panel (c), we also note that here operators c_σ correspond to the original fermionic operators). The hole correlation function has an exponential decay indicating that we cannot characterize the system as a Luttinger liquid of individual holes. On the

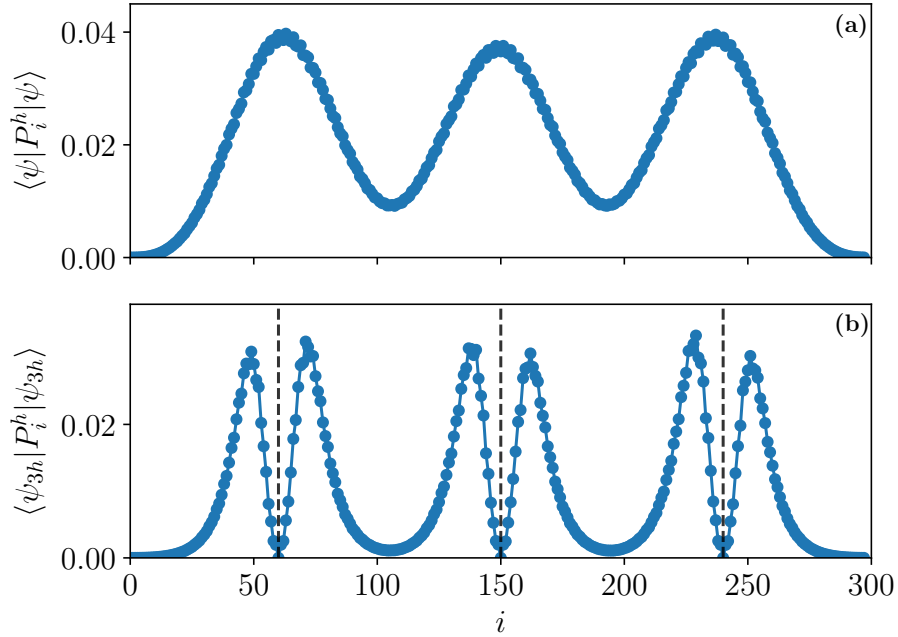


Figure 7.16: Hole density on the fermionic zigzag ladder (a) for the case of $N_h = 6$ and $N_m = 9$ at $J/t = 0.05$. Hole density of the projected wavefunction $|\psi_{3h}\rangle$ (b) which has three holes fixed at the positions specified by the dashed lines.

other hand, the correlation function for pairs exhibits a much slower decay, which for large distances approaches a power-law decay with oscillations with a characteristic length scale $1/(\pi n_B)$ set by the pair density $n_B = N_h/(2L) = N_m/(2L)$ as predicted by Luttinger liquid theory (Giamarchi, 2003). This indicates that a paired Luttinger liquid appears when the number of magnons is equal to the number of holes and $J/t < 2$.

7.4.6.2 Pair density wave

In the earlier discussion of energetics we pointed out evidence of strong repulsive interactions between pentamers. The repulsive interactions between pentamers provides the opportunity to explore a many-body phase of pairs of holes. We will now discuss numerical evidence that pentamers form a crystal like phase. We call this state a pair density wave phase because every pentamer is a charge two object. The hole density presented in Fig. 7.16 provides a strong indication of the pair density wave. In a system with six holes we find three strong peaks in the density with very low density between the peaks. This suggests that 2H3M pentamers are strongly localized. Moreover by fixing the position of three holes and computing the hole density for the remaining three ones we observe that the latter are strongly localized close to the positions of the three fixed holes, see Fig. 7.16 panel (b). In the middle region between two bound pairs of holes the probability of finding another hole is negligible. Furthermore these densities seem very similar to the one found for a single pentamer in Fig. 7.10 panel (b). Before concluding this discussion we point out that to rigorously define a crystal phase in 1d in the thermodynamic limit requires spontaneous breaking of discrete translational symmetry. Breaking of

translational symmetry is only possible for rational densities of pentamers. For irrational densities one can at most find quasi-long range order. Presence or absence of the long range crystal order is expected to depend strongly on the precise pentamer density. To identify true long range order in numerics calls for analyzing large system sizes. We postpone this investigation to subsequent publications.

7.5 Spin-1/2 bosons in the zigzag ladder

7.5.1 Anti-bound states

The fermionic $t - J$ model in a zigzag ladder presents the unique opportunity to explore the attraction between holes and magnons and thus attractive bound states coming from kinetic frustration. On the other hand, repulsive hole-magnon bound states (antibound states) driven by kinetic frustration can be found in the bosonic case, see the discussion in Sec. 7.4.1. These states are also characterized by having the hole and magnon close in real space but their energy is higher than the scattering continuum, see Fig. 7.4. Thus these are not the groundstate of the system. As we will show there is a direct transformation relating the hole-magnon bound state in both models.

7.5.2 The Bose-Fermi mapping

As we have anticipated in Sec. 7.4.1 the $t - J$ model close to fully polarized insulating states can be written in the form of Eq. (7.16) where there is a relative minus sign in hopping terms between the fermionic and bosonic system. Moreover the superexchange coupling also changes sign when going from bosons to fermions $J = \pm 4t^2/U$ being positive for fermions and negative for bosons (Duan et al., 2003; Anderson, 1950; Hofstetter et al., 2002). This establishes a connection between the fermionic and bosonic $t - J$ models,

$$\hat{H}_{t-J}^F \iff -\hat{H}_{t-J}^B. \quad (7.30)$$

If a hole-magnon bound state appears below the scattering continuum for the fermionic case it also appears above the continuum for the bosonic case, see Fig. 7.4. This sets a connection between attractive (fermionic) and repulsive (bosonic) bound states for $t - J$ models.

This symmetry allows us to relate the time evolution presented in Sec. 7.4.3 for a fermionic system to the one that could be obtained for a bosonic system. Since the two Hamiltonians are related by a minus sign $\hat{H}_{t-J}^F \iff -\hat{H}_{t-J}^B$ but the procedure satisfies dynamical symmetry analogous to the one discussed in Ref. (Schneider et al., 2012) we expect the time evolution to be identical in both cases. Therefore far-from-equilibrium probes as the ones presented in Sec. 7.4.5 can be used either to detect attractive (fermionic) or repulsive (bosonic) bound states.

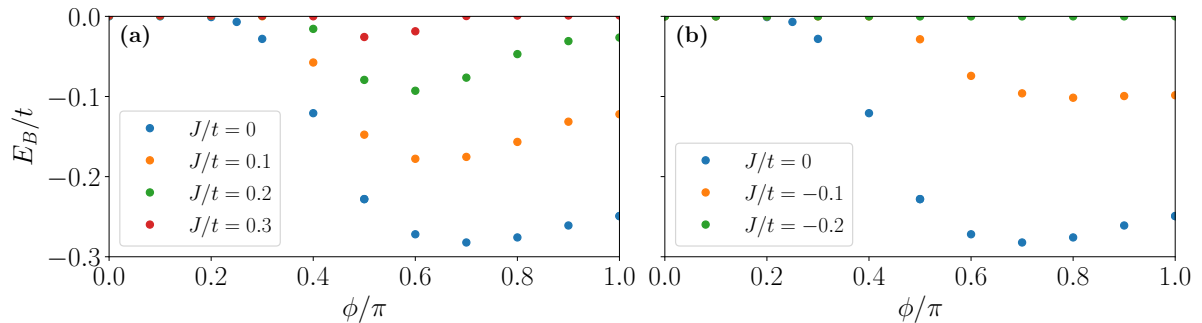


Figure 7.17: Binding energy of the hole-magnon for a square ladder as a function of the perpendicular magnetic flux for different values of the superexchange interaction. The fermionic case corresponds to (a) and the bosonic one to (b).

7.6 Spin-1/2 fermions and bosons in a square ladder with a perpendicular magnetic flux

A single hole propagating in a ferromagnetic background in a non-bipartite lattice always experiences kinetic frustration. However in a square lattice the kinetic energy of a single hole can also become frustrated if different paths contribute with different relative phases. Therefore we explore the formation of hole-magnon bound states in a square ladder with magnetic flux.

The single hole spectrum for the regular ladder with flux is symmetric under a change of sign of the single particle hopping, see Sec. 7.2.2. Thus starting with a spin polarized band insulator for fermions or a Mott insulator of bosons with $n = 1$, we expect to find identical single particle spectra of individual holes. This proves that attractive bound states are present for both bosonic and fermionic systems, in contrast to the zigzag ladder studied above, where fermionic systems present a bound state while bosonic ones present an antibound state. In Fig. 7.17 we present the binding energies for the fermionic case, panel (a) ($J/t > 0$), and the bosonic one, panel (b) ($J/t < 0$). Since we still have the property that fermionic and bosonic models written in terms of hole and magnon operators differ by the sign, we infer that in both systems attractive and repulsive bound states are present. The wavefunction that describes an attractive/repulsive bound state for fermions also describes a repulsive/attractive bound state for bosons.

7.7 Conclusions and outlook

The main result of our work is a demonstration of the effective attractive interaction arising from kinetic frustration of distinguishable particles. These interactions lead to formation of several types of multi-particle complexes, which can then result in several types of interesting many-body phases. In this chapter we focused on two component Bose and Fermi mixtures and two types of frustrated lattices: zigzag ladders and square ladders with a flux. We studied the regimes close to fully polarized insulating states, when these systems can be naturally described in terms of doped holes and magnons, i.e. flipped spins. We made concrete predictions for the phase diagrams of these models including identifying the

most stable multi-particle bound states and understanding many-body states that emerge from the interaction of such composites. We expect that qualitatively, the results of our work should be valid to general models with kinetic frustration.

We used analysis of binding energies and correlation functions to discern the lowest energy multi-particle bound states for different values of the interaction strength and several representative density ratios. Examination of the correlation functions also allowed us to scrutinize the internal structure of these multi-particle bound states. We show that the system has a tendency to create an antiferromagnetic background around the position of the hole. This antiferromagnetic background acts as an effective potential to the hole which confines it in this region. This object can be understood as a multi-particle bound state of many magnons and a single hole and we term it an antiferromagnetic spinbag. When adding a second hole to the system an effective attraction between the two holes can be found. We show that the minimal configuration exhibiting a pair of two holes is a pentamer composed of two holes and three magnons.

We identified a generic dynamic symmetry between the fermionic and bosonic Hubbard models close to spin polarized insulating states. We demonstrated that expressing these models in terms of the hole and magnon operators gives rise to effective Hamiltonians which differ only in the overall sign. This symmetry maps the low energy states of the fermionic model to the high energy states of the bosonic model. Therefore when a bound state is present in the fermionic system we should find an antibound state for the bosonic system and vice versa: a bound state for bosonic system implies an antibound state for the fermionic system.

We discussed dynamical experiments which can be used to probe formation of multiparticle bound states. In particular, we considered a protocol for a fermionic system in a zigzag ladder in which a hole and a flipped spin are initialized on neighboring sites. After the hole and the magnon are released, we find that their coherent dynamics can be decomposed into two contributions: in the first one the hole and the magnon expand essentially independently of each other, and in the second one they move together. The latter part can be understood by observing that the initial configuration has a large overlap with the 1H1M bound state, which results in the hole-magnon pair expanding as a whole. Because of the dynamic symmetry between the fermionic and bosonic models, this procedure can be applied either for detecting a bound state for fermions or an antibound state for bosons. Moreover this probe could be generalized to systems with more holes or magnons in order to detect larger multi-particle bound or antibound states.

Our work extends beyond analysis of individual multi-particle bound states. We discuss several many-body phases that can be understood from the perspective of self organization of the multi-particle bound states. We argue that higher order correlation functions provide direct signatures of the emergent many-body states of composite objects and review two concrete examples. Our first example is a Luttinger liquid of 1 hole - 1 magnon pairs. We show that in this case composite operators for the hole-magnon pairs exhibit much slower spatial decay than operators of the original particles. The second example we discuss is a crystal of pentamers, in which every pentamer is comprised of two holes and three magnons. We refer to this phase as a pair density wave state since a pentamer is a charge two object.

Our work on multi-particle bound state formation due to kinetic frustration can be extended in several directions. Powerful experimental tools developed for cold atomic ensembles in optical lattices allow to satisfy two criteria at the same time: relevance to current technologies and richness of theoretically expected phenomena. A promising direction is to analyze ladders in which tunneling/interactions within the chains and between them are different. Applying potential gradients also allows to realize mixed dimensional systems, in which along certain directions there is exchange interaction but no single particle tunneling (Grusdt et al., 2018b). In the case of bosonic systems one can also consider Hubbard models in which interactions are not $SU(2)$ symmetric. This should translate into the anisotropy of exchange interactions (Jepsen et al., 2020a, 2021). We discussed in Sec. 7.4 that the Ising part of the interaction contributes to the repulsive interaction between a magnon and a hole. Thus by making the z -axis part of the exchange interaction stronger, we expect to find suppression of magnon-hole binding, which should in turn affect stability of all multi-particle composites. A more detailed analysis of multi-particle formation and self-organization in systems with magnetic flux is also an interesting future directions. By adding an external perpendicular magnetic flux the frustration can be increased and thus provide a stronger binding. For the square ladder we find that binding becomes stronger around $\Phi/\pi \approx 0.7$. This should make multi-particle systems, for which we find binding energies to be small, easier to observe in experiments.

Our results indicate that hole pairing is strongly suppressed for ladders relative to the 2D case. A possible explanation is that the hole pairs in two dimensions form at finite angular momentum and in ladders they are suppressed because they cannot fully expand in the perpendicular direction. From the results of Ref. (Zhang et al., 2018b) one expects that 2D systems exhibit hole pairing arising from formation of 2 holes - 1 magnon trimers. An interesting question then is to extend our work to a larger number of legs and study the transition from the quasi-1D geometry to the full 2D one.

The antiferromagnetic spinbags that we find provide an intriguing analogy to the quark bag model used to explain the asymptotic freedom of QCD. In our system the antiferromagnetic background provides an effective static potential to the holes. While holes are fast degrees of freedom, they become trapped inside these antiferromagnetic regions. A possible future perspective would be to exploit this analogy and study the backreaction of the bag to the hole movement. We expect that this will allow to find excitations of composite particles in our system that are analogous to excitations of hadrons considered in the context of the bag model (Hasenfratz and Kuti, 1978). In particular we anticipate vibrational modes, that can be visualized as a hole “rattling” inside the AF bag, as well as surface modes, that correspond to local displacements of the bag with respect to its equilibrium position around the hole. The latter family of excitations should be particularly interesting in the 2D setting. Finally, this analogy could be used to explore other directions with the goal of providing new insight into interesting open questions regarding the nature of confinement. One particularly intriguing question is to use an experimental platform of frustrated quantum systems to realize an analogue of the transition between the hadronic and paired phases, expected in QCD at higher density. Many questions remain poorly understood regarding this phase transition, including the possibility of some intermediate exotic phases. In our frustrated system a similar situation could be explored in the “pentamer phase” when the density of holes to magnons is fixed at $2/3$ but individual densities are being increased. As the

density of pentamers increases, they should start to overlap, and at some critical density holes may become “liberated” from the bags. This will correspond to breaking of pentamers, however, we expect that residual interaction between holes will still result in their pairing. Understanding this transition, including exploring the possibility of other phases, is an interesting open question.

MAGNETISM INDUCED BY KINETIC FRUSTRATION

In Chapter 7 we have shown that charge carriers propagating in a frustrated geometry develop strong correlations with the spin degrees of freedom to alleviate the kinetic frustration. The strong correlations manifest themselves in the formation of strongly bound charge-spin composites resulting in a strong modification of the magnetic properties of the system. In this chapter we show how by changing charge carrier concentration one can tune between the antiferromagnetic and ferromagnetic interactions. Achieving such an electric control of magnetism is a long standing goal in condensed matter physics. It will not only provide new insights into magnetism of itinerant electron systems but also holds the promise of realizing new types of devices that combine long term robustness of magnetic memory with the fast electric control ([Awschalom and Flatté, 2007](#); [Wolf et al., 2001](#)). Electrically controlled magnetism has been studied in the past. The most studied example comes from magnetic semiconductors ([Ohno et al., 2000](#); [Chattopadhyay et al., 2001](#); [Kaminski and Das Sarma, 2002](#); [Boukari et al., 2002](#); [Jungwirth et al., 2006](#); [Lee et al., 2009](#); [Nishitani et al., 2010](#); [Sawicki et al., 2010](#); [Li et al., 2012](#); [Wen Chang et al., 2013](#); [Matsukura et al., 2015](#)). In this class of materials, conduction band electrons control the interaction between the localized spins, making it possible to modify the ferromagnetic Curie transition temperature by applying a gate voltage ([Ahn et al., 2006](#); [Matsukura et al., 2015](#)). Interplay of charge carrier dynamics and magnetism is also crucial for understanding the rich phase diagram of Colossal Magneto Resistance manganite materials ([Millis et al., 1996](#); [Tokura, 2000](#); [Salamon and Jaime, 2001](#); [Tokura, 2006](#)).

Our work builds upon earlier studies by Nagaoka ([Nagaoka, 1966](#)) and Thouless ([Thouless, 1965](#)) and Haerter and Shastry ([Haerter and Shastry, 2005](#)) of magnetism in Fermi-Hubbard type models in the limit of large interaction strength U . Nagaoka's theorem states that on a square lattice the ground state of a an almost half-filled Fermi-Hubbard model with a single hole is a ferromagnetic state. Haerter and Shastry extended these arguments to triangular lattices and demonstrated that for the same conditions the ground state exhibits antiferromagnetic correlations. The key argument of

our work is based on considering a Fermi-Hubbard model on triangular lattices in the regime when single particle tunneling t is much smaller than the local interaction U , the band is close to half-filling, i.e. one fermion per site ($\nu = 1$), and temperature is much higher than the superexchange energy $J = 4t^2/U$, but comparable to the single particle tunneling t . While naively one expects to find no magnetic interactions in this regime at $\nu = 1$, we demonstrate that doping the system away from $\nu = 1$ introduces antiferro- and ferromagnetic interactions for hole and electron dopings, respectively. Our results are in good agreement with the observed magnetism in fermionic cold atom systems with a triangular optical lattice (Xu et al., 2022a) and are consistent with the reported spin susceptibility measurements in transition metal dichalcogenide (TMDC) moiré materials for $T \geq 4$ K (Tang et al., 2020). In both cases a transition between ferro- and antiferromagnetic interactions has been observed close to filling factor $\nu = 1$ (Tang et al., 2020; Xu et al., 2022a). Moreover, recent experiments and theoretical calculations have reported large values of on-site interaction $U/t \sim 20$ (Zhang et al., 2020; Tang et al., 2020) which motivates us to focus on the $U/t \gg 1$ regime. Our work is also related to the recent observation of ferromagnetism in the Wigner crystal states of electrons at temperatures exceeding the expected superexchange interactions (Hossain et al., 2020; Kim et al., 2022).

Previous works have extensively studied the magnetic properties of the Fermi-Hubbard model in the triangular lattice at zero temperature. At $\nu = 1$, a disordered chiral spin liquid is expected at intermediate values of interaction $U/t \sim 10$ while a 120° spiral antiferromagnetic order appears for strong interactions $U/t \gtrsim 12$ (Koretsune et al., 2007; Sahebsara and Sénéchal, 2008; Clay et al., 2008; Watanabe et al., 2008; Galanakis et al., 2009; Yoshioka et al., 2009; Yang et al., 2010; Kokalj and McKenzie, 2013; Yamada, 2014; Li et al., 2014; Tocchio et al., 2014; Laubach et al., 2015; Mishmash et al., 2015; Shirakawa et al., 2017; Szasz et al., 2020; Szasz and Motruk, 2021; Cookmeyer et al., 2021; Wietek et al., 2021; Chen et al., 2022). Moreover, the ground state properties have recently been analysed when the system is doped away from $\nu = 1$ (Zhu et al., 2022). However, we do not focus on the magnetic ground state properties but on the finite temperatures ones, see also (Haerter et al., 2006). In the context of cold atoms in optical lattices, magnetic correlations induced by propagation of fermions at high temperature has been previously suggested for the square lattice (Kanász-Nagy et al., 2017).

Our work highlights the importance of magnetic polarons in correlated Mott insulators (L. N. Bulaevskii and Khomskii, 1968; Trugman, 1988; Schmitt-Rink et al., 1988; Shraiman and Siggia, 1988b; Sachdev, 1989; Kane et al., 1989; Dagotto et al., 1989; Auerbach, 1998; Nagaev, 2001; Grusdt et al., 2018a; Koepsell et al., 2019; Soriano and Katsnelson, 2020). Most of the previous studies of magnetic polarons in the Fermi-Hubbard model focused on the square lattice. They are believed to play a crucial role in unusual properties of high- T_c cuprates, including both the pseudogap regime and d-wave superconductivity. Magnetic polarons on triangular lattices have also been a subject of theoretical studies (Iordanskii and Smirnov, 1980; Zhang et al., 2018a; van de Kraats et al., 2022). It is expected that they also play an important role in defining properties of moiré materials. Their relevance for moiré materials has been suggested previously in (Davydova et al., 2022; Lee et al., 2022; Zhang and Fu, 2022).

In this chapter we study the effects of kinetic frustration on the magnetic properties of the Fermi-

Hubbard model in a triangular lattice. In Sec. 8.1 we demonstrate how magnetic interactions can be tuned by changing carrier concentration at finite temperature. We present the numerical details of our simulations together with the study of the linear and non-linear magnetic response. In Sec. 8.2 we explore the many-body phases induced by kinetic frustration at zero temperature. We report the appearance of a magnetic polaron gas phase, the formation of spinbags and study the effects of a non-local interaction. Finally, in Sec. 8.3 we discuss the importance of our results to cold atoms experiments and present a high temperature expansion for a three-point correlator.

8.1 Kinetic magnetism at finite temperature

To show the appearance of magnetic interactions from kinetic frustration at finite and zero temperature we consider spin- $\frac{1}{2}$ fermions described by a single-band Fermi-Hubbard model,

$$\hat{H}_{\text{FH}} = -t \sum_{\langle i,j \rangle, \sigma} \left(\hat{c}_{i,\sigma}^\dagger \hat{c}_{j,\sigma} + \text{H.c.} \right) + U \sum_i \hat{n}_{i,\uparrow} \hat{n}_{i,\downarrow} - \frac{h}{2} \sum_i (\hat{n}_{i,\uparrow} - \hat{n}_{i,\downarrow}), \quad (8.1)$$

where U is the on-site repulsion, t is the hopping strength and h is an external magnetic field. We define the filling of the system $\nu = 1 + \epsilon$ and we study the magnetic phases at finite temperature while changing the doping of the system from a hole doped regime ($\epsilon < 0$) to a doublon doped one ($\epsilon > 0$). In the strongly interacting regime $U/t \rightarrow \infty$ the single-band Fermi-Hubbard model Eq. (8.1) can be mapped into the $t - J$ model,

$$\hat{H}_{t-J} = -t \hat{\mathcal{P}} \left[\sum_{\langle i,j \rangle, \sigma} \left(\hat{c}_{i,\sigma}^\dagger \hat{c}_{j,\sigma} + \text{H.c.} \right) \right] \hat{\mathcal{P}} + J \sum_{\langle i,j \rangle} \left(\mathbf{S}_i \mathbf{S}_j - \frac{1}{4} \hat{n}_i \hat{n}_j \right) - h \sum_i S_i^z, \quad (8.2)$$

where we introduce the superexchange coupling $J = 4t^2/U$ characterizing the strength of the magnetic correlations at $\nu = 1$, the projector $\hat{\mathcal{P}}$ which projects out doubly occupied sites in the hole doped regime ($\epsilon < 0$) and holes in the doublon doped regime ($\epsilon > 1$), the total particle number in a given site $\hat{n}_i = \hat{n}_{i,\uparrow} + \hat{n}_{i,\downarrow}$ and the spin operators $S_i^\alpha = \frac{1}{2} \hat{c}_{i,a}^\dagger \sigma_{ab}^\alpha \hat{c}_{i,b}$, being σ_{ab}^α the Pauli matrices.

In the strongly interacting regime $U/t \rightarrow \infty$ ($J/t = 0$) for $\nu = 1$, the magnetic properties of the system are accurately described by a model of decoupled spins, that can be polarized by a magnetic field of the order of temperature $h \sim k_B T$. However, if the system is doped away from $\nu = 1$, the movement of charge carriers can induce different forms of magnetism. In a non-bipartite geometry the propagation of a single fermionic hole is frustrated in a polarized background (Haerter and Shastry, 2005; Sposetti et al., 2014; Zhang et al., 2018a), as we have shown in Chapter 7 at zero temperature. This can be seen from a high- T expansion in the strongly interacting regime, for further details on the high-temperature expansion see Sec. 8.3.1. Let us consider a spin polarized background with a single hole propagating through it. By fixing the initial and final points of the propagation we have two sets of paths characterized by the order n of the high- T expansion in βt . Since the fermionic hole has an effective negative hopping (Haerter and Shastry, 2005; Sposetti et al., 2014; Zhang et al., 2018a) we see that odd paths contribute with an opposite sign than even paths. This gives a destructive interference

pattern in the hole propagation (Haerter and Shastry, 2005; Sposetti et al., 2014). However, if the background is not fully spin polarized then the destructive interference is suppressed when different hole trajectories result in distinguishable spin configurations. Thus kinetic energy of a hole can be lowered by inducing antiferromagnetic spin correlations around it. This effect is commonly referred to as antiferromagnetic correlations releasing kinetic frustration for a single hole. It underlies the effective antiferromagnetic interactions in hole doped Mott insulators in triangular lattices. This effect is closely related to formation of a hole-magnon bound state in the case of spin polarized Mott insulators in triangular lattices discussed in Chapter 7 and in Refs. (Zhang et al., 2018a). When we consider the doublon doped regime ($\nu > 1$) the propagation of doublons in the case of spin polarized background, is not frustrated since they effectively have a positive hopping. Furthermore, different doublon trajectories interfere constructively, in the case of ferromagnetic background, but not in the antiferromagnetic environment. In the latter case, different trajectories lead to distinguishable spin configurations. This induces an effective ferromagnetic interaction at ($\nu > 1$) (Hanisch et al., 1995; Kanász-Nagy et al., 2017). Notice that this transition between antiferromagnetic and ferromagnetic interactions by changing the doping at $\nu = 1$ can only occur in a non-bipartite geometry. In a bipartite one there cannot be a destructive interference pattern since all paths contribute with the same sign in the high- T expansion, see Sec. 8.3.1.

The appearance of kinetic magnetism has strong consequences in the magnetic properties of the system at finite temperature. When the typical temperatures are much higher than the superexchange interaction $J = 4t^2/U$ we expect a paramagnetic phase at $\nu = 1$. However, if the temperature is of the order of the hopping strength $k_B T \sim t$ we still expect to see the tendency to Haerter-Shastry antiferromagnetism in the hole doped regime ($\nu < 1$) and Nagaoka-Thouless ferromagnetism in the doublon doped one ($\nu > 1$). In order to unravel the effects of kinetic magnetism at zero and finite temperature we will employ unbiased Tensor Network, see Fig. 8.1.

8.1.1 Numerical details

Due to the many competing orders in non-bipartite lattices we will employ unbiased Tensor Network simulations in two sets of frustrated geometries: a zigzag ladder and four- and six-legged triangular cylinders, see Fig.8.1. We rely on unbiased numerical simulations due to the strong spin-charge coupling and the appearance of multi-body correlations which will not be captured by simple mean-field theories. Moreover our simulations allow to discern the different magnetic phases at finite and zero temperature.

To study the finite temperature properties using Tensor Networks we use purification to represent the finite temperature density matrix as an MPS in a doubled Hilbert. We implement the $U(1)$ symmetry associated with charge conservation to fix the number of particle but we do not fix the net magnetization (Barthel, 2016). Starting from an infinite temperature state we progressively cool down the system by applying the Boltzmann factor $e^{-\delta\beta\hat{H}/2}$ to our MPS using the MPO W_I technique (Zaletel et al., 2015a) that allows to take into account the long-range interactions induced in the quasi-1D systems. The cooling process is performed using matrix product states of maximum bond dimension

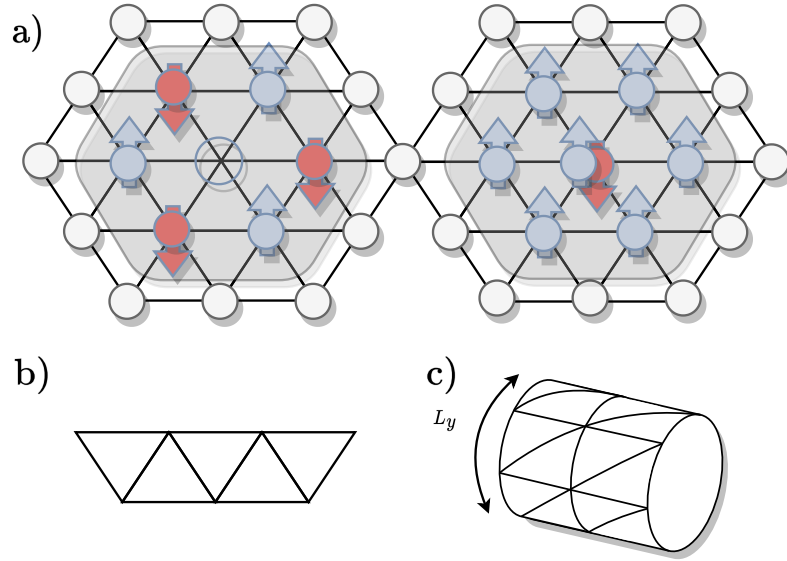


Figure 8.1: For the filling factor $\nu = 1$ and at temperatures much larger than the superexchange interaction $k_B T > J$ we find a system of essentially decoupled spins. However when a single hole (doublon) is introduced on top of the spin incoherent Mott insulator antiferromagnetic (ferromagnetic) correlations appear surrounding it, see panel a). Triangular lattice geometries analyzed in this chapter: b) zigzag ladder and c) four- and six-legged triangular cylinders.

$\chi = 512$. To measure the spin susceptibility χ_s we use fluctuation theorem,

$$\chi_s k_B T = \langle \hat{M}^2 \rangle - \langle \hat{M} \rangle^2, \quad \text{with,} \quad \hat{M} = \sum_i S_i^z \quad (8.3)$$

being N_s the number of sites in the system. For studying the many-body phases at zero temperature we employ DMRG and iDMRG simulations. The DMRG simulations are obtained in systems with x periodic boundary conditions to have faster convergence with system size. Our iDMRG simulations allow to access the properties of the system in the thermodynamic limit. To simulate the Fermi-Hubbard in the limit $U/t \rightarrow \infty$ we project out the Hilbert space: for $\nu > 1$ ($\nu < 1$) doublons (holes) are projected out.

8.1.2 Linear response: magnetic susceptibility

The tendency towards magnetic order can be inferred from the magnetic susceptibility χ_s of the system. Upon doping we see an enhancement (suppression) of magnetic susceptibility above (below) $\nu = 1$ at low temperatures, see Fig. 8.2 panel a). This indicates the appearance of antiferromagnetic (ferromagnetic) correlations in the hole (doublon) doped regime as expected. On the other hand, we observe a suppression of magnetic susceptibility above and below $\nu = 1$ at large temperatures. This can be understood as holes and doublons are spinless particles that effectively reduce the possible total spin of the system thus reducing the magnetic susceptibility.

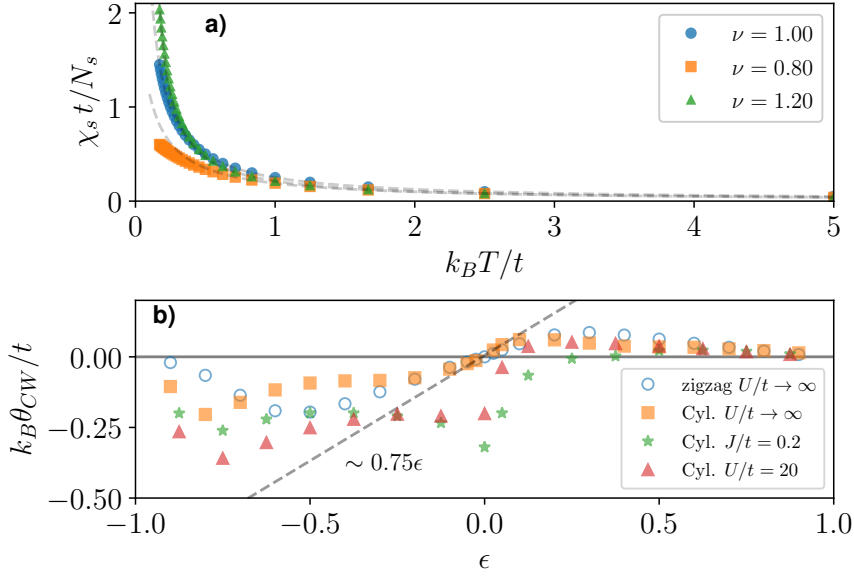


Figure 8.2: Panel a): Magnetic susceptibility per site as a function of temperature for three different dopings $\nu = 1 + \epsilon$ corresponding to a system with exactly one fermion per site ($\epsilon = 0$), a hole doped system ($\epsilon < 0$) and a doublon doped one ($\epsilon > 0$) in a zigzag ladder 20×2 . Dashed lines correspond to fits using the Curie-Weiss law Eq. (8.4). Panel b): Curie-Weiss temperature θ_{CW} as a function of doping $\nu = 1 + \epsilon$ at $h = 0$ for a 20×2 zigzag ladder (empty circles) and a 10×4 triangular cylinder (filled symbols) at different values of the on-site interaction U/t . Simulations with the $t - J$ model Eq. (8.2) (circles, squares and stars) are performed by projecting out doublons (holes) for $\nu > 1$ ($\nu < 1$). On the other hand, triangles correspond to simulations of the full Fermi-Hubbard model Eq. (8.1). The dashed line indicates the linear dependence of the Curie-Weiss temperature with doping close to one electron per site for $U/t \rightarrow \infty$.

In order to quantify the different contributions to the magnetic susceptibility we fit the Curie-Weiss law,

$$\frac{\chi_s t}{N_s} = \frac{C}{T - \theta_{CW}}, \quad (8.4)$$

to our data at temperatures ($5 \gtrsim k_B T / t \gtrsim 1$), where C is the Curie constant and θ_{CW} is the Curie-Weiss temperature. The Curie-Weiss temperature denotes the tendency towards ferromagnetism ($\theta_{CW} > 0$) or antiferromagnetism ($\theta_{CW} < 0$) at intermediate temperatures. However at high temperatures, the constant C dominates the dependence of the magnetic susceptibility with temperature. The Curie constant can be easily determined by taking into account the contribution of each spin to the spin susceptibility,

$$C = \frac{1}{3} S(S+1)(1 - |\epsilon|). \quad (8.5)$$

Thus it decreases upon doping since the number of spins is reduced. We have checked that our fits precisely return a Curie constant given by Eq. (8.5). On the other hand, the Curie-Weiss temperature

changes sign at $\nu = 1$ confirming the transition from antiferromagnetic to ferromagnetic interactions in the system, see Fig. 8.2 panel b). We observe a linear tendency of the Curie-Weiss temperature with ϵ close to $\nu = 1$, $\theta_{\text{CW}}/t \sim 0.75\epsilon$ in the strongly interacting regime $U/t \rightarrow \infty$. This suggests the appearance of effective magnetic interactions due to charge motion $J_{\text{eff}} \propto -et$. Moreover the same linear tendency is observed in the zigzag ladder and the triangular cylinders, see Fig. 8.2b). We observe deviations from the linear tendency at larger dopings in all geometries. In the electron doped regime the Curie-Weiss temperature saturates and starts to decrease approaching zero smoothly. In the hole doped regime the critical temperature still decreases up to dopings $\epsilon \sim -0.8$ where it reaches a minimum and then increases up to zero.

To establish closer connections with experiments we study the effects of a finite but large on-site interaction on the Curie-Weiss temperature. We choose the value $U/t = 20$ since it is relevant for both TMDC heterostructures and cold atom systems. Let us clarify that even much larger U/t ratios are expected in TMDC heterostructures, depending on the materials chosen. The finite on-site interaction enhances the antiferromagnetic interactions since it induces an antiferromagnetic superexchange coupling $J = 4t^2/U$, increasing in absolute value the Curie-Weiss temperature on the hole doped side, see Fig. 8.2b). Moreover, ferromagnetic correlations are suppressed and we observe that the transition from antiferro- to ferromagnetic correlations is shifted to finite electron doping $\nu_c > 1$. This is in accordance with the experimental observation in Refs. (Tang et al., 2020; Xu et al., 2022a). We also perform a comparison between the Curie-Weiss temperature extracted from the $t-J$ model and the full Fermi-Hubbard model. The full Fermi-Hubbard model compared to the $t-J$ shows stronger antiferromagnetic (ferromagnetic) correlations in the hole (electron) doped side and weaker antiferromagnetic correlations at $\nu = 1$, see Fig. 8.2b). The discrepancies can be understood by recalling the differences between the two models at zero temperature. While the $t-J$ model predicts stronger antiferromagnetic correlations as U/t decreases at $\nu = 1$, the full Fermi-Hubbard model shows a transition from an a 120° spiral antiferromagnetic order to a chiral spin liquid around $U/t \sim 10$, denoting the overestimation of antiferromagnetic correlations in the $t-J$ model with respect to the full Fermi-Hubbard model (Koretsune et al., 2007; Sahebsara and S en echal, 2008; Clay et al., 2008; Watanabe et al., 2008; Galanakis et al., 2009; Yoshioka et al., 2009; Yang et al., 2010; Kokalj and McKenzie, 2013; Yamada, 2014; Li et al., 2014; Tocchio et al., 2014; Laubach et al., 2015; Mishmash et al., 2015; Shirakawa et al., 2017; Szasz et al., 2020; Szasz and Motruk, 2021; Cookmeyer et al., 2021; Wietek et al., 2021; Chen et al., 2022).

To understand the competition between superexchange antiferromagnetism and kinetic magnetism we assume that both effects contribute independently to the Curie-Weiss temperature. In the strongly interacting regime $U \gg t$ where the $t-J$ model Eq. (8.2) is a good description of the Fermi-Hubbard model Eq. (8.1) we expect a shift of the critical temperature θ_{CW} at $\nu = 1$. A high-temperature expansion leads to the result $\theta_{\text{CW}}(\nu = 1) = 3J/2$, which agrees very well with our numerical results, see Fig. 8.2b). Considering that each spin contributes independently to the Curie-Weiss temperature around half-filling ($\nu \sim 1$), we can approximate it by,

$$\theta_{\text{CW}} \sim \frac{3}{2}J(1 - |\epsilon|) - 0.75t\epsilon. \quad (8.6)$$

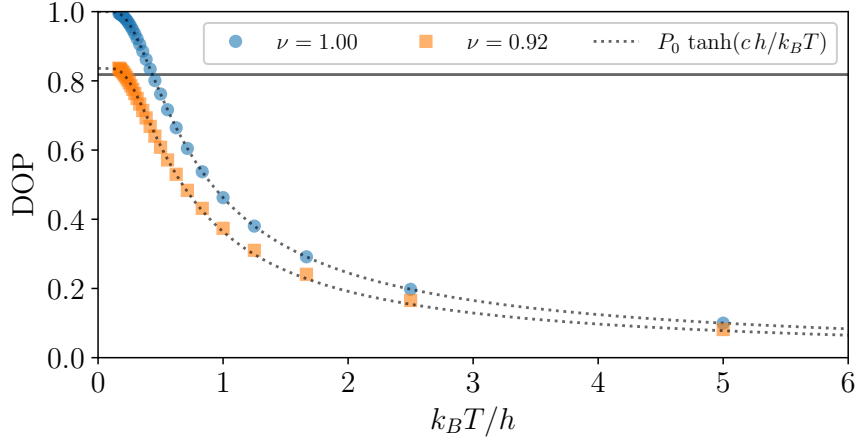


Figure 8.3: Degree of polarization (DOP) as a function of temperature over magnetic field $k_B T/h$ at different dopings ν at a fixed ratio $h/t = 1/4$ for a 6×6 triangular cylinder at $J/t = 0$. Dotted lines show the fit $P_0 \tanh(ch/k_B T)$. Continuous black line shows the polarization expected for a magnetic polaron gas Eq. (8.9).

Thus the effective magnetic interaction has two contributions. In this situation the antiferromagnetic to ferromagnetic transition is shifted to the electron doped regime $\epsilon_c \sim 2J/t$. Thus a finite density of doublons is needed to cancel out the intrinsic antiferromagnetic superexchange interaction, in accordance with our numerical simulations. Furthermore, Eq. (8.6) shows that the dependence of the Curie-Weiss temperature on hole-doping ($\epsilon < 0$) changes at $J/t \sim 1/2$. The Curie-Weiss temperature increases (decreases) in absolute value with hole-doping for smaller (larger) values of the superexchange interaction $J/t < 1/2$ ($J/t > 1/2$). Therefore, the critical superexchange interaction $J/t = 1/2$ signals a crossover from antiferromagnetic correlations induced by charge motion to antiferromagnetic correlations induced by superexchange processes. Our numerical simulations show that the Fermi-Hubbard model at $U/t = 20$ is already in the crossover regime since the Curie-Weiss temperature is almost constant with hole-doping close to half-filling, see Fig. 8.2b).

8.1.3 Non-linear response: saturation field

The linear magnetic response of the system at temperatures $t \sim k_B T \gg J$ has allowed us to determine the tendency to antiferromagnetic (ferromagnetic) order in the hole (electron) doped regime. To study the formation of many-body phases we study the nonlinear magnetic response as the system is cooled down. We define the degree of polarization (DOP) of the system as two times the magnetization density m per single fermion in the system,

$$\text{DOP} \equiv \frac{2m}{1 - |\epsilon|}. \quad (8.7)$$

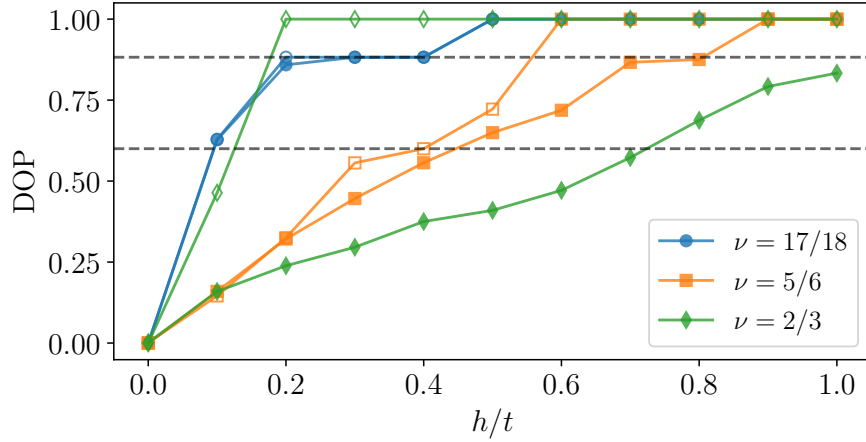


Figure 8.4: Degree of polarization (DOP) of an infinite triangular cylinder of $L_y = 6$ as a function of the external magnetic field h at different filling factors ν at $J/t = 0$ and at zero temperature. Filled (empty) symbols correspond to the case $V/t = 0$ ($V/t = 6$), see Eq. (8.10). Dashed line indicates the polarization plateau expected for the magnetic polaron gas at $\nu = 17/18, 5/6$, see Eq. (8.9).

A fully polarized system is characterized by $\text{DOP} = 1$ independently of the number of fermions. In order to quantify the effects of hole doping on the DOP we fit the generalized law

$$\text{DOP} = P_0 \tanh(ch/k_B T), \quad (8.8)$$

to our data, where we introduce the maximum polarization P_0 and the renormalization factor c . At $\nu = 1$ the system follows a paramagnetic response as a function of the external magnetic field, ($P_0 = 1$, $c = 1/2$), see Fig 8.3. At fixed magnetic field, the polarization increases as the system is cooled down until it becomes fully polarized at zero temperature. However upon hole doping the polarization is reduced. We observe that at fixed ratio $h/k_B T$ doping changes the polarization which points to the appearance of an effective antiferromagnetic interaction ($c < 1/2$) mediated by charge carriers. Moreover the system does not develop full polarization even at arbitrarily small temperatures ($P_0 < 1$). This indicates a phase transition to the formation of antiferromagnetic domains. In particular, for the chosen value of the magnetic field the system at small temperatures $k_B T < t$ is in a magnetic polaron phase. In this phase each hole is attached with a spin flip (magnon) forming a hole-magnon bound state. Due to this effect the polarization in the magnetic polaron gas is linked to the hole density by,

$$P_0 = \frac{1 - 3|\epsilon|}{1 - |\epsilon|}. \quad (8.9)$$

Therefore, this phase is characterized by a fixed polarization and a gap to single particle excitations. The magnetic polaron gas phase has already been studied in Chapter 7 for the zigzag ladder geometry.

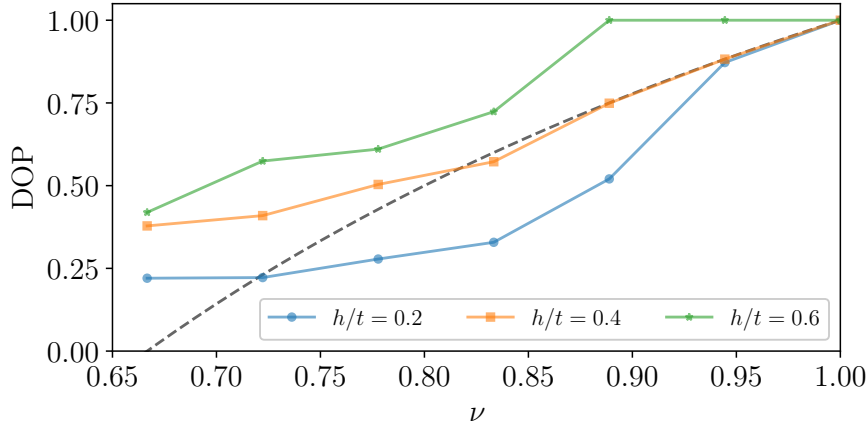


Figure 8.5: Degree of polarization (DOP) of an infinite triangular cylinder of $L_y = 6$ as a function of the filling factor ν at different magnetic fields h/t in the limit $U/t \rightarrow \infty$, at zero temperature and zero non-local interaction $V/t = 0$. Dashed line indicates the degree of polarization expected for the non-interacting magnetic polaron gas, see Eq. (8.9).

8.2 Kinetic magnetic phases at zero temperature

The non-linear magnetic response of the system to an external magnetic field at finite temperature has allowed us to discern the appearance of a kinetically induced magnetic phase. To further elucidate the many-body phases appearing in the $U/t \rightarrow \infty$ limit we study the non-linear response at zero temperature, see Fig. 8.4. We observe a large saturation magnetic field of the order of the hopping strength. At low dopings ($1 > \nu \gtrsim 0.9$) the system has a sudden drop of polarization at a critical magnetic field determined by the binding energy of the hole-magnon bound state $h_c/t \sim 0.5t$. This effect resembles the one expected in metamagnetic materials. At this point the system has a first order phase transition from a fully polarized phase $\text{DOP} = 1$ to a magnetic polaron gas with a polarization given by Eq. (8.9). We locate the magnetic polaron gas in the range of magnetic field $h/t \in [0.2, 0.4]$ and for small dopings $\nu > 0.85$. As the hole density increases the polarization plateau and the jump of polarization start to disappear. Moreover, the DOP is not given by Eq. (8.9), see Fig. 8.5 where we present how the degree of polarization changes with hole doping at fixed magnetic field. At filling factors $\nu < 0.85$ different magnetic polarons start to overlap and we cannot rely on the simple picture of a weakly interacting gas of magnetic polarons. Instead of a sharp transition from a fully polarized state to a magnetic polaron gas we observe a smooth crossover in a wide range of magnetic field. In this region of magnetic field we expect a phase coexistence between magnetic polarons and bare holes. This phase coexistence is accompanied by a sudden change of slope in the degree of polarization as a function of magnetic field.

At small magnetic fields the system linearly polarizes with the magnetic field, see Fig. 8.4. In this regime we observe phase separation into two domains with different hole densities, see inset panel of Fig. 8.6. One domain has zero doping and is fully spin polarized due to a finite magnetic

field and vanishing superexchange interaction $J/t = 0$, the other domain is "hole rich" and exhibits antiferromagnetic correlations due to kinetic magnetism. This supports the idea of antiferromagnetic spin bags (ASBs). Holes are effectively confined inside these bags since they release their kinetic frustration by moving through an antiferromagnetic background. At small magnetic fields different holes share a common ASB. When the magnetic field is very small the size of the bag becomes very large and the entire system can form an antiferromagnetic order with a few number of holes. As the magnetic field is increased the size of the bag is reduced and the magnetization increases. Thus a larger number of holes is needed in order to create an antiferromagnetic order through the entire system. The ASB has associated an optimum density of holes n_m which can be related to their localization length, see Fig. 8.6. For arbitrary small magnetic fields the bag is very large and this density drops to zero. For increasing magnetic fields the bag shrinks and the hole density increases. By further increasing the magnetic field the bag becomes so small that only a small number of holes can be accommodated within it. Thus the hole density starts to decrease again. At a critical magnetic field $h/t \sim 0.12$ the ASB is so small that only a single hole can fit inside a single bag. Thus indicating a transition from effective attractive to repulsive interactions between magnetic polarons. We point out the unusual feature of the effective interaction between magnetic polarons: it depends on the magnetic field. The unusual effective interaction between magnetic polarons comes from the competition between the effective antiferromagnetic interactions and the Zeeman energy gain.

While in the "plain-vanilla" Fermi-Hubbard model Eq. (8.1) we find global phase separation, we expect that introducing additional interactions, such as long range interactions, can result in other interesting phases, including the paired state and stripe order. The former may be relevant to superconductivity in moiré systems. While we study below how the magnetic properties are affected by adding non-local interactions in the Fermi-Hubbard model, the formation of paired phases is a subject of current study and it goes beyond the scope of this Thesis.

8.2.1 Effects of non-local interactions

Finally, we study the effects of including a density-density nearest-neighbor repulsive interaction with strength V in Hamiltonian (8.1). Non-local interaction effects are especially important for understanding the physics of TMDC moiré systems, since large values of the non-local Coulomb interaction are expected (Regan et al., 2020). The Hamiltonian of the system is given by,

$$\hat{H} = \hat{H}_{\text{FH}} + V \sum_{\langle i,j \rangle} \hat{n}_i \hat{n}_j. \quad (8.10)$$

In Fig. 8.4 we show how the non-linear magnetic response at zero temperature changes when such interaction is included. Kinetic antiferromagnetism is robust with respect to this interaction at small hole dopings and the polarization curve is not altered. At low doping factors, the charge-charge interaction given by Eq. (8.10) cannot affect the magnetic properties of the system, which are determined by the effective spin-charge coupling induced by kinetic frustration. However, at rational fillings, such as $\nu = 2/3$, we observe a fast polarization of the system with magnetic field when a non-local interaction

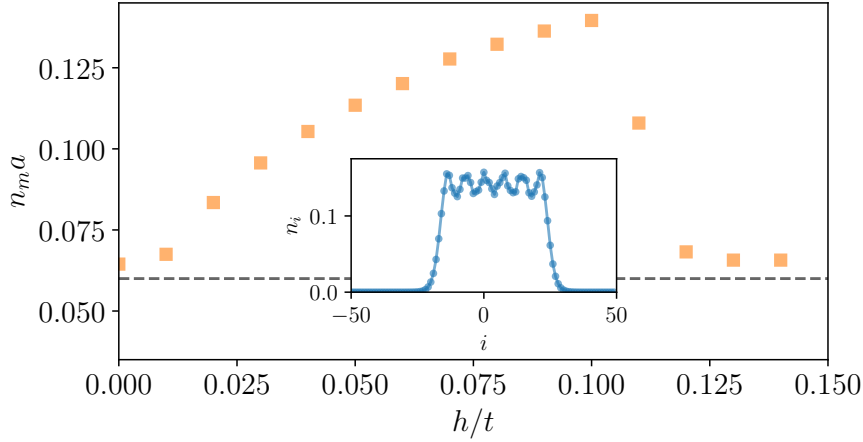


Figure 8.6: Main panel: Optimal hole density $n_m a$ of the antiferromagnetic spin bag as a function of the external magnetic field h/t at $U/t \rightarrow \infty$ for a zigzag ladder with 50×2 sites and $N_h = 6$ holes. Dashed line indicates the mean density of the deconfined phase. Inset panel: Hole number as a function of the lattice index at $h/t = 0.1$ for the same system as in the main panel.

is included. This effect can be explained by the formation of a Mott-Wigner state in which the holes become immobile (Regan et al., 2020), leading to a strong suppression of kinetic magnetism.

8.3 Applications for cold atom experiments

Our results are not only relevant for TMDC heterostructures but they also have strong implications for ultracold atomic systems in triangular optical lattices (Struck et al., 2011; Yang et al., 2021; Xu et al., 2022a). Specifically, spin-charge correlations could be accessed in systems with a quantum gas microscope (Bakr et al., 2009; Sherson et al., 2010; Parsons et al., 2015; Cheuk et al., 2015; Omran et al., 2015; Haller et al., 2015; Edge et al., 2015; Greif et al., 2016; Brown et al., 2017; Weitenberg et al., 2011; Yang et al., 2021). These experimental systems can be used to measure higher order correlation functions which that will allow a direct detection of the antiferromagnetic (ferromagnetic) polaron in the hole (doublon) doped regime. In Fig. 8.7 we present the plaquette charge-spin-spin correlation function in the hole doped regime ($\nu < 1$) and the doublon doped one ($\nu > 1$) as a function of temperature. In the hole (doublon) doped regime antiferromagnetic (ferromagnetic) correlations appear around the doped charge as the system is cooled down. Similar correlations have been observed in the hole doped regime (Garwood et al., 2022). Thus we conclude that site resolved correlations could be used as a fingerprint of kinetic magnetism.

8.3.1 High-temperature expansion

The appearance of magnetic correlations around charge carriers at temperatures $k_B T \gtrsim t$ can be understood from a high temperature expansion. When a single charge carrier is doped into the system in the strongly interacting regime $U/t \rightarrow \infty$, it permutes the spins as it hops around the lattice. The

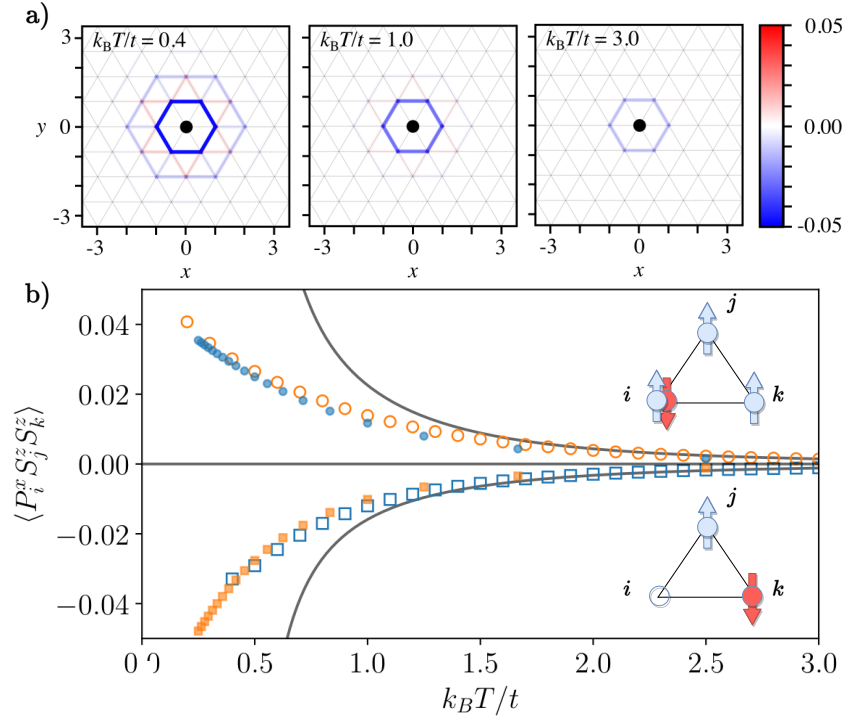


Figure 8.7: Panel a): Charge-spin-spin correlation function in a full two-dimensional triangular 20×20 lattice obtained via Monte Carlo simulations at three different temperatures. Monte Carlo simulations have been performed by Dr. Marton Kanazs-Nagy, see (Morera et al., 2022) for details on the calculation. The black circle denotes the hole position and the links show the strength of the spin-spin correlations with colour. Panel b): Charge-spin-spin correlation function as a function of temperature for a six-legged triangular cylinder with $L_x = 6$ with a single hole (blue dots) and with a single doublon (orange squares). P_i^x denotes a projector which fixes the charge position at site i . Filled (open) symbols correspond to the Tensor Network (Monte Carlo) results. Continuous lines show the high-T expansion Eq. (8.15). We also show a schematic representation of the antiferro- and ferromagnetic correlations surrounding the hole and the doublon respectively.

Hamiltonian simplifies to,

$$\hat{H}_t = t \sum_{i'i} \hat{a}_{i'}^\dagger \hat{a}_i \mathcal{P}_{i'i}, \quad (8.11)$$

where \hat{a}_i denotes the charge carrier annihilation operator and $\mathcal{P}_{i'i}$ moves the spin from site i' . We consider that the hole case is given by $t > 0$ and the doublon by $t < 0$ due to anticommutation relations of the fermionic operators. The correlations between any pair of spins will vanish when the charge carrier is not present and for vanishing superexchange interaction $J/t = 0$ and magnetic field $h/t = 0$. However, these correlations are modified by the entanglement of the charge carrier and the surrounding spins due to its imaginary time propagation, leading to the formation of a magnetic

polaron. The charge-spin-spin correlation function is given by,

$$\langle P_i^x S_j^z S_k^z \rangle = \frac{\text{Tr}_s \left(\hat{a}_i S_j^z S_k^z e^{-\beta H_t} \hat{a}_i^\dagger \right)}{\text{Tr}_s \left(\hat{a}_i e^{-\beta H_t} \hat{a}_i^\dagger \right)}, \quad (8.12)$$

where $\text{Tr}_s(\dots)$ denotes the trace over all possible spin states. Due to translational invariance, we can assume that the charge carrier is always at the origin $i = 0$. We determine the charge-spin-spin correlation function Eq. (8.12) by expanding the Boltzmann factor $e^{-\beta H_t}$ in powers of $\beta = 1/(k_B T)$, leading to terms $\frac{(-\beta H_t)^n}{n!}$. Each of these terms correspond to a closed path of length n performed by the charge carrier. Due to the sign of these terms, the charge carrier picks up a phase factor $(-\text{sign}(t))^n$ at each order of the expansion, leading to both positive and negative contributions to the charge-spin-spin correlations in the frustrated triangular lattice for the hole case $t > 0$, which results in a destructive pattern of interference leading to an antiferromagnetic polaron cloud (Haerter and Shastry, 2005). However, the phase factor is always positive when the charge carrier corresponds to a doublon $t < 0$. Therefore, there is a constructive pattern of interference and the polaron cloud is ferromagnetic. Note that the destructive pattern of interference can only be present in a non-bipartite geometry where the lengths of the paths n can be odd and even. In a bipartite geometry the length of the paths n has to be even and all terms contribute with the same sign leading to a constructive pattern of interference for both holes and doublons. Therefore, ferromagnetic correlations are expected in a bipartite geometry for $\nu < 1$ and $\nu > 1$ (Nagaoka, 1966; Thouless, 1965).

To compute the high temperature expansion of the charge-spin-spin correlation we focus on the null magnetic field case $h/t = 0$ where the probability of having a spin up or down is the same $p_\uparrow = p_\downarrow = 1/2$. However, the generalization to arbitrary probabilities is straightforward and can be found in our work (Morera et al., 2022). When the charge carrier propagates through the lattice it leaves behind a string of permuted spins. We can decompose the permutation effect of the charge carrier for a given path $\mathcal{P}_{\text{path}} h_{i_n}^\dagger h_{i_0} = \mathcal{P}_{i_n i_{n-1}} \dots \mathcal{P}_{i_2 i_1} \mathcal{P}_{i_1 0} h_{i_n}^\dagger h_0$ as $\mathcal{P}_{\text{path}} = \mathcal{P}_{i_n i_{n-1}} \dots \mathcal{P}_{i_2 i_1} \mathcal{P}_{i_1 0}$. Since we have to take traces over the spin environment only permutations restoring the initial configuration must be taken into account. Therefore, we only need to account for paths returning to the origin $i_n = 0$, and all spins permuted by $\mathcal{P}_{\text{path}}$ must be identical. The path permutation can be decomposed $\mathcal{P}_{\text{path}} = \prod_k \mathcal{C}_p$ as a product of irreducible permutation cycles \mathcal{C}_p . Therefore, the partition function of the system is given by,

$$\mathcal{Z} = \text{Tr}_s \left(\hat{a}_i e^{-\beta H_t} \hat{a}_i^\dagger \right) = \sum_n \frac{(-\text{sign}(t)\beta t)^n}{n!} \sum_{\mathcal{P}, L(\mathcal{P})=n} \prod_k \frac{2}{2^{\#\mathcal{C}_p}}, \quad (8.13)$$

where $L(\mathcal{P})$ is the length of the path, the second sum is performed over all paths of length n and $\#\mathcal{C}_p$ denotes the number of spins in the irreducible cycle. Similarly, we can compute the contribution in the numerator of Eq. (8.12). The contribution depends whether the sites j and k belong to one of the irreducible permutations \mathcal{C}_p . If j and k are not part of any irreducible permutation cycle, or belong to different irreducible permutation cycles, then the contribution vanishes since the probability of each spin state is equal $p_\uparrow = p_\downarrow = 1/2$. However, when the two sites belong to the same irreducible cycle

\mathcal{C}_p , then the two spin states have to be identical and the correlation function contributes with a factor $S_j^z S_k^z = 1/4$. Taking into account these considerations we obtain the contribution,

$$\gamma_{jk} \equiv \text{Tr}_s \left(\hat{a}_i S_j^z S_k^z e^{-\beta H_t} \hat{a}_i^\dagger \right) = \sum_n \frac{(-\text{sign}(t)\beta t)^n}{n!} \sum_{\mathcal{P}, L(\mathcal{P})=n} \frac{1}{4} \prod_{\mathcal{C}_p, (j,k) \in \mathcal{C}_p} \frac{2}{2^{\#\mathcal{C}_p}} \quad (8.14)$$

The contributions Eq. (8.13) and Eq. (8.14) can be obtained analytically by drawing all paths up to a certain length. We have carried out such a calculation up to paths of length $n = 5$, leading to the charge-spin-spin correlation function,

$$\begin{aligned} \langle P_i^x S_j^z S_k^z \rangle &= \frac{\gamma_{jk}}{\mathcal{Z}} \\ \mathcal{Z} &= 1 + 6 \frac{(\beta t)^2}{2!} - 6 \frac{(\beta t)^3}{3!} + 72 \frac{(\beta t)^4}{4!} - \frac{630}{4} \frac{(\beta t)^5}{5!} + \mathcal{O}(\beta t)^6, \\ \gamma_{jk} &= -\frac{1}{4} \frac{(\beta t)^3}{3!} + \frac{3}{8} \frac{(\beta t)^4}{4!} - \frac{93}{16} \frac{(\beta t)^5}{5!} + \mathcal{O}(\beta t)^6. \end{aligned} \quad (8.15)$$

These analytical expressions provide a good estimation of the charge-spin-spin correlation function for temperatures $k_B T \gtrsim t$, see Fig. 8.7.

8.4 Conclusions and outlook

In this chapter we have shown how effective magnetic interactions arise due to the motion of charge carriers in a frustrated geometry at finite and zero temperatures. In the strongly interacting regime $U/t \rightarrow \infty$ the superexchange interaction is suppressed. However effective magnetic interactions due to motion of charge carriers are relevant when the system is doped away from half-filling. Due to kinetic frustration these effective magnetic interactions change sign close to half-filling. Thus a magnetic transition from an antiferromagnet to a ferromagnet is expected when moving from a hole doped to an doublon doped regime. We also point out the relationship of these effective magnetic interactions with the formation of magnetic polarons. We observe the formation of a magnetic polaron gas and phase separation into antiferromagnetic spin bags at temperatures below the hopping strength.

Our results are relevant for recent experiments with TMDCs heterostructures and cold atoms in triangular optical lattice which both have observed a transition from antiferromagnetic to ferromagnetic interactions close to half-filling (Tang et al., 2020; Xu et al., 2022a). Moreover the direct detection of magnetic polarons could be achieved in ultracold atoms laboratories through measurements of charge-spin correlations. Our work also highlights the occurrence of hole pairing through magnetic polaron binding. This could be relevant to explain the appearance of superconducting states near Mott insulators. However, the stabilization of paired phases through non-local interactions or other mechanism is a subject of current study.

CONCLUSIONS AND FUTURE PERSPECTIVES

In this Thesis, we have explored the formation of various many-body phases when attractive and repulsive interactions compete in a low dimensional lattice system. We have examined different scenarios where competing interactions appear due to the presence of quantum fluctuations, multi-body effects, perturbative effects, or geometric frustration.

9.1 Ultracold atomic quantum liquids induced by direct interactions in optical lattices

In the first part of this Thesis, we have investigated the formation of quantum liquids in ultracold atomic systems loaded in high one-dimensional optical lattices. We have developed a general theory to characterize quantum liquids in one-dimensional lattice systems based on their thermodynamic and quantum properties. The conclusions of each chapter are the following:

- In Chapter 4, we have demonstrated the existence of quantum liquids in the two-component Bose-Hubbard model with repulsive intraspecies and attractive interspecies interactions. Quantum fluctuations drive the liquefaction in the weakly interacting regime, while dimerization and multi-body effects liquefy the system in the strongly interacting regime. A phase transition occurs between these two regimes characterized by the opening of a gap in the spin sector.
- In Chapter 5, we have shown that the combination of an attractive dipolar interaction together with superexchange processes liquefies a single-component bosonic system described by the Bose-Hubbard model in the strongly interacting regime.
- In Chapter 5, we have proved that one-dimensional quantum gases exhibit a universal equation of state whereas quantum liquids feature non-universal thermodynamic properties. We have

shown that the equilibrium density of a quantum liquid is a non-universal property, whilst the equilibrium energy is universal. Finally, we have demonstrated that the saturation density of the quantum droplets is also non-universal, while the tails of the droplet profile decay in a universal way, dictated solely by the equilibrium energy of the respective quantum liquid.

There are many directions that could be pursued to expand our studies on quantum liquids in the near future. First of all, it is appealing to try a self-consistent Gaussian theory to describe the weakly interacting liquid phase of the two-component Bose-Hubbard model. However, we have shown that the strongly interacting regime requires capturing four-body interactions to properly describe the liquid-to-gas transition. Therefore, more general non-Gaussian states should be employed to capture these multi-body correlations. Moreover, recent experiments have shown that the system exhibits strong three-body losses (Cabrera et al., 2018), which should be studied in detail for the one-dimensional lattice system. In particular, we expect that such strong three-body losses could give rise to effective hard-core three-body interactions and stabilize quantum liquids in other regimes of parameters (Daley et al., 2009).

In the case of the single-component dipolar system, we could use Gaussian states to self-consistently solve the Hartree-Fock decoupling and study the liquefaction of the system. Specifically, we could explore the liquefaction of a fully polarized fermionic system interacting with attractive dipolar forces. Our DMRG simulations suggest that such a system has a liquid phase that cannot be captured with our perturbative theory. Hence, we could employ a self-consistent Gaussian solution to improve our theory. Furthermore, we anticipate that generalized non-Gaussian states could also be utilized by identifying an appropriate unitary that solves the two-body problem exactly, thereby accounting for two-body correlations accurately (Shi et al., 2018). Similar non-Gaussian states have been employed to efficiently solve the polaron problem (Shi et al., 2018). Additionally, we need to analyze the possible connections to superconducting states. A quantum liquid of fully polarized fermions could be a solution to create a p-wave superconductor, avoiding phase separation. Thus, we need to further investigate the pairing in these systems and the nature of correlations. In addition, extensions to 2D are highly desirable and we should study the occurrence of long-range order in the pairing sector. However, to properly describe the 2D situation we must take into account the anisotropic nature of the dipolar interaction.

In terms of the non-universality of quantum liquids in one dimension, we need to derive the general transformation, if such a transformation exists, that relates two quantum liquids with identical binding energies. The transformation will allow us to relate the thermodynamic properties of two quantum liquids in one dimension with identical binding energies. We expect that the transformation will be a scaling transformation because the non-universality of quantum liquids is connected to the differences in their equilibrium densities. Therefore, two quantum liquids will exhibit universal behavior once a density scaling is performed. Furthermore, we need to perform further analysis to understand the continuum limit of non-renormalizable lattice models. Models such as the extended Bose-Hubbard model studied in this Thesis have a non-trivial continuum limit, and we have already seen that correlation functions exhibit a singular behavior at short distances, which should be regularized before taking the continuum limit. Renormalizing the continuum limit of extended Bose-Hubbard models will allow

to simulate continuum physics with lattice systems. For example, continuum 2D hard-core bosonic systems could be simulated by employing a 2D Heisenberg XXZ Hamiltonian.

We envision that the quantum liquid phases described in this Thesis could be experimentally produced in the near future in current ultracold atom laboratories. However, the effects of various factors, such as transverse confinement, temperature, and finite experiment lifetime, must be studied to understand their impact on the experimental observation of these quantum liquids. Transverse confinement can be incorporated through self-consistent dimensional reduction of the system. Temperature effects can be analyzed using similar techniques as those presented in Chapter 8. Particular attention should be given to thermal instability mechanisms that arise for quantum liquids (De Rosi et al., 2021). Finally, we can use our tensor network techniques to simulate real-time evolutions, such as those presented in experiments with quantum droplets (Cabrera et al., 2018).

9.2 Binding induced by kinetic frustration: applications to cold atoms and moiré systems

In the second part of this Thesis we have explored how kinetic frustration induces effective interactions in spin-1/2 systems. When a quantum particle moves through a frustrated geometry, its different propagation paths interfere destructively, causing the particle to lose part of its kinetic energy. A concept known as kinetic frustration. The original frustrated particle can partially release its kinetic frustration by combining with a second distinguishable particle forming a bound state. As a result, an effective interaction arises solely from kinetic energy and frustration. The conclusions of each chapter are the following:

- In Chapter 7, we have shown for spin-1/2 Fermi and Bose systems in different frustrated ladder geometries that kinetic frustration leads to a strong spin-charge coupling, creating a plethora of multi-body composites. Moreover, the many-body phases are understood as a self-organization of these multi-body composites.
- In Chapter 8, we have demonstrated that kinetic frustration induces a magnetic transition from an antiferromagnet to a ferromagnet for a spin-1/2 fermionic system loaded in a triangular geometry when doped away from half-filling. In addition, we have illustrated the formation of different magnetic phases at low temperatures, which can be understood as the self-organization of magnetic polarons.

An interesting avenue for further research in kinetic frustration is the occurrence of paired phases induced by magnetic correlations. In Chapter 8, we have shown that two holes feel an effective attractive interaction when a small magnetic field is applied to the system. Each hole is surrounded by an antiferromagnetic environment induced by kinetic frustration, and the system can minimize its energy if the two holes share a common background. Thus, the effective hole-hole interaction can be tuned from attractive to repulsive depending on the magnetic field. The attractive interaction between holes offers a promising avenue for studying superconducting states in triangular geometries, which could

lead to exciting applications in TMD heterostructures and ultimately explain the emergence of superconducting states in MATBG. However, a mechanism for stabilizing superconducting states against phase separation needs to be introduced, and a proper analysis of the quantum many-body phases as a function of Coulomb strength, carrier concentration, magnetic field, and temperature should be performed. Moreover, magnetic polarons induced by kinetic frustration could be detected in ultracold atom experiments using photoexcitation measurements. The binding energy of the composite is set by the tunneling strength, and therefore, the associated peak in the photoexcitation spectrum could be easily resolved in current experiments. Performing simulations of the photoexcitation spectrum and determining the robustness of the peaks against temperature and other sources of smearing could motivate future experimental investigations in experiments with cold atoms or TMDs.

We believe that kinetic frustration will have a significant impact in near future cold atom experiments using a quantum gas microscope. Such experiments have demonstrated the ability of cold atoms to simulate the Hubbard Hamiltonian and have deeply characterized the Hubbard model in two-dimensional square lattices. The natural progression is to move to non-bipartite geometries, such as the 2D triangular one, where kinetic frustration plays a decisive role. A recent experiment [Xu et al. \(2022a\)](#) has already observed the antiferromagnetic to ferromagnetic transition close to half-filling that we studied in Chapter 8. However, the experiment was conducted in a regime with not-so-strong interactions, and hence, the interactions should be increased or tunneling should be reduced. Once the strongly interacting regime is reached, and the temperature is low enough, it would be interesting to explore the dependence of magnetic correlations on the lattice geometry. The recent experiment has already demonstrated the ability to tune the geometry, and we expect a magnetic transition from ferromagnetism to antiferromagnetism below half-filling as the geometry changes from a square to a triangular one. Additionally, the magnetic polaron could be directly resolved with a quantum gas microscope, and its properties could be studied as a function of temperature and interaction strength. Finally, the bipolaron problem could be explored, and we expect that the effective attraction between magnetic polarons could be mediated by the magnetic background. Thus, fermionic cold atom systems with a triangular optical lattice could be one of the first examples of a quantum simulator of a TMD heterostructure, which could be very relevant to understanding the formation of superconducting states in triangular geometries.

TMD heterostructures offer exciting possibilities for quantum simulation since these compounds offer the possibility of simulating the Hubbard model in a triangular geometry. Further analysis of the quantum many-body phases at low temperatures is necessary, particularly with regard to the paired phases that appear at low magnetic fields and temperatures. These paired phases offer a new avenue to bring these heterostructures into a superconducting state. However, to accurately simulate these compounds, extensions of the “plain-vanilla” Hubbard model should be considered, as discussed in Sec. 3.2. Disorder and the non-local Coulomb interaction may play significant roles in these systems, and band hybridization could be relevant to understanding the many-body phases at low temperatures. As a result, *ab initio* exact diagonalization techniques should be employed to self-consistently account for all of these effects. We hope that these simulations will provide new insights into TMD heterostructures. Additionally, the spectrum of these heterostructures is not yet

well understood, and we anticipate that kinetic frustration could lead to new excitonic states that could be observed in the photoexcitation spectrum of the material.

TENSOR NETWORK ALGORITHMS

A.1 Density matrix renormalization group

A.1.1 Renormalization group perspective

We start by describing the DMRG algorithm based on its renormalization group perspective, originally introduced by S. White ([White, 1992, 1993](#)). The basic idea of DMRG (and any other numerical renormalization technique) is that, in order to describe the physics of a many-body system, we do not need to know the full Hilbert space; instead, we can remove some degrees of freedom from our system and truncate the Hilbert space. Starting from a well-known microscopic Hamiltonian, the size of the system is increased, and new degrees of freedom are added while others are integrated out, modifying the real Hamiltonian into an effective and simpler one that can properly capture the physics of the system.

The renormalization group theory has been successful and widely applied in particle physics and condensed matter systems based on Wilson's and Kadanoff's perspectives ([Kadanoff, 1966](#); [Wilson, 1971a,b](#); [Wilson and Fisher, 1972](#); [Wilson, 1975](#)). Following the success of the numerical renormalization group in describing the physics of the Kondo problem ([Wilson, 1975](#)), researchers attempted to extend the technique to solve other quantum many-body systems, such as the Heisenberg or Hubbard models. The original idea was to replace the truncation of energy levels with a decimation procedure, in which sites are iteratively added to the system and the Hamiltonian is projected out at each iteration based on the lowest-energy states. However, this approach led to poor results when applied to quantum many-body systems, and it was found to be unable to even solve the simplest problem for a numerical renormalization group: a single particle in a box ([White and Noack, 1992](#)). As illustrated in ([White and Noack, 1992](#); [Schollwöck, 2005](#)), the procedure fails because the ground state of a box of size $2l$ cannot be decomposed using the N eigenstates of a box of size l . The eigenstates of a box of size l have nodes at l , while the ground state of the box of size $2l$ has a maximum exactly at l . Therefore, the system of size $2l$ cannot be properly described by two isolated blocks of size l . This simple problem already brings to our attention the concept of quantum entanglement. When a ground state

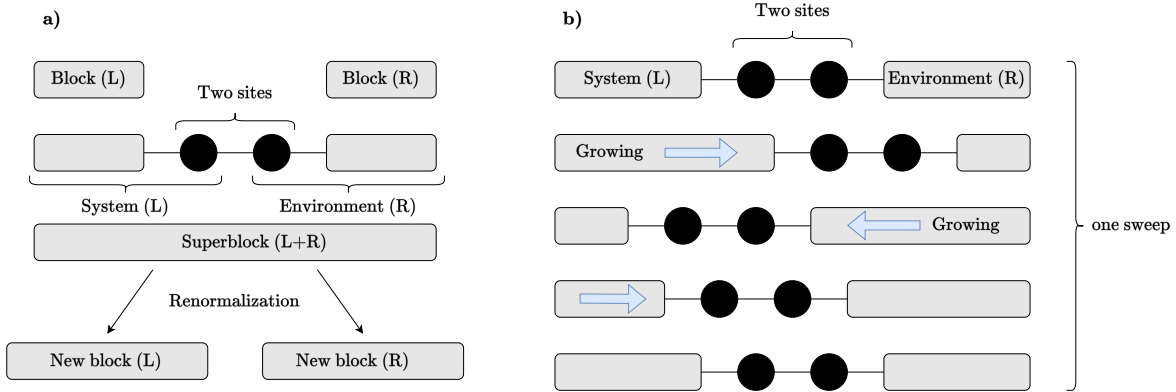


Figure A.1: Schematic representation of the DMRG algorithm. In panel a) we show the infinite-DMRG procedure. Two blocks are initially created and coupled to a single site respectively. In this way we construct the system (L) and its environment (R). Then, the superblock is constructed and a renormalization procedure is performed to obtain the new blocks L and R for the next iteration of DMRG. In panel b) we show the finite-size DMRG in which a full sweep procedure is represented.

of a system cannot be written simply as the direct product of two groundstates of the corresponding subsystems, then there are intrinsic correlations that an energy-based numerical renormalization group cannot capture. With this idea in mind, we introduce the DMRG algorithm.

Let us start by considering a system of size l (a block in the original DMRG terminology), as shown in Fig. A.1 a). It has an associated Hilbert space H^l with dimension M_L and an eigenbasis spanned by the states $|m_L\rangle$. The Hamiltonian of the system is denoted by \hat{H}_L . Now, if we introduce an extra lattice site with a local basis spanned by the states $|s_L\rangle$ of dimension S_L , we can enlarge the system. The total basis of the system is then given by the direct product of the two bases: $|m_L, s_L\rangle \equiv |m_L\rangle \otimes |s_L\rangle$. We denote the system of size l plus the single site as system L . We now embed this system into an environment, which has been constructed in a similar manner to the system, and we name it R , as shown in Fig. A.1 a). The environment is obtained by combining a system of size l and a single site, similar to the system. If reflection symmetry is a good symmetry of the total Hamiltonian and it is not broken by the ground state, then the environment can be computed by just copying the system and swapping its order, as shown in Fig. A.1 a). The total system, formed by system L plus environment R , now has a size of $2l + 2$ sites and its ground state can be found by performing exact diagonalization of the corresponding matrix of size $M_L S_L S_R M_R$.

$$|\psi\rangle = \sum_{m_L=1}^{M_L} \sum_{s_L=1}^{S_L} \sum_{s_R=1}^{S_R} \sum_{m_R=1}^{M_R} \psi_{m_L, s_L, s_R, m_R} |m_L, s_L, s_R, m_R\rangle = \sum_{i=1}^{N_L} \sum_{j=1}^{N_R} \psi_{i,j} |i, j\rangle, \quad (\text{A.1})$$

where $\psi_{m_L, s_L, s_R, m_R} = \langle m_L, s_L, s_R, m_R | \psi \rangle \equiv \psi_{i,j}$ and we denote the orthonormal basis of the system L (environment R) spanned by the states $|i\rangle = |m_L, s_L\rangle$ ($|j\rangle = |s_R, m_R\rangle$) with dimension $N_L = M_L S_L$ ($N_R = M_R S_R$). If the size l of the system L is relatively small, we can perform such diagonalization exactly. However, we want to iterate the process to simulate larger systems at each step. Thus, at some point, the basis dimension will be too large, and we will not be able to perform an exact diagonalization.

Then, we need a way of truncating our basis. The DMRG algorithm considers truncation based on the entanglement between the system and environment. If the state $|\psi\rangle$ is a pure state, then it can be characterized by its reduced density matrix,

$$\hat{\rho}_L = \text{Tr}_R |\psi\rangle\langle\psi| = \sum_{s_r=1}^{S_R} \sum_{m_R=1}^{M_R} |\langle\psi|_{s_R, m_R}\rangle|^2. \quad (\text{A.2})$$

Its matrix representation reads,

$$\langle i|\hat{\rho}_L|i'\rangle = \sum_j \psi_{i',j}^* \psi_{i,j}. \quad (\text{A.3})$$

The reduced density matrix is a semi-definite operator with N_L eigenvalues $\lambda_\alpha \geq 0$ and eigenvectors $|\psi_L^\alpha\rangle$ which we can order such that $\lambda_1 \geq \lambda_2 \geq \lambda_3 \dots$. After proper normalization of the state $\langle\psi|\psi\rangle = 1$, the eigenvalues of the reduced density matrix must add up to one,

$$\text{Tr}_L(\hat{\rho}_L) = \sum_{\alpha=1}^{N_L} \lambda_\alpha = 1. \quad (\text{A.4})$$

The reduced density matrix provides a prescription for the truncation procedure. We keep $\tilde{M}_L < N_L$ states $|\psi_L^\alpha\rangle$ with larger eigenvalues λ_α and discard the rest of them. Let us discuss how this truncation procedure affects the physical observables of the total system. Any local operator \hat{O} acting on the system L can be written as,

$$O = \langle\psi|\hat{O}|\psi\rangle = \text{Tr}_L(\hat{\rho}_L \hat{O}) = \sum_{\alpha=1}^{N_L} \lambda_\alpha \langle\psi_L^\alpha|\hat{O}|\psi_L^\alpha\rangle. \quad (\text{A.5})$$

Then, after truncation we obtain an approximate expression for the expectation value,

$$\tilde{O} = \frac{\sum_{\alpha=1}^{\tilde{M}_L} \lambda_\alpha \langle\psi_L^\alpha|\hat{O}|\psi_L^\alpha\rangle}{1 - \sum_{\alpha=\tilde{M}_L+1}^{N_L} \lambda_\alpha} \approx \sum_{\alpha=1}^{\tilde{M}_L} \lambda_\alpha \langle\psi_L^\alpha|\hat{O}|\psi_L^\alpha\rangle, \quad (\text{A.6})$$

where in the last step we have assumed that the error in the norm is a second order effect in the truncation process. In practice, one usually renormalizes the truncated reduced density matrix such that the new singular values are properly normalized. In this way, the error associated to any local observable after truncation is bounded by the discarded weights of the reduced density matrix $\epsilon(\tilde{M}_L)$,

$$|O - \tilde{O}| \approx \sum_{\alpha=\tilde{M}_L+1}^{N_L} \lambda_\alpha \langle\psi_L^\alpha|\hat{O}|\psi_L^\alpha\rangle \leq \epsilon(\tilde{M}_L) \max_\alpha \langle\psi_L^\alpha|\hat{O}|\psi_L^\alpha\rangle, \quad \text{with,} \quad \epsilon(\tilde{M}_L) = 1 - \sum_{\alpha=\tilde{M}_L+1}^{N_L} \lambda_\alpha. \quad (\text{A.7})$$

Therefore, if the eigenvalues of the reduced density matrix decay sufficiently fast, the truncation procedure introduces small errors for any local observable.

As we have anticipated, the quantum many-body state $|\psi\rangle$ cannot be written in general as the

direct product of the ground state for system L and environment R . This hints at the formation of non-trivial quantum correlations between the system and its environment, and more importantly, the appearance of quantum entanglement (White, 1992, 1993). Let us consider the total ground state of the system plus environment $|\psi\rangle$, which we represent as a $N_L \times N_R$ -matrix ψ_{ij} . We can always decompose a rectangular matrix performing a singular value decomposition (SVD) $\psi = U\Lambda V^T$, with U a $N_L \times N_R$ semi-unitary matrix (or isometric) since only the columns form an orthonormal basis, Λ is a $N_R \times N_R$ -diagonal matrix with entries $\Lambda_{\alpha\alpha} = \sqrt{\lambda_\alpha}$, called singular values, and V^T is a $N_R \times N_R$ unitary matrix. We have assumed, without loss of generality, that $N_L \geq N_R$. Then, we can decompose the total state of the system as,

$$|\psi\rangle = \sum_{i=1}^{N_L} \sum_{j=1}^{N_R} \sum_{\alpha=1}^{N_R} U_{i\alpha} \sqrt{\lambda_\alpha} V_{\alpha j}^T |i\rangle |j\rangle = \sum_{\alpha=1}^{N_R} \sqrt{\lambda_\alpha} |\psi_L^\alpha\rangle |\psi_R^\alpha\rangle, \quad (\text{A.8})$$

where we introduce the orthonormal basis of the system and environment,

$$|\psi_L^\alpha\rangle = \sum_{i=1}^{N_L} U_{i\alpha} |i\rangle, \quad \text{and}, \quad |\psi_R^\alpha\rangle = \sum_{j=1}^{N_R} V_{\alpha j}^T |j\rangle. \quad (\text{A.9})$$

The SVD of a quantum state is called Schmidt decomposition. Moreover, it allows us to obtain the reduced density matrix of either the system $\hat{\rho}_L$ or environment $\hat{\rho}_R$,

$$\hat{\rho}_L = \sum_{\alpha=1}^{\min(N_L, N_R)} \lambda_\alpha |\psi_L^\alpha\rangle \langle \psi_L^\alpha|, \quad \hat{\rho}_R = \sum_{\alpha=1}^{\min(N_L, N_R)} \lambda_\alpha |\psi_R^\alpha\rangle \langle \psi_R^\alpha|, \quad (\text{A.10})$$

which are characterized by the same set of eigenvalues. Although the total system is described by a pure state, the reduced density matrices describe a general mixed state. Therefore, we can associate a von Neumann entropy to these density matrices, which is usually called entanglement entropy S_E , and is defined by,

$$S_E(\hat{\rho}_L) = S_E(\hat{\rho}_R) = \sum_{\alpha=1}^{\min(N_L, N_R)} -\lambda_\alpha \log(\lambda_\alpha). \quad (\text{A.11})$$

In this way, by truncating the number of singular values of the reduced density matrix we are restricting the maximum amount of entanglement between the system and its environment.

By choosing a proper maximum number m of singular values of the reduced density matrix, we can increase the system size while fixing the dimensionality of the Hilbert space to m . That is, the m left eigenstates $|\psi_L^\alpha\rangle$ or right eigenstates $|\psi_R^\alpha\rangle$ form a reduced basis in which we can project the operators of the system or environment. The projectors \hat{P}_L and \hat{P}_R are defined by putting the first m left $|\psi_L^\alpha\rangle$ and $|\psi_R^\alpha\rangle$ right eigenvectors in columns, respectively. For example, the original system Hamiltonian \hat{H}_{l+1} of dimension $M_L S_L \times M_L S_L$ is reduced to $\hat{P}_L^T \hat{H}_{l+1} \hat{P}_L$, which has dimension $m \times m$. The same procedure is applied to the environment. Now we are in position of formalizing the DMRG algorithm, see Fig. A.1 a),

1. Construct a small block system L of size l with a Hilbert space of dimension M_L . Since we start with small system sizes (e.g. one site) this construction can be done in an exact way. Similarly, construct an environment R .
2. Couple the block to a single site with a Hilbert space of dimension S_L . Repeat the same procedure for the environment R .
3. Couple the system and environment forming a superblock of size $l_L + l_R + 2$ and find its ground state by means of a large sparse matrix diagonalization algorithm such as the Lanczos one.
4. Construct the reduced density matrix of the system and find its m largest singular values. Construct the projectors \hat{P}_L and \hat{P}_R and project all desired observables in the new reduced basis. After projecting the system of size $l_L + 1$ and environment of size $l_R + 1$, restart with step 2.
5. The algorithm is iterated until the desired system size is reached.

The DMRG algorithm above was originally named infinite-DMRG (iDMRG) since it aims to reach the thermodynamic limit of the total system. However, it was shown that it does not lead to very precise results for certain problems where inhomogeneities become relevant, since at the initial steps, the algorithm does not have information about long-scale structures of the problem. Therefore, the DMRG algorithm is extended by considering a second stage, usually called finite-size DMRG. First, we perform iDMRG until a desired length of the system is reached. Then, we repeat the DMRG procedure, but instead of growing both blocks (system and environment), one of the two blocks grows while the other shrinks, as shown in Fig. A.1b. The truncation procedure is only performed on the growing block. Therefore, it is convenient to have stored all representations of operators of the block that is shrinking. When the environment becomes a single site, then we reverse the procedure. Now, the environment grows and the system shrinks until the system becomes a single site, and we reverse the procedure again. We conclude a single iteration when the system and environment have the same size again. The full procedure of growing and shrinking both blocks is called a “sweep”. Each time a sweep is performed, we find a better representation of the ground state of the system with a fixed total system size. Typically, one needs dozens or hundreds of sweeps to find a very good representation of the ground state of the system depending on the problem considered. While one could argue that the algorithm could be trapped in local minima denoting the formation of metastable solutions, we can always study the convergence of the ground state as a function of the number of states kept in the simulation m . Usually, one has to find a convergence of the ground state in both the number of sweeps performed and the number of states m kept in the simulations.

A.1.2 Variational perspective

Although DMRG was originally developed as a numerical renormalization group, it has since been reinterpreted as a variational method in the subspace of MPS (Schollwöck, 2011b), as discussed in Sec. 1.3. Indeed, the ground state of certain types of systems can be expressed as an MPS ansatz that can be updated using a variational method. Quantum information theory has provided insights into

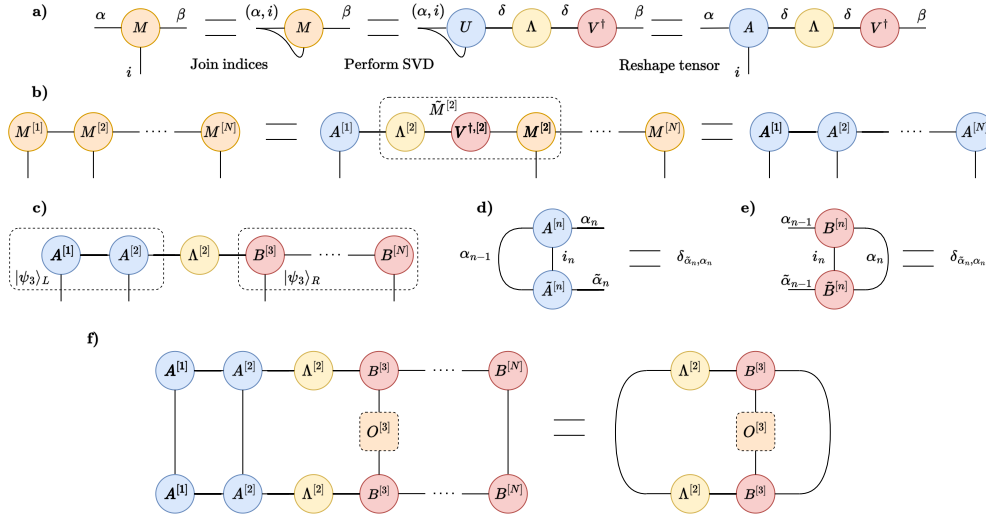


Figure A.2: Graphical representation of different tensor network operations. In a) an SVD for a rank-3 tensor and in b) an MPS is brought to left canonical form. In c) we graphically represent an MPS in mixed canonical form. In d) and e) we show the left and right orthogonality conditions, respectively. In f) we represent the vacuum expectation value $\langle \psi | O^{[3]} | \psi \rangle$ of a local operator $O^{[3]}$ acting on site $n = 3$ of an MPS in mixed canonical form.

the efficiency of DMRG, directly linking it to the entanglement of the system (Vidal, 2003; Vidal et al., 2003; Orús and Latorre, 2004). Nowadays, the DMRG algorithm is one of the most powerful methods for simulating low-dimensional systems. The algorithm is characterized by describing states with a maximum amount of entanglement, which is given by the number of singular values of the reduced density matrix, as discussed in Sec. A.1.1. Therefore, the set of states described by DMRG satisfies the so-called “area law,” as discussed in Sec. 1.3, meaning that their entanglement entropy does not grow with the system size but with its area. For a 1D system, the area law implies that the entanglement entropy is constant and does not depend on the size of the system. Let us now rewrite the DMRG algorithm in the language of tensor networks.

A.1.2.1 Canonical form

First, we introduce a useful concept in the MPS representation of a state: the canonical form. The matrices forming the MPS representation, see Eq. (1.2), have a gauge freedom, and they can always be redefined at a given site n ,

$$M_n \rightarrow \tilde{M}_n \equiv M_n X, \quad M_{n+1} \rightarrow X^{-1} M_{n+1}, \quad (\text{A.12})$$

without changing the state. The canonical form consists of exploiting this gauge freedom to bring the state into its SVD, see Eq. (A.8). Given a general tensor M of size $\chi_1 \times d \times \chi_2$ we can always perform

an SVD by first bringing it in a matrix form,

$$M_{\alpha,\beta}^i = M_{(i,\alpha),\beta} = \sum_{\delta} U_{(i,\alpha),\delta} \Lambda_{\delta,\delta} V_{\delta,\beta}^{\dagger} = \sum_{\delta} A_{\alpha,\delta}^i \Lambda_{\delta,\delta} V_{\delta,\beta}^{\dagger}, \quad (\text{A.13})$$

where we have replaced U by a set of d matrices of dimensions $\chi_1 \times \chi_2$, see Fig. A.2 a). If we want to bring the complete state into its canonical form, we just have to repeat the procedure at every site and group different tensors together, as shown in Fig. A.2 b). This leads to the canonical form of a general state.

$$|\psi\rangle = \sum_{i_1, i_2, \dots, i_N} A^{[1], i_1} A^{[2], i_2} \dots A^{[N], i_N} |i_1, i_2, \dots, i_N\rangle, \quad (\text{A.14})$$

where we simplify the notation since virtuals indices are contracted, $A_{\alpha_{n-1}, \alpha_n}^{[n], i_n} = U_{(i_n, \alpha_{n-1}), \alpha_n}^{[n]}$ and we denote the total number of sites as N . The canonical form allows us to find an orthonormality condition due to the isometric properties $U^{\dagger}U = I$ of the SVD, see Fig. A.2 d),

$$\delta_{\alpha_n, \tilde{\alpha}_n} = \sum_{i_n, \alpha_{n-1}} (U^{\dagger})_{\alpha_n, (i_n, \alpha_{n-1})} U_{(i_n, \alpha_{n-1}), \tilde{\alpha}_n} = \sum_{i_n, \alpha_{n-1}} A_{\alpha_n, \alpha_{n-1}}^{\dagger i_n} A_{\alpha_{n-1}, \tilde{\alpha}_n}^{i_n}, \quad (\text{A.15})$$

which is usually called left normalization. It is called left normalization because the original matrices U are isometries and then $AA^{\dagger} \neq I$. When the state is written in the form of Eq. (A.14) with left-normalized matrices, we call it a state in left canonical form. Note that the same procedure could be performed starting from the right of the state instead of from its left. In this way, we will end up with a state written as,

$$|\psi\rangle = \sum_{i_1, i_2, \dots, i_N} B^{[1], i_1} B^{[2], i_2} \dots B^{[N], i_N} |i_1, i_2, \dots, i_N\rangle, \quad (\text{A.16})$$

where the tensors are given by $B_{\alpha_{n-1}, \alpha_n}^{[n], i_n} = (V^{\dagger})_{(i_n, \alpha_{n-1}), \alpha_n}^{[n]}$. Because of the SVD property $VV^{\dagger} = I$ we have the following normalization condition,

$$\delta_{\alpha_n, \tilde{\alpha}_n} = \sum_{i_n, \alpha_{n-1}} B_{\alpha_n, \alpha_{n-1}}^{i_n} B_{\alpha_{n-1}, \tilde{\alpha}_n}^{\dagger i_n}, \quad (\text{A.17})$$

which is called right normalization. When the state is written in the form of Eq. (A.16) with right normalized matrices, we call it a state in right canonical form. Finally, there is a third way of proceeding which consists of mixing the left and right canonical form, which is called mixed canonical form. We take an arbitrary site n and perform SVDs to its left (right) sites to form a left (right) canonical form. The resulting state has the form, see Fig. A.2 c),

$$|\psi\rangle = \sum_{i_1, i_2, \dots, i_N} A^{[1], i_1} \dots A^{[n], i_n} \Lambda^{[n]} B^{[n], i_{n+1}} \dots B^{[N], i_N} |i_1, \dots, i_N\rangle. \quad (\text{A.18})$$

The mixed canonical form of the state resembles the Schmidt decomposition introduced in Eq. (A.8). Indeed, we can rewrite the state as,

$$|\psi\rangle = \sum_{\psi_n} \sqrt{\lambda_{\psi_n}} |\psi_n\rangle_L |\psi_n\rangle_R, \quad (\text{A.19})$$

where,

$$|\psi_n\rangle_L = \sum_{i_1, \dots, i_n} A^{[1], i_1} \dots A^{[n], i_n} |i_1, \dots, i_n\rangle, \quad (\text{A.20})$$

$$|\psi_n\rangle_R = \sum_{i_{n+1}, \dots, i_N} B^{[n+1], i_{n+1}} \dots B^{[N], i_N} |i_{n+1}, \dots, i_N\rangle, \quad (\text{A.21})$$

and $\sqrt{\lambda_{\psi_n}}$ are the entries of the diagonal matrix $\Lambda^{[n]}$. That is, if the states given by Eq. (A.20) and Eq. (A.21) form an orthonormal basis then, the mixed canonical form corresponds to the Schmidt decomposition and $\Lambda^{[n]}$ has as entries the singular values of the reduced density matrices. This is the case by construction since we have defined the matrices A and B to fulfill the orthonormality conditions given by Eq. (A.15) and Eq. (A.17), respectively. The mixed canonical form allows us to immediately read the singular values of a given site n . Moreover, it allows us to simplify the calculations of local observables in our state. Consider a local operator \hat{O} acting on site $n = 3$. The vacuum expectation value $\langle \psi | \hat{O} | \psi \rangle$ will require the contraction of our MPS which can become computationally very demanding, see Fig. A.2 f). However, the tensor contractions become trivial if our MPS is in mixed canonical form due to the orthonormality conditions, see Fig. A.2 f). Thus, the evaluation of local observables is greatly simplified.

In principle, one can always write a generalized pure quantum state represented by,

$$|\psi\rangle = \sum_{i_1, \dots, i_n} \psi_{i_1, i_2, \dots, i_N} |i_1, \dots, i_N\rangle, \quad (\text{A.22})$$

in a mixed canonical form given by Eq. (A.18) (Vidal, 2003). However, given a Hilbert space of local dimension d , the tensor $\psi_{i_1, i_2, \dots, i_N}$ will have d^N coefficients. Bringing the exact quantum state into its mixed canonical form becomes exponentially demanding with the number of sites in the system. In practice, we set a maximum bond dimension χ_{\max} in our simulations and truncate the matrices A and B such that we do not surpass this dimension. Recall that the bond dimension denotes the dimension of the links that are contracted in the MPS. This truncation procedure is based on selecting the subspace spanned by the eigenvectors of the reduced density matrix with larger singular values, as explained in Sec.A.1.1 from the renormalization group perspective of DMRG. Thus, the bond dimension χ relates to the maximum number of states m kept in the DMRG simulation explained in Sec.A.1.1. They correspond to a cutoff on the maximum quantum entanglement of the system. It is important to note that this truncation procedure breaks the mixed canonical form since we are altering the matrices A and B . However, if the discarded weights of the singular values are small, then we can ignore this source of error.

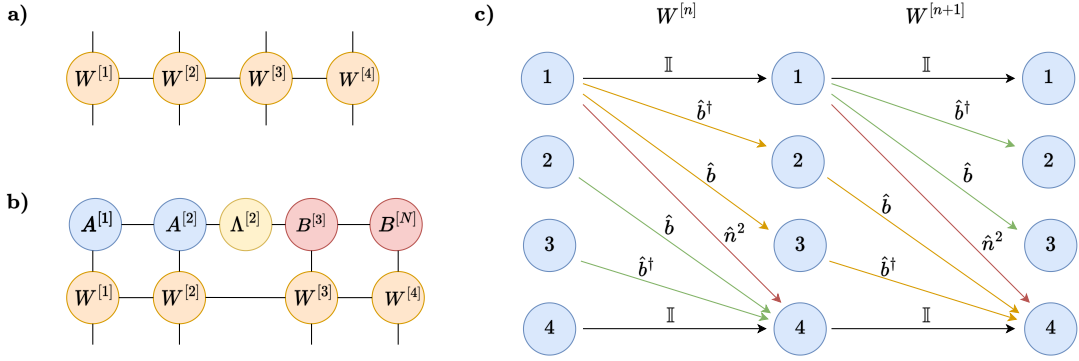


Figure A.3: MPO representation of a general operator in a). An MPO acting on an MPS in mixed canonical form in b). In c) we represent a finite state machine for sites n and $n + 1$ where the blue dots represent the state of the machine and arrows denote the possible transitions. In yellow (red) we remark the transitions returning the operators $\hat{b}_n^\dagger \hat{b}_{n+1}$ (\hat{n}_n) and $\hat{b}_{n+1}^\dagger \hat{b}_n$ (\hat{n}_{n+1}), and similarly for the green arrows.

A.1.2.2 Matrix product operator

After introducing the canonical form of an MPS, we have to introduce another concept that is relevant to the implementation of DMRG with tensor networks. We need a tensor network representation of the operators that act on our Hilbert space, namely a matrix product operator (MPO). An MPO is a generalization of an MPS to an operator,

$$\hat{O} = \sum_{\substack{i_1, \dots, i_N \\ i'_1, \dots, i'_N}} W^{[1], i_1, i'_1} W^{[2], i_1, i'_1} \dots W^{[N], i_N, i'_N} |i_1, \dots, i_N\rangle \langle i'_1, \dots, i'_N|, \quad (\text{A.23})$$

where $W^{[n], i_n, i'_n}$ are $D \times D$ matrices, see Fig. A.3 a) for a graphical representation of an MPO. Now, every site has two vertical lines denoting the ingoing and outgoing physical states. An MPO representation of a given operator is a very convenient way to perform calculations such as applying an operator to a state, $\hat{O}|\psi\rangle$. Let us see how such an operation can be written as a tensor network contraction,

$$\begin{aligned} \hat{O}|\psi\rangle &= \sum_{i_1, \dots, i_N} W^{[1], i_1, i'_1} M^{[1], i'_1} \dots W^{[N], i_N, i'_N} M^{[N], i'_N} |i_1, \dots, i_N\rangle \\ &= \sum_{i_1, \dots, i_N} N^{[1], i_1} \dots N^{[N], i_N} |i_1, \dots, i_N\rangle \equiv |\phi\rangle. \end{aligned} \quad (\text{A.24})$$

Therefore, contracting an MPO to an MPS returns a new MPS with matrices of dimension $d \times \chi^2 \times D^2$, see Fig. A.3 b) for a representation of the MPO to MPS contraction. Thus, an operation that will appear to grow exponentially with the number of sites is reduced to a polynomial problem of order $\mathcal{O}(Nd^2\chi^2D^2)$. Many other operations can be performed with MPOs such that adding two MPOs, compressing them, etc, see (Schollwöck, 2011a) for a detailed discussion on different operations and their complexity.

We are interested in obtaining an MPO representation of a many-body quantum Hamiltonian \hat{H} . Let us consider as an example a simplified Bose-Hubbard Hamiltonian,

$$\hat{H} = -t \sum_i \left(\hat{b}_i^\dagger \hat{b}_{i+1} + \text{H.c.} \right) + \frac{U}{2} \sum_i \hat{n}_i^2. \quad (\text{A.25})$$

This may seem a complicated Hamiltonian that its MPO representation would require a very large dimension D . However, we have to recall that Eq. (A.25) stands for a simplified notation denoting that each operator acts in a site which is a subspace of the total Hilbert space formed by the direct tensor product of each site. Therefore, the explicit form of the Hamiltonian is given by,

$$\begin{aligned} \hat{H} = & -t \left(\hat{b}_1^\dagger \otimes \hat{b}_2 \otimes \hat{I} \cdots \otimes \hat{I} + \hat{I} \otimes \hat{b}_2^\dagger \otimes \hat{b}_3 \otimes \hat{I} \cdots \otimes \hat{I} + \cdots + \hat{I} \otimes \hat{I} \otimes \cdots \hat{b}_{N-1}^\dagger \otimes \hat{b}_N \right) + \\ & -t \left(\hat{b}_1 \otimes \hat{b}_2^\dagger \otimes \hat{I} \cdots \otimes \hat{I} + \hat{I} \otimes \hat{b}_2 \otimes \hat{b}_3^\dagger \otimes \hat{I} \cdots \otimes \hat{I} + \cdots + \hat{I} \otimes \hat{I} \otimes \cdots \hat{b}_{N-1} \otimes \hat{b}_N^\dagger \right) + \\ & + \frac{U}{2} \left(\hat{n}_1^2 \otimes \hat{I} \cdots \otimes \hat{I} + \hat{I} \otimes \hat{n}_2^2 \otimes \hat{I} \cdots \otimes \hat{I} + \cdots + \hat{I} \otimes \hat{I} \otimes \hat{n}_N^2 \right). \end{aligned} \quad (\text{A.26})$$

In this way, the MPO representation of the Hamiltonian becomes more transparent, since one can read the structure of sums of tensor products. We just need to find a set of N matrices that, by multiplying them, we obtain the tensor product representation of the Hamiltonian Eq.(A.26). The matrix representation can be obtained by inspecting Eq.(A.26) for small systems and trying to extrapolate for arbitrary sites or by a more elegant approach based on finite state machines (Crosswhite and Bacon, 2008; Paeckel et al., 2017), which we discuss in the following, see Fig A.3 c). Each element of Eq. (A.26) corresponds to a string. Each string is composed of a combination of identities and three possible operators corresponding to \hat{b}_i^\dagger , \hat{b}_i , and \hat{n}_i^2 . Moreover, note that the creation and annihilation operators always appear in neighboring sites. Therefore, we can define four possible states: 1, 2, 3, and 4, that the string can have in a given site. State 1 corresponds to having only identities to the left of the site. States 2 and 3 correspond to having one operator \hat{b}_i^\dagger and \hat{b}_i just to the left of the site, respectively. State 4 corresponds to completed, where there is an operator \hat{n}_i^2 to the left or a pair $\hat{b}^\dagger \hat{b}$. Starting from the leftmost site, we move to the right and check the state of the string. Different transitions are possible. Transition $1 \rightarrow 1$ occurs when we encounter a new identity and no other operator. Transitions $1 \rightarrow 2$ and $1 \rightarrow 3$ occur when we encounter an operator \hat{b}_i^\dagger or \hat{b}_i . Transitions $2 \rightarrow 4$, $3 \rightarrow 4$, and $1 \rightarrow 4$ occur when we encounter an operator \hat{b}_i , \hat{b}_i^\dagger , and \hat{n}_i^2 , respectively. Finally, we have $5 \rightarrow 5$ when the string is completed. The states and their transitions define our finite state machine which can be encoded in a matrix representation corresponding to the matrices of our MPO,

$$W^{[i]} = \begin{bmatrix} \hat{I} & \hat{b}^\dagger & \hat{b} & \frac{U}{2} \hat{n}^2 \\ 0 & 0 & 0 & -t \hat{b}^\dagger \\ 0 & 0 & 0 & -t \hat{b} \\ 0 & 0 & 0 & \hat{I} \end{bmatrix}, \quad W^{[1]} = \begin{bmatrix} \hat{I} & -t \hat{b}^\dagger & -t \hat{b} & \frac{U}{2} \hat{n}^2 \end{bmatrix}, \quad W^{[N]} = \begin{bmatrix} \frac{U}{2} \hat{n}^2 \\ \hat{b} \\ \hat{b}^\dagger \\ \hat{I} \end{bmatrix}. \quad (\text{A.27})$$

By multiplying these matrices one can see that the Hamiltonian (A.26) is recovered. Therefore, we have provided a general recipe based on finite state machines to construct an efficient MPO representation

of a given Hamiltonian. One might think that such construction can only work for Hamiltonians that interact locally. In general, this is the case, but there are a few exceptions. The most important one corresponds to interactions that decay exponentially with the distance between two particles. Let us consider the following Hamiltonian,

$$\hat{H} = \sum_{i < j} e^{-|i-j|/\xi} \hat{n}_i \hat{n}_j = \sum_{i < j} \lambda^{|i-j|} \hat{n}_i \hat{n}_j, \quad (\text{A.28})$$

where we introduce $\lambda = e^{-1/\xi}$. The finite state machine describing such a Hamiltonian has three possible states, namely 1, 2, and 3, corresponding to identities to the left, a single \hat{n} to the left, and completed (i.e., two \hat{n} to the left), respectively. The possible transitions are as follows: $1 \rightarrow 1$, $1 \rightarrow 2$, $2 \rightarrow 2$, $2 \rightarrow 3$, and $3 \rightarrow 3$. Then, the matrix representation is given by,

$$W^{[i]} = \begin{bmatrix} \hat{I} & \hat{n} & 0 \\ 0 & \lambda \hat{n} & \lambda \hat{n} \\ 0 & 0 & \hat{I} \end{bmatrix}, \quad (\text{A.29})$$

which again requires a small matrix to represent the exponential decaying interaction. However, for a general decaying interaction $V(|i-j|)$ the matrix representation of the finite state machine can become very complex. In practice, one can try to fit the decaying interaction as a sum of p exponentials by minimizing their difference (Pirvu et al., 2010),

$$\min_{c_k, \lambda_k} \sum_{r=1}^N |V(|r|) - \sum_{k=1}^p c_k \lambda_k^{|r|}|. \quad (\text{A.30})$$

In this way, systems with interactions decaying as a power-law $1/|i-j|^\alpha$ can be simulated. This is the approach that has been employed in Chapter 5.

A.1.2.3 DMRG in the tensor network language

We are now in position to formulate the DMRG algorithm in the language of tensor networks (Schollwöck, 2011a). Given an MPO representation of the Hamiltonian \hat{H} and an MPS $|\psi\rangle$ with bond dimension χ , we want to minimize the energy with respect to the variational parameters given by the matrix elements of the tensors $M^{[n]}$,

$$\min_{M^{[n]}} \frac{\langle \psi | \hat{H} | \psi \rangle}{\langle \psi | \psi \rangle}. \quad (\text{A.31})$$

However, performing a minimization procedure for all tensors at once seems like an unreasonable task. Therefore, at a given iteration, we will update just some local tensors while keeping the rest of them fixed. Usually, there are two versions of DMRG depending on whether the local update is performed for a single tensor (single-site DMRG) or two tensors at once (two-site DMRG), see e.g. (Schollwöck, 2011a). We are going to discuss the latter, which bears many similarities with the renormalization

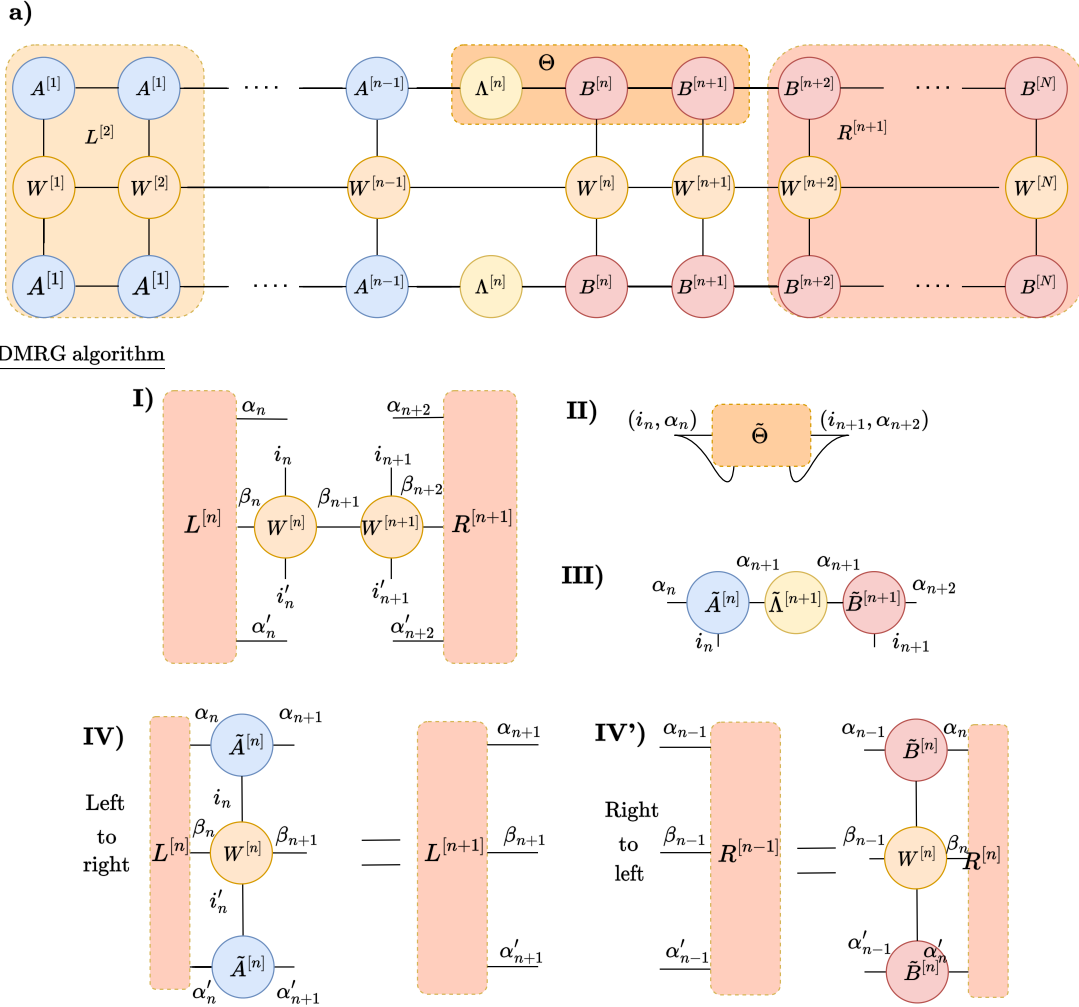


Figure A.4: In a) we represent the graphical contraction returning the energy of an MPS in mixed canonical form, see Eq. (A.39). We remark the two-site wavefunction Θ , one of the left environments $L^{[2]}$ and one of the right environments $R^{[n+1]}$. In b) we present the DMRG algorithm. I) the effective Hamiltonian acting on sites n and $n + 1$ is constructed. II) the ground state $\tilde{\Theta}$ is obtained and III) an SVD is performed. IV) the left or IV') the right environment is updated.

group algorithm explained in Sec. A.1.1. The idea is to find the representation of the Hamiltonian in the subspace spanned by the basis $\{|\alpha_n\rangle_L, i_n, i_{n+1}, |\alpha_{n+2}\rangle_R\}$, where $|\alpha_n\rangle_L$ ($|\alpha_{n+2}\rangle_R$) is the left (right) Schmidt eigenvector, i_n and i_{n+1} are the local Hilbert basis on site n and $n + 1$, respectively. The wavefunction in such a basis is expressed as,

$$|\psi\rangle = \sum_{i_n, i_{n+1}, \alpha_n, \alpha_{n+1}} \Theta_{\alpha_n, \alpha_{n+2}}^{i_n, i_{n+1}} |\alpha_n\rangle_L |i_n\rangle |i_{n+1}\rangle |\alpha_{n+2}\rangle_R, \quad (\text{A.32})$$

where we introduce the tensor $\Theta_{\alpha_n, \alpha_{n+2}}^{i_n, i_{n+1}}$ giving the coefficients of the wavefunction, see Fig. A.4. If the MPS is written in mixed canonical form respect to site n , see Eq. (A.18), then the tensor Θ is given

by,

$$\Theta_{\alpha_n, \alpha_{n+2}}^{i_n, i_{n+1}} = \sum_{\alpha_{n+1}} \Lambda_{\alpha_n, \alpha_n}^{[n]} B_{\alpha_n, \alpha_{n+1}}^{[n] i_n} B_{\alpha_{n+1}, \alpha_{n+2}}^{[n+1] i_{n+1}}, \quad (\text{A.33})$$

which has a dimension $\chi_n \times d^2 \times \chi_{n+2}$. The tensor Θ spans our variational space and we need to find the projection of the Hamiltonian onto that space, which we name the effective Hamiltonian. That is, the matrix elements of the effective Hamiltonian are given by,

$$\begin{aligned} & \langle \alpha_n, i_n i_{n+1} \alpha_{n+2} | \hat{H} | \alpha'_n, i'_n i'_{n+1} \alpha'_{n+2} \rangle \quad (\text{A.34}) \\ &= \sum_{\substack{i_1, \dots, i_N \\ i'_1, \dots, i'_N}} W^{[1], i_1, i'_1} W^{[2], i_1, i'_1} \dots W^{[N], i_N, i'_N} \\ & \langle \alpha_n |_L | i_1, \dots, i_N \rangle \langle \alpha_{n+2} |_R | i_1, \dots, i_N \rangle \langle i'_1, \dots, i'_N | \alpha'_n \rangle_L \langle i'_1, \dots, i'_N | \alpha'_{n+2} \rangle_R \\ &= \sum_{\substack{i_1, \dots, i_N \\ i'_1, \dots, i'_N}} W^{[1], i_1, i'_1} W^{[2], i_1, i'_1} \dots W^{[N], i_N, i'_N} \\ & \left(A^{*[1], i_1} \dots A^{*[n], i_n} \right) \left(B^{*[n+2], i_{n+2}} \dots B^{*[N], i_N} \right) \left(A^{*[1], i'_1} \dots A^{*[n], i'_n} \right) \left(B^{[n+2], i'_{n+2}} \dots B^{[N], i'_N} \right) \\ &\equiv \sum_{\beta_n, \beta_{n+1}, \beta_{n+2}} L_{\alpha_n \alpha'_n}^{[n], \beta_n} W_{\beta_n \beta_{n+1}}^{i_n, i'_n} W_{\beta_{n+1} \beta_{n+2}}^{i_{n+1}, i'_{n+1}} R_{\alpha_{n+2} \alpha'_{n+2}}^{[n+2] \beta_{n+2}}, \end{aligned}$$

where we have employed Eq. (A.20) and Eq. (A.21), and we have introduced the left and right environments,

$$L_{\alpha_n \alpha'_n}^{[n], \beta_n} = \sum_{\alpha_1, \alpha'_1, \beta_i; i < n} \left[\sum_{i_1, i'_1} A^{*[1], i_1} W_{\beta_1, \beta_2}^{[1], i_1, i'_1} A_{\alpha'_1, \alpha'_2}^{[1], i'_1} \dots \right. \quad (\text{A.35}) \\ \left. \left[\sum_{i_{n-1}, i'_{n-1}} A^{*[n-1], i_{n-1}} W_{\beta_{n-1}, \beta_n}^{[n-1], i_{n-1}, i'_{n-1}} A_{\alpha'_{n-1}, \alpha'_n}^{[n-1], i'_{n-1}} \right], \right.$$

$$\begin{aligned} R_{\alpha_{n+2} \alpha'_{n+2}}^{[n+2] \beta_{n+2}} &= \sum_{\alpha_1, \alpha'_1, \beta_i; i > n+2} \left[\sum_{i_{n+2}, i'_{n+2}} B^{*[n+2], i_{n+2}} W_{\beta_{n+2}, \beta_{n+3}}^{[1], i_{n+2}, i'_{n+2}} B_{\alpha'_{n+2}, \alpha'_{n+3}}^{[n+2], i'_{n+2}} \dots \right. \quad (\text{A.36}) \\ & \left. \left[\sum_{i_N, i'_N} B^{*[N], i_N} W_{\beta_N, \beta_{N+1}}^{[N], i_N, i'_N} B_{\alpha'_N, \alpha'_{N+1}}^{[N], i'_N} \right]. \right. \end{aligned}$$

Therefore, the representation of the Hamiltonian in the two-site subspace is given by the partial contraction of all A tensors with the Hamiltonian tensors W to the left of site n and the contraction of all B tensors with the Hamiltonian tensors W to the right of site $n+2$, see Fig. A.4 for a graphical representation of such contraction. The construction of the left and right environments can be done efficiently by following an iterative procedure similar to the one explained in Sec. A.1.1 for constructing the system and environment blocks. We can obtain a recursive expression relating the environments

with $n - 1$ and n sites,

$$L_{\alpha_n \alpha'_n}^{[n], \beta_n} = \sum_{\substack{i_{n-1}, i'_{n-1} \\ \alpha_{n-1}, \alpha'_{n-1}, \beta_{n-1}}} A_{\alpha_{n-1}, \alpha_n}^{*[n-1], i_{n-1}} W_{\beta_{n-1}, \beta_n}^{[n-1], i_{n-1}, i'_{n-1}} L_{\alpha_{n-1} \alpha'_{n-1}}^{[n-1], \beta_{n-1}} A_{\alpha'_{n-1}, \alpha'_n}^{[n-1], i'_{n-1}}, \quad (\text{A.37})$$

$$R_{\alpha_{n+2} \alpha'_{n+2}}^{[n+2], \beta_{n+2}} = \sum_{\substack{i_{n+2}, i'_{n+2} \\ \alpha_{n+2}, \alpha'_{n+2}, \beta_{n+2}}} B_{\alpha_{n+2}, \alpha_{n+3}}^{*[n+2], i_{n+2}} W_{\beta_{n+2}, \beta_{n+3}}^{[1], i_{n+2}, i'_{n+2}} R_{\alpha_{n+3} \alpha'_{n+3}}^{[n+3], \beta_{n+3}} B_{\alpha'_{n+2}, \alpha'_{n+3}}^{[n+2], i'_{n+2}}, \quad (\text{A.38})$$

with a boundary condition $L_{\alpha_0, \alpha'_0}^{[0], \beta_0} = R_{\alpha_N, \alpha'_N}^{[N], \beta_N} = 1$, where the indices correspond to dummy indices which can take only the value 1. In practice, it is advisable to store environments with different numbers of sites separately as they will be used in different iterations of the DMRG algorithm, as explained in Sec. A.1.1.

Finally, the energy $E = \langle \psi | \hat{H} | \psi \rangle$ of our MPS is given by,

$$E = \sum_{\substack{i_n, i_{n+1}, i'_n, i'_{n+1} \\ \alpha_n, \alpha_{n+2}, \alpha'_n, \alpha'_{n+2} \\ \beta_n, \beta_{n+2}, \beta'_n, \beta'_{n+2}}} \Theta_{\alpha'_n, \alpha'_{n+2}}^{*i'_n, i'_{n+1}} L_{\alpha_n \alpha'_n}^{[n], \beta_n} W_{\beta_n \beta_{n+1}}^{i_n, i'_n} W_{\beta_{n+1} \beta_{n+2}}^{i_{n+1}, i'_{n+1}} R_{\alpha_{n+2} \alpha'_{n+2}}^{[n+2], \beta_{n+2}} \Theta_{\alpha_n, \alpha_{n+2}}^{i_n, i_{n+1}}, \quad (\text{A.39})$$

and our MPS is normalized to unity by requiring $\text{Tr}(\Lambda^{[n]}) = 1$ as aforementioned, see Fig. A.4 a) for a graphical representation of the energy. The energy minimization is performed in the two-site subspace where the variational parameters are the entries of the tensor Θ . To perform such an energy minimization we can reshape the effective Hamiltonian Eq. (A.34) into a matrix of dimension $\chi_n \chi_{n+2} d^2 \times \chi_n \chi_{n+2} d^2$ and find its ground state vector given by $\tilde{\Theta}$. In practice, this minimization is performed using a Lanczos algorithm which requires to compute the action of the effective Hamiltonian over the state, similarly to Eq. (A.39). The contraction becomes more efficient when we contract the tensors L , W , W and R to Θ one after another. Once we have determined the new state $\tilde{\Theta}$ we reshape into a matrix of dimension $\chi_n d \times \chi_{n+2} d$ and perform an SVD,

$$\tilde{\Theta}_{(i_n, \alpha_n), (i_{n+1}, \alpha_{n+2})} = \sum_{\alpha_{n+1}} \tilde{A}_{(i_n, \alpha_n), \alpha_{n+1}}^{[n]} \tilde{\Lambda}_{\alpha_{n+1}, \alpha_{n+1}}^{[n+1]} \tilde{B}_{\alpha_{n+1}, (i_{n+1}, \alpha_{n+2})}^{[n+1]}. \quad (\text{A.40})$$

Due to the isometric properties of the \tilde{A} and \tilde{B} matrices, the orthonormality conditions Eq. (A.15) and Eq. (A.17) also hold for our updated state. Therefore, the diagonal matrix $\tilde{\Lambda}$ contains the Schmidt values of our updated state with respect to the bond connecting the sites n and $n + 1$. It is important to remark that after such a procedure, the bond dimension has grown from χ_{n+1} to $d\chi_{n+1}$. Thus, the dimensions of our matrices grow exponentially with the number of iterations, as the procedure is iterated. As explained in Sec. A.1.1, we put a cutoff on the maximum bond dimension χ_{\max} . Then, we move to the next iteration by defining the new two-site wavefunction,

$$\Theta_{\alpha_{n+1}, \alpha_{n+3}}^{i_{n+1}, i_{n+2}} = \sum_{\alpha_{n+2}} \tilde{\Lambda}_{\alpha_{n+1}, \alpha_{n+1}}^{[n+1]} \tilde{B}_{\alpha_{n+1}, \alpha_{n+2}}^{[n+1], i_{n+1}} B_{\alpha_{n+2}, \alpha_{n+3}}^{[n+2], i_{n+2}}, \quad (\text{A.41})$$

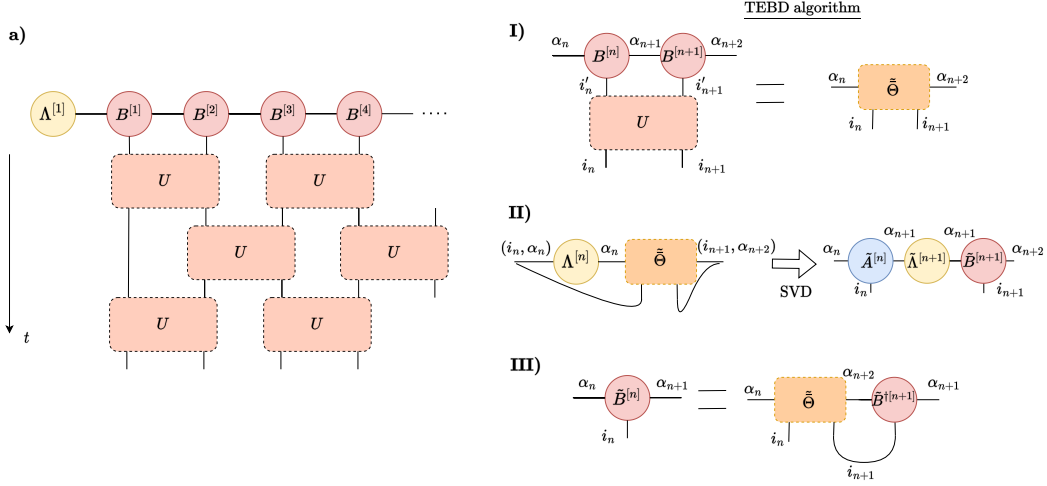


Figure A.5: In a) the unitary time evolution is applied on an MPS in right canonical form using the Suzuki-Trotter decomposition, see the main text. In b) we represent the TEBD algorithm. I) a two-site unitary gate is applied on the two-site wavefunction. II) an SVD is performed to obtain the MPS representation of the state after a single step of the time evolution. III) the tensor at site n is updated, see Eq. (A.49).

$$\Theta_{\alpha_{n-1}, \alpha_{n+1}}^{i_{n-1}, i_n} = \sum_{\alpha_n} A_{\alpha_{n-1}, \alpha_n}^{[n-1], i_{n-1}} \tilde{A}_{\alpha_n, \alpha_{n+1}}^{[n], i_n} \tilde{\Lambda}_{\alpha_{n+1}, \alpha_{n+1}}^{[n+1]} \quad (\text{A.42})$$

depending on whether we move to the right or to the left, respectively. The procedure defines a single iteration of the DMRG algorithm. After updating all the A and B matrices and have returned to the initial site n we call it a “sweep” in analogy with Sec. A.1.1. This concludes the implementation of the DMRG algorithm in the language of tensor networks. In Fig. A.4 b) we present a graphical representation of the DMRG algorithm in the language of tensor networks.

A.2 Time-evolving block decimation algorithm

The DMRG algorithm is a powerful method to obtain the ground state of a quantum many-body Hamiltonian. However, we are also interested in studying non-equilibrium phenomena and therefore need to perform real-time evolution. Many algorithms have been proposed for performing such a task, but we focus on the time-evolving block decimation (TEBD) algorithm (Vidal, 2004).

TEBD is based on the Suzuki-Trotter expansion of the exponential of a sum of two non-commuting operators (Suzuki, 1976),

$$e^{(\hat{O}_1 + \hat{O}_2)\epsilon} \approx e^{\epsilon \hat{O}_1} e^{\epsilon \hat{O}_2} + \mathcal{O}(\epsilon^2), \quad (\text{A.43})$$

where $\epsilon \ll 1$ is a small parameter. Let us consider that our Hamiltonian has finite range couplings that

only connect two neighboring sites, such that it can be decomposed as the sum of two terms,

$$\hat{H} = \sum_{i=1}^{N/2-1} \hat{h}^{[2n,2n+1]} + \sum_{i=0}^{N/2-1} \hat{h}^{[2n+1,2n+2]}. \quad (\text{A.44})$$

Note that the two terms share a common site, leading to the following commutation relations,

$$\left[\hat{h}^{[2n,2n+1]}, \hat{h}^{[2m+1,2m+2]} \right] \begin{cases} \neq 0 & \text{if } n = m \text{ or } 2m + 2 = 2n, \\ = 0 & \text{otherwise.} \end{cases} \quad (\text{A.45})$$

Hamiltonians with longer range coupling can also be simulated by introducing swap gates (Stoudenmire and White, 2010). The real-time evolution operator is obtained by the action of the unitary operator $\hat{U} = e^{-i\hat{H}t}$. By discretizing the time evolution into N_t steps with a small time step $\delta t = t/N_t \ll 1$, we can decompose the total time evolution as the product of N_t single steps $e^{-i\hat{H}\delta t}$, for which we can apply the Suzuki-Trotter expansion Eq. (A.43), leading to,

$$e^{-i\hat{H}\delta t} \approx \prod_{i=1}^{N/2-1} e^{-i\hat{h}^{[2n,2n+1]}\delta t} \prod_{i=0}^{N/2-1} e^{-i\hat{h}^{[2n+1,2n+2]}\delta t}. \quad (\text{A.46})$$

Therefore, the time evolution is decomposed as the product of two-site operators which we already know how to apply to our MPS wavefunction, see Fig. A.5 a) for a graphical representation. The two-site unitary gate is defined as follows,

$$U_{i'_n, i'_{n+1}}^{i_n, i_{n+1}} = \langle i'_n, i'_{n+1} | e^{-i\hat{h}^{[2n,2n+1]}\delta t} | i_n, i_{n+1} \rangle, \quad (\text{A.47})$$

and we need to apply it to the two-site wavefunction already defined in the DMRG algorithm, see Eq. (A.33),

$$\tilde{\Theta}_{\alpha_n, \alpha_{n+2}}^{i_n, i_{n+1}} = \sum_{i'_n, i'_{n+1}} U_{i'_n, i'_{n+1}}^{i_n, i_{n+1}} \Theta_{\alpha_n, \alpha_{n+2}}^{i'_n, i'_{n+1}}. \quad (\text{A.48})$$

Then, we perform an SVD of the updated state, see Eq. (A.40), and truncate the bond dimension up to χ_{\max} . In practice, this algorithm is usually performed in a right or left canonical form. Therefore, the updated tensors read in the right canonical form,

$$\tilde{B}_{\alpha_n, \alpha_{n+1}}^{[n], i_n} = \left(\Lambda^{[n]} \right)_{\alpha_n, \alpha_n}^{-1} \tilde{A}_{(i_n, \alpha_n), \alpha_{n+1}}^{[n]} \tilde{\Lambda}_{\alpha_{n+1}, \alpha_{n+1}}^{[n+1]}, \quad \tilde{B}_{\alpha_{n+1}, \alpha_{n+2}}^{[n+1], i_{n+1}} = \tilde{B}_{\alpha_{n+1}, (i_{n+1}, \alpha_{n+2})}^{[n+1]}. \quad (\text{A.49})$$

Note that the updated tensor involves performing an inverse of the singular values which can become very small for very large matrices leading to a source of numerical instability. In Ref. (Hastings, 2009) it was proposed an alternative way to avoid such matrix inversion. Consider the following two-site

wavefunction,

$$\bar{\Theta}_{\alpha_n, \alpha_{n+2}}^{i_n, i_{n+1}} = \sum_{\alpha_{n+1}} B_{\alpha_n, \alpha_{n+1}}^{[n]i_n} B_{\alpha_{n+1}, \alpha_{n+2}}^{[n+1]i_{n+1}} = \Lambda_{\alpha_n, \alpha_n}^{[n]} \Theta_{\alpha_n, \alpha_{n+2}}^{i_n, i_{n+1}}, \quad (\text{A.50})$$

for which we apply the two-site unitary gate,

$$\tilde{\Theta}_{\alpha_n, \alpha_{n+2}}^{i_n, i_{n+1}} = \sum_{i'_n, i'_{n+1}} U_{i'_n, i'_{n+1}}^{i_n, i_{n+1}} \bar{\Theta}_{\alpha_n, \alpha_{n+2}}^{i'_n, i'_{n+1}} = \Lambda_{\alpha_n, \alpha_n}^{[n]} \tilde{\Theta}_{\alpha_n, \alpha_{n+2}}^{i_n, i_{n+1}}. \quad (\text{A.51})$$

Then, the updated $\tilde{B}^{[n]}$ reads,

$$\tilde{B}_{\alpha_n, \alpha_{n+1}}^{[n], i_n} = \sum_{i_{n+1}, \alpha_{n+2}} \tilde{\Theta}_{\alpha_n, \alpha_{n+2}}^{i_n, i_{n+1}} \tilde{B}_{\alpha_{n+1}, \alpha_{n+2}}^{\dagger [n+1], i_{n+1}}, \quad (\text{A.52})$$

which leads to the same result as Eq. (A.49) at the cost of a matrix multiplication and avoids the matrix inversion. We have used the right orthonormality relation Eq. (A.17). In Fig. A.5 we present a graphical representation of the TEBD algorithm.

Let us also remark that imaginary time evolution $t = -i\tau$ can also be performed in an analogous way to obtain the ground state of the system. However, we recommend employing DMRG for such a task as it shows better convergence than imaginary time evolution with TEBD and can simulate systems with long-range couplings as discussed in Sec. (A.1.2.2).

There are two main sources of error in the TEBD algorithm. One error is introduced by the Suzuki-Trotter decomposition Eq. (A.43) which leads to an overall error that grows linearly in time ($t\delta t^2$). Therefore, we can scale down the error by choosing smaller time steps or employing a higher-order decomposition of the Suzuki-Trotter expansion. On the other hand, the second source of error comes from the matrix truncation to χ_{\max} that we perform at each SVD. The error introduced by the truncation remains small if the entanglement entropy does not increase too much in time. However, Lieb-Robinson bounds tell us that the entanglement entropy can grow up to linearly in time, $S_E(t) \leq S_E(0) + ct$, where c is some characteristic speed of sound followed by the quasi-particles of the system (Lieb and Robinson, 1972). In many cases, this upper bound is saturated during the time evolution (Calabrese and Cardy, 2005). Therefore, to properly simulate the time evolution with the family of MPS, we need matrices with a dimension that grows exponentially in time, $\chi(t) \propto \lambda^t$, leading to an exponential increase in numerical complexity. Thus, if we keep our matrices at a fixed bond dimension χ_{\max} we are committing an exponential error in time making the simulation to break down at a critical time. However, TEBD has been successfully applied to study many non-equilibrium phenomena of strongly correlated one-dimensional systems which can be captured at short or intermediate times. In the main part of this thesis we have employed another algorithm based on the time dependent variational principle (TDVP) (Haegeman et al., 2011, 2016). This algorithm projects the time evolution in the manifold spanned by MPS with fixed bond dimension χ_{\max} and it conserves all the good quantum charges of the Hamiltonian. Moreover, it allows to perform real and imaginary time evolution of systems with long-range couplings.

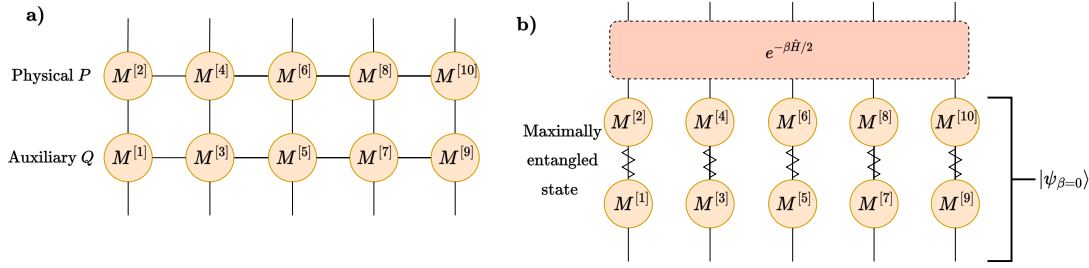


Figure A.6: In a) we represent a general density matrix in space P as the product of two 1D MPS living on dimensions P and Q which form a square ladder geometry. In b) we show the form of a general thermal density matrix at temperature β that can be obtained by applying the imaginary time evolution over the infinite temperature density matrix represented by the direct product of maximally entangled states between the spaces P and Q .

Let us also remark that both the DMRG and TEBD algorithms can be extended to simulate infinite systems, leading to the so-called iDMRG and infinite-TEBD (iTEBD) algorithms (Vidal, 2007b). The strategy is to assume translational invariance within a unit cell comprised of n sites and repeat it throughout the system. We do not provide an explicit explanation of the iDMRG and iTEBD algorithm extensions with respect to DMRG and TEBD, and readers interested in more details can consult (Schollwöck, 2011a).

A.3 Finite temperature through purification

So far, we have discussed tensor network algorithms for obtaining the ground state of a quantum many-body system and studying time-dependent problems. In this section, we explain how tensor network algorithms can be extended to study finite temperature properties based on the purification of a general mixed state (Verstraete et al., 2004; Barthel et al., 2009).

Consider a set of orthonormal states $|\phi\rangle_P$ which live in the Hilbert space \mathcal{H}^P . A general density matrix $\hat{\rho}_P$ can always be obtained by performing the partial trace of a pure state $|\psi\rangle$ living in an enlarged Hilbert space $\mathcal{H}^P \otimes \mathcal{H}^Q$, where \mathcal{H}^Q is an auxiliary “ancilla” subspace,

$$\hat{\rho}_P = \sum_{\phi} \lambda_{\phi}^2 |\phi\rangle_P \langle\phi|_P = \text{Tr}_Q |\psi\rangle \langle\psi|, \quad \text{with,} \quad |\psi\rangle = \sum_{\phi} \lambda_{\phi} |\phi\rangle_P |\phi\rangle_Q. \quad (\text{A.53})$$

Therefore, any density matrix can be represented by an MPS in an enlarged Hilbert space. In practice, the auxiliary space can be just a “copy” of the original Hilbert space $\mathcal{H}^Q = \mathcal{H}^P$ and a one-dimensional density matrix is mapped to a pure state living on a ladder geometry, as shown in Fig. A.6 a). In particular, we are interested in the family of equilibrium density matrices,

$$\hat{\rho}_{\beta} = \frac{1}{Z(\beta)} e^{-\beta \hat{H}}, \quad (\text{A.54})$$

where $Z(\beta) = \text{Tr}_P(e^{-\beta\hat{H}})$, which can always be purified by diagonalizing the Hamiltonian,

$$|\psi_\beta\rangle = \frac{1}{\sqrt{Z(\beta)}} \sum_m e^{-\beta E_m/2} |m\rangle_P |m\rangle_Q, \quad (\text{A.55})$$

where E_m and $|m\rangle$ are the eigenvalues and eigenvectors of the Hamiltonian. This purification of equilibrium states is called thermofield double (TFD) purification. However, it is important to note that the purification is not unique, as any unitary operation acting on the auxiliary space leaves Eq. (A.53) invariant. Furthermore, the purification scheme ensures that the density matrix $\hat{\rho}_\beta$ is positive semi-definite by construction.

To obtain the TFD purification, we need to diagonalize the Hamiltonian, which is an unreasonable task to perform with MPS algorithms. However, there is one exception, which is the infinite-temperature density matrix $\hat{\rho}_{\beta=0}$. Consider a system of N sites with a local Hilbert space of dimension d with a set of orthonormal states $|\sigma_n\rangle$ at each site n . Then, the infinite temperature density matrix corresponds to the identity in any basis,

$$\hat{\rho}_{\beta=0} = \left(\frac{1}{d}\hat{I}\right)^{\otimes N}. \quad (\text{A.56})$$

As the density matrix factorizes from rung to rung it can be represented by an MPS of bond dimension $\chi = 1$ along the physical direction. In each physical site, we have to construct the identity operator which is given by,

$$\frac{1}{d}\hat{I} = \frac{1}{d} \sum_\sigma |\sigma\rangle_P \langle\sigma|_P, \quad (\text{A.57})$$

and the associated TFD state is a maximally entangled state along the rung,

$$|\psi_{\beta=0}\rangle = \prod_n \frac{1}{\sqrt{d}} \sum_\sigma |\sigma_n\rangle_P |\sigma_n\rangle_Q. \quad (\text{A.58})$$

In practice, the gauge freedom given by the application of unitaries in the auxiliary space allows us to transform the state $|\psi_{\beta=0}\rangle$ into other states that exploit the underlying symmetries of the physical Hamiltonian (Barthel, 2016) or have a reduced amount of entanglement (Hauschild et al., 2018). Finally, we can relate the density matrix at finite temperature to the infinite temperature one,

$$\hat{\rho}_\beta = \frac{1}{Z(\beta)} e^{-\beta\hat{H}/2} \hat{I} e^{-\beta\hat{H}/2} = \frac{Z(0)}{Z(\beta)} e^{-\beta\hat{H}/2} \hat{\rho}_{\beta=0} e^{-\beta\hat{H}/2}. \quad (\text{A.59})$$

We conclude that the TFD state at an arbitrary temperature can be obtained by applying imaginary time evolution up to $-i\beta/2$ to the infinite temperature TFD state,

$$|\psi_\beta\rangle = \frac{1}{\sqrt{\langle\psi_{\beta=0}|e^{-\beta\hat{H}}|\psi_{\beta=0}\rangle}} e^{-\beta\hat{H}/2} |\psi_{\beta=0}\rangle, \quad (\text{A.60})$$

which can be simulated by employing standard MPS algorithms simulating the time evolution where the Hamiltonian acts only on the physical space $\hat{H} \otimes \hat{1}_Q$, see Fig. A.6 b). Any expectation value at finite temperature can be evaluated,

$$\langle \hat{O} \rangle_\beta = \text{Tr}_P(\hat{O} \hat{\rho}_\beta) = \frac{Z(0)}{Z(\beta)} \langle \psi_{\beta=0} | e^{-\beta \hat{H}/2} \hat{O} e^{-\beta \hat{H}/2} | \psi_{\beta=0} \rangle. \quad (\text{A.61})$$

Moreover, the normalization factor of the pure state gives us access to thermodynamic properties of the system. This becomes transparent by evaluating the expectation value of the identity operator,

$$1 = \langle \hat{I} \rangle_\beta = \text{Tr}_P(\hat{\rho}_\beta) = \langle \psi_{\beta=0} | e^{-\beta \hat{H}} | \psi_{\beta=0} \rangle \frac{Z(0)}{Z(\beta)} \rightarrow Z(\beta) = Z(0) \langle \psi_{\beta=0} | e^{-\beta \hat{H}} | \psi_{\beta=0} \rangle. \quad (\text{A.62})$$

Therefore, we can obtain the partition function by keeping track of the normalization factors during the imaginary time evolution.

Appendix B

LINEAR PREDICTOR ALGORITHM

In this Thesis we have employed tensor network algorithms to simulate the time dependence of different correlation functions, see e.g. Sec. 5.5. The main drawback of using tensor networks is the limited time in which such evolution can be properly and efficiently simulated. One-dimensional systems out-of-equilibrium typically feature an increasing linear entanglement entropy in time (Calabrese and Cardy, 2005) and therefore, tensor network algorithms at a fixed bond dimension can only describe the time evolution up to a maximum time (Paeckel et al., 2019). Further simulation of the time evolution requires increasing the bond dimension, which increases the computational time and restricts the maximum time available in the numerical simulation to t_{\max} . Typically, we perform a Fourier transform of the space-time dependent signal to a frequency-momentum dependent signal that can have severe ringing effects since the signal is suddenly cut at time t_{\max} . To avoid ringing effects of the Fourier transform one has to employ a window function such as a Gaussian one centered at time $t = 0$. However, the Gaussian window throws away most of the data and causes a strong overbroadening of the peaks in the momentum-frequency domain. To avoid these issues a linear predictor algorithm was introduced in (White and Affleck, 2008; Barthel et al., 2009). The main idea behind this algorithm is to extrapolate the data to longer times $t > t_{\max}$ in the momentum-time domain and then employ a Gaussian window to throw away the extrapolation but keeping most of the original data. The algorithm is able to avoid overbroadening and ringing effects caused by the finite time-evolution.

Given a time series of complex numbers x_0, x_1, \dots, x_N at equidistant times t_0, t_1, \dots, t_N , with $t_n = n\Delta t$ and $t_{\max} \equiv N\Delta t$, the linear predictor algorithm extrapolates the time series to x_{N+1}, x_{N+2}, \dots . In particular, the linear predictor algorithm assumes that any element of the time series can be expressed as a linear combination of the p previous elements,

$$y_n = - \sum_{i=1}^p c_i x_{n-i}, \quad (\text{B.1})$$

where c_i are complex coefficients that have to be determined and y_n is the approximate element obtained by the linear predictor algorithm. To determine the coefficients c_i we minimize the least-

square error between the predicted values y_n and the original data x_n in a time window $n \in (t_{\text{fit}} - t_{\text{fit}}, t_{\text{max}}]/\Delta t \equiv n \in \mathcal{N}$,

$$E = \sum_{n \in \mathcal{N}} |y_n - x_n|^2. \quad (\text{B.2})$$

The time interval t_{fit} has to be chosen large enough to have a decent amount of data points, but avoiding collecting short-term effects that do not represent long-term evolution. (White and Affleck, 2008; Barthel et al., 2009). We choose $t_{\text{fit}} = t_{\text{max}}/2$ as in (Barthel et al., 2009). Moreover, the number of parameters p is chosen such that $p\Delta t = t_{\text{fit}}/2$. The minimization of the least-square error with respect to the coefficients c_i leads to the solution,

$$\mathbf{c} = -\mathbf{R}^{-1}\mathbf{r}, \quad \text{with,} \quad R_{ij} = \sum_{n \in \mathcal{N}} x_{n-i}^* x_{n-j}, \quad \text{and,} \quad r_i = \sum_{n \in \mathcal{N}} x_{n-i}^* x_n, \quad (\text{B.3})$$

where $\mathbf{c} = [c_1, \dots, c_p]^T$. The main computational work to obtain the coefficients c_i comes from the inversion of the matrix R_{ij} . To remedy the numerical instabilities arising from arbitrary small eigenvalues, we regularize the matrix $\mathbf{R}^{-1} \rightarrow (\mathbf{R} + \epsilon \mathbb{I})^{-1}$, where we choose $\epsilon = 10^{-10}$ in our numerical simulations. Once the coefficients c_i are obtained one can extrapolate the data to an arbitrary time step $N + m$ by successively applying a matrix-vector multiplication,

$$y_{N+m} = \mathbf{A}^m \mathbf{x}_N, \quad \text{with,} \quad A = \begin{bmatrix} -a_1 & -a_2 & \dots & -a_{p-1} & -a_p \\ 1 & 0 & \dots & 0 & 0 \\ 0 & 1 & \dots & 0 & 0 \\ \vdots & \ddots & \ddots & \ddots & \vdots \\ 0 & 0 & \dots & 1 & 0 \end{bmatrix}, \quad \text{and,} \quad \mathbf{x}_N = [x_{N-1}, \dots, x_{N-p}]^T. \quad (\text{B.4})$$

By diagonalizing the matrix $\mathbf{P}^{-1}\mathbf{A}\mathbf{P} = \text{diag}(\lambda_1, \dots, \lambda_p)$ one can rewrite the prediction for the data as,

$$y_{N+m} = \sum_{i,j=1}^p P_{ij} x_j (\mathbf{P})_{ij}^{-1} \lambda_i^m. \quad (\text{B.5})$$

Therefore, the predicted data for times $t > t_{\text{max}}$ is composed by an oscillatory and an exponential function,

$$y(t) = \sum_{i=1}^p C_i e^{i\omega_i t - \eta_i t}. \quad (\text{B.6})$$

We consider exponential increasing contributions $|\lambda_i| > 1$ to be numerical artifacts and therefore, unphysical. To avoid these artifacts we choose to set them to zero $\lambda_i \rightarrow 0$, see (Barthel et al., 2009). Therefore, the linear predictor algorithm is able to extrapolate a time series to infinite times as long as it can be represented by a superposition of oscillatory contributions and exponential decaying

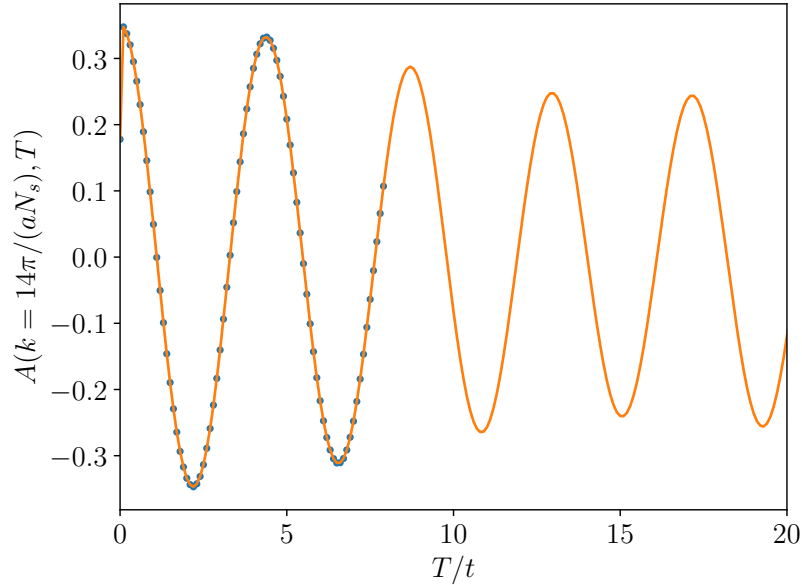


Figure B.1: Characteristic time-evolution of the dynamic structure factor in the momentum-time domain for a given momentum $k = 14\pi/(aN_s)$, being a the lattice spacing and N_s the number of sites comprising the 1D lattice. The Hamiltonian of the system is an extended Bose-Hubbard model including a dipolar interaction presented in Sec. 5.2 with on-site interaction $U/t = 20$, dipolar strength $V/t = -1/2$, particle number $N = 25$ and number of sites $N_s = 50$. Dots represent the time-evolution obtained with a two-site update TDVP algorithm with a maximum bond dimension $\chi = 800$ and the continuous line represents the prediction obtained for longer times using the linear predictor algorithm with the parameters given in the main text.

functions. This is the typical situation of the response functions studied in Sec. 5.5. Although, the space-time correlation function of a critical 1D system at zero temperature has a power-law decay in time (Giamarchi, 2003) it can be well represented by a superposition of decaying exponential functions.

In practice, we will employ the linear predictor algorithm to extrapolate correlation functions in the momentum-time domain. Trying to extrapolate correlation functions in the space-time domain for longer times can be very dramatic since correlation functions in space-time domain usually present a sound cone structure resulting in a sudden increase of the correlation function at a time $t_c = x/c_s$, being c_s the speed of sound of the system. This behavior cannot be well represented by the linear predictor algorithm. Therefore, it is better to first perform a Fourier transform to the momentum domain where the correlation function is smoother. After performing the linear predictor extrapolation we throw away most of the predicted data using a Gaussian window function to avoid the presence of numerical artifacts. The purpose of using the linear prediction algorithm is to avoid the ringing and overbroadening effects discussed above. In Fig. B.1 we present a typical time evolution of a correlation function in momentum-time domain and show the predicted values obtained by the linear predictor algorithm at times longer than those given by the simulation.

BIBLIOGRAPHY

- Abad, M. and Recati, A. A study of coherently coupled two-component bose-einstein condensates. *The European Physical Journal D*, 67(7):148, Jul 2013. ISSN 1434-6079. doi: 10.1140/epjd/e2013-40053-2. URL <https://doi.org/10.1140/epjd/e2013-40053-2>.
- Abouelkomsan, A., Liu, Z., and Bergholtz, E. J. Particle-hole duality, emergent fermi liquids, and fractional chern insulators in moiré flatbands. *Phys. Rev. Lett.*, 124:106803, Mar 2020. doi: 10.1103/PhysRevLett.124.106803. URL <https://link.aps.org/doi/10.1103/PhysRevLett.124.106803>.
- Ahn, C. H., Bhattacharya, A., Di Ventura, M., Eckstein, J. N., Frisbie, C. D., Gershenson, M. E., Goldman, A. M., Inoue, I. H., Mannhart, J., Millis, A. J., Morpurgo, A. F., Natelson, D., and Triscone, J.-M. Electrostatic modification of novel materials. *Rev. Mod. Phys.*, 78:1185–1212, Nov 2006. doi: 10.1103/RevModPhys.78.1185. URL <https://link.aps.org/doi/10.1103/RevModPhys.78.1185>.
- Aidelsburger, M., Atala, M., Lohse, M., Barreiro, J. T., Paredes, B., and Bloch, I. Realization of the hofstadter hamiltonian with ultracold atoms in optical lattices. *Phys. Rev. Lett.*, 111:185301, Oct 2013. doi: 10.1103/PhysRevLett.111.185301. URL <https://link.aps.org/doi/10.1103/PhysRevLett.111.185301>.
- Aidelsburger, M., Barbiero, L., Bermudez, A., Chanda, T., Dauphin, A., González-Cuadra, D., Grzybowski, P. R., Hands, S., Jendrzejewski, F., Jünemann, J., Juzeliūnas, G., Kasper, V., Piga, A., Ran, S.-J., Rizzi, M., Sierra, G., Tagliacozzo, L., Tirrito, E., Zache, T. V., Zakrzewski, J., Zohar, E., and Lewenstein, M. Cold atoms meet lattice gauge theory. *Philosophical Transactions of the Royal Society of London Series A*, 380(2216):20210064, Feb. 2022. doi: 10.1098/rsta.2021.0064.
- Alexandrov, A. S. *Polarons in advanced materials*. Canopus Pub, Dordrecht, 2007. ISBN 978-1-4020-6348-0.
- An, F. A., Meier, E. J., and Gadway, B. Direct observation of chiral currents and magnetic reflection in atomic flux lattices. *Science Advances*, 3(4), 2017. doi: 10.1126/sciadv.1602685. URL <https://advances.sciencemag.org/content/3/4/e1602685>.

- Anderson, M. H., Ensher, J. R., Matthews, M. R., Wieman, C. E., and Cornell, E. A. Observation of bose-einstein condensation in a dilute atomic vapor. *Science*, 269(5221):198–201, 1995. doi: 10.1126/science.269.5221.198. URL <https://www.science.org/doi/abs/10.1126/science.269.5221.198>.
- Anderson, P. W. Antiferromagnetism. theory of superexchange interaction. *Phys. Rev.*, 79:350–356, Jul 1950. doi: 10.1103/PhysRev.79.350. URL <https://link.aps.org/doi/10.1103/PhysRev.79.350>.
- Anderson, R., Wang, F., Xu, P., Venu, V., Trotzky, S., Chevy, F., and Thywissen, J. H. Conductivity spectrum of ultracold atoms in an optical lattice. *Phys. Rev. Lett.*, 122:153602, Apr 2019. doi: 10.1103/PhysRevLett.122.153602. URL <https://link.aps.org/doi/10.1103/PhysRevLett.122.153602>.
- Andreev, A. F. and Bashkin, E. P. Three-velocity hydrodynamics of superfluid solutions. *Sov. Phys.-JETP*, 42:164, 1976.
- Andrei, E. Y., Efetov, D. K., Jarillo-Herrero, P., MacDonald, A. H., Mak, K. F., Senthil, T., Tutuc, E., Yazdani, A., and Young, A. F. The marvels of moiré materials. *Nature Reviews Materials*, 6(3): 201–206, Mar 2021. ISSN 2058-8437. doi: 10.1038/s41578-021-00284-1. URL <https://doi.org/10.1038/s41578-021-00284-1>.
- Aramthottil, A. S., Lacki, M., Santos, L., and Zakrzewski, J. The role of interaction-induced tunneling in the dynamics of polar lattice bosons. 2023.
- Ashcroft, N. *Solid state physics*. Holt, Rinehart and Winston, New York, 1976. ISBN 978-0030839931.
- Ashkin, A. Trapping of atoms by resonance radiation pressure. *Phys. Rev. Lett.*, 40:729–732, Mar 1978. doi: 10.1103/PhysRevLett.40.729. URL <https://link.aps.org/doi/10.1103/PhysRevLett.40.729>.
- Astrakharchik, G. E., Blume, D., Giorgini, S., and Granger, B. E. Quasi-one-dimensional bose gases with a large scattering length. *Phys. Rev. Lett.*, 92:030402, Jan 2004. doi: 10.1103/PhysRevLett.92.030402. URL <https://link.aps.org/doi/10.1103/PhysRevLett.92.030402>.
- Astrakharchik, G. E., Boronat, J., Kurbakov, I. L., Lozovik, Y. E., and Mazzanti, F. Low-dimensional weakly interacting bose gases: Nonuniversal equations of state. *Phys. Rev. A*, 81:013612, Jan 2010. doi: 10.1103/PhysRevA.81.013612. URL <https://link.aps.org/doi/10.1103/PhysRevA.81.013612>.
- Astrakharchik, G. E., Krutitsky, K. V., Lewenstein, M., and Mazzanti, F. One-dimensional bose gas in optical lattices of arbitrary strength. *Phys. Rev. A*, 93:021605, Feb 2016. doi: 10.1103/PhysRevA.93.021605. URL <https://link.aps.org/doi/10.1103/PhysRevA.93.021605>.
- Astrakharchik, G. E., Krutitsky, K. V., Lewenstein, M., Mazzanti, F., and Boronat, J. Optical lattices as a tool to study defect-induced superfluidity. *Phys. Rev. A*, 96:033606, Sep 2017. doi: 10.1103/PhysRevA.96.033606. URL <https://link.aps.org/doi/10.1103/PhysRevA.96.033606>.

- Atala, M., Aidelsburger, M., Lohse, M., Barreiro, J. T., Paredes, B., and Bloch, I. Observation of chiral currents with ultracold atoms in bosonic ladders. *Nature Physics*, 10(8):588–593, Aug 2014. ISSN 1745-2481. doi: 10.1038/nphys2998. URL <https://doi.org/10.1038/nphys2998>.
- Auerbach, A. *Interacting electrons and quantum magnetism*. Graduate Texts in Contemporary Physics. Springer, New York, NY, 1 edition, June 1998.
- Awschalom, D. D. and Flatté, M. E. Challenges for semiconductor spintronics. *Nature Physics*, 3(3): 153–159, Mar 2007. ISSN 1745-2481. doi: 10.1038/nphys551. URL <https://doi.org/10.1038/nphys551>.
- Bañuls, M. C. Tensor network algorithms: A route map. *Annual Review of Condensed Matter Physics*, 14(1):173–191, 2023. doi: 10.1146/annurev-conmatphys-040721-022705. URL <https://doi.org/10.1146/annurev-conmatphys-040721-022705>.
- Baier, S., Mark, M. J., Petter, D., Aikawa, K., Chomaz, L., Cai, Z., Baranov, M., Zoller, P., and Ferlaino, F. Extended bose-hubbard models with ultracold magnetic atoms. *Science*, 352(6282): 201–205, 2016. ISSN 0036-8075. doi: 10.1126/science.aac9812.
- Baillie, D., Wilson, R. M., Bisset, R. N., and Blakie, P. B. Self-bound dipolar droplet: A localized matter wave in free space. *Phys. Rev. A*, 94:021602, Aug 2016a. doi: 10.1103/PhysRevA.94.021602. URL <http://link.aps.org/doi/10.1103/PhysRevA.94.021602>.
- Baillie, D., Wilson, R. M., Bisset, R. N., and Blakie, P. B. Self-bound dipolar droplet: A localized matter wave in free space. *Phys. Rev. A*, 94:021602, Aug 2016b. doi: 10.1103/PhysRevA.94.021602. URL <https://link.aps.org/doi/10.1103/PhysRevA.94.021602>.
- Bakr, W. S., Gillen, J. I., Peng, A., Fölling, S., and Greiner, M. A quantum gas microscope for detecting single atoms in a hubbard-regime optical lattice. *Nature*, 462(7269):74–77, Nov 2009. ISSN 1476-4687. doi: 10.1038/nature08482. URL <https://doi.org/10.1038/nature08482>.
- Bakr, W. S., Peng, A., Tai, M. E., Ma, R., Simon, J., Gillen, J. I., Fölling, S., Pollet, L., and Greiner, M. Probing the superfluid-to-mott insulator transition at the single-atom level. *Science*, 329(5991):547–550, 2010. doi: 10.1126/science.1192368. URL <https://www.science.org/doi/abs/10.1126/science.1192368>.
- Banuls, M. C., Cichy, K., Cirac, J. I., Jansen, K., and Kühn, S. Tensor Networks and their use for Lattice Gauge Theories. *PoS, LATTICE2018:022*, 2019. doi: 10.22323/1.334.0022.
- Bañuls, M. C., Blatt, R., Catani, J., Celi, A., Cirac, J. I., Dalmonte, M., Fallani, L., Jansen, K., Lewenstein, M., Montangero, S., Muschik, C. A., Reznik, B., Rico, E., Tagliacozzo, L., Van Acoleyen, K., Verstraete, F., Wiese, U.-J., Wingate, M., Zakrzewski, J., and Zoller, P. Simulating lattice gauge theories within quantum technologies. *The European Physical Journal D*, 74(8):165, Aug 2020. ISSN 1434-6079. doi: 10.1140/epjd/e2020-100571-8. URL <https://doi.org/10.1140/epjd/e2020-100571-8>.

- Barford, W. and Kim, J. H. Spinless fermions on frustrated lattices in a magnetic field. *Phys. Rev. B*, 43:559–568, Jan 1991. doi: 10.1103/PhysRevB.43.559. URL <https://link.aps.org/doi/10.1103/PhysRevB.43.559>.
- Barranco, M., Guardiola, R., Hernández, S., Mayol, R., Navarro, J., and Pi, M. Helium nanodroplets: An overview. *J. Low Temp. Phys.*, 142(1):1, 2006. ISSN 1573-7357. doi: 10.1007/s10909-005-9267-0. URL <https://doi.org/10.1007/s10909-005-9267-0>.
- Barthel, T. Matrix product purifications for canonical ensembles and quantum number distributions. *Phys. Rev. B*, 94:115157, Sep 2016. doi: 10.1103/PhysRevB.94.115157. URL <https://link.aps.org/doi/10.1103/PhysRevB.94.115157>.
- Barthel, T., Schollwöck, U., and White, S. R. Spectral functions in one-dimensional quantum systems at finite temperature using the density matrix renormalization group. *Phys. Rev. B*, 79:245101, Jun 2009. doi: 10.1103/PhysRevB.79.245101. URL <https://link.aps.org/doi/10.1103/PhysRevB.79.245101>.
- Baumann, K., Guerlin, C., Brennecke, F., and Esslinger, T. Dicke quantum phase transition with a superfluid gas in an optical cavity. *Nature*, 464(7293):1301–1306, Apr 2010. ISSN 1476-4687. doi: 10.1038/nature09009. URL <https://doi.org/10.1038/nature09009>.
- Beane, S. R. Ground-state energy of the interacting bose gas in two dimensions: An explicit construction. *Phys. Rev. A*, 82:063610, Dec 2010. doi: 10.1103/PhysRevA.82.063610. URL <https://link.aps.org/doi/10.1103/PhysRevA.82.063610>.
- Beane, S. R. Effective-range corrections to the ground-state energy of the weakly-interacting bose gas in two dimensions. *The European Physical Journal D*, 72(3):55, Mar 2018. ISSN 1434-6079. doi: 10.1140/epjd/e2018-80713-y. URL <https://doi.org/10.1140/epjd/e2018-80713-y>.
- Becca, F. and Sorella, S. *Quantum Monte Carlo Approaches for Correlated Systems*. Cambridge University Press, 2017. doi: 10.1017/9781316417041.
- Bedaque, P. F. and van Kolck, U. Effective field theory for few-nucleon systems. *Annual Review of Nuclear and Particle Science*, 52(1):339–396, 2002. doi: 10.1146/annurev.nucl.52.050102.090637.
- Bergeman, T., Moore, M. G., and Olshanii, M. Atom-atom scattering under cylindrical harmonic confinement: Numerical and analytic studies of the confinement induced resonance. *Phys. Rev. Lett.*, 91:163201, Oct 2003. doi: 10.1103/PhysRevLett.91.163201. URL <https://link.aps.org/doi/10.1103/PhysRevLett.91.163201>.
- Biamonte, J. and Bergholm, V. Tensor networks in a nutshell. 2017.
- Bistritzer, R. and MacDonald, A. H. Moiré bands in twisted double-layer graphene. *Proceedings of the National Academy of Sciences*, 108(30):12233–12237, 2011. doi: 10.1073/pnas.1108174108. URL <https://www.pnas.org/doi/abs/10.1073/pnas.1108174108>.

- Bloch, I. Ultracold quantum gases in optical lattices. *Nature Physics*, 1(1):23–30, Oct 2005. ISSN 1745-2481. doi: 10.1038/nphys138. URL <https://doi.org/10.1038/nphys138>.
- Bloch, I., Dalibard, J., and Zwirger, W. Many-body physics with ultracold gases. *Rev. Mod. Phys.*, 80:885–964, Jul 2008. doi: 10.1103/RevModPhys.80.885. URL <https://link.aps.org/doi/10.1103/RevModPhys.80.885>.
- Bloch, I., Dalibard, J., and Nascimbène, S. Quantum simulations with ultracold quantum gases. *Nature Physics*, 8(4):267–276, Apr 2012. ISSN 1745-2481. doi: 10.1038/nphys2259. URL <https://doi.org/10.1038/nphys2259>.
- Bohrdt, A., Greif, D., Demler, E., Knap, M., and Grusdt, F. Angle-resolved photoemission spectroscopy with quantum gas microscopes. *Phys. Rev. B*, 97:125117, Mar 2018. doi: 10.1103/PhysRevB.97.125117. URL <https://link.aps.org/doi/10.1103/PhysRevB.97.125117>.
- Boll, M., Hilker, T. A., Salomon, G., Omran, A., Nespolo, J., Pollet, L., Bloch, I., and Gross, C. Spin- and density-resolved microscopy of antiferromagnetic correlations in fermi-hubbard chains. *Science*, 353(6305):1257–1260, 2016. doi: 10.1126/science.aag1635. URL <https://www.science.org/doi/abs/10.1126/science.aag1635>.
- Böttcher, F., Schmidt, J.-N., Wenzel, M., Hertkorn, J., Guo, M., Langen, T., and Pfau, T. Transient supersolid properties in an array of dipolar quantum droplets. *Phys. Rev. X*, 9:011051, Mar 2019a. doi: 10.1103/PhysRevX.9.011051. URL <https://link.aps.org/doi/10.1103/PhysRevX.9.011051>.
- Böttcher, F., Wenzel, M., Schmidt, J.-N., Guo, M., Langen, T., Ferrier-Barbut, I., Pfau, T., Bombín, R., Sánchez-Baena, J., Boronat, J., and Mazzanti, F. Dilute dipolar quantum droplets beyond the extended gross-pitaevskii equation. *Phys. Rev. Research*, 1:033088, Nov 2019b. doi: 10.1103/PhysRevResearch.1.033088. URL <https://link.aps.org/doi/10.1103/PhysRevResearch.1.033088>.
- Boukari, H., Kossacki, P., Bertolini, M., Ferrand, D., Cibert, J., Tatarenko, S., Wasiela, A., Gaj, J. A., and Dietl, T. Light and electric field control of ferromagnetism in magnetic quantum structures. *Phys. Rev. Lett.*, 88:207204, May 2002. doi: 10.1103/PhysRevLett.88.207204. URL <https://link.aps.org/doi/10.1103/PhysRevLett.88.207204>.
- Braaten, E. and Hammer, H.-W. Universality in few-body systems with large scattering length. *Physics Reports*, 428(5):259–390, 2006. ISSN 0370-1573. doi: <https://doi.org/10.1016/j.physrep.2006.03.001>. URL <https://www.sciencedirect.com/science/article/pii/S0370157306000822>.
- Bradley, C. C., Sackett, C. A., Tollett, J. J., and Hulet, R. G. Evidence of bose-einstein condensation in an atomic gas with attractive interactions. *Phys. Rev. Lett.*, 75:1687–1690, Aug 1995. doi: 10.1103/PhysRevLett.75.1687. URL <https://link.aps.org/doi/10.1103/PhysRevLett.75.1687>.
- Bridgeman, J. C. and Chubb, C. T. Hand-waving and interpretive dance: an introductory course on tensor networks. *Journal of Physics A: Mathematical and Theoretical*, 50(22):223001, may 2017. doi: 10.1088/1751-8121/aa6dc3. URL <https://dx.doi.org/10.1088/1751-8121/aa6dc3>.

- Britton, J. W., Sawyer, B. C., Keith, A. C., Wang, C.-C. J., Freericks, J. K., Uys, H., Biercuk, M. J., and Bollinger, J. J. Engineered two-dimensional ising interactions in a trapped-ion quantum simulator with hundreds of spins. *Nature*, 484(7395):489–492, Apr 2012. ISSN 1476-4687. doi: 10.1038/nature10981. URL <https://doi.org/10.1038/nature10981>.
- Browaeys, A. and Lahaye, T. Many-body physics with individually controlled rydberg atoms. *Nature Physics*, 16(2):132–142, Feb 2020. ISSN 1745-2481. doi: 10.1038/s41567-019-0733-z. URL <https://doi.org/10.1038/s41567-019-0733-z>.
- Brown, P. T., Mitra, D., Guardado-Sanchez, E., Schauß, P., Kondov, S. S., Khatami, E., Paiva, T., Trivedi, N., Huse, D. A., and Bakr, W. S. Spin-imbalance in a 2d fermi-hubbard system. *Science*, 357(6358):1385–1388, 2017. ISSN 0036-8075. doi: 10.1126/science.aam7838. URL <https://science.sciencemag.org/content/357/6358/1385>.
- Brown, R. C., Wyllie, R., Koller, S. B., Goldschmidt, E. A., Foss-Feig, M., and Porto, J. V. Two-dimensional superexchange-mediated magnetization dynamics in an optical lattice. *Science*, 348(6234):540–544, 2015. ISSN 0036-8075. doi: 10.1126/science.aaa1385. URL <https://science.sciencemag.org/content/348/6234/540>.
- Bulgac, A. Dilute quantum droplets. *Phys. Rev. Lett.*, 89:050402, Jul 2002. doi: 10.1103/PhysRevLett.89.050402. URL <https://link.aps.org/doi/10.1103/PhysRevLett.89.050402>.
- Bultinck, N., Chatterjee, S., and Zaletel, M. P. Mechanism for anomalous hall ferromagnetism in twisted bilayer graphene. *Phys. Rev. Lett.*, 124:166601, Apr 2020a. doi: 10.1103/PhysRevLett.124.166601. URL <https://link.aps.org/doi/10.1103/PhysRevLett.124.166601>.
- Bultinck, N., Khalaf, E., Liu, S., Chatterjee, S., Vishwanath, A., and Zaletel, M. P. Ground state and hidden symmetry of magic-angle graphene at even integer filling. *Phys. Rev. X*, 10:031034, Aug 2020b. doi: 10.1103/PhysRevX.10.031034. URL <https://link.aps.org/doi/10.1103/PhysRevX.10.031034>.
- Cabrera, C. R., Tanzi, L., Sanz, J., Naylor, B., Thomas, P., Cheiney, P., and Tarruell, L. Quantum liquid droplets in a mixture of bose-einstein condensates. *Science*, 359(6373):301–304, 2018. doi: 10.1126/science.aao5686.
- Calabrese, P. and Cardy, J. Entanglement entropy and quantum field theory. *Journal of Statistical Mechanics: Theory and Experiment*, 2004(06):P06002, jun 2004. doi: 10.1088/1742-5468/2004/06/P06002. URL <https://dx.doi.org/10.1088/1742-5468/2004/06/P06002>.
- Calabrese, P. and Cardy, J. Evolution of entanglement entropy in one-dimensional systems. *Journal of Statistical Mechanics: Theory and Experiment*, 2005(04):P04010, apr 2005. doi: 10.1088/1742-5468/2005/04/P04010. URL <https://dx.doi.org/10.1088/1742-5468/2005/04/P04010>.
- Calabrese, P. and Lefevre, A. Entanglement spectrum in one-dimensional systems. *Phys. Rev. A*, 78:032329, Sep 2008. doi: 10.1103/PhysRevA.78.032329. URL <https://link.aps.org/doi/10.1103/PhysRevA.78.032329>.

- Calogero, F. and Degasperis, A. Comparison between the exact and hartree solutions of a one-dimensional many-body problem. *Phys. Rev. A*, 11:265–269, Jan 1975. doi: 10.1103/PhysRevA.11.265. URL <https://link.aps.org/doi/10.1103/PhysRevA.11.265>.
- Cao, T., Wang, G., Han, W., Ye, H., Zhu, C., Shi, J., Niu, Q., Tan, P., Wang, E., Liu, B., and Feng, J. Valley-selective circular dichroism of monolayer molybdenum disulphide. *Nature Communications*, 3(1):887, Jun 2012. ISSN 2041-1723. doi: 10.1038/ncomms1882. URL <https://doi.org/10.1038/ncomms1882>.
- Cao, Y., Fatemi, V., Demir, A., Fang, S., Tomarken, S. L., Luo, J. Y., Sanchez-Yamagishi, J. D., Watanabe, K., Taniguchi, T., Kaxiras, E., Ashoori, R. C., and Jarillo-Herrero, P. Correlated insulator behaviour at half-filling in magic-angle graphene superlattices. *Nature*, 556(7699):80–84, Apr 2018a. ISSN 1476-4687. doi: 10.1038/nature26154. URL <https://doi.org/10.1038/nature26154>.
- Cao, Y., Fatemi, V., Fang, S., Watanabe, K., Taniguchi, T., Kaxiras, E., and Jarillo-Herrero, P. Unconventional superconductivity in magic-angle graphene superlattices. *Nature*, 556(7699):43–50, Apr 2018b. ISSN 1476-4687. doi: 10.1038/nature26160. URL <https://doi.org/10.1038/nature26160>.
- Caux, J.-S. and Calabrese, P. Dynamical density-density correlations in the one-dimensional bose gas. *Phys. Rev. A*, 74:031605, Sep 2006. doi: 10.1103/PhysRevA.74.031605. URL <https://link.aps.org/doi/10.1103/PhysRevA.74.031605>.
- Cazalilla, M. A. One-dimensional optical lattices and impenetrable bosons. *Phys. Rev. A*, 67:053606, May 2003. doi: 10.1103/PhysRevA.67.053606. URL <https://link.aps.org/doi/10.1103/PhysRevA.67.053606>.
- Cazalilla, M. A. Bosonizing one-dimensional cold atomic gases. *Journal of Physics B: Atomic, Molecular and Optical Physics*, 37(7):S1–S47, mar 2004a. doi: 10.1088/0953-4075/37/7/051. URL <https://doi.org/10.1088/0953-4075/37/7/051>.
- Cazalilla, M. A. Differences between the tonks regimes in the continuum and on the lattice. *Phys. Rev. A*, 70:041604, Oct 2004b. doi: 10.1103/PhysRevA.70.041604. URL <https://link.aps.org/doi/10.1103/PhysRevA.70.041604>.
- Cazalilla, M. A., Citro, R., Giamarchi, T., Orignac, E., and Rigol, M. One dimensional bosons: From condensed matter systems to ultracold gases. *Rev. Mod. Phys.*, 83:1405–1466, Dec 2011. doi: 10.1103/RevModPhys.83.1405. URL <https://link.aps.org/doi/10.1103/RevModPhys.83.1405>.
- Celi, A., Massignan, P., Ruseckas, J., Goldman, N., Spielman, I. B., Juzeliūnas, G., and Lewenstein, M. Synthetic gauge fields in synthetic dimensions. *Phys. Rev. Lett.*, 112:043001, Jan 2014. doi: 10.1103/PhysRevLett.112.043001. URL <https://link.aps.org/doi/10.1103/PhysRevLett.112.043001>.

- Chan, G. K.-L. and Sharma, S. The density matrix renormalization group in quantum chemistry. *Annual Review of Physical Chemistry*, 62(1):465–481, 2011. doi: 10.1146/annurev-physchem-032210-103338. URL <https://doi.org/10.1146/annurev-physchem-032210-103338>. PMID: 21219144.
- Chang, D. E., Douglas, J. S., González-Tudela, A., Hung, C.-L., and Kimble, H. J. Colloquium: Quantum matter built from nanoscopic lattices of atoms and photons. *Rev. Mod. Phys.*, 90:031002, Aug 2018. doi: 10.1103/RevModPhys.90.031002. URL <https://link.aps.org/doi/10.1103/RevModPhys.90.031002>.
- Chattopadhyay, A., Das Sarma, S., and Millis, A. J. Transition temperature of ferromagnetic semiconductors: A dynamical mean field study. *Phys. Rev. Lett.*, 87:227202, Nov 2001. doi: 10.1103/PhysRevLett.87.227202. URL <https://link.aps.org/doi/10.1103/PhysRevLett.87.227202>.
- Chen, B.-B., Chen, Z., Gong, S.-S., Sheng, D. N., Li, W., and Weichselbaum, A. Quantum spin liquid with emergent chiral order in the triangular-lattice hubbard model. *Phys. Rev. B*, 106:094420, Sep 2022. doi: 10.1103/PhysRevB.106.094420. URL <https://link.aps.org/doi/10.1103/PhysRevB.106.094420>.
- Cheneau, M., Barmettler, P., Poletti, D., Endres, M., Schauß, P., Fukuhara, T., Gross, C., Bloch, I., Kollath, C., and Kuhr, S. Light-cone-like spreading of correlations in a quantum many-body system. *Nature*, 481(7382):484–487, Jan. 2012. doi: 10.1038/nature10748. URL <https://doi.org/10.1038/nature10748>.
- Chernikov, A., Berkelbach, T. C., Hill, H. M., Rigosi, A., Li, Y., Aslan, B., Reichman, D. R., Hybertsen, M. S., and Heinz, T. F. Exciton binding energy and nonhydrogenic rydberg series in monolayer ws_2 . *Phys. Rev. Lett.*, 113:076802, Aug 2014. doi: 10.1103/PhysRevLett.113.076802. URL <https://link.aps.org/doi/10.1103/PhysRevLett.113.076802>.
- Cheuk, L. W., Nichols, M. A., Okan, M., Gersdorf, T., Ramasesh, V. V., Bakr, W. S., Lompe, T., and Zwierlein, M. W. Quantum-gas microscope for fermionic atoms. *Phys. Rev. Lett.*, 114:193001, May 2015. doi: 10.1103/PhysRevLett.114.193001. URL <https://link.aps.org/doi/10.1103/PhysRevLett.114.193001>.
- Chin, C., Grimm, R., Julienne, P., and Tiesinga, E. Feshbach resonances in ultracold gases. *Rev. Mod. Phys.*, 82:1225–1286, Apr 2010. doi: 10.1103/RevModPhys.82.1225. URL <https://link.aps.org/doi/10.1103/RevModPhys.82.1225>.
- Chomaz, L., Baier, S., Petter, D., Mark, M. J., Wächtler, F., Santos, L., and Ferlaino, F. Quantum-fluctuation-driven crossover from a dilute bose-einstein condensate to a macrodroplet in a dipolar quantum fluid. *Phys. Rev. X*, 6:041039, Nov 2016. doi: 10.1103/PhysRevX.6.041039. URL <https://link.aps.org/doi/10.1103/PhysRevX.6.041039>.
- Chomaz, L., Petter, D., Ilzhöfer, P., Natale, G., Trautmann, A., Politi, C., Durastante, G., van Bijnen, R. M. W., Patscheider, A., Sohmen, M., Mark, M. J., and Ferlaino, F. Long-lived and

- transient supersolid behaviors in dipolar quantum gases. *Phys. Rev. X*, 9:021012, Apr 2019. doi: 10.1103/PhysRevX.9.021012. URL <https://link.aps.org/doi/10.1103/PhysRevX.9.021012>.
- Chotia, A., Neyenhuis, B., Moses, S. A., Yan, B., Covey, J. P., Foss-Feig, M., Rey, A. M., Jin, D. S., and Ye, J. Long-lived dipolar molecules and feshbach molecules in a 3d optical lattice. *Phys. Rev. Lett.*, 108:080405, Feb 2012. doi: 10.1103/PhysRevLett.108.080405. URL <https://link.aps.org/doi/10.1103/PhysRevLett.108.080405>.
- Chu, S., Hollberg, L., Bjorkholm, J. E., Cable, A., and Ashkin, A. Three-dimensional viscous confinement and cooling of atoms by resonance radiation pressure. *Phys. Rev. Lett.*, 55:48–51, Jul 1985. doi: 10.1103/PhysRevLett.55.48. URL <https://link.aps.org/doi/10.1103/PhysRevLett.55.48>.
- Chu, S., Bjorkholm, J. E., Ashkin, A., and Cable, A. Experimental observation of optically trapped atoms. *Phys. Rev. Lett.*, 57:314–317, Jul 1986. doi: 10.1103/PhysRevLett.57.314. URL <https://link.aps.org/doi/10.1103/PhysRevLett.57.314>.
- Cifuentes, M. V. *Few quantum particles on one dimensional lattices*. PhD thesis, Humboldt-Universität zu Berlin, Mathematisch-Naturwissenschaftliche Fakultät I, 2010.
- Cincio, L. and Vidal, G. Characterizing topological order by studying the ground states on an infinite cylinder. *Phys. Rev. Lett.*, 110:067208, Feb 2013. doi: 10.1103/PhysRevLett.110.067208. URL <https://link.aps.org/doi/10.1103/PhysRevLett.110.067208>.
- Cirac, J. I. and Zoller, P. Quantum computations with cold trapped ions. *Phys. Rev. Lett.*, 74:4091–4094, May 1995. doi: 10.1103/PhysRevLett.74.4091. URL <https://link.aps.org/doi/10.1103/PhysRevLett.74.4091>.
- Cirac, J. I. and Zoller, P. A scalable quantum computer with ions in an array of microtraps. *Nature*, 404(6778):579–581, Apr 2000. ISSN 1476-4687. doi: 10.1038/35007021. URL <https://doi.org/10.1038/35007021>.
- Clay, R. T., Li, H., and Mazumdar, S. Absence of superconductivity in the half-filled band hubbard model on the anisotropic triangular lattice. *Phys. Rev. Lett.*, 101:166403, Oct 2008. doi: 10.1103/PhysRevLett.101.166403. URL <https://link.aps.org/doi/10.1103/PhysRevLett.101.166403>.
- Coleman, S. There are no Goldstone bosons in two dimensions. *Communications in Mathematical Physics*, 31(4):259 – 264, 1973.
- Cookmeyer, T., Motruk, J., and Moore, J. E. Four-spin terms and the origin of the chiral spin liquid in mott insulators on the triangular lattice. *Phys. Rev. Lett.*, 127:087201, Aug 2021. doi: 10.1103/PhysRevLett.127.087201. URL <https://link.aps.org/doi/10.1103/PhysRevLett.127.087201>.
- Cooper, N. R. and Dalibard, J. Reaching fractional quantum hall states with optical flux lattices. *Phys. Rev. Lett.*, 110:185301, Apr 2013. doi: 10.1103/PhysRevLett.110.185301. URL <https://link.aps.org/doi/10.1103/PhysRevLett.110.185301>.

- Courteille, P., Freeland, R. S., Heinzen, D. J., van Abeelen, F. A., and Verhaar, B. J. Observation of a feshbach resonance in cold atom scattering. *Phys. Rev. Lett.*, 81:69–72, Jul 1998. doi: 10.1103/PhysRevLett.81.69. URL <https://link.aps.org/doi/10.1103/PhysRevLett.81.69>.
- Crosswhite, G. M. and Bacon, D. Finite automata for caching in matrix product algorithms. *Phys. Rev. A*, 78:012356, Jul 2008. doi: 10.1103/PhysRevA.78.012356. URL <https://link.aps.org/doi/10.1103/PhysRevA.78.012356>.
- Cudazzo, P., Tokatly, I. V., and Rubio, A. Dielectric screening in two-dimensional insulators: Implications for excitonic and impurity states in graphane. *Phys. Rev. B*, 84:085406, Aug 2011. doi: 10.1103/PhysRevB.84.085406. URL <https://link.aps.org/doi/10.1103/PhysRevB.84.085406>.
- Czejdo, A. J., Drut, J. E., Hou, Y., McKenney, J. R., and Morrell, K. J. Virial coefficients of trapped and untrapped three-component fermions with three-body forces in arbitrary spatial dimensions. *Phys. Rev. A*, 101:063630, Jun 2020. doi: 10.1103/PhysRevA.101.063630. URL <https://link.aps.org/doi/10.1103/PhysRevA.101.063630>.
- Dagotto, E., Moreo, A., and Barnes, T. Hubbard model with one hole: Ground-state properties. *Phys. Rev. B*, 40:6721–6725, Oct 1989. doi: 10.1103/PhysRevB.40.6721. URL <https://link.aps.org/doi/10.1103/PhysRevB.40.6721>.
- Daley, A. J., Kollath, C., Schollwöck, U., and Vidal, G. Time-dependent density-matrix renormalization-group using adaptive effective hilbert spaces. *Journal of Statistical Mechanics: Theory and Experiment*, 2004(04):P04005, apr 2004. doi: 10.1088/1742-5468/2004/04/P04005. URL <https://dx.doi.org/10.1088/1742-5468/2004/04/P04005>.
- Daley, A. J., Taylor, J. M., Diehl, S., Baranov, M., and Zoller, P. Atomic three-body loss as a dynamical three-body interaction. *Phys. Rev. Lett.*, 102:040402, Jan 2009. doi: 10.1103/PhysRevLett.102.040402. URL <https://link.aps.org/doi/10.1103/PhysRevLett.102.040402>.
- Dalibard, J. and Cohen-Tannoudji, C. Laser cooling below the doppler limit by polarization gradients: simple theoretical models. *J. Opt. Soc. Am. B*, 6(11):2023–2045, Nov 1989. doi: 10.1364/JOSAB.6.002023. URL <https://opg.optica.org/josab/abstract.cfm?URI=josab-6-11-2023>.
- Dalibard, J., Gerbier, F., Juzeliūnas, G., and Öhberg, P. Colloquium: Artificial gauge potentials for neutral atoms. *Rev. Mod. Phys.*, 83:1523–1543, Nov 2011. doi: 10.1103/RevModPhys.83.1523. URL <https://link.aps.org/doi/10.1103/RevModPhys.83.1523>.
- Dashen, R., Ma, S.-k., and Bernstein, H. J. *s*-matrix formulation of statistical mechanics. *Phys. Rev.*, 187:345–370, Nov 1969. doi: 10.1103/PhysRev.187.345. URL <https://link.aps.org/doi/10.1103/PhysRev.187.345>.
- Davis, K. B., Mewes, M. O., Andrews, M. R., van Druten, N. J., Durfee, D. S., Kurn, D. M., and Ketterle, W. Bose-einstein condensation in a gas of sodium atoms. *Phys. Rev. Lett.*, 75:3969–3973, Nov 1995. doi: 10.1103/PhysRevLett.75.3969. URL <https://link.aps.org/doi/10.1103/PhysRevLett.75.3969>.

- Davisson, C. J. and Germer, L. H. Reflection of electrons by a crystal of nickel. *Proceedings of the National Academy of Sciences*, 14(4):317–322, 1928. doi: 10.1073/pnas.14.4.317. URL <https://www.pnas.org/doi/abs/10.1073/pnas.14.4.317>.
- Davydova, M., Zhang, Y., and Fu, L. 2022. doi: 10.48550/arxiv.2206.01221. URL <https://arxiv.org/abs/2206.01221>.
- De Chiara, G., Rizzi, M., Rossini, D., and Montangero, S. Density matrix renormalization group for dummies. *Journal of Computational and Theoretical Nanoscience*, 5(7), 2008.
- de Miranda, M. H. G., Chotia, A., Neyenhuis, B., Wang, D., Quéméner, G., Ospelkaus, S., Bohn, J. L., Ye, J., and Jin, D. S. Controlling the quantum stereodynamics of ultracold bimolecular reactions. *Nature Physics*, 7(6):502–507, Jun 2011. ISSN 1745-2481. doi: 10.1038/nphys1939. URL <https://doi.org/10.1038/nphys1939>.
- De Rosi, G., Astrakharchik, G. E., and Massignan, P. Thermal instability, evaporation, and thermodynamics of one-dimensional liquids in weakly interacting bose-bose mixtures. *Phys. Rev. A*, 103:043316, Apr 2021. doi: 10.1103/PhysRevA.103.043316. URL <https://link.aps.org/doi/10.1103/PhysRevA.103.043316>.
- D’Errico, C., Burchianti, A., Prevedelli, M., Salasnich, L., Ancilotto, F., Modugno, M., Minardi, F., and Fort, C. Observation of quantum droplets in a heteronuclear bosonic mixture. *Phys. Rev. Research*, 1:033155, Dec 2019. doi: 10.1103/PhysRevResearch.1.033155. URL <https://link.aps.org/doi/10.1103/PhysRevResearch.1.033155>.
- des Cloizeaux, J. and Pearson, J. J. Spin-wave spectrum of the antiferromagnetic linear chain. *Phys. Rev.*, 128:2131–2135, Dec 1962. doi: 10.1103/PhysRev.128.2131. URL <https://link.aps.org/doi/10.1103/PhysRev.128.2131>.
- Deuchert, A., Sakmann, K., Streltsov, A. I., Alon, O. E., and Cederbaum, L. S. Dynamics and symmetries of a repulsively bound atom pair in an infinite optical lattice. *Phys. Rev. A*, 86:013618, Jul 2012. doi: 10.1103/PhysRevA.86.013618. URL <https://link.aps.org/doi/10.1103/PhysRevA.86.013618>.
- Deuretzbacher, F., Cremon, J. C., and Reimann, S. M. Ground-state properties of few dipolar bosons in a quasi-one-dimensional harmonic trap. *Phys. Rev. A*, 81:063616, Jun 2010. doi: 10.1103/PhysRevA.81.063616. URL <https://link.aps.org/doi/10.1103/PhysRevA.81.063616>.
- Devakul, T., Crépel, V., Zhang, Y., and Fu, L. Magic in twisted transition metal dichalcogenide bilayers. *Nature Communications*, 12(1):6730, Nov 2021. ISSN 2041-1723. doi: 10.1038/s41467-021-27042-9. URL <https://doi.org/10.1038/s41467-021-27042-9>.
- Douglas, J. S., Habibian, H., Hung, C.-L., Gorshkov, A. V., Kimble, H. J., and Chang, D. E. Quantum many-body models with cold atoms coupled to photonic crystals. *Nature Photonics*, 9(5):326–331, May 2015. ISSN 1749-4893. doi: 10.1038/nphoton.2015.57. URL <https://doi.org/10.1038/nphoton.2015.57>.

- Dowling, J. P. and Milburn, G. J. Quantum technology: the second quantum revolution. *Philos. Trans. A Math. Phys. Eng. Sci.*, 361(1809):1655–1674, Aug. 2003.
- Drut, J. E., McKenney, J. R., Daza, W. S., Lin, C. L., and Ordóñez, C. R. Quantum anomaly and thermodynamics of one-dimensional fermions with three-body interactions. *Phys. Rev. Lett.*, 120: 243002, Jun 2018. doi: 10.1103/PhysRevLett.120.243002. URL <https://link.aps.org/doi/10.1103/PhysRevLett.120.243002>.
- Duan, L.-M., Demler, E., and Lukin, M. D. Controlling spin exchange interactions of ultracold atoms in optical lattices. *Phys. Rev. Lett.*, 91:090402, Aug 2003. doi: 10.1103/PhysRevLett.91.090402. URL <https://link.aps.org/doi/10.1103/PhysRevLett.91.090402>.
- Edge, G. J. A., Anderson, R., Jervis, D., McKay, D. C., Day, R., Trotzky, S., and Thywissen, J. H. Imaging and addressing of individual fermionic atoms in an optical lattice. *Phys. Rev. A*, 92: 063406, Dec 2015. doi: 10.1103/PhysRevA.92.063406. URL <https://link.aps.org/doi/10.1103/PhysRevA.92.063406>.
- Ehlers, G., White, S. R., and Noack, R. M. Hybrid-space density matrix renormalization group study of the doped two-dimensional hubbard model. *Phys. Rev. B*, 95:125125, Mar 2017. doi: 10.1103/PhysRevB.95.125125. URL <https://link.aps.org/doi/10.1103/PhysRevB.95.125125>.
- Einstein, A. Über einen die Erzeugung und Verwandlung des Lichtes betreffenden heuristischen Gesichtspunkt. *Annalen der Physik*, 322(6):132–148, Jan. 1905. doi: 10.1002/andp.19053220607.
- Eisert, J., Cramer, M., and Plenio, M. B. Colloquium: Area laws for the entanglement entropy. *Rev. Mod. Phys.*, 82:277–306, Feb 2010. doi: 10.1103/RevModPhys.82.277. URL <https://link.aps.org/doi/10.1103/RevModPhys.82.277>.
- Ejima, S., Fehske, H., and Gebhard, F. Dynamic density-density correlations in interacting bose gases on optical lattices. *Journal of Physics: Conference Series*, 391:012143, dec 2012a. doi: 10.1088/1742-6596/391/1/012143. URL <https://doi.org/10.1088/1742-6596/391/1/012143>.
- Ejima, S., Fehske, H., Gebhard, F., zu Münster, K., Knap, M., Arrigoni, E., and von der Linden, W. Characterization of mott-insulating and superfluid phases in the one-dimensional bose-hubbard model. *Phys. Rev. A*, 85:053644, May 2012b. doi: 10.1103/PhysRevA.85.053644. URL <https://link.aps.org/doi/10.1103/PhysRevA.85.053644>.
- Evenbly, G. and Vidal, G. Algorithms for entanglement renormalization. *Phys. Rev. B*, 79:144108, Apr 2009. doi: 10.1103/PhysRevB.79.144108. URL <https://link.aps.org/doi/10.1103/PhysRevB.79.144108>.
- Evenbly, G. and Vidal, G. Tensor network states and geometry. *Journal of Statistical Physics*, 145(4): 891–918, Nov 2011. ISSN 1572-9613. doi: 10.1007/s10955-011-0237-4. URL <https://doi.org/10.1007/s10955-011-0237-4>.

- Evenbly, G. and Vidal, G. Tensor network renormalization. *Phys. Rev. Lett.*, 115:180405, Oct 2015. doi: 10.1103/PhysRevLett.115.180405. URL <https://link.aps.org/doi/10.1103/PhysRevLett.115.180405>.
- Fannes, M., Nachtergaele, B., and Werner, R. F. Finitely correlated states on quantum spin chains. *Communications in Mathematical Physics*, 144(3):443–490, Mar 1992. ISSN 1432-0916. doi: 10.1007/BF02099178. URL <https://doi.org/10.1007/BF02099178>.
- Ferrier-Barbut, I., Kadau, H., Schmitt, M., Wenzel, M., and Pfau, T. Observation of quantum droplets in a strongly dipolar bose gas. *Phys. Rev. Lett.*, 116:215301, May 2016. doi: 10.1103/PhysRevLett.116.215301. URL <http://link.aps.org/doi/10.1103/PhysRevLett.116.215301>.
- Ferrier-Barbut, I., Wenzel, M., Böttcher, F., Langen, T., Isoard, M., Stringari, S., and Pfau, T. Scissors mode of dipolar quantum droplets of dysprosium atoms. *Phys. Rev. Lett.*, 120:160402, Apr 2018. doi: 10.1103/PhysRevLett.120.160402. URL <https://link.aps.org/doi/10.1103/PhysRevLett.120.160402>.
- Fetter, A. and Walecka, J. *Quantum Theory of Many-particle Systems*. Dover Books on Physics. Dover Publications, 2003. ISBN 9780486428277. URL <https://books.google.es/books?id=Owekf1s83b0C>.
- Feynman, R. P. Simulating physics with computers. *International Journal of Theoretical Physics*, 21(6):467–488, Jun 1982. ISSN 1572-9575. doi: 10.1007/BF02650179. URL <https://doi.org/10.1007/BF02650179>.
- Fisher, M. P. A., Weichman, P. B., Grinstein, G., and Fisher, D. S. Boson localization and the superfluid-insulator transition. *Phys. Rev. B*, 40:546–570, Jul 1989. doi: 10.1103/PhysRevB.40.546. URL <https://link.aps.org/doi/10.1103/PhysRevB.40.546>.
- Fox, A. *Optical Properties of Solids*. Oxford master series in condensed matter physics. Oxford University Press, 2001. ISBN 9780198506126. URL <https://books.google.es/books?id=-5bVBBaAoaGoC>.
- Friis, N., Marty, O., Maier, C., Hempel, C., Holzäpfel, M., Jurcevic, P., Plenio, M. B., Huber, M., Roos, C., Blatt, R., and Lanyon, B. Observation of entangled states of a fully controlled 20-qubit system. *Phys. Rev. X*, 8:021012, Apr 2018. doi: 10.1103/PhysRevX.8.021012. URL <https://link.aps.org/doi/10.1103/PhysRevX.8.021012>.
- Fukuhara, T., Kantian, A., Endres, M., Cheneau, M., Schauß, P., Hild, S., Bellem, D., Schollwöck, U., Giamarchi, T., Gross, C., Bloch, I., and Kuhr, S. Quantum dynamics of a mobile spin impurity. *Nature Phys.*, 9(4):235–241, Feb. 2013a. doi: 10.1038/nphys2561. URL <https://doi.org/10.1038/nphys2561>.
- Fukuhara, T., Schauß, P., Endres, M., Hild, S., Cheneau, M., Bloch, I., and Gross, C. Microscopic observation of magnon bound states and their dynamics. *Nature*, 502(7469):76–79, Oct 2013b. ISSN 1476-4687. doi: 10.1038/nature12541. URL <https://doi.org/10.1038/nature12541>.

- Galanakis, D., Stanescu, T. D., and Phillips, P. Mott transition on a triangular lattice. *Phys. Rev. B*, 79:115116, Mar 2009. doi: 10.1103/PhysRevB.79.115116. URL <https://link.aps.org/doi/10.1103/PhysRevB.79.115116>.
- Garwood, D., Mongkolkeha, J., Liu, L., Yang, J., and Schauss, P. Site-resolved observables in the doped spin-imbalanced triangular hubbard model. *Phys. Rev. A*, 106:013310, Jul 2022. doi: 10.1103/PhysRevA.106.013310. URL <https://link.aps.org/doi/10.1103/PhysRevA.106.013310>.
- Geim, A. K. and Grigorieva, I. V. Van der waals heterostructures. *Nature*, 499(7459):419–425, Jul 2013. ISSN 1476-4687. doi: 10.1038/nature12385. URL <https://doi.org/10.1038/nature12385>.
- Gemelke, N., Zhang, X., Hung, C.-L., and Chin, C. In situ observation of incompressible mott-insulating domains in ultracold atomic gases. *Nature*, 460(7258):995–998, Aug 2009. ISSN 1476-4687. doi: 10.1038/nature08244. URL <https://doi.org/10.1038/nature08244>.
- Gerlach, W. and Stern, O. Der experimentelle Nachweis der Richtungsquantelung im Magnetfeld. *Zeitschrift fur Physik*, 9(1):349–352, Dec. 1922. doi: 10.1007/BF01326983.
- Ghiotto, A., Shih, E.-M., Pereira, G. S. S. G., Rhodes, D. A., Kim, B., Zang, J., Millis, A. J., Watanabe, K., Taniguchi, T., Hone, J. C., Wang, L., Dean, C. R., and Pasupathy, A. N. Quantum criticality in twisted transition metal dichalcogenides. *Nature*, 597(7876):345–349, Sep 2021. ISSN 1476-4687. doi: 10.1038/s41586-021-03815-6. URL <https://doi.org/10.1038/s41586-021-03815-6>.
- Giamarchi, T. *Quantum Physics in One Dimension*. Oxford University Press, 12 2003. ISBN 9780198525004. doi: 10.1093/acprof:oso/9780198525004.001.0001. URL <https://doi.org/10.1093/acprof:oso/9780198525004.001.0001>.
- Giuliano, D., Rossini, D., Sodano, P., and Trombettoni, A. Xxz spin- $\frac{1}{2}$ representation of a finite- u bose-hubbard chain at half-integer filling. *Phys. Rev. B*, 87:035104, Jan 2013. doi: 10.1103/PhysRevB.87.035104. URL <https://link.aps.org/doi/10.1103/PhysRevB.87.035104>.
- Goldman, N., Budich, J. C., and Zoller, P. Topological quantum matter with ultracold gases in optical lattices. *Nature Physics*, 12(7):639–645, Jul 2016. ISSN 1745-2481. doi: 10.1038/nphys3803. URL <https://doi.org/10.1038/nphys3803>.
- González-Tudela, A., Hung, C.-L., Chang, D. E., Cirac, J. I., and Kimble, H. J. Subwavelength vacuum lattices and atom–atom interactions in two-dimensional photonic crystals. *Nature Photonics*, 9(5): 320–325, May 2015. ISSN 1749-4893. doi: 10.1038/nphoton.2015.54. URL <https://doi.org/10.1038/nphoton.2015.54>.
- Greene, C. H., Giannakeas, P., and Pérez-Ríos, J. Universal few-body physics and cluster formation. *Rev. Mod. Phys.*, 89:035006, Aug 2017. doi: 10.1103/RevModPhys.89.035006. URL <https://link.aps.org/doi/10.1103/RevModPhys.89.035006>.

- Greif, D., Parsons, M. F., Mazurenko, A., Chiu, C. S., Blatt, S., Huber, F., Ji, G., and Greiner, M. Site-resolved imaging of a fermionic mott insulator. *Science*, 351(6276):953–957, 2016. ISSN 0036-8075. doi: 10.1126/science.aad9041. URL <https://science.sciencemag.org/content/351/6276/953>.
- Greiner, M. Ultracold quantum gases in three-dimensional optical lattice potentials, April 2003. URL <http://nbn-resolving.de/urn:nbn:de:bvb:19-9683>.
- Greiner, M., Mandel, O., Esslinger, T., Hänsch, T. W., and Bloch, I. Quantum phase transition from a superfluid to a mott insulator in a gas of ultracold atoms. *Nature*, 415(6867):39–44, Jan 2002. ISSN 1476-4687. doi: 10.1038/415039a. URL <https://doi.org/10.1038/415039a>.
- Grusdt, F., Kánasz-Nagy, M., Bohrdt, A., Chiu, C. S., Ji, G., Greiner, M., Greif, D., and Demler, E. Parton theory of magnetic polarons: Mesonic resonances and signatures in dynamics. *Phys. Rev. X*, 8:011046, Mar 2018a. doi: 10.1103/PhysRevX.8.011046. URL <https://link.aps.org/doi/10.1103/PhysRevX.8.011046>.
- Grusdt, F., Zhu, Z., Shi, T., and Demler, E. Meson formation in mixed-dimensional t-J models. *SciPost Phys.*, 5:57, 2018b. doi: 10.21468/SciPostPhys.5.6.057. URL <https://scipost.org/10.21468/SciPostPhys.5.6.057>.
- Guardado-Sanchez, E., Brown, P. T., Mitra, D., Devakul, T., Huse, D. A., Schauf, P., and Bakr, W. S. Probing the quench dynamics of antiferromagnetic correlations in a 2d quantum ising spin system. *Phys. Rev. X*, 8:021069, Jun 2018. doi: 10.1103/PhysRevX.8.021069. URL <https://link.aps.org/doi/10.1103/PhysRevX.8.021069>.
- Guijarro, G., Pricoupenko, A., Astrakharchik, G. E., Boronat, J., and Petrov, D. S. One-dimensional three-boson problem with two- and three-body interactions. *Phys. Rev. A*, 97:061605, Jun 2018. doi: 10.1103/PhysRevA.97.061605. URL <https://link.aps.org/doi/10.1103/PhysRevA.97.061605>.
- Guo, M., Böttcher, F., Hertkorn, J., Schmidt, J.-N., Wenzel, M., Büchler, H. P., Langen, T., and Pfau, T. The low-energy goldstone mode in a trapped dipolar supersolid. *Nature*, 574(7778):386–389, Oct 2019. ISSN 1476-4687. doi: 10.1038/s41586-019-1569-5. URL <https://doi.org/10.1038/s41586-019-1569-5>.
- Gutzwiller, M. C. Effect of correlation on the ferromagnetism of transition metals. *Phys. Rev. Lett.*, 10:159–162, Mar 1963. doi: 10.1103/PhysRevLett.10.159. URL <https://link.aps.org/doi/10.1103/PhysRevLett.10.159>.
- Haegeman, J., Cirac, J. I., Osborne, T. J., Pižorn, I., Verschelde, H., and Verstraete, F. Time-dependent variational principle for quantum lattices. *Phys. Rev. Lett.*, 107:070601, Aug 2011. doi: 10.1103/PhysRevLett.107.070601. URL <https://link.aps.org/doi/10.1103/PhysRevLett.107.070601>.
- Haegeman, J., Cirac, J. I., Osborne, T. J., and Verstraete, F. Calculus of continuous matrix product states. *Phys. Rev. B*, 88:085118, Aug 2013. doi: 10.1103/PhysRevB.88.085118. URL <https://link.aps.org/doi/10.1103/PhysRevB.88.085118>.

- Haegeman, J., Lubich, C., Oseledets, I., Vandereycken, B., and Verstraete, F. Unifying time evolution and optimization with matrix product states. *Phys. Rev. B*, 94:165116, Oct 2016. doi: 10.1103/PhysRevB.94.165116. URL <https://link.aps.org/doi/10.1103/PhysRevB.94.165116>.
- Haerter, J. O. and Shastry, B. S. Kinetic antiferromagnetism in the triangular lattice. *Phys. Rev. Lett.*, 95:087202, Aug 2005. doi: 10.1103/PhysRevLett.95.087202. URL <https://link.aps.org/doi/10.1103/PhysRevLett.95.087202>.
- Haerter, J. O., Peterson, M. R., and Shastry, B. S. Finite-temperature properties of the triangular lattice t - j model and applications to Na_xCoO_2 . *Phys. Rev. B*, 74:245118, Dec 2006. doi: 10.1103/PhysRevB.74.245118. URL <https://link.aps.org/doi/10.1103/PhysRevB.74.245118>.
- Haldane, F. D. M. Model for a quantum hall effect without landau levels: Condensed-matter realization of the "parity anomaly". *Phys. Rev. Lett.*, 61:2015–2018, Oct 1988. doi: 10.1103/PhysRevLett.61.2015. URL <https://link.aps.org/doi/10.1103/PhysRevLett.61.2015>.
- Haller, E., Hudson, J., Kelly, A., Cotta, D. A., Peaudecerf, B., Bruce, G. D., and Kuhr, S. Single-atom imaging of fermions in a quantum-gas microscope. *Nature Physics*, 11(9):738–742, Sep 2015. ISSN 1745-2481. doi: 10.1038/nphys3403. URL <https://doi.org/10.1038/nphys3403>.
- Hammer, H.-W., Nogga, A., and Schwenk, A. Colloquium: Three-body forces: From cold atoms to nuclei. *Rev. Mod. Phys.*, 85:197–217, Jan 2013. doi: 10.1103/RevModPhys.85.197. URL <https://link.aps.org/doi/10.1103/RevModPhys.85.197>.
- Hanisch, T., Kleine, B., Ritzl, A., and Müller-Hartmann, E. Ferromagnetism in the hubbard model: instability of the nagaoka state on the triangular, honeycomb and kagome lattices. *Annalen der Physik*, 507(4):303–328, 1995.
- Hansen, J. P. and McDonald, I. R. *Theory of Simple Liquids*. Academic Press, Oxford, 2013.
- Hasenfratz, P. and Kuti, J. The quark bag model. *Physics Reports*, 40(2):75 – 179, 1978. ISSN 0370-1573. doi: [https://doi.org/10.1016/0370-1573\(78\)90076-5](https://doi.org/10.1016/0370-1573(78)90076-5). URL <http://www.sciencedirect.com/science/article/pii/0370157378900765>.
- Hastings, M. B. An area law for one-dimensional quantum systems. *Journal of Statistical Mechanics: Theory and Experiment*, 2007(08):P08024, aug 2007. doi: 10.1088/1742-5468/2007/08/P08024. URL <https://dx.doi.org/10.1088/1742-5468/2007/08/P08024>.
- Hastings, M. B. Light-cone matrix product. *Journal of Mathematical Physics*, 50(9):095207, 2009. doi: 10.1063/1.3149556. URL <https://doi.org/10.1063/1.3149556>.
- Hauschild, J. and Pollmann, F. Efficient numerical simulations with Tensor Networks: Tensor Network Python (TeNPy). *SciPost Phys. Lect. Notes*, page 5, 2018. doi: 10.21468/SciPostPhysLectNotes.5. URL <https://scipost.org/10.21468/SciPostPhysLectNotes.5>.

- Hauschild, J., Leviatan, E., Bardarson, J. H., Altman, E., Zaletel, M. P., and Pollmann, F. Finding purifications with minimal entanglement. *Phys. Rev. B*, 98:235163, Dec 2018. doi: 10.1103/PhysRevB.98.235163. URL <https://link.aps.org/doi/10.1103/PhysRevB.98.235163>.
- Hazzard, K. R. A., Gadway, B., Foss-Feig, M., Yan, B., Moses, S. A., Covey, J. P., Yao, N. Y., Lukin, M. D., Ye, J., Jin, D. S., and Rey, A. M. Many-body dynamics of dipolar molecules in an optical lattice. *Phys. Rev. Lett.*, 113:195302, Nov 2014. doi: 10.1103/PhysRevLett.113.195302. URL <https://link.aps.org/doi/10.1103/PhysRevLett.113.195302>.
- He, F., Zhou, Y., Ye, Z., Cho, S.-H., Jeong, J., Meng, X., and Wang, Y. Moiré patterns in 2d materials: A review. *ACS Nano*, 15(4):5944–5958, Apr 2021. ISSN 1936-0851. doi: 10.1021/acsnano.0c10435. URL <https://doi.org/10.1021/acsnano.0c10435>.
- Hejazi, K., Liu, C., Shapourian, H., Chen, X., and Balents, L. Multiple topological transitions in twisted bilayer graphene near the first magic angle. *Phys. Rev. B*, 99:035111, Jan 2019. doi: 10.1103/PhysRevB.99.035111. URL <https://link.aps.org/doi/10.1103/PhysRevB.99.035111>.
- Henkel, N., Nath, R., and Pohl, T. Three-dimensional roton excitations and supersolid formation in rydberg-excited bose-einstein condensates. *Phys. Rev. Lett.*, 104:195302, May 2010. doi: 10.1103/PhysRevLett.104.195302. URL <https://link.aps.org/doi/10.1103/PhysRevLett.104.195302>.
- Hilker, T. A., Salomon, G., Grusdt, F., Omran, A., Boll, M., Demler, E., Bloch, I., and Gross, C. Revealing hidden antiferromagnetic correlations in doped hubbard chains via string correlators. *Science*, 357(6350):484–487, 2017. ISSN 0036-8075. doi: 10.1126/science.aam8990. URL <https://science.sciencemag.org/content/357/6350/484>.
- Hofstetter, W., Cirac, J. I., Zoller, P., Demler, E., and Lukin, M. D. High-temperature superfluidity of fermionic atoms in optical lattices. *Phys. Rev. Lett.*, 89:220407, Nov 2002. doi: 10.1103/PhysRevLett.89.220407. URL <https://link.aps.org/doi/10.1103/PhysRevLett.89.220407>.
- Hohenberg, P. C. Existence of long-range order in one and two dimensions. *Phys. Rev.*, 158:383–386, Jun 1967. doi: 10.1103/PhysRev.158.383. URL <https://link.aps.org/doi/10.1103/PhysRev.158.383>.
- Hossain, M. S., Ma, M. K., Rosales, K. A. V., Chung, Y. J., Pfeiffer, L. N., West, K. W., Baldwin, K. W., and Shayegan, M. Observation of spontaneous ferromagnetism in a two-dimensional electron system. *Proceedings of the National Academy of Sciences*, 117(51):32244–32250, 2020.
- Hou, Y. and Drut, J. E. Fourth- and fifth-order virial coefficients from weak coupling to unitarity. *Phys. Rev. Lett.*, 125:050403, Jul 2020. doi: 10.1103/PhysRevLett.125.050403. URL <https://link.aps.org/doi/10.1103/PhysRevLett.125.050403>.
- Hou, Y., Czejdo, A. J., DeChant, J., Shill, C. R., and Drut, J. E. Leading- and next-to-leading-order semiclassical approximation to the first seven virial coefficients of spin-1/2 fermions across spatial dimensions. *Phys. Rev. A*, 100:063627, Dec 2019. doi: 10.1103/PhysRevA.100.063627. URL <https://link.aps.org/doi/10.1103/PhysRevA.100.063627>.

- Hu, A., Mathey, L., Danshita, I., Tiesinga, E., Williams, C. J., and Clark, C. W. Counterflow and paired superfluidity in one-dimensional bose mixtures in optical lattices. *Phys. Rev. A*, 80: 023619, Aug 2009. doi: 10.1103/PhysRevA.80.023619. URL <https://link.aps.org/doi/10.1103/PhysRevA.80.023619>.
- Hu, H. and Liu, X.-J. Consistent theory of self-bound quantum droplets with bosonic pairing. *Phys. Rev. Lett.*, 125:195302, Nov 2020. doi: 10.1103/PhysRevLett.125.195302. URL <https://link.aps.org/doi/10.1103/PhysRevLett.125.195302>.
- Huang, K. and Yang, C. N. Quantum-mechanical many-body problem with hard-sphere interaction. *Phys. Rev.*, 105:767–775, Feb 1957. doi: 10.1103/PhysRev.105.767. URL <https://link.aps.org/doi/10.1103/PhysRev.105.767>.
- Huang, X., Wang, T., Miao, S., Wang, C., Li, Z., Lian, Z., Taniguchi, T., Watanabe, K., Okamoto, S., Xiao, D., Shi, S.-F., and Cui, Y.-T. Correlated insulating states at fractional fillings of the ws_2/wse_2 moiré lattice. *Nature Physics*, 17(6):715–719, Jun 2021. ISSN 1745-2481. doi: 10.1038/s41567-021-01171-w. URL <https://doi.org/10.1038/s41567-021-01171-w>.
- Hubbard, J. Electron correlations in narrow energy bands. *Proc. R. Soc. Lond.*, A276238–257, 1963.
- Hänsch, T. and Schawlow, A. Cooling of gases by laser radiation. *Optics Communications*, 13(1): 68–69, 1975. ISSN 0030-4018. doi: [https://doi.org/10.1016/0030-4018\(75\)90159-5](https://doi.org/10.1016/0030-4018(75)90159-5). URL <https://www.sciencedirect.com/science/article/pii/0030401875901595>.
- Inouye, S., Andrews, M. R., Stenger, J., Miesner, H.-J., Stamper-Kurn, D. M., and Ketterle, W. Observation of feshbach resonances in a bose–einstein condensate. *Nature*, 392(6672):151–154, Mar 1998. ISSN 1476-4687. doi: 10.1038/32354. URL <https://doi.org/10.1038/32354>.
- Itano, W. M., Bollinger, J. J., Tan, J. N., Jelenković, B., Huang, X.-P., and Wineland, D. J. Bragg diffraction from crystallized ion plasmas. *Science*, 279(5351):686–689, 1998. doi: 10.1126/science.279.5351.686. URL <https://www.science.org/doi/abs/10.1126/science.279.5351.686>.
- Iucci, A., Cazalilla, M. A., Ho, A. F., and Giamarchi, T. Energy absorption of a bose gas in a periodically modulated optical lattice. *Phys. Rev. A*, 73:041608, Apr 2006. doi: 10.1103/PhysRevA.73.041608. URL <https://link.aps.org/doi/10.1103/PhysRevA.73.041608>.
- Jaksch, D., Bruder, C., Cirac, J. I., Gardiner, C. W., and Zoller, P. Cold bosonic atoms in optical lattices. *Phys. Rev. Lett.*, 81:3108–3111, Oct 1998. doi: 10.1103/PhysRevLett.81.3108. URL <https://link.aps.org/doi/10.1103/PhysRevLett.81.3108>.
- Jepsen, P. N., Amato-Grill, J., Dimitrova, I., Ho, W. W., Demler, E., and Ketterle, W. Spin transport in a tunable heisenberg model realized with ultracold atoms. *Nature*, 588(7838):403–407, Dec 2020a. ISSN 1476-4687. doi: 10.1038/s41586-020-3033-y. URL <https://doi.org/10.1038/s41586-020-3033-y>.

- Jepsen, P. N., Amato-Grill, J., Dimitrova, I., Ho, W. W., Demler, E., and Ketterle, W. Spin transport in a tunable heisenberg model realized with ultracold atoms. *Nature*, 588(7838):403–407, Dec. 2020b. doi: 10.1038/s41586-020-3033-y. URL <https://doi.org/10.1038/s41586-020-3033-y>.
- Jepsen, P. N., Ho, W. W., Amato-Grill, J., Dimitrova, I., Demler, E., and Ketterle, W. 2021.
- Jin, C., Tao, Z., Li, T., Xu, Y., Tang, Y., Zhu, J., Liu, S., Watanabe, K., Taniguchi, T., Hone, J. C., Fu, L., Shan, J., and Mak, K. F. Stripe phases in wse₂/ws₂ moiré superlattices. *Nature Materials*, 20(7):940–944, Jul 2021. ISSN 1476-4660. doi: 10.1038/s41563-021-00959-8. URL <https://doi.org/10.1038/s41563-021-00959-8>.
- Jones, A. M., Yu, H., Ghimire, N. J., Wu, S., Aivazian, G., Ross, J. S., Zhao, B., Yan, J., Mandrus, D. G., Xiao, D., Yao, W., and Xu, X. Optical generation of excitonic valley coherence in monolayer wse₂. *Nature Nanotechnology*, 8(9):634–638, Sep 2013. ISSN 1748-3395. doi: 10.1038/nnano.2013.151. URL <https://doi.org/10.1038/nnano.2013.151>.
- Jotzu, G., Messer, M., Desbuquois, R., Lebrat, M., Uehlinger, T., Greif, D., and Esslinger, T. Experimental realization of the topological haldane model with ultracold fermions. *Nature*, 515(7526):237–240, Nov 2014. ISSN 1476-4687. doi: 10.1038/nature13915. URL <https://doi.org/10.1038/nature13915>.
- Juliá-Díaz, B., Dagnino, D., Günter, K. J., Graß, T., Barberán, N., Lewenstein, M., and Dalibard, J. Strongly correlated states of a small cold-atom cloud from geometric gauge fields. *Phys. Rev. A*, 84:053605, Nov 2011. doi: 10.1103/PhysRevA.84.053605. URL <https://link.aps.org/doi/10.1103/PhysRevA.84.053605>.
- Jung, J., Raoux, A., Qiao, Z., and MacDonald, A. H. Ab initio theory of moiré superlattice bands in layered two-dimensional materials. *Phys. Rev. B*, 89:205414, May 2014. doi: 10.1103/PhysRevB.89.205414. URL <https://link.aps.org/doi/10.1103/PhysRevB.89.205414>.
- Jungwirth, T., Sinova, J., Mašek, J., Kučera, J., and MacDonald, A. H. Theory of ferromagnetic (iii,mn)v semiconductors. *Rev. Mod. Phys.*, 78:809–864, Aug 2006. doi: 10.1103/RevModPhys.78.809. URL <https://link.aps.org/doi/10.1103/RevModPhys.78.809>.
- Kadanoff, L. P. Scaling laws for ising models near T_c . *Physics Physique Fizika*, 2:263–272, Jun 1966. doi: 10.1103/PhysicsPhysiqueFizika.2.263. URL <https://link.aps.org/doi/10.1103/PhysicsPhysiqueFizika.2.263>.
- Kaminski, A. and Das Sarma, S. Polaron percolation in diluted magnetic semiconductors. *Phys. Rev. Lett.*, 88:247202, May 2002. doi: 10.1103/PhysRevLett.88.247202. URL <https://link.aps.org/doi/10.1103/PhysRevLett.88.247202>.
- Kanamori, J. Electron Correlation and Ferromagnetism of Transition Metals. *Progress of Theoretical Physics*, 30(3):275–289, 09 1963. ISSN 0033-068X. doi: 10.1143/PTP.30.275. URL <https://doi.org/10.1143/PTP.30.275>.

- Kanász-Nagy, M., Lovas, I., Grusdt, F., Greif, D., Greiner, M., and Demler, E. A. Quantum correlations at infinite temperature: The dynamical nagaoka effect. *Phys. Rev. B*, 96:014303, Jul 2017. doi: 10.1103/PhysRevB.96.014303. URL <https://link.aps.org/doi/10.1103/PhysRevB.96.014303>.
- Kane, C. L., Lee, P. A., and Read, N. Motion of a single hole in a quantum antiferromagnet. *Phys. Rev. B*, 39:6880–6897, Apr 1989. doi: 10.1103/PhysRevB.39.6880. URL <https://link.aps.org/doi/10.1103/PhysRevB.39.6880>.
- Kang, J. and Vafeek, O. Symmetry, maximally localized wannier states, and a low-energy model for twisted bilayer graphene narrow bands. *Phys. Rev. X*, 8:031088, Sep 2018. doi: 10.1103/PhysRevX.8.031088. URL <https://link.aps.org/doi/10.1103/PhysRevX.8.031088>.
- Kao, W., Li, K.-Y., Lin, K.-Y., Gopalakrishnan, S., and Lev, B. L. Topological pumping of a 1d dipolar gas into strongly correlated prethermal states. *Science*, 371(6526):296–300, 2021. ISSN 0036-8075. doi: 10.1126/science.abb4928. URL <https://science.sciencemag.org/content/371/6526/296>.
- Kartashov, Y. V., Astrakharchik, G. E., Malomed, B. A., and Torner, L. Frontiers in multidimensional self-trapping of nonlinear fields and matter. *Nat. Rev. Phys.*, 1(3):185–197, Feb. 2019. doi: 10.1038/s42254-019-0025-7. URL <https://doi.org/10.1038/s42254-019-0025-7>.
- Keldysh, L. V. Coulomb interaction in thin semiconductor and semimetal films. *Soviet Journal of Experimental and Theoretical Physics Letters*, 29:658, June 1979.
- Kim, K.-S., Murthy, C., Pandey, A., and Kivelson, S. A. Interstitial-induced ferromagnetism in a two-dimensional wigner crystal. 2022. doi: 10.48550/arxiv.2206.07191. URL <https://arxiv.org/abs/2206.07191>.
- Kinoshita, T., Wenger, T., and Weiss, D. S. Observation of a one-dimensional tonks-girardeau gas. *Science*, 305(5687):1125–1128, 2004. doi: 10.1126/science.1100700. URL <https://www.science.org/doi/abs/10.1126/science.1100700>.
- Kitaev, A. and Preskill, J. Topological entanglement entropy. *Phys. Rev. Lett.*, 96:110404, Mar 2006. doi: 10.1103/PhysRevLett.96.110404. URL <https://link.aps.org/doi/10.1103/PhysRevLett.96.110404>.
- Kitaev, A. Y. Unpaired majorana fermions in quantum wires. *Physics-Uspeski*, 44(10S):131, oct 2001. doi: 10.1070/1063-7869/44/10S/S29. URL <https://dx.doi.org/10.1070/1063-7869/44/10S/S29>.
- Klümper, A., Schadschneider, A., and Zittartz, J. Matrix product ground states for one-dimensional spin-1 quantum antiferromagnets. *Europhysics Letters*, 24(4):293, nov 1993. doi: 10.1209/0295-5075/24/4/010. URL <https://dx.doi.org/10.1209/0295-5075/24/4/010>.
- Koepsell, J., Vijayan, J., Sompet, P., Grusdt, F., Hilker, T. A., Demler, E., Salomon, G., Bloch, I., and Gross, C. Imaging magnetic polarons in the doped fermi–hubbard model. *Nature*, 572(7769):

- 358–362, Aug 2019. ISSN 1476-4687. doi: 10.1038/s41586-019-1463-1. URL <https://doi.org/10.1038/s41586-019-1463-1>.
- Kokalj, J. and McKenzie, R. H. Thermodynamics of a bad metal–mott insulator transition in the presence of frustration. *Phys. Rev. Lett.*, 110:206402, May 2013. doi: 10.1103/PhysRevLett.110.206402. URL <https://link.aps.org/doi/10.1103/PhysRevLett.110.206402>.
- Koretsune, T., Motome, Y., and Furusaki, A. Exact diagonalization study of mott transition in the hubbard model on an anisotropic triangular lattice. *Journal of the Physical Society of Japan*, 76(7): 074719, 2007. doi: 10.1143/JPSJ.76.074719.
- Koshino, M., Yuan, N. F. Q., Koretsune, T., Ochi, M., Kuroki, K., and Fu, L. Maximally localized wannier orbitals and the extended hubbard model for twisted bilayer graphene. *Phys. Rev. X*, 8: 031087, Sep 2018. doi: 10.1103/PhysRevX.8.031087. URL <https://link.aps.org/doi/10.1103/PhysRevX.8.031087>.
- Kramers, H. L’interaction entre les atomes magnétogènes dans un cristal paramagnétique. *Physica*, 1(1):182–192, 1934. ISSN 0031-8914. doi: [https://doi.org/10.1016/S0031-8914\(34\)90023-9](https://doi.org/10.1016/S0031-8914(34)90023-9). URL <https://www.sciencedirect.com/science/article/pii/S0031891434900239>.
- Kruis, H. V., McCulloch, I. P., Nussinov, Z., and Zaanen, J. Geometry and the hidden order of luttinger liquids: The universality of squeezed space. *Phys. Rev. B*, 70:075109, Aug 2004. doi: 10.1103/PhysRevB.70.075109. URL <https://link.aps.org/doi/10.1103/PhysRevB.70.075109>.
- Krutitsky, K. V. Ultracold bosons with short-range interaction in regular optical lattices. *Phys. Rep.*, 607:1–101, 2016. ISSN 0370-1573. doi: <https://doi.org/10.1016/j.physrep.2015.10.004>. URL <https://www.sciencedirect.com/science/article/pii/S0370157315004366>.
- Kuklov, A., Prokof’ev, N., and Svistunov, B. Superfluid-superfluid phase transitions in a two-component bose-einstein condensate. *Phys. Rev. Lett.*, 92:030403, Jan 2004a. doi: 10.1103/PhysRevLett.92.030403. URL <https://link.aps.org/doi/10.1103/PhysRevLett.92.030403>.
- Kuklov, A., Prokof’ev, N., and Svistunov, B. Commensurate two-component bosons in an optical lattice: Ground state phase diagram. *Phys. Rev. Lett.*, 92:050402, Feb 2004b. doi: 10.1103/PhysRevLett.92.050402. URL <https://link.aps.org/doi/10.1103/PhysRevLett.92.050402>.
- Kunitski, M., Guan, Q., Maschkiwitz, H., Hahnenbruch, J., Eckart, S., Zeller, S., Kalinin, A., Schöffler, M., Schmidt, L. P. H., Jahnke, T., Blume, D., and Dörner, R. Ultrafast manipulation of the weakly bound helium dimer. *Nature Physics*, 17(2):174–178, Feb 2021. ISSN 1745-2481. doi: 10.1038/s41567-020-01081-3. URL <https://doi.org/10.1038/s41567-020-01081-3>.
- Kwan, Y. H., Hu, Y., Simon, S. H., and Parameswaran, S. A. Exciton band topology in spontaneous quantum anomalous hall insulators: Applications to twisted bilayer graphene. *Phys. Rev. Lett.*, 126: 137601, Mar 2021. doi: 10.1103/PhysRevLett.126.137601. URL <https://link.aps.org/doi/10.1103/PhysRevLett.126.137601>.

- König, S., Lee, D., and Hammer, H.-W. Non-relativistic bound states in a finite volume. *Annals of Physics*, 327(6):1450–1471, 2012. ISSN 0003-4916.
- L. N. Bulaevskii, E. L. N. and Khomskii, D. I. A new type of auto-localized state of a conduction electron in an antiferromagnetic semiconductor. *Zh. Eksp. Teor. Fiz.*, 54:1562, 1968.
- Labuhn, H., Barredo, D., Ravets, S., de Léséleuc, S., Macrì, T., Lahaye, T., and Browaeys, A. Tunable two-dimensional arrays of single Rydberg atoms for realizing quantum Ising models. *Nature*, 534(7609):667–670, June 2016. ISSN 0028-0836, 1476-4687. doi: 10.1038/nature18274. URL <http://www.nature.com/articles/nature18274>.
- Lagoin, C., Bhattacharya, U., Grass, T., Chhajlany, R. W., Salamon, T., Baldwin, K., Pfeiffer, L., Lewenstein, M., Holzmann, M., and Dubin, F. Extended bose–hubbard model with dipolar excitons. *Nature*, 609(7927):485–489, Sept. 2022. doi: 10.1038/s41586-022-05123-z. URL <https://doi.org/10.1038/s41586-022-05123-z>.
- Lahaye, T., Menotti, C., Santos, L., Lewenstein, M., and Pfau, T. The physics of dipolar bosonic quantum gases. *Reports on Progress in Physics*, 72(12):126401, nov 2009. doi: 10.1088/0034-4885/72/12/126401. URL <https://dx.doi.org/10.1088/0034-4885/72/12/126401>.
- Lanczos, C. An iteration method for the solution of the eigenvalue problem of linear differential and integral operators. *J. Res. Natl. Bur. Stand. B*, 45:255–282, 1950. doi: 10.6028/jres.045.026.
- Lanyon, B. P., Hempel, C., Nigg, D., Müller, M., Gerritsma, R., Zähringer, F., Schindler, P., Barreiro, J. T., Rambach, M., Kirchmair, G., Hennrich, M., Zoller, P., Blatt, R., and Roos, C. F. Universal digital quantum simulation with trapped ions. *Science*, 334(6052):57–61, 2011. doi: 10.1126/science.1208001. URL <https://www.science.org/doi/abs/10.1126/science.1208001>.
- Laubach, M., Thomale, R., Platt, C., Hanke, W., and Li, G. Phase diagram of the hubbard model on the anisotropic triangular lattice. *Phys. Rev. B*, 91:245125, Jun 2015. doi: 10.1103/PhysRevB.91.245125. URL <https://link.aps.org/doi/10.1103/PhysRevB.91.245125>.
- Ledwith, P. J., Tarnopolsky, G., Khalaf, E., and Vishwanath, A. Fractional chern insulator states in twisted bilayer graphene: An analytical approach. *Phys. Rev. Res.*, 2:023237, May 2020. doi: 10.1103/PhysRevResearch.2.023237. URL <https://link.aps.org/doi/10.1103/PhysRevResearch.2.023237>.
- Lee, H.-J., Helgren, E., and Hellman, F. Gate-controlled magnetic properties of the magnetic semiconductor (zn,co)o. *Applied Physics Letters*, 94(21):212106, 2009.
- Lee, K., Sharma, P., Vafek, O., and Changlani, H. J. Triangular lattice hubbard model physics at intermediate temperatures. 2022. doi: 10.48550/arxiv.2209.00664. URL <https://arxiv.org/abs/2209.00664>.

- Leggett, A. *Quantum Liquids: Bose Condensation and Cooper Pairing in Condensed-matter Systems*. Oxford graduate texts in mathematics. OUP Oxford, 2006. ISBN 9780198526438. URL <https://books.google.es/books?id=PiRRAAAAMAAJ>.
- Levin, M. and Nave, C. P. Tensor renormalization group approach to two-dimensional classical lattice models. *Phys. Rev. Lett.*, 99:120601, Sep 2007. doi: 10.1103/PhysRevLett.99.120601. URL <https://link.aps.org/doi/10.1103/PhysRevLett.99.120601>.
- Levin, M. and Wen, X.-G. Detecting topological order in a ground state wave function. *Phys. Rev. Lett.*, 96:110405, Mar 2006. doi: 10.1103/PhysRevLett.96.110405. URL <https://link.aps.org/doi/10.1103/PhysRevLett.96.110405>.
- Lewenstein, M., Sanpera, A., and Ahufinger, V. *Ultracold Atoms in Optical Lattices*. Oxford University Press, Mar. 2012. doi: 10.1093/acprof:oso/9780199573127.001.0001. URL <https://doi.org/10.1093/acprof:oso/9780199573127.001.0001>.
- Li, G., Antipov, A. E., Rubtsov, A. N., Kirchner, S., and Hanke, W. Competing phases of the hubbard model on a triangular lattice: Insights from the entropy. *Phys. Rev. B*, 89:161118, Apr 2014. doi: 10.1103/PhysRevB.89.161118. URL <https://link.aps.org/doi/10.1103/PhysRevB.89.161118>.
- Li, L., Guo, Y., Cui, X. Y., Zheng, R., Ohtani, K., Kong, C., Ceguerra, A. V., Moody, M. P., Ye, J. D., Tan, H. H., Jagadish, C., Liu, H., Stampfl, C., Ohno, H., Ringer, S. P., and Matsukura, F. Magnetism of co-doped zno epitaxially grown on a zno substrate. *Phys. Rev. B*, 85:174430, May 2012. doi: 10.1103/PhysRevB.85.174430. URL <https://link.aps.org/doi/10.1103/PhysRevB.85.174430>.
- Li, W., Dhar, A., Deng, X., Kasamatsu, K., Barbiero, L., and Santos, L. Disorderless quasi-localization of polar gases in one-dimensional lattices. *Phys. Rev. Lett.*, 124:010404, Jan 2020. doi: 10.1103/PhysRevLett.124.010404. URL <https://link.aps.org/doi/10.1103/PhysRevLett.124.010404>.
- Lian, B., Song, Z.-D., Regnault, N., Efetov, D. K., Yazdani, A., and Bernevig, B. A. Twisted bilayer graphene. iv. exact insulator ground states and phase diagram. *Phys. Rev. B*, 103:205414, May 2021. doi: 10.1103/PhysRevB.103.205414. URL <https://link.aps.org/doi/10.1103/PhysRevB.103.205414>.
- Liang, S. and Pang, H. Approximate diagonalization using the density matrix renormalization-group method: A two-dimensional-systems perspective. *Phys. Rev. B*, 49:9214–9217, Apr 1994. doi: 10.1103/PhysRevB.49.9214. URL <https://link.aps.org/doi/10.1103/PhysRevB.49.9214>.
- Lieb, E. H. and Liniger, W. Exact analysis of an interacting bose gas. i. the general solution and the ground state. *Phys. Rev.*, 130:1605–1616, May 1963. doi: 10.1103/PhysRev.130.1605. URL <https://link.aps.org/doi/10.1103/PhysRev.130.1605>.
- Lieb, E. H. and Robinson, D. W. The finite group velocity of quantum spin systems. *Communications in Mathematical Physics*, 28(3):251 – 257, 1972.

- Lienhard, V., de Léséleuc, S., Barredo, D., Lahaye, T., Browaeys, A., Schuler, M., Henry, L.-P., and Läuchli, A. M. Observing the space- and time-dependent growth of correlations in dynamically tuned synthetic ising models with antiferromagnetic interactions. *Phys. Rev. X*, 8:021070, Jun 2018. doi: 10.1103/PhysRevX.8.021070. URL <https://link.aps.org/doi/10.1103/PhysRevX.8.021070>.
- Lin, H. Q. Exact diagonalization of quantum-spin models. *Phys. Rev. B*, 42:6561–6567, Oct 1990. doi: 10.1103/PhysRevB.42.6561. URL <https://link.aps.org/doi/10.1103/PhysRevB.42.6561>.
- Lippmann, B. A. and Schwinger, J. Variational principles for scattering processes. i. *Phys. Rev.*, 79: 469–480, Aug 1950. doi: 10.1103/PhysRev.79.469. URL <https://link.aps.org/doi/10.1103/PhysRev.79.469>.
- Liu, J. and Dai, X. Theories for the correlated insulating states and quantum anomalous hall effect phenomena in twisted bilayer graphene. *Phys. Rev. B*, 103:035427, Jan 2021. doi: 10.1103/PhysRevB.103.035427. URL <https://link.aps.org/doi/10.1103/PhysRevB.103.035427>.
- Liu, J., Liu, J., and Dai, X. Pseudo landau level representation of twisted bilayer graphene: Band topology and implications on the correlated insulating phase. *Phys. Rev. B*, 99:155415, Apr 2019. doi: 10.1103/PhysRevB.99.155415. URL <https://link.aps.org/doi/10.1103/PhysRevB.99.155415>.
- Liu, Y., Weiss, N. O., Duan, X., Cheng, H.-C., Huang, Y., and Duan, X. Van der waals heterostructures and devices. *Nature Reviews Materials*, 1(9):16042, Jul 2016. ISSN 2058-8437. doi: 10.1038/natrevmats.2016.42. URL <https://doi.org/10.1038/natrevmats.2016.42>.
- Lloyd, S. Universal quantum simulators. *Science*, 273(5278):1073–1078, 1996. doi: 10.1126/science.273.5278.1073. URL <https://www.science.org/doi/abs/10.1126/science.273.5278.1073>.
- Lopes dos Santos, J. M. B., Peres, N. M. R., and Castro Neto, A. H. Graphene bilayer with a twist: Electronic structure. *Phys. Rev. Lett.*, 99:256802, Dec 2007. doi: 10.1103/PhysRevLett.99.256802. URL <https://link.aps.org/doi/10.1103/PhysRevLett.99.256802>.
- lordanskil, S. V. and Smirnov, A. V. Hole concentration dependence of the curie temperature of (ga,mn)sb in a field-effect structure. *Zh. Eksp. Teor. Fiz.*, 79:1942—1953, 1980.
- Lukin, M. D., Fleischhauer, M., Cote, R., Duan, L. M., Jaksch, D., Cirac, J. I., and Zoller, P. Dipole blockade and quantum information processing in mesoscopic atomic ensembles. *Phys. Rev. Lett.*, 87:037901, Jun 2001. doi: 10.1103/PhysRevLett.87.037901. URL <https://link.aps.org/doi/10.1103/PhysRevLett.87.037901>.
- Lüscher, M. Volume dependence of the energy spectrum in massive quantum field theories. II. Scattering states. *Communications in Mathematical Physics*, 105(2):153 – 188, 1986a. doi: cmp/1104115329. URL <https://doi.org/>.
- Lüscher, M. Volume dependence of the energy spectrum in massive quantum field theories. I. Stable particle states. *Communications in Mathematical Physics*, 104(2):177 – 206, 1986b. doi: cmp/1104114998. URL <https://doi.org/>.

- Mak, K. F., He, K., Shan, J., and Heinz, T. F. Control of valley polarization in monolayer mos2 by optical helicity. *Nature Nanotechnology*, 7(8):494–498, Aug 2012. ISSN 1748-3395. doi: 10.1038/nnano.2012.96. URL <https://doi.org/10.1038/nnano.2012.96>.
- Manzeli, S., Ovchinnikov, D., Pasquier, D., Yazyev, O. V., and Kis, A. 2d transition metal dichalcogenides. *Nature Reviews Materials*, 2(8):17033, Jun 2017. ISSN 2058-8437. doi: 10.1038/natrevmats.2017.33. URL <https://doi.org/10.1038/natrevmats.2017.33>.
- Marzari, N., Mostofi, A. A., Yates, J. R., Souza, I., and Vanderbilt, D. Maximally localized wannier functions: Theory and applications. *Rev. Mod. Phys.*, 84:1419–1475, Oct 2012. doi: 10.1103/RevModPhys.84.1419. URL <https://link.aps.org/doi/10.1103/RevModPhys.84.1419>.
- Matsukura, F., Tokura, Y., and Ohno, H. Control of magnetism by electric fields. *Nature Nanotechnology*, 10(3):209–220, Mar 2015. ISSN 1748-3395. doi: 10.1038/nnano.2015.22. URL <https://doi.org/10.1038/nnano.2015.22>.
- Mattheiss, L. F. Band structures of transition-metal-dichalcogenide layer compounds. *Phys. Rev. B*, 8: 3719–3740, Oct 1973. doi: 10.1103/PhysRevB.8.3719. URL <https://link.aps.org/doi/10.1103/PhysRevB.8.3719>.
- McCulloch, I. P. and Gulácsi, M. The non-abelian density matrix renormalization group algorithm. *Europhysics Letters*, 57(6):852, mar 2002. doi: 10.1209/epl/i2002-00393-0. URL <https://dx.doi.org/10.1209/epl/i2002-00393-0>.
- McGuire, J. B. Interacting fermions in one dimension. ii. attractive potential. *Journal of Mathematical Physics*, 7(1):123–132, 1966. doi: 10.1063/1.1704798.
- Mele, E. J. Commensuration and interlayer coherence in twisted bilayer graphene. *Phys. Rev. B*, 81: 161405, Apr 2010. doi: 10.1103/PhysRevB.81.161405. URL <https://link.aps.org/doi/10.1103/PhysRevB.81.161405>.
- Merino, J., Powell, B. J., and McKenzie, R. H. Ferromagnetism, paramagnetism, and a curie-weiss metal in an electron-doped hubbard model on a triangular lattice. *Phys. Rev. B*, 73:235107, Jun 2006. doi: 10.1103/PhysRevB.73.235107. URL <https://link.aps.org/doi/10.1103/PhysRevB.73.235107>.
- Mermin, N. D. Crystalline order in two dimensions. *Phys. Rev.*, 176:250–254, Dec 1968. doi: 10.1103/PhysRev.176.250. URL <https://link.aps.org/doi/10.1103/PhysRev.176.250>.
- Mermin, N. D. and Wagner, H. Absence of ferromagnetism or antiferromagnetism in one- or two-dimensional isotropic heisenberg models. *Phys. Rev. Lett.*, 17:1133–1136, Nov 1966. doi: 10.1103/PhysRevLett.17.1133. URL <https://link.aps.org/doi/10.1103/PhysRevLett.17.1133>.
- Mezard, M., Parisi, G., and Virasoro, M. *Spin Glass Theory And Beyond: An Introduction To The Replica Method And Its Applications*. World Scientific Lecture Notes In Physics. World Scientific

- Publishing Company, 1987. ISBN 9789813103917. URL <https://books.google.es/books?id=DwY8DQAAQBAJ>.
- Millis, A. J., Shraiman, B. I., and Mueller, R. Dynamic jahn-teller effect and colossal magnetoresistance in $\text{La}_{1-x}\text{Sr}_x\text{MnO}_3$. *Phys. Rev. Lett.*, 77:175–178, Jul 1996. doi: 10.1103/PhysRevLett.77.175. URL <https://link.aps.org/doi/10.1103/PhysRevLett.77.175>.
- Mishmash, R. V., González, I., Melko, R. G., Motrunich, O. I., and Fisher, M. P. A. Continuous mott transition between a metal and a quantum spin liquid. *Phys. Rev. B*, 91:235140, Jun 2015. doi: 10.1103/PhysRevB.91.235140. URL <https://link.aps.org/doi/10.1103/PhysRevB.91.235140>.
- Mitchell, T. B., Bollinger, J. J., Dubin, D. H. E., Huang, X.-P., Itano, W. M., and Baughman, R. H. Direct observations of structural phase transitions in planar crystallized ion plasmas. *Science*, 282(5392):1290–1293, 1998. doi: 10.1126/science.282.5392.1290. URL <https://www.science.org/doi/abs/10.1126/science.282.5392.1290>.
- Miyake, H., Siviloglou, G. A., Kennedy, C. J., Burton, W. C., and Ketterle, W. Realizing the harper hamiltonian with laser-assisted tunneling in optical lattices. *Phys. Rev. Lett.*, 111:185302, Oct 2013. doi: 10.1103/PhysRevLett.111.185302. URL <https://link.aps.org/doi/10.1103/PhysRevLett.111.185302>.
- Molina-Vilaplana, J. Holographic geometries of one-dimensional gapped quantum systems from tensor network states. *Journal of High Energy Physics*, 2013(5):24, May 2013. ISSN 1029-8479. doi: 10.1007/JHEP05(2013)024. URL [https://doi.org/10.1007/JHEP05\(2013\)024](https://doi.org/10.1007/JHEP05(2013)024).
- Montangero, S. *Introduction to Tensor Network Methods: Numerical simulations of low-dimensional many-body quantum systems*. 01 2018. ISBN 978-3-030-01408-7. doi: 10.1007/978-3-030-01409-4.
- Monz, T., Schindler, P., Barreiro, J. T., Chwalla, M., Nigg, D., Coish, W. A., Harlander, M., Hänsel, W., Hennrich, M., and Blatt, R. 14-qubit entanglement: Creation and coherence. *Phys. Rev. Lett.*, 106:130506, Mar 2011. doi: 10.1103/PhysRevLett.106.130506. URL <https://link.aps.org/doi/10.1103/PhysRevLett.106.130506>.
- Morales-Durán, N., Hu, N. C., Potasz, P., and MacDonald, A. H. Nonlocal interactions in moiré hubbard systems. *Phys. Rev. Lett.*, 128:217202, May 2022. doi: 10.1103/PhysRevLett.128.217202. URL <https://link.aps.org/doi/10.1103/PhysRevLett.128.217202>.
- Morera, I., Kanász-Nagy, M., Smolenski, T., Ciorciaro, L., Imamoğlu, A., and Demler, E. High-temperature kinetic magnetism in triangular lattices. 2022. doi: 10.48550/arXiv.2209.05398. URL <https://arxiv.org/abs/2209.05398>.
- Moritz, H., Stöferle, T., Köhl, M., and Esslinger, T. Exciting collective oscillations in a trapped 1d gas. *Phys. Rev. Lett.*, 91:250402, Dec 2003. doi: 10.1103/PhysRevLett.91.250402. URL <https://link.aps.org/doi/10.1103/PhysRevLett.91.250402>.

- Motruk, J., Zaletel, M. P., Mong, R. S. K., and Pollmann, F. Density matrix renormalization group on a cylinder in mixed real and momentum space. *Phys. Rev. B*, 93:155139, Apr 2016. doi: 10.1103/PhysRevB.93.155139. URL <https://link.aps.org/doi/10.1103/PhysRevB.93.155139>.
- Mott, N. F. Metal-insulator transition. *Rev. Mod. Phys.*, 40:677–683, Oct 1968. doi: 10.1103/RevModPhys.40.677. URL <https://link.aps.org/doi/10.1103/RevModPhys.40.677>.
- Mottl, R., Brennecke, F., Baumann, K., Landig, R., Donner, T., and Esslinger, T. Roton-type mode softening in a quantum gas with cavity-mediated long-range interactions. *Science*, 336(6088):1570–1573, 2012. doi: 10.1126/science.1220314. URL <https://www.science.org/doi/abs/10.1126/science.1220314>.
- Mueller, T. and Malic, E. Exciton physics and device application of two-dimensional transition metal dichalcogenide semiconductors. *npj 2D Materials and Applications*, 2(1):29, Sep 2018. ISSN 2397-7132. doi: 10.1038/s41699-018-0074-2. URL <https://doi.org/10.1038/s41699-018-0074-2>.
- Münstermann, P., Fischer, T., Maunz, P., Pinkse, P. W. H., and Rempe, G. Observation of cavity-mediated long-range light forces between strongly coupled atoms. *Phys. Rev. Lett.*, 84:4068–4071, May 2000. doi: 10.1103/PhysRevLett.84.4068. URL <https://link.aps.org/doi/10.1103/PhysRevLett.84.4068>.
- Nagaev, E. Self-trapped states of charge carriers in magnetic semiconductors. *Journal of Magnetism and Magnetic Materials*, 110(1):39–60, 1992. ISSN 0304-8853. doi: [https://doi.org/10.1016/0304-8853\(92\)90011-C](https://doi.org/10.1016/0304-8853(92)90011-C). URL <https://www.sciencedirect.com/science/article/pii/030488539290011C>.
- Nagaev, E. L. Magnetic polarons (ferions) of complicated structure. *Journal of Experimental and Theoretical Physics Letters*, 74(8):431–435, Oct 2001. ISSN 1090-6487. doi: 10.1134/1.1430001. URL <https://doi.org/10.1134/1.1430001>.
- Nagaoka, Y. Ferromagnetism in a narrow, almost half-filled s band. *Phys. Rev.*, 147:392–405, Jul 1966. doi: 10.1103/PhysRev.147.392. URL <https://link.aps.org/doi/10.1103/PhysRev.147.392>.
- Natale, G., van Bijnen, R. M. W., Patscheider, A., Petter, D., Mark, M. J., Chomaz, L., and Ferlaino, F. Excitation spectrum of a trapped dipolar supersolid and its experimental evidence. *Phys. Rev. Lett.*, 123:050402, Aug 2019. doi: 10.1103/PhysRevLett.123.050402. URL <https://link.aps.org/doi/10.1103/PhysRevLett.123.050402>.
- Natale, G., Bland, T., Gschwendtner, S., Lafforgue, L., Grün, D. S., Patscheider, A., Mark, M. J., and Ferlaino, F. Strongly dipolar gases in a one-dimensional lattice: Bloch oscillations and matter-wave localization. *arXiv preprint arXiv:2205.03280*, pages –, 2022. doi: 10.48550/ARXIV.2205.03280. URL <https://arxiv.org/abs/2205.03280>.
- Nespolo, J., Astrakharchik, G. E., and Recati, A. Andreev–bashkin effect in superfluid cold gases mixtures. *New Journal of Physics*, 19(12):125005, dec 2017. doi: 10.1088/1367-2630/aa93a0. URL <https://doi.org/10.1088/1367-2630/aa93a0>.

- Neyenhuis, B., Yan, B., Moses, S. A., Covey, J. P., Chotia, A., Petrov, A., Kotochigova, S., Ye, J., and Jin, D. S. Anisotropic polarizability of ultracold polar $^{40}\text{K}^{87}\text{Rb}$ molecules. *Phys. Rev. Lett.*, 109: 230403, Dec 2012. doi: 10.1103/PhysRevLett.109.230403. URL <https://link.aps.org/doi/10.1103/PhysRevLett.109.230403>.
- Ni, K.-K., Ospelkaus, S., de Miranda, M. H. G., Pe'er, A., Neyenhuis, B., Zirbel, J. J., Kotochigova, S., Julienne, P. S., Jin, D. S., and Ye, J. A high phase-space-density gas of polar molecules. *Science*, 322(5899):231–235, 2008. doi: 10.1126/science.1163861. URL <https://www.science.org/doi/abs/10.1126/science.1163861>.
- Ni, K.-K., Ospelkaus, S., Wang, D., Quéméner, G., Neyenhuis, B., de Miranda, M. H. G., Bohn, J. L., Ye, J., and Jin, D. S. Dipolar collisions of polar molecules in the quantum regime. *Nature*, 464(7293):1324–1328, Apr 2010. ISSN 1476-4687. doi: 10.1038/nature08953. URL <https://doi.org/10.1038/nature08953>.
- Nichols, M. A., Cheuk, L. W., Okan, M., Hartke, T. R., Mendez, E., Senthil, T., Khatami, E., Zhang, H., and Zwierlein, M. W. Spin transport in a mott insulator of ultracold fermions. *Science*, 363(6425):383–387, 2019. ISSN 0036-8075. doi: 10.1126/science.aat4387. URL <https://science.sciencemag.org/content/363/6425/383>.
- Nishida, Y. Universal bound states of one-dimensional bosons with two- and three-body attractions. *Phys. Rev. A*, 97:061603, Jun 2018. doi: 10.1103/PhysRevA.97.061603. URL <https://link.aps.org/doi/10.1103/PhysRevA.97.061603>.
- Nishino, T. and Okunishi, K. Corner transfer matrix renormalization group method. *Journal of the Physical Society of Japan*, 65(4):891–894, 1996. doi: 10.1143/JPSJ.65.891. URL <https://doi.org/10.1143/JPSJ.65.891>.
- Nishino, T. and Okunishi, K. Corner transfer matrix algorithm for classical renormalization group. *Journal of the Physical Society of Japan*, 66(10):3040–3047, 1997. doi: 10.1143/JPSJ.66.3040. URL <https://doi.org/10.1143/JPSJ.66.3040>.
- Nishio, Y., Maeshima, N., Gendiar, A., and Nishino, T. Tensor product variational formulation for quantum systems. 2004.
- Nishitani, Y., Chiba, D., Endo, M., Sawicki, M., Matsukura, F., Dietl, T., and Ohno, H. Curie temperature versus hole concentration in field-effect structures of $\text{Ga}_{1-x}\text{Mn}_x\text{As}$. *Phys. Rev. B*, 81: 045208, Jan 2010. doi: 10.1103/PhysRevB.81.045208. URL <https://link.aps.org/doi/10.1103/PhysRevB.81.045208>.
- Norcia, M. A., Politi, C., Klaus, L., Poli, E., Sohmen, M., Mark, M. J., Bisset, R. N., Santos, L., and Ferlaino, F. Two-dimensional supersolidity in a dipolar quantum gas. *Nature*, 596(7872):357–361, Aug 2021. ISSN 1476-4687. doi: 10.1038/s41586-021-03725-7. URL <https://doi.org/10.1038/s41586-021-03725-7>.

- Novoselov, K. S., Mishchenko, A., Carvalho, A., and Castro Neto, A. H. 2d materials and van der waals heterostructures. *Science*, 353(6298):aac9439, Jul 2016. doi: 10.1126/science.aac9439. URL <https://doi.org/10.1126/science.aac9439>.
- Ogata, M. and Shiba, H. Bethe-ansatz wave function, momentum distribution, and spin correlation in the one-dimensional strongly correlated hubbard model. *Phys. Rev. B*, 41:2326–2338, Feb 1990. doi: 10.1103/PhysRevB.41.2326. URL <https://link.aps.org/doi/10.1103/PhysRevB.41.2326>.
- Ohno, H., Chiba, D., Matsukura, F., Omiya, T., Abe, E., Dietl, T., Ohno, Y., and Ohtani, K. Electric-field control of ferromagnetism. *Nature*, 408(6815):944–946, Dec 2000. ISSN 1476-4687. doi: 10.1038/35050040. URL <https://doi.org/10.1038/35050040>.
- Oleś, B. and Sacha, K. N-conserving bogoliubov vacuum of a two-component bose–einstein condensate: density fluctuations close to a phase-separation condition. *Journal of Physics A: Mathematical and Theoretical*, 41(14):145005, mar 2008. doi: 10.1088/1751-8113/41/14/145005. URL <https://dx.doi.org/10.1088/1751-8113/41/14/145005>.
- Olshanii, M. Atomic scattering in the presence of an external confinement and a gas of impenetrable bosons. *Phys. Rev. Lett.*, 81:938–941, Aug 1998. doi: 10.1103/PhysRevLett.81.938. URL <https://link.aps.org/doi/10.1103/PhysRevLett.81.938>.
- Omran, A., Boll, M., Hilker, T. A., Kleinlein, K., Salomon, G., Bloch, I., and Gross, C. Microscopic observation of pauli blocking in degenerate fermionic lattice gases. *Phys. Rev. Lett.*, 115:263001, Dec 2015. doi: 10.1103/PhysRevLett.115.263001. URL <https://link.aps.org/doi/10.1103/PhysRevLett.115.263001>.
- Orús, R. Exploring corner transfer matrices and corner tensors for the classical simulation of quantum lattice systems. *Phys. Rev. B*, 85:205117, May 2012. doi: 10.1103/PhysRevB.85.205117. URL <https://link.aps.org/doi/10.1103/PhysRevB.85.205117>.
- Orús, R. Tensor networks for complex quantum systems. *Nature Reviews Physics*, 1(9):538–550, Sep 2019. ISSN 2522-5820. doi: 10.1038/s42254-019-0086-7. URL <https://doi.org/10.1038/s42254-019-0086-7>.
- Orús, R. and Latorre, J. I. Universality of entanglement and quantum-computation complexity. *Phys. Rev. A*, 69:052308, May 2004. doi: 10.1103/PhysRevA.69.052308. URL <https://link.aps.org/doi/10.1103/PhysRevA.69.052308>.
- Orús, R. and Vidal, G. Simulation of two-dimensional quantum systems on an infinite lattice revisited: Corner transfer matrix for tensor contraction. *Phys. Rev. B*, 80:094403, Sep 2009. doi: 10.1103/PhysRevB.80.094403. URL <https://link.aps.org/doi/10.1103/PhysRevB.80.094403>.
- Ospelkaus, C., Ospelkaus, S., Humbert, L., Ernst, P., Sengstock, K., and Bongs, K. Ultracold heteronuclear molecules in a 3d optical lattice. *Phys. Rev. Lett.*, 97:120402, Sep 2006. doi: 10.1103/PhysRevLett.97.120402. URL <https://link.aps.org/doi/10.1103/PhysRevLett.97.120402>.

- Ospelkaus, S., Ni, K.-K., Quéméner, G., Neyenhuis, B., Wang, D., de Miranda, M. H. G., Bohn, J. L., Ye, J., and Jin, D. S. Controlling the hyperfine state of rovibronic ground-state polar molecules. *Phys. Rev. Lett.*, 104:030402, Jan 2010a. doi: 10.1103/PhysRevLett.104.030402. URL <https://link.aps.org/doi/10.1103/PhysRevLett.104.030402>.
- Ospelkaus, S., Ni, K.-K., Wang, D., de Miranda, M. H. G., Neyenhuis, B., Quéméner, G., Julienne, P. S., Bohn, J. L., Jin, D. S., and Ye, J. Quantum-state controlled chemical reactions of ultracold potassium-rubidium molecules. *Science*, 327(5967):853–857, 2010b. doi: 10.1126/science.1184121. URL <https://www.science.org/doi/abs/10.1126/science.1184121>.
- Östlund, S. and Rommer, S. Thermodynamic limit of density matrix renormalization. *Phys. Rev. Lett.*, 75:3537–3540, Nov 1995. doi: 10.1103/PhysRevLett.75.3537. URL <https://link.aps.org/doi/10.1103/PhysRevLett.75.3537>.
- Ota, M. and Astrakharchik, G. E. Beyond Lee-Huang-Yang description of self-bound Bose mixtures. *SciPost Phys.*, 9:020, 2020. doi: 10.21468/SciPostPhys.9.2.020. URL <https://scipost.org/10.21468/SciPostPhys.9.2.020>.
- Paeckel, S., Köhler, T., and Manmana, S. R. Automated construction of $U(1)$ -invariant matrix-product operators from graph representations. *SciPost Phys.*, 3:035, 2017. doi: 10.21468/SciPostPhys.3.5.035. URL <https://scipost.org/10.21468/SciPostPhys.3.5.035>.
- Paeckel, S., Köhler, T., Swoboda, A., Manmana, S. R., Schollwöck, U., and Hubig, C. Time-evolution methods for matrix-product states. *Annals of Physics*, 411:167998, 2019. ISSN 0003-4916. doi: <https://doi.org/10.1016/j.aop.2019.167998>. URL <https://www.sciencedirect.com/science/article/pii/S0003491619302532>.
- Page, D. N. Average entropy of a subsystem. *Phys. Rev. Lett.*, 71:1291–1294, Aug 1993. doi: 10.1103/PhysRevLett.71.1291. URL <https://link.aps.org/doi/10.1103/PhysRevLett.71.1291>.
- Pan, J., Yi, S., and Shi, T. Quantum phases of self-bound droplets of bose-bose mixtures. *Phys. Rev. Res.*, 4:043018, Oct 2022. doi: 10.1103/PhysRevResearch.4.043018. URL <https://link.aps.org/doi/10.1103/PhysRevResearch.4.043018>.
- Papp, S. B., Pino, J. M., and Wieman, C. E. Tunable articleibility in a dual-species bose-einstein condensate. *Phys. Rev. Lett.*, 101:040402, Jul 2008. doi: 10.1103/PhysRevLett.101.040402. URL <https://link.aps.org/doi/10.1103/PhysRevLett.101.040402>.
- Paredes, B., Widera, A., Murg, V., Mandel, O., Fölling, S., Cirac, I., Shlyapnikov, G. V., Hänsch, T. W., and Bloch, I. Tonks–girardeau gas of ultracold atoms in an optical lattice. *Nature*, 429(6989): 277–281, May 2004. ISSN 1476-4687. doi: 10.1038/nature02530. URL <https://doi.org/10.1038/nature02530>.
- Parisi, L. and Giorgini, S. Quantum droplets in one-dimensional bose mixtures: A quantum monte carlo study. *Phys. Rev. A*, 102:023318, Aug 2020. doi: 10.1103/PhysRevA.102.023318. URL <https://link.aps.org/doi/10.1103/PhysRevA.102.023318>.

- Parisi, L., Astrakharchik, G. E., and Giorgini, S. Spin dynamics and andreev-bashkin effect in mixtures of one-dimensional bose gases. *Phys. Rev. Lett.*, 121:025302, Jul 2018. doi: 10.1103/PhysRevLett.121.025302. URL <https://link.aps.org/doi/10.1103/PhysRevLett.121.025302>.
- Parisi, L., Astrakharchik, G. E., and Giorgini, S. Liquid state of one-dimensional bose mixtures: A quantum monte carlo study. *Phys. Rev. Lett.*, 122:105302, Mar 2019. doi: 10.1103/PhysRevLett.122.105302. URL <https://link.aps.org/doi/10.1103/PhysRevLett.122.105302>.
- Parsons, M. F., Huber, F., Mazurenko, A., Chiu, C. S., Setiawan, W., Wooley-Brown, K., Blatt, S., and Greiner, M. Site-resolved imaging of fermionic ${}^6\text{Li}$ in an optical lattice. *Phys. Rev. Lett.*, 114:213002, May 2015. doi: 10.1103/PhysRevLett.114.213002. URL <https://link.aps.org/doi/10.1103/PhysRevLett.114.213002>.
- Pastukhov, V. Ground-state properties of dilute one-dimensional bose gas with three-body repulsion. *Physics Letters A*, 383(9):894–897, 2019. ISSN 0375-9601.
- Paul, W. Electromagnetic traps for charged and neutral particles. *Rev. Mod. Phys.*, 62:531–540, Jul 1990. doi: 10.1103/RevModPhys.62.531. URL <https://link.aps.org/doi/10.1103/RevModPhys.62.531>.
- Pereira, R. G., White, S. R., and Affleck, I. Exact edge singularities and dynamical correlations in spin-1/2 chains. *Phys. Rev. Lett.*, 100:027206, Jan 2008. doi: 10.1103/PhysRevLett.100.027206. URL <https://link.aps.org/doi/10.1103/PhysRevLett.100.027206>.
- Perez-Garcia, D., Verstraete, F., Wolf, M. M., and Cirac, J. I. Matrix product state representations. *Quantum Info. Comput.*, 7(5):401–430, jul 2007. ISSN 1533-7146.
- Pethick, C. J. and Smith, H. *Bose–Einstein Condensation in Dilute Gases*. Cambridge University Press, 2 edition, 2008. doi: 10.1017/CBO9780511802850.
- Petrosyan, D., Schmidt, B., Anglin, J. R., and Fleischhauer, M. Quantum liquid of repulsively bound pairs of particles in a lattice. *Phys. Rev. A*, 76:033606, Sep 2007. doi: 10.1103/PhysRevA.76.033606. URL <https://link.aps.org/doi/10.1103/PhysRevA.76.033606>.
- Petrov, D. S. Quantum mechanical stabilization of a collapsing bose-bose mixture. *Phys. Rev. Lett.*, 115:155302, Oct 2015. doi: 10.1103/PhysRevLett.115.155302. URL <https://link.aps.org/doi/10.1103/PhysRevLett.115.155302>.
- Petrov, D. S. Liquid beyond the van der waals paradigm. *Nature Physics*, 14(3):211–212, Mar 2018. ISSN 1745-2481. doi: 10.1038/s41567-018-0052-9. URL <https://doi.org/10.1038/s41567-018-0052-9>.
- Petrov, D. S. and Astrakharchik, G. E. Ultradilute low-dimensional liquids. *Phys. Rev. Lett.*, 117:100401, Sep 2016. doi: 10.1103/PhysRevLett.117.100401. URL <https://link.aps.org/doi/10.1103/PhysRevLett.117.100401>.

- Phillips, W. D. and Metcalf, H. Laser deceleration of an atomic beam. *Phys. Rev. Lett.*, 48:596–599, Mar 1982. doi: 10.1103/PhysRevLett.48.596. URL <https://link.aps.org/doi/10.1103/PhysRevLett.48.596>.
- Pirvu, B., Murg, V., Cirac, J. I., and Verstraete, F. Matrix product operator representations. *New Journal of Physics*, 12(2):025012, feb 2010. doi: 10.1088/1367-2630/12/2/025012. URL <https://doi.org/10.1088/1367-2630/12/2/025012>.
- Pitaevskii, L. P. *Bose-Einstein condensation*. Clarendon Press, Oxford New York, 2003. ISBN 978-0198507192.
- Planck, M. Ueber das gesetz der energieverteilung im normalspectrum. *Annalen der Physik*, 309(3): 553–563, 1901. doi: <https://doi.org/10.1002/andp.19013090310>. URL <https://onlinelibrary.wiley.com/doi/abs/10.1002/andp.19013090310>.
- Po, H. C., Zou, L., Vishwanath, A., and Senthil, T. Origin of mott insulating behavior and superconductivity in twisted bilayer graphene. *Phys. Rev. X*, 8:031089, Sep 2018. doi: 10.1103/PhysRevX.8.031089. URL <https://link.aps.org/doi/10.1103/PhysRevX.8.031089>.
- Po, H. C., Zou, L., Senthil, T., and Vishwanath, A. Faithful tight-binding models and fragile topology of magic-angle bilayer graphene. *Phys. Rev. B*, 99:195455, May 2019. doi: 10.1103/PhysRevB.99.195455. URL <https://link.aps.org/doi/10.1103/PhysRevB.99.195455>.
- Pogorelov, I., Feldker, T., Marciniak, C. D., Postler, L., Jacob, G., Kriegelsteiner, O., Podlesnic, V., Meth, M., Negnevitsky, V., Stadler, M., Höfer, B., Wächter, C., Lakhmanskiy, K., Blatt, R., Schindler, P., and Monz, T. Compact ion-trap quantum computing demonstrator. *PRX Quantum*, 2:020343, Jun 2021. doi: 10.1103/PRXQuantum.2.020343. URL <https://link.aps.org/doi/10.1103/PRXQuantum.2.020343>.
- Pollmann, F. and Turner, A. M. Detection of symmetry-protected topological phases in one dimension. *Phys. Rev. B*, 86:125441, Sep 2012. doi: 10.1103/PhysRevB.86.125441. URL <https://link.aps.org/doi/10.1103/PhysRevB.86.125441>.
- Pollmann, F., Mukerjee, S., Turner, A. M., and Moore, J. E. Theory of finite-entanglement scaling at one-dimensional quantum critical points. *Phys. Rev. Lett.*, 102:255701, Jun 2009. doi: 10.1103/PhysRevLett.102.255701. URL <https://link.aps.org/doi/10.1103/PhysRevLett.102.255701>.
- Porras, D. and Cirac, J. I. Quantum manipulation of trapped ions in two dimensional coulomb crystals. *Phys. Rev. Lett.*, 96:250501, Jun 2006. doi: 10.1103/PhysRevLett.96.250501. URL <https://link.aps.org/doi/10.1103/PhysRevLett.96.250501>.
- Preiss, P. M., Ma, R., Tai, M. E., Lukin, A., Rispoli, M., Zupancic, P., Lahini, Y., Islam, R., and Greiner, M. Strongly correlated quantum walks in optical lattices. *Science*, 347(6227):1229–1233, 2015. ISSN 0036-8075. doi: 10.1126/science.1260364. URL <https://science.sciencemag.org/content/347/6227/1229>.

- Pricoupenko, A. and Petrov, D. S. Dimer-dimer zero crossing and dilute dimerized liquid in a one-dimensional mixture. *Phys. Rev. A*, 97:063616, Jun 2018. doi: 10.1103/PhysRevA.97.063616. URL <https://link.aps.org/doi/10.1103/PhysRevA.97.063616>.
- Pricoupenko, A. and Petrov, D. S. Three-body interaction near a narrow two-body zero crossing. *Phys. Rev. A*, 100:042707, Oct 2019. doi: 10.1103/PhysRevA.100.042707. URL <https://link.aps.org/doi/10.1103/PhysRevA.100.042707>.
- Pricoupenko, A. and Petrov, D. S. Higher-order effective interactions for bosons near a two-body zero crossing. *Phys. Rev. A*, 103:033326, Mar 2021. doi: 10.1103/PhysRevA.103.033326. URL <https://link.aps.org/doi/10.1103/PhysRevA.103.033326>.
- Pricoupenko, L. Pure confinement-induced trimer in one-dimensional atomic waveguides. *Phys. Rev. A*, 97:061604, Jun 2018. doi: 10.1103/PhysRevA.97.061604. URL <https://link.aps.org/doi/10.1103/PhysRevA.97.061604>.
- Pricoupenko, L. Three-body pseudopotential for atoms confined in one dimension. *Phys. Rev. A*, 99:012711, Jan 2019. doi: 10.1103/PhysRevA.99.012711. URL <https://link.aps.org/doi/10.1103/PhysRevA.99.012711>.
- Pupillo, G., Micheli, A., Boninsegni, M., Lesanovsky, I., and Zoller, P. Strongly correlated gases of rydberg-dressed atoms: Quantum and classical dynamics. *Phys. Rev. Lett.*, 104:223002, Jun 2010. doi: 10.1103/PhysRevLett.104.223002. URL <https://link.aps.org/doi/10.1103/PhysRevLett.104.223002>.
- Qiu, D. Y., da Jornada, F. H., and Louie, S. G. Optical spectrum of mos_2 : Many-body effects and diversity of exciton states. *Phys. Rev. Lett.*, 111:216805, Nov 2013. doi: 10.1103/PhysRevLett.111.216805. URL <https://link.aps.org/doi/10.1103/PhysRevLett.111.216805>.
- Radisavljevic, B., Radenovic, A., Brivio, J., Giacometti, V., and Kis, A. Single-layer mos_2 transistors. *Nature Nanotechnology*, 6(3):147–150, Mar 2011. ISSN 1748-3395. doi: 10.1038/nnano.2010.279. URL <https://doi.org/10.1038/nnano.2010.279>.
- Radzihovsky, L., Park, J., and Weichman, P. B. Superfluid transitions in bosonic atom-molecule mixtures near a feshbach resonance. *Phys. Rev. Lett.*, 92:160402, Apr 2004. doi: 10.1103/PhysRevLett.92.160402. URL <https://link.aps.org/doi/10.1103/PhysRevLett.92.160402>.
- Ramasubramaniam, A. Large excitonic effects in monolayers of molybdenum and tungsten dichalcogenides. *Phys. Rev. B*, 86:115409, Sep 2012. doi: 10.1103/PhysRevB.86.115409. URL <https://link.aps.org/doi/10.1103/PhysRevB.86.115409>.
- Ran, S.-J., Tirrito, E., Peng, C., Chen, X., Tagliacozzo, L., Su, G., and Lewenstein, M. Tensor network contractions : Methods and applications to quantum many-body systems. 2020. doi: 10.1007/978-3-030-34489-4. URL <https://doi.org/10.1007/978-3-030-34489-4>.

- Raventós, D., Graß, T., Lewenstein, M., and Juliá-Díaz, B. Cold bosons in optical lattices: a tutorial for exact diagonalization. *Journal of Physics B: Atomic, Molecular and Optical Physics*, 50(11):113001, may 2017. doi: 10.1088/1361-6455/aa68b1. URL <https://dx.doi.org/10.1088/1361-6455/aa68b1>.
- Regan, E. C., Wang, D., Jin, C., Bakti Utama, M. I., Gao, B., Wei, X., Zhao, S., Zhao, W., Zhang, Z., Yumigeta, K., Blei, M., Carlström, J. D., Watanabe, K., Taniguchi, T., Tongay, S., Crommie, M., Zettl, A., and Wang, F. Mott and generalized wigner crystal states in wse2/ws2 moiré superlattices. *Nature*, 579(7799):359–363, Mar 2020. ISSN 1476-4687. doi: 10.1038/s41586-020-2092-4. URL <https://doi.org/10.1038/s41586-020-2092-4>.
- Ren, Y. and Anderson, P. W. Asymptotic correlation functions in the one-dimensional hubbard model with applications to high- t_c superconductivity. *Phys. Rev. B*, 48:16662–16672, Dec 1993. doi: 10.1103/PhysRevB.48.16662. URL <https://link.aps.org/doi/10.1103/PhysRevB.48.16662>.
- Repellin, C. and Senthil, T. Chern bands of twisted bilayer graphene: Fractional chern insulators and spin phase transition. *Phys. Rev. Res.*, 2:023238, May 2020. doi: 10.1103/PhysRevResearch.2.023238. URL <https://link.aps.org/doi/10.1103/PhysRevResearch.2.023238>.
- Ritsch, H., Domokos, P., Brennecke, F., and Esslinger, T. Cold atoms in cavity-generated dynamical optical potentials. *Rev. Mod. Phys.*, 85:553–601, Apr 2013. doi: 10.1103/RevModPhys.85.553. URL <https://link.aps.org/doi/10.1103/RevModPhys.85.553>.
- Rommer, S. and Östlund, S. Class of ansatz wave functions for one-dimensional spin systems and their relation to the density matrix renormalization group. *Phys. Rev. B*, 55:2164–2181, Jan 1997. doi: 10.1103/PhysRevB.55.2164. URL <https://link.aps.org/doi/10.1103/PhysRevB.55.2164>.
- Roth, R. and Burnett, K. Dynamic structure factor of ultracold bose and fermi gases in optical lattices. *Journal of Physics B: Atomic, Molecular and Optical Physics*, 37(19):3893–3907, sep 2004. doi: 10.1088/0953-4075/37/19/009. URL <https://doi.org/10.1088/0953-4075/37/19/009>.
- Rytova, N. S. The screened potential of a point charge in a thin film. *Moscow University Physics Bulletin*, 3(3):18, 1967.
- Sachdev, S. Hole motion in a quantum néel state. *Phys. Rev. B*, 39:12232–12247, Jun 1989. doi: 10.1103/PhysRevB.39.12232. URL <https://link.aps.org/doi/10.1103/PhysRevB.39.12232>.
- Sachdev, S. *Quantum phase transitions*. Cambridge University Press, Cambridge New York, 2011. ISBN 978-0521514682.
- Saffman, M., Walker, T. G., and Mølmer, K. Quantum information with rydberg atoms. *Rev. Mod. Phys.*, 82:2313–2363, Aug 2010. doi: 10.1103/RevModPhys.82.2313. URL <https://link.aps.org/doi/10.1103/RevModPhys.82.2313>.

- Sahebsara, P. and Sénéchal, D. Hubbard model on the triangular lattice: Spiral order and spin liquid. *Phys. Rev. Lett.*, 100:136402, Mar 2008. doi: 10.1103/PhysRevLett.100.136402. URL <https://link.aps.org/doi/10.1103/PhysRevLett.100.136402>.
- Sakmann, K., Streltsov, A. I., Alon, O. E., and Cederbaum, L. S. Quantum dynamics of attractive versus repulsive bosonic josephson junctions: Bose-hubbard and full-hamiltonian results. *Phys. Rev. A*, 82:013620, Jul 2010. doi: 10.1103/PhysRevA.82.013620. URL <https://link.aps.org/doi/10.1103/PhysRevA.82.013620>.
- Salamon, M. B. and Jaime, M. The physics of manganites: Structure and transport. *Rev. Mod. Phys.*, 73:583–628, Aug 2001. doi: 10.1103/RevModPhys.73.583. URL <https://link.aps.org/doi/10.1103/RevModPhys.73.583>.
- Savary, L. and Balents, L. Quantum spin liquids: a review. *Reports on Progress in Physics*, 80(1):016502, nov 2016. doi: 10.1088/0034-4885/80/1/016502. URL <https://dx.doi.org/10.1088/0034-4885/80/1/016502>.
- Sawicki, M., Chiba, D., Korbecka, A., Nishitani, Y., Majewski, J. A., Matsukura, F., Dietl, T., and Ohno, H. Experimental probing of the interplay between ferromagnetism and localization in (ga, mn)as. *Nature Physics*, 6(1):22–25, Jan 2010. ISSN 1745-2481. doi: 10.1038/nphys1455. URL <https://doi.org/10.1038/nphys1455>.
- Schmitt, M., Wenzel, M., Böttcher, F., Ferrier-Barbut, I., and Pfau, T. Self-bound droplets of a dilute magnetic quantum liquid. *Nature*, 539(7628):259–262, Nov. 2016. doi: 10.1038/nature20126. URL <https://doi.org/10.1038/nature20126>.
- Schmitt-Rink, S., Varma, C. M., and Ruckenstein, A. E. Spectral function of holes in a quantum antiferromagnet. *Phys. Rev. Lett.*, 60:2793–2796, Jun 1988. doi: 10.1103/PhysRevLett.60.2793. URL <https://link.aps.org/doi/10.1103/PhysRevLett.60.2793>.
- Schneider, U., Hackermüller, L., Ronzheimer, J. P., Will, S., Braun, S., Best, T., Bloch, I., Demler, E., Mandt, S., Rasch, D., and Rosch, A. Fermionic transport and out-of-equilibrium dynamics in a homogeneous hubbard model with ultracold atoms. *Nature Physics*, 8(3):213–218, Mar 2012. ISSN 1745-2481. doi: 10.1038/nphys2205. URL <https://doi.org/10.1038/nphys2205>.
- Schollwöck, U. The density-matrix renormalization group. *Rev. Mod. Phys.*, 77:259–315, Apr 2005. doi: 10.1103/RevModPhys.77.259. URL <https://link.aps.org/doi/10.1103/RevModPhys.77.259>.
- Schollwöck, U. The density-matrix renormalization group in the age of matrix product states. *Annals of Physics*, 326(1):96–192, 2011a. ISSN 0003-4916. doi: <https://doi.org/10.1016/j.aop.2010.09.012>. URL <https://www.sciencedirect.com/science/article/pii/S0003491610001752>. January 2011 Special Issue.
- Schollwöck, U. The density-matrix renormalization group in the age of matrix product states. *Annals of Physics*, 326(1):96–192, 2011b. ISSN 0003-4916. doi: <https://doi.org/10.1016/j.aop.2010.09>.

012. URL <https://www.sciencedirect.com/science/article/pii/S0003491610001752>. January 2011 Special Issue.
- Schuch, N., Wolf, M. M., Verstraete, F., and Cirac, J. I. Computational complexity of projected entangled pair states. *Phys. Rev. Lett.*, 98:140506, Apr 2007. doi: 10.1103/PhysRevLett.98.140506. URL <https://link.aps.org/doi/10.1103/PhysRevLett.98.140506>.
- Schuch, N., Wolf, M. M., Verstraete, F., and Cirac, J. I. Simulation of quantum many-body systems with strings of operators and monte carlo tensor contractions. *Phys. Rev. Lett.*, 100:040501, Jan 2008. doi: 10.1103/PhysRevLett.100.040501. URL <https://link.aps.org/doi/10.1103/PhysRevLett.100.040501>.
- Scott, A., Eilbeck, J., and Gilhøj, H. Quantum lattice solitons. *Physica D: Nonlinear Phenomena*, 78(3):194 – 213, 1994. ISSN 0167-2789. doi: [https://doi.org/10.1016/0167-2789\(94\)90115-5](https://doi.org/10.1016/0167-2789(94)90115-5). URL <http://www.sciencedirect.com/science/article/pii/0167278994901155>.
- Sekino, Y. and Nishida, Y. Quantum droplet of one-dimensional bosons with a three-body attraction. *Phys. Rev. A*, 97:011602, Jan 2018. doi: 10.1103/PhysRevA.97.011602. URL <https://link.aps.org/doi/10.1103/PhysRevA.97.011602>.
- Semeghini, G., Ferioli, G., Masi, L., Mazzinghi, C., Wolswijk, L., Minardi, F., Modugno, M., Modugno, G., Inguscio, M., and Fattori, M. Self-bound quantum droplets of atomic mixtures in free space. *Phys. Rev. Lett.*, 120:235301, Jun 2018. doi: 10.1103/PhysRevLett.120.235301. URL <https://link.aps.org/doi/10.1103/PhysRevLett.120.235301>.
- Shallcross, S., Sharma, S., and Pankratov, O. A. Quantum interference at the twist boundary in graphene. *Phys. Rev. Lett.*, 101:056803, Aug 2008. doi: 10.1103/PhysRevLett.101.056803. URL <https://link.aps.org/doi/10.1103/PhysRevLett.101.056803>.
- Sharpe, A. L., Fox, E. J., Barnard, A. W., Finney, J., Watanabe, K., Taniguchi, T., Kastner, M. A., and Goldhaber-Gordon, D. Emergent ferromagnetism near three-quarters filling in twisted bilayer graphene. *Science*, 365(6453):605–608, 2019. ISSN 0036-8075. doi: 10.1126/science.aaw3780. URL <https://science.sciencemag.org/content/365/6453/605>.
- Sheffer, Y. and Stern, A. Chiral magic-angle twisted bilayer graphene in a magnetic field: Landau level correspondence, exact wave functions, and fractional chern insulators. *Phys. Rev. B*, 104:L121405, Sep 2021. doi: 10.1103/PhysRevB.104.L121405. URL <https://link.aps.org/doi/10.1103/PhysRevB.104.L121405>.
- Sherson, J. F., Weitenberg, C., Endres, M., Cheneau, M., Bloch, I., and Kuhr, S. Single-atom-resolved fluorescence imaging of an atomic mott insulator. *Nature*, 467(7311):68–72, Sep 2010. ISSN 1476-4687. doi: 10.1038/nature09378. URL <https://doi.org/10.1038/nature09378>.
- Sheshadri, K., Krishnamurthy, H. R., Pandit, R., and Ramakrishnan, T. V. Superfluid and insulating phases in an interacting-boson model: Mean-field theory and the rpa. *Europhysics Letters*, 22(4):257,

- may 1993. doi: 10.1209/0295-5075/22/4/004. URL <https://dx.doi.org/10.1209/0295-5075/22/4/004>.
- Shi, T., Demler, E., and Ignacio Cirac, J. Variational study of fermionic and bosonic systems with non-gaussian states: Theory and applications. *Annals of Physics*, 390:245–302, 2018. ISSN 0003-4916. doi: <https://doi.org/10.1016/j.aop.2017.11.014>. URL <https://www.sciencedirect.com/science/article/pii/S0003491617303251>.
- Shirakawa, T., Tohyama, T., Kokalj, J., Sota, S., and Yunoki, S. Ground-state phase diagram of the triangular lattice hubbard model by the density-matrix renormalization group method. *Phys. Rev. B*, 96:205130, Nov 2017. doi: 10.1103/PhysRevB.96.205130. URL <https://link.aps.org/doi/10.1103/PhysRevB.96.205130>.
- Shraiman, B. I. and Siggia, E. D. Two-particle excitations in antiferromagnetic insulators. *Phys. Rev. Lett.*, 60:740–743, Feb 1988a. doi: 10.1103/PhysRevLett.60.740. URL <https://link.aps.org/doi/10.1103/PhysRevLett.60.740>.
- Shraiman, B. I. and Siggia, E. D. Mobile vacancies in a quantum heisenberg antiferromagnet. *Phys. Rev. Lett.*, 61:467–470, Jul 1988b. doi: 10.1103/PhysRevLett.61.467. URL <https://link.aps.org/doi/10.1103/PhysRevLett.61.467>.
- Singh, S. and Vidal, G. Tensor network states and algorithms in the presence of a global su(2) symmetry. *Phys. Rev. B*, 86:195114, Nov 2012. doi: 10.1103/PhysRevB.86.195114. URL <https://link.aps.org/doi/10.1103/PhysRevB.86.195114>.
- Singh, S., Pfeifer, R. N. C., and Vidal, G. Tensor network decompositions in the presence of a global symmetry. *Phys. Rev. A*, 82:050301, Nov 2010. doi: 10.1103/PhysRevA.82.050301. URL <https://link.aps.org/doi/10.1103/PhysRevA.82.050301>.
- Singh, S., Pfeifer, R. N. C., and Vidal, G. Tensor network states and algorithms in the presence of a global u(1) symmetry. *Phys. Rev. B*, 83:115125, Mar 2011. doi: 10.1103/PhysRevB.83.115125. URL <https://link.aps.org/doi/10.1103/PhysRevB.83.115125>.
- Smoleński, T., Dolgirev, P. E., Kuhlenkamp, C., Popert, A., Shimazaki, Y., Back, P., Lu, X., Kroner, M., Watanabe, K., Taniguchi, T., Esterlis, I., Demler, E., and Imamoğlu, A. Signatures of wigner crystal of electrons in a monolayer semiconductor. *Nature*, 595(7865):53–57, Jul 2021. ISSN 1476-4687. doi: 10.1038/s41586-021-03590-4. URL <https://doi.org/10.1038/s41586-021-03590-4>.
- Song, Z., Wang, Z., Shi, W., Li, G., Fang, C., and Bernevig, B. A. All magic angles in twisted bilayer graphene are topological. *Phys. Rev. Lett.*, 123:036401, Jul 2019. doi: 10.1103/PhysRevLett.123.036401. URL <https://link.aps.org/doi/10.1103/PhysRevLett.123.036401>.
- Song, Z.-D., Lian, B., Regnault, N., and Bernevig, B. A. Twisted bilayer graphene. ii. stable symmetry anomaly. *Phys. Rev. B*, 103:205412, May 2021. doi: 10.1103/PhysRevB.103.205412. URL <https://link.aps.org/doi/10.1103/PhysRevB.103.205412>.

- Sørensen, A. S., Demler, E., and Lukin, M. D. Fractional quantum hall states of atoms in optical lattices. *Phys. Rev. Lett.*, 94:086803, Mar 2005. doi: 10.1103/PhysRevLett.94.086803. URL <https://link.aps.org/doi/10.1103/PhysRevLett.94.086803>.
- Soriano, D. and Katsnelson, M. I. Magnetic polaron and antiferromagnetic-ferromagnetic transition in doped bilayer CrI_3 . *Phys. Rev. B*, 101:041402, Jan 2020. doi: 10.1103/PhysRevB.101.041402. URL <https://link.aps.org/doi/10.1103/PhysRevB.101.041402>.
- Sowiński, T. and Ángel García-March, M. One-dimensional mixtures of several ultracold atoms: a review. *Reports on Progress in Physics*, 82(10):104401, sep 2019. doi: 10.1088/1361-6633/ab3a80. URL <https://dx.doi.org/10.1088/1361-6633/ab3a80>.
- Spielman, I. B., Phillips, W. D., and Porto, J. V. Mott-insulator transition in a two-dimensional atomic bose gas. *Phys. Rev. Lett.*, 98:080404, Feb 2007. doi: 10.1103/PhysRevLett.98.080404. URL <https://link.aps.org/doi/10.1103/PhysRevLett.98.080404>.
- Spielman, I. B., Phillips, W. D., and Porto, J. V. Condensate fraction in a 2d bose gas measured across the mott-insulator transition. *Phys. Rev. Lett.*, 100:120402, Mar 2008. doi: 10.1103/PhysRevLett.100.120402. URL <https://link.aps.org/doi/10.1103/PhysRevLett.100.120402>.
- Splendiani, A., Sun, L., Zhang, Y., Li, T., Kim, J., Chim, C.-Y., Galli, G., and Wang, F. Emerging photoluminescence in monolayer mos₂. *Nano Letters*, 10(4):1271–1275, Apr 2010. ISSN 1530-6984. doi: 10.1021/nl903868w. URL <https://doi.org/10.1021/nl903868w>.
- Sposetti, C. N., Bravo, B., Trumper, A. E., Gazza, C. J., and Manuel, L. O. Classical antiferromagnetism in kinetically frustrated electronic models. *Phys. Rev. Lett.*, 112:187204, May 2014. doi: 10.1103/PhysRevLett.112.187204. URL <https://link.aps.org/doi/10.1103/PhysRevLett.112.187204>.
- Stöferle, T., Moritz, H., Schori, C., Köhl, M., and Esslinger, T. Transition from a strongly interacting 1d superfluid to a mott insulator. *Phys. Rev. Lett.*, 92:130403, Mar 2004. doi: 10.1103/PhysRevLett.92.130403. URL <https://link.aps.org/doi/10.1103/PhysRevLett.92.130403>.
- Stoudenmire, E. M. and White, S. R. Minimally entangled typical thermal state algorithms. *New Journal of Physics*, 12(5):055026, may 2010. doi: 10.1088/1367-2630/12/5/055026. URL <https://dx.doi.org/10.1088/1367-2630/12/5/055026>.
- Struck, J., Ölschläger, C., Targat, R. L., Soltan-Panahi, P., Eckardt, A., Lewenstein, M., Windpassinger, P., and Sengstock, K. Quantum simulation of frustrated classical magnetism in triangular optical lattices. *Science*, 333(6045):996–999, 2011. doi: 10.1126/science.1207239.
- Struck, J., Ölschläger, C., Weinberg, M., Hauke, P., Simonet, J., Eckardt, A., Lewenstein, M., Sengstock, K., and Windpassinger, P. Tunable gauge potential for neutral and spinless particles in driven optical lattices. *Phys. Rev. Lett.*, 108:225304, May 2012. doi: 10.1103/PhysRevLett.108.225304. URL <https://link.aps.org/doi/10.1103/PhysRevLett.108.225304>.

- Sun, B. and Pindzola, M. S. Bogoliubov modes and the static structure factor for a two-species bose–einstein condensate. *Journal of Physics B: Atomic, Molecular and Optical Physics*, 43(5): 055301, feb 2010. doi: 10.1088/0953-4075/43/5/055301. URL <https://dx.doi.org/10.1088/0953-4075/43/5/055301>.
- Suzuki, M. Generalized trotter’s formula and systematic approximants of exponential operators and inner derivations with applications to many-body problems. *Communications in Mathematical Physics*, 51(2):183–190, Jun 1976. ISSN 1432-0916. doi: 10.1007/BF01609348. URL <https://doi.org/10.1007/BF01609348>.
- Swingle, B. Entanglement renormalization and holography. *Phys. Rev. D*, 86:065007, Sep 2012. doi: 10.1103/PhysRevD.86.065007. URL <https://link.aps.org/doi/10.1103/PhysRevD.86.065007>.
- Szasz, A. and Motruk, J. Phase diagram of the anisotropic triangular lattice hubbard model. *Phys. Rev. B*, 103:235132, Jun 2021. doi: 10.1103/PhysRevB.103.235132. URL <https://link.aps.org/doi/10.1103/PhysRevB.103.235132>.
- Szasz, A., Motruk, J., Zaletel, M. P., and Moore, J. E. Chiral spin liquid phase of the triangular lattice hubbard model: A density matrix renormalization group study. *Phys. Rev. X*, 10:021042, May 2020. doi: 10.1103/PhysRevX.10.021042. URL <https://link.aps.org/doi/10.1103/PhysRevX.10.021042>.
- Tagliacozzo, L., de Oliveira, T. R., Iblisdir, S., and Latorre, J. I. Scaling of entanglement support for matrix product states. *Phys. Rev. B*, 78:024410, Jul 2008. doi: 10.1103/PhysRevB.78.024410. URL <https://link.aps.org/doi/10.1103/PhysRevB.78.024410>.
- Tai, M. E., Lukin, A., Rispoli, M., Schittko, R., Menke, T., Borgnia, D., Preiss, P. M., Grusdt, F., Kaufman, A. M., and Greiner, M. Microscopy of the interacting harper–hofstadter model in the two-body limit. *Nature*, 546(7659):519–523, Jun 2017. ISSN 1476-4687. doi: 10.1038/nature22811. URL <https://doi.org/10.1038/nature22811>.
- Tang, Y., Li, L., Li, T., Xu, Y., Liu, S., Barmak, K., Watanabe, K., Taniguchi, T., MacDonald, A. H., Shan, J., and Mak, K. F. Simulation of hubbard model physics in wse₂/ws₂ moiré superlattices. *Nature*, 579(7799):353–358, Mar 2020. ISSN 1476-4687. doi: 10.1038/s41586-020-2085-3. URL <https://doi.org/10.1038/s41586-020-2085-3>.
- Tanzi, L., Lucioni, E., Famà, F., Catani, J., Fioretti, A., Gabbanini, C., Bisset, R. N., Santos, L., and Modugno, G. Observation of a dipolar quantum gas with metastable supersolid properties. *Phys. Rev. Lett.*, 122:130405, Apr 2019a. doi: 10.1103/PhysRevLett.122.130405. URL <https://link.aps.org/doi/10.1103/PhysRevLett.122.130405>.
- Tanzi, L., Rocuzzo, S. M., Lucioni, E., Famà, F., Fioretti, A., Gabbanini, C., Modugno, G., Recati, A., and Stringari, S. Supersolid symmetry breaking from compressional oscillations in a dipolar quantum gas. *Nature*, 574(7778):382–385, Oct 2019b. ISSN 1476-4687. doi: 10.1038/s41586-019-1568-6. URL <https://doi.org/10.1038/s41586-019-1568-6>.

- Tarnopolsky, G., Kruchkov, A. J., and Vishwanath, A. Origin of magic angles in twisted bilayer graphene. *Phys. Rev. Lett.*, 122:106405, Mar 2019. doi: 10.1103/PhysRevLett.122.106405. URL <https://link.aps.org/doi/10.1103/PhysRevLett.122.106405>.
- Taylor, J. R. *Scattering Theory: The quantum Theory on Nonrelativistic Collisions*. Wiley, New York, 1972.
- Thouless, D. J. Exchange in solid ^3He and the Heisenberg Hamiltonian. *Proceedings of the Physical Society*, 86(5):893–904, Nov. 1965. doi: 10.1088/0370-1328/86/5/301.
- Tocchio, L. F., Gros, C., Valentí, R., and Becca, F. One-dimensional spin liquid, collinear, and spiral phases from uncoupled chains to the triangular lattice. *Phys. Rev. B*, 89:235107, Jun 2014. doi: 10.1103/PhysRevB.89.235107. URL <https://link.aps.org/doi/10.1103/PhysRevB.89.235107>.
- Tokuno, A. and Giamarchi, T. Spectroscopy for cold atom gases in periodically phase-modulated optical lattices. *Phys. Rev. Lett.*, 106:205301, May 2011. doi: 10.1103/PhysRevLett.106.205301. URL <https://link.aps.org/doi/10.1103/PhysRevLett.106.205301>.
- Tokura, Y., editor. *Colossal Magnetoresistive Oxides*. Advances in Condensed Matter Science. Taylor & Francis, London, England, May 2000.
- Tokura, Y. Critical features of colossal magnetoresistive manganites. *Reports on Progress in Physics*, 69(3):797–851, feb 2006. doi: 10.1088/0034-4885/69/3/r06. URL <https://doi.org/10.1088/0034-4885/69/3/r06>.
- Tommasini, P., de Passos, E. J. V., de Toledo Piza, A. F. R., Hussein, M. S., and Timmermans, E. Bogoliubov theory for mutually coherent condensates. *Phys. Rev. A*, 67:023606, Feb 2003. doi: 10.1103/PhysRevA.67.023606. URL <https://link.aps.org/doi/10.1103/PhysRevA.67.023606>.
- Toulouse, G., Vannimenus, J., and Maillard, J. Spin glasses and roughening transition. *Journal de Physique Lettres*, 38(22):459–461, 1977. doi: 10.1051/jphyslet:019770038022045900. URL <https://hal.science/jpa-00231420>.
- Trefzger, C., Menotti, C., and Lewenstein, M. Pair-supersolid phase in a bilayer system of dipolar lattice bosons. *Phys. Rev. Lett.*, 103:035304, Jul 2009. doi: 10.1103/PhysRevLett.103.035304. URL <https://link.aps.org/doi/10.1103/PhysRevLett.103.035304>.
- Trefzger, C., Menotti, C., Capogrosso-Sansone, B., and Lewenstein, M. Ultracold dipolar gases in optical lattices. *Journal of Physics B: Atomic, Molecular and Optical Physics*, 44(19):193001, sep 2011. doi: 10.1088/0953-4075/44/19/193001. URL <https://doi.org/10.1088/0953-4075/44/19/193001>.
- Trotzky, S., Cheinet, P., Fölling, S., Feld, M., Schnorrberger, U., Rey, A. M., Polkovnikov, A., Demler, E. A., Lukin, M. D., and Bloch, I. Time-resolved observation and control of superexchange interactions with ultracold atoms in optical lattices. *Science*, 319(5861):295–299, 2008a. ISSN 0036-8075. doi: 10.1126/science.1150841. URL <https://science.sciencemag.org/content/319/5861/295>.

- Trotzky, S., Cheinet, P., Fölling, S., Feld, M., Schnorrberger, U., Rey, A. M., Polkovnikov, A., Demler, E. A., Lukin, M. D., and Bloch, I. Time-resolved observation and control of superexchange interactions with ultracold atoms in optical lattices. *Science*, 319(5861):295–299, 2008b. doi: 10.1126/science.1150841. URL <https://www.science.org/doi/abs/10.1126/science.1150841>.
- Trugman, S. A. Interaction of holes in a hubbard antiferromagnet and high-temperature superconductivity. *Phys. Rev. B*, 37:1597–1603, Feb 1988. doi: 10.1103/PhysRevB.37.1597. URL <https://link.aps.org/doi/10.1103/PhysRevB.37.1597>.
- Ugeda, M. M., Bradley, A. J., Shi, S.-F., da Jornada, F. H., Zhang, Y., Qiu, D. Y., Ruan, W., Mo, S.-K., Hussain, Z., Shen, Z.-X., Wang, F., Louie, S. G., and Crommie, M. F. Giant bandgap renormalization and excitonic effects in a monolayer transition metal dichalcogenide semiconductor. *Nature Materials*, 13(12):1091–1095, Dec 2014. ISSN 1476-4660. doi: 10.1038/nmat4061. URL <https://doi.org/10.1038/nmat4061>.
- Vaidya, V. D., Guo, Y., Kroeze, R. M., Ballantine, K. E., Kollár, A. J., Keeling, J., and Lev, B. L. Tunable-range, photon-mediated atomic interactions in multimode cavity qed. *Phys. Rev. X*, 8: 011002, Jan 2018. doi: 10.1103/PhysRevX.8.011002. URL <https://link.aps.org/doi/10.1103/PhysRevX.8.011002>.
- Valiente, M. From few to many body degrees of freedom. *Few-Body Systems*, 59(5):101, Jun 2018. ISSN 1432-5411. doi: 10.1007/s00601-018-1421-8. URL <https://doi.org/10.1007/s00601-018-1421-8>.
- Valiente, M. Three-body repulsive forces among identical bosons in one dimension. *Phys. Rev. A*, 100:013614, Jul 2019. doi: 10.1103/PhysRevA.100.013614. URL <https://link.aps.org/doi/10.1103/PhysRevA.100.013614>.
- Valiente, M. Bose-fermi dualities for arbitrary one-dimensional quantum systems in the universal low-energy regime. *Phys. Rev. A*, 102:053304, Nov 2020. doi: 10.1103/PhysRevA.102.053304. URL <https://link.aps.org/doi/10.1103/PhysRevA.102.053304>.
- Valiente, M. Universal duality transformations in interacting one-dimensional quantum systems. *Phys. Rev. A*, 103:L021302, Feb 2021. doi: 10.1103/PhysRevA.103.L021302. URL <https://link.aps.org/doi/10.1103/PhysRevA.103.L021302>.
- Valiente, M. and Pastukhov, V. Anomalous frequency shifts in a one-dimensional trapped bose gas. *Phys. Rev. A*, 99:053607, May 2019. doi: 10.1103/PhysRevA.99.053607. URL <https://link.aps.org/doi/10.1103/PhysRevA.99.053607>.
- Valiente, M. and Petrosyan, D. Two-particle states in the hubbard model. *Journal of Physics B: Atomic, Molecular and Optical Physics*, 41(16):161002, aug 2008. doi: 10.1088/0953-4075/41/16/161002. URL <https://dx.doi.org/10.1088/0953-4075/41/16/161002>.

- Valiente, M. and Petrosyan, D. Scattering resonances and two-particle bound states of the extended hubbard model. *Journal of Physics B: Atomic, Molecular and Optical Physics*, 42(12):121001, jun 2009a. doi: 10.1088/0953-4075/42/12/121001. URL <https://doi.org/10.1088/0953-4075/42/12/121001>.
- Valiente, M. and Petrosyan, D. Scattering resonances and two-particle bound states of the extended hubbard model. *J. Phys. B: At. Mol. Opt. Phys.*, 42(12):121001, jun 2009b. doi: 10.1088/0953-4075/42/12/121001. URL <https://doi.org/10.1088/0953-4075/42/12/121001>.
- Valiente, M. and Zinner, N. T. Effective field theory of interactions on the lattice. *Few-Body Systems*, 56(11):845–851, Dec 2015. ISSN 1432-5411. doi: 10.1007/s00601-015-0991-y. URL <https://doi.org/10.1007/s00601-015-0991-y>.
- Valiente, M., Petrosyan, D., and Saenz, A. Three-body bound states in a lattice. *Phys. Rev. A*, 81: 011601, Jan 2010. doi: 10.1103/PhysRevA.81.011601. URL <https://link.aps.org/doi/10.1103/PhysRevA.81.011601>.
- van de Kraats, J., Nielsen, K. K., and Bruun, G. M. Holes and magnetic polarons in a triangular lattice antiferromagnet. 2022. doi: 10.48550/arXiv.2209.05131. URL <https://arxiv.org/abs/2209.05131>.
- van Oosten, D., van der Straten, P., and Stoof, H. T. C. Quantum phases in an optical lattice. *Phys. Rev. A*, 63:053601, Apr 2001. doi: 10.1103/PhysRevA.63.053601. URL <https://link.aps.org/doi/10.1103/PhysRevA.63.053601>.
- Vannimenus, J. and Toulouse, G. Theory of the frustration effect. ii. ising spins on a square lattice. *Journal of Physics C: Solid State Physics*, 10(18):L537, sep 1977. doi: 10.1088/0022-3719/10/18/008. URL <https://dx.doi.org/10.1088/0022-3719/10/18/008>.
- Verstraete, F. and Cirac, J. I. Renormalization algorithms for quantum-many body systems in two and higher dimensions. 2004.
- Verstraete, F. and Cirac, J. I. Continuous matrix product states for quantum fields. *Phys. Rev. Lett.*, 104:190405, May 2010. doi: 10.1103/PhysRevLett.104.190405. URL <https://link.aps.org/doi/10.1103/PhysRevLett.104.190405>.
- Verstraete, F., García-Ripoll, J. J., and Cirac, J. I. Matrix product density operators: Simulation of finite-temperature and dissipative systems. *Phys. Rev. Lett.*, 93:207204, Nov 2004. doi: 10.1103/PhysRevLett.93.207204. URL <https://link.aps.org/doi/10.1103/PhysRevLett.93.207204>.
- Verstraete, F., Wolf, M. M., Perez-Garcia, D., and Cirac, J. I. Criticality, the area law, and the computational power of projected entangled pair states. *Phys. Rev. Lett.*, 96:220601, Jun 2006. doi: 10.1103/PhysRevLett.96.220601. URL <https://link.aps.org/doi/10.1103/PhysRevLett.96.220601>.

- Vidal, G. Efficient classical simulation of slightly entangled quantum computations. *Phys. Rev. Lett.*, 91:147902, Oct 2003. doi: 10.1103/PhysRevLett.91.147902. URL <https://link.aps.org/doi/10.1103/PhysRevLett.91.147902>.
- Vidal, G. Efficient simulation of one-dimensional quantum many-body systems. *Phys. Rev. Lett.*, 93:040502, Jul 2004. doi: 10.1103/PhysRevLett.93.040502. URL <https://link.aps.org/doi/10.1103/PhysRevLett.93.040502>.
- Vidal, G. Entanglement renormalization. *Phys. Rev. Lett.*, 99:220405, Nov 2007a. doi: 10.1103/PhysRevLett.99.220405. URL <https://link.aps.org/doi/10.1103/PhysRevLett.99.220405>.
- Vidal, G. Classical simulation of infinite-size quantum lattice systems in one spatial dimension. *Phys. Rev. Lett.*, 98:070201, Feb 2007b. doi: 10.1103/PhysRevLett.98.070201. URL <https://link.aps.org/doi/10.1103/PhysRevLett.98.070201>.
- Vidal, G., Latorre, J. I., Rico, E., and Kitaev, A. Entanglement in quantum critical phenomena. *Phys. Rev. Lett.*, 90:227902, Jun 2003. doi: 10.1103/PhysRevLett.90.227902. URL <https://link.aps.org/doi/10.1103/PhysRevLett.90.227902>.
- Wächtler, F. and Santos, L. Ground-state properties and elementary excitations of quantum droplets in dipolar bose-einstein condensates. *Phys. Rev. A*, 94:043618, Oct 2016. doi: 10.1103/PhysRevA.94.043618. URL <https://link.aps.org/doi/10.1103/PhysRevA.94.043618>.
- Walker, T. G. and Saffman, M. Consequences of zeeman degeneracy for the van der waals blockade between rydberg atoms. *Phys. Rev. A*, 77:032723, Mar 2008. doi: 10.1103/PhysRevA.77.032723. URL <https://link.aps.org/doi/10.1103/PhysRevA.77.032723>.
- Wang, G., Marie, X., Gerber, I., Amand, T., Lagarde, D., Bouet, L., Vidal, M., Balocchi, A., and Urbaszek, B. Giant enhancement of the optical second-harmonic emission of wse₂ monolayers by laser excitation at exciton resonances. *Phys. Rev. Lett.*, 114:097403, Mar 2015. doi: 10.1103/PhysRevLett.114.097403. URL <https://link.aps.org/doi/10.1103/PhysRevLett.114.097403>.
- Wannier, G. H. Antiferromagnetism. the triangular ising net. *Phys. Rev.*, 79:357–364, Jul 1950. doi: 10.1103/PhysRev.79.357. URL <https://link.aps.org/doi/10.1103/PhysRev.79.357>.
- Watanabe, T., Yokoyama, H., Tanaka, Y., and Inoue, J. Predominant magnetic states in the hubbard model on anisotropic triangular lattices. *Phys. Rev. B*, 77:214505, Jun 2008. doi: 10.1103/PhysRevB.77.214505. URL <https://link.aps.org/doi/10.1103/PhysRevB.77.214505>.
- Weichselbaum, A. Non-abelian symmetries in tensor networks: A quantum symmetry space approach. *Annals of Physics*, 327(12):2972–3047, 2012. ISSN 0003-4916. doi: <https://doi.org/10.1016/j.aop.2012.07.009>. URL <https://www.sciencedirect.com/science/article/pii/S0003491612001121>.
- Weitenberg, C., Endres, M., Sherson, J. F., Cheneau, M., Schauß, P., Fukuhara, T., Bloch, I., and Kuhr, S. Single-spin addressing in an atomic mott insulator. *Nature*, 471(7338):319–324, Mar 2011. ISSN 1476-4687. doi: 10.1038/nature09827. URL <https://doi.org/10.1038/nature09827>.

- Wen Chang, H., Akita, S., Matsukura, F., and Ohno, H. Hole concentration dependence of the curie temperature of (ga,mn)sb in a field-effect structure. *Applied Physics Letters*, 103(14):142402, 2013.
- White, S. R. Density matrix formulation for quantum renormalization groups. *Phys. Rev. Lett.*, 69: 2863–2866, Nov 1992. doi: 10.1103/PhysRevLett.69.2863. URL <https://link.aps.org/doi/10.1103/PhysRevLett.69.2863>.
- White, S. R. Density-matrix algorithms for quantum renormalization groups. *Phys. Rev. B*, 48:10345–10356, Oct 1993. doi: 10.1103/PhysRevB.48.10345. URL <https://link.aps.org/doi/10.1103/PhysRevB.48.10345>.
- White, S. R. and Affleck, I. Density matrix renormalization group analysis of the nagaoka polaron in the two-dimensional $t-j$ model. *Phys. Rev. B*, 64:024411, Jun 2001. doi: 10.1103/PhysRevB.64.024411. URL <https://link.aps.org/doi/10.1103/PhysRevB.64.024411>.
- White, S. R. and Affleck, I. Spectral function for the $s = 1$ heisenberg antiferromagnetic chain. *Phys. Rev. B*, 77:134437, Apr 2008. doi: 10.1103/PhysRevB.77.134437. URL <https://link.aps.org/doi/10.1103/PhysRevB.77.134437>.
- White, S. R. and Feiguin, A. E. Real-time evolution using the density matrix renormalization group. *Phys. Rev. Lett.*, 93:076401, Aug 2004. doi: 10.1103/PhysRevLett.93.076401. URL <https://link.aps.org/doi/10.1103/PhysRevLett.93.076401>.
- White, S. R. and Noack, R. M. Real-space quantum renormalization groups. *Phys. Rev. Lett.*, 68: 3487–3490, Jun 1992. doi: 10.1103/PhysRevLett.68.3487. URL <https://link.aps.org/doi/10.1103/PhysRevLett.68.3487>.
- White, S. R. and Scalapino, D. J. Hole and pair structures in the t - j model. *Phys. Rev. B*, 55:6504–6517, Mar 1997. doi: 10.1103/PhysRevB.55.6504. URL <https://link.aps.org/doi/10.1103/PhysRevB.55.6504>.
- Whittaker, E. T. and Watson, G. N. *A Course of Modern Analysis*. Cambridge Mathematical Library. Cambridge University Press, 4 edition, 1996. doi: 10.1017/CBO9780511608759.
- Wietek, A., Rossi, R., Šimkovic, F., Klett, M., Hansmann, P., Ferrero, M., Stoudenmire, E. M., Schäfer, T., and Georges, A. Mott insulating states with competing orders in the triangular lattice hubbard model. *Phys. Rev. X*, 11:041013, Oct 2021. doi: 10.1103/PhysRevX.11.041013. URL <https://link.aps.org/doi/10.1103/PhysRevX.11.041013>.
- Wilson, K. G. Renormalization group and critical phenomena. i. renormalization group and the kadanoff scaling picture. *Phys. Rev. B*, 4:3174–3183, Nov 1971a. doi: 10.1103/PhysRevB.4.3174. URL <https://link.aps.org/doi/10.1103/PhysRevB.4.3174>.
- Wilson, K. G. Renormalization group and critical phenomena. ii. phase-space cell analysis of critical behavior. *Phys. Rev. B*, 4:3184–3205, Nov 1971b. doi: 10.1103/PhysRevB.4.3184. URL <https://link.aps.org/doi/10.1103/PhysRevB.4.3184>.

- Wilson, K. G. The renormalization group: Critical phenomena and the kondo problem. *Rev. Mod. Phys.*, 47:773–840, Oct 1975. doi: 10.1103/RevModPhys.47.773. URL <https://link.aps.org/doi/10.1103/RevModPhys.47.773>.
- Wilson, K. G. and Fisher, M. E. Critical exponents in 3.99 dimensions. *Phys. Rev. Lett.*, 28:240–243, Jan 1972. doi: 10.1103/PhysRevLett.28.240. URL <https://link.aps.org/doi/10.1103/PhysRevLett.28.240>.
- Winkler, K., Thalhammer, G., Lang, F., Grimm, R., Hecker Denschlag, J., Daley, A. J., Kantian, A., Büchler, H. P., and Zoller, P. Repulsively bound atom pairs in an optical lattice. *Nature*, 441(7095): 853–856, Jun 2006. ISSN 1476-4687. doi: 10.1038/nature04918. URL <https://doi.org/10.1038/nature04918>.
- Wolf, S. A., Awschalom, D. D., Buhrman, R. A., Daughton, J. M., von Molnár, S., Roukes, M. L., Chtchelkanova, A. Y., and Treger, D. M. Spintronics: A spin-based electronics vision for the future. *Science*, 294(5546):1488–1495, 2001. doi: 10.1126/science.1065389.
- Wu, F. and Das Sarma, S. Collective excitations of quantum anomalous hall ferromagnets in twisted bilayer graphene. *Phys. Rev. Lett.*, 124:046403, Jan 2020. doi: 10.1103/PhysRevLett.124.046403. URL <https://link.aps.org/doi/10.1103/PhysRevLett.124.046403>.
- Wu, F., Lovorn, T., and MacDonald, A. H. Topological exciton bands in moiré heterojunctions. *Phys. Rev. Lett.*, 118:147401, Apr 2017. doi: 10.1103/PhysRevLett.118.147401. URL <https://link.aps.org/doi/10.1103/PhysRevLett.118.147401>.
- Wu, F., Lovorn, T., and MacDonald, A. H. Theory of optical absorption by interlayer excitons in transition metal dichalcogenide heterobilayers. *Phys. Rev. B*, 97:035306, Jan 2018a. doi: 10.1103/PhysRevB.97.035306. URL <https://link.aps.org/doi/10.1103/PhysRevB.97.035306>.
- Wu, F., Lovorn, T., Tutuc, E., and MacDonald, A. H. Hubbard model physics in transition metal dichalcogenide moiré bands. *Phys. Rev. Lett.*, 121:026402, Jul 2018b. doi: 10.1103/PhysRevLett.121.026402. URL <https://link.aps.org/doi/10.1103/PhysRevLett.121.026402>.
- Xiao, D., Yao, W., and Niu, Q. Valley-contrasting physics in graphene: Magnetic moment and topological transport. *Phys. Rev. Lett.*, 99:236809, Dec 2007. doi: 10.1103/PhysRevLett.99.236809. URL <https://link.aps.org/doi/10.1103/PhysRevLett.99.236809>.
- Xiao, D., Liu, G.-B., Feng, W., Xu, X., and Yao, W. Coupled spin and valley physics in monolayers of mos_2 and other group-vi dichalcogenides. *Phys. Rev. Lett.*, 108:196802, May 2012. doi: 10.1103/PhysRevLett.108.196802. URL <https://link.aps.org/doi/10.1103/PhysRevLett.108.196802>.
- Xu, M., Kendrick, L. H., Kale, A., Gang, Y., Ji, G., Scalettar, R. T., Lebrat, M., and Greiner, M. Doping a frustrated fermi-hubbard magnet. 2022a. doi: 10.48550/arXiv.2212.13983. URL <https://arxiv.org/abs/2212.13983>.

- Xu, X., Yao, W., Xiao, D., and Heinz, T. F. Spin and pseudospins in layered transition metal dichalcogenides. *Nature Physics*, 10(5):343–350, May 2014. ISSN 1745-2481. doi: 10.1038/nphys2942. URL <https://doi.org/10.1038/nphys2942>.
- Xu, Y., Kang, K., Watanabe, K., Taniguchi, T., Mak, K. F., and Shan, J. A tunable bilayer hubbard model in twisted wse2. *Nature Nanotechnology*, 17(9):934–939, Sep 2022b. ISSN 1748-3395. doi: 10.1038/s41565-022-01180-7. URL <https://doi.org/10.1038/s41565-022-01180-7>.
- Yamada, A. Magnetic properties and mott transition in the hubbard model on the anisotropic triangular lattice. *Phys. Rev. B*, 89:195108, May 2014. doi: 10.1103/PhysRevB.89.195108. URL <https://link.aps.org/doi/10.1103/PhysRevB.89.195108>.
- Yamada, T. Fermi-Liquid Theory of Linear Antiferromagnetic Chains. *Progress of Theoretical Physics*, 41(4):880–890, 04 1969. ISSN 0033-068X. doi: 10.1143/PTP.41.880. URL <https://doi.org/10.1143/PTP.41.880>.
- Yang, H.-Y., Läuchli, A. M., Mila, F., and Schmidt, K. P. Effective spin model for the spin-liquid phase of the hubbard model on the triangular lattice. *Phys. Rev. Lett.*, 105:267204, Dec 2010. doi: 10.1103/PhysRevLett.105.267204. URL <https://link.aps.org/doi/10.1103/PhysRevLett.105.267204>.
- Yang, J., Liu, L., Mongkolkiattichai, J., and Schauss, P. Site-resolved imaging of ultracold fermions in a triangular-lattice quantum gas microscope. *PRX Quantum*, 2:020344, Jun 2021. doi: 10.1103/PRXQuantum.2.020344. URL <https://link.aps.org/doi/10.1103/PRXQuantum.2.020344>.
- Yankowitz, M., Xue, J., Cormode, D., Sanchez-Yamagishi, J. D., Watanabe, K., Taniguchi, T., Jarillo-Herrero, P., Jacquod, P., and LeRoy, B. J. Emergence of superlattice dirac points in graphene on hexagonal boron nitride. *Nature Physics*, 8(5):382–386, May 2012. ISSN 1745-2481. doi: 10.1038/nphys2272. URL <https://doi.org/10.1038/nphys2272>.
- Yao, W., Xiao, D., and Niu, Q. Valley-dependent optoelectronics from inversion symmetry breaking. *Phys. Rev. B*, 77:235406, Jun 2008. doi: 10.1103/PhysRevB.77.235406. URL <https://link.aps.org/doi/10.1103/PhysRevB.77.235406>.
- Ye, Z., Cao, T., O’Brien, K., Zhu, H., Yin, X., Wang, Y., Louie, S. G., and Zhang, X. Probing excitonic dark states in single-layer tungsten disulphide. *Nature*, 513(7517):214–218, Sep 2014. ISSN 1476-4687. doi: 10.1038/nature13734. URL <https://doi.org/10.1038/nature13734>.
- Yoshioka, T., Koga, A., and Kawakami, N. Quantum phase transitions in the hubbard model on a triangular lattice. *Phys. Rev. Lett.*, 103:036401, Jul 2009. doi: 10.1103/PhysRevLett.103.036401. URL <https://link.aps.org/doi/10.1103/PhysRevLett.103.036401>.
- Zaanen, J., Osman, O. Y., Kruis, H. V., Nussinov, Z., and Tworzydło, J. The geometric order of stripes and luttinger liquids. *Philosophical Magazine B*, 81(10):1485–1531, 2001. doi: 10.1080/13642810108208566.

- Zaletel, M. P., Mong, R. S. K., Karrasch, C., Moore, J. E., and Pollmann, F. Time-evolving a matrix product state with long-ranged interactions. *Phys. Rev. B*, 91:165112, Apr 2015a. doi: 10.1103/PhysRevB.91.165112. URL <https://link.aps.org/doi/10.1103/PhysRevB.91.165112>.
- Zaletel, M. P., Mong, R. S. K., Karrasch, C., Moore, J. E., and Pollmann, F. Time-evolving a matrix product state with long-ranged interactions. *Phys. Rev. B*, 91:165112, Apr 2015b. doi: 10.1103/PhysRevB.91.165112. URL <https://link.aps.org/doi/10.1103/PhysRevB.91.165112>.
- Zeihner, J., van Bijnen, R., Schauf, P., Hild, S., Choi, J.-y., Pohl, T., Bloch, I., and Gross, C. Many-body interferometry of a rydberg-dressed spin lattice. *Nature Physics*, 12(12):1095–1099, Dec 2016. ISSN 1745-2481. doi: 10.1038/nphys3835. URL <https://doi.org/10.1038/nphys3835>.
- Zeng, H., Dai, J., Yao, W., Xiao, D., and Cui, X. Valley polarization in mos2 monolayers by optical pumping. *Nature Nanotechnology*, 7(8):490–493, Aug 2012. ISSN 1748-3395. doi: 10.1038/nnano.2012.95. URL <https://doi.org/10.1038/nnano.2012.95>.
- Zhang, C., Gong, C., Nie, Y., Min, K.-A., Liang, C., Oh, Y. J., Zhang, H., Wang, W., Hong, S., Colombo, L., Wallace, R. M., and Cho, K. Systematic study of electronic structure and band alignment of monolayer transition metal dichalcogenides in van der waals heterostructures. *2D Materials*, 4(1):015026, nov 2016. doi: 10.1088/2053-1583/4/1/015026. URL <https://dx.doi.org/10.1088/2053-1583/4/1/015026>.
- Zhang, J. M. and Dong, R. X. Exact diagonalization: the bose–hubbard model as an example. *European Journal of Physics*, 31(3):591, apr 2010. doi: 10.1088/0143-0807/31/3/016. URL <https://dx.doi.org/10.1088/0143-0807/31/3/016>.
- Zhang, S.-S., Zhu, W., and Batista, C. D. Pairing from strong repulsion in triangular lattice hubbard model. *Phys. Rev. B*, 97:140507, Apr 2018a. doi: 10.1103/PhysRevB.97.140507. URL <https://link.aps.org/doi/10.1103/PhysRevB.97.140507>.
- Zhang, S.-S., Zhu, W., and Batista, C. D. Pairing from strong repulsion in triangular lattice hubbard model. *Phys. Rev. B*, 97:140507, Apr 2018b. doi: 10.1103/PhysRevB.97.140507. URL <https://link.aps.org/doi/10.1103/PhysRevB.97.140507>.
- Zhang, Y. and Fu, L. Pseudogap metal and magnetization plateau from doping moiré mott insulator. 2022. doi: 10.48550/arXiv.2209.05430. URL <https://arxiv.org/abs/2209.05430>.
- Zhang, Y., Yuan, N. F. Q., and Fu, L. Moiré quantum chemistry: Charge transfer in transition metal dichalcogenide superlattices. *Phys. Rev. B*, 102:201115, Nov 2020. doi: 10.1103/PhysRevB.102.201115. URL <https://link.aps.org/doi/10.1103/PhysRevB.102.201115>.
- Zhang, Y.-H., Sheng, D. N., and Vishwanath, A. Su(4) chiral spin liquid, exciton supersolid, and electric detection in moiré bilayers. *Phys. Rev. Lett.*, 127:247701, Dec 2021. doi: 10.1103/PhysRevLett.127.247701. URL <https://link.aps.org/doi/10.1103/PhysRevLett.127.247701>.

- Zhou, Y., Sung, J., Brutschea, E., Esterlis, I., Wang, Y., Scuri, G., Gelly, R. J., Heo, H., Taniguchi, T., Watanabe, K., Zaránd, G., Lukin, M. D., Kim, P., Demler, E., and Park, H. Bilayer wigner crystals in a transition metal dichalcogenide heterostructure. *Nature*, 595(7865):48–52, Jul 2021. ISSN 1476-4687. doi: 10.1038/s41586-021-03560-w. URL <https://doi.org/10.1038/s41586-021-03560-w>.
- Zhu, Z., Sheng, D. N., and Vishwanath, A. Doped mott insulators in the triangular-lattice hubbard model. *Phys. Rev. B*, 105:205110, May 2022. doi: 10.1103/PhysRevB.105.205110. URL <https://link.aps.org/doi/10.1103/PhysRevB.105.205110>.
- Zhu, Z. Y., Cheng, Y. C., and Schwingenschlögl, U. Giant spin-orbit-induced spin splitting in two-dimensional transition-metal dichalcogenide semiconductors. *Phys. Rev. B*, 84:153402, Oct 2011. doi: 10.1103/PhysRevB.84.153402. URL <https://link.aps.org/doi/10.1103/PhysRevB.84.153402>.
- Zohar, E., Cirac, J. I., and Reznik, B. Quantum simulations of lattice gauge theories using ultracold atoms in optical lattices. *Reports on Progress in Physics*, 79(1):014401, dec 2015. doi: 10.1088/0034-4885/79/1/014401. URL <https://dx.doi.org/10.1088/0034-4885/79/1/014401>.